Inelastic diffractive event classification in proton-proton collision with the CMS experiment

Zur Erlangung des akademischen Grades eines
Doktors der Naturwissenschaften
bei der KIT-Fakultät Physik
des Karlsruher Instituts für Technologie (KIT)

genehmigte
DISSERTATION
von

Melike Akbiyik
aus der Türkey, Yüksekova

Tag der mündlichen Prüfung: 13.07.2018
Referent: Prof. Dr. Thomas Müller
Korreferent: Prof. Dr. Dr. h.c. Johannes Blümer
Betreuer: Dr. Ralf Ulrich

Abstract

This thesis is devoted to diffraction physics at the CERN LHC. The experimental part of the work studies rapidity gap production in the run 2 data samples recorded by the CMS experiment at $\sqrt{s} = 13\,\text{TeV}$. A multivariate analysis method based on boosted decision trees is developed to determine the cross-section of individual single diffractive (SD) and double diffractive (DD) processes. Diffractive interactions are characterized by rapidity gaps, which are regions in the detector devoid of particles and can be measured with a combination of central tracking and very forward calorimeters such as CASTOR. In hadronic collisions, most of the primary energy flows in the forward direction, which is why the forward region is in particular extremely important to characterize events. An event classifier is used to distinguish which process belongs to a specific inelastic event. This event classification is done with the charged particle tracks reconstructed in the silicon pixel detector in combination with all calorimeter towers of CMS. The efficiency and purity are optimized. The classification uses global observations made by CMS in the huge acceptance region $-6.6 < \eta < 5.2$, and down as close as possible to the noise levels. Such a comprehensive multivariate study has never been attempted before. The advantage is an optimal use of CMS for diffractive event classification and thus, a high precision of the measurement. One result of this thesis is an indication of a very slow rise of the single diffractive cross section at the highest energies. Some event generators are challenged by these data. It could be that this is first signs of protons becoming fully opaque in a central collision.

Zusammenfassung

Ziel der Arbeit ist es diffraktive Physik am CERN LHC zu untersuchen. Der experimentelle Teil der Arbeit befasst sich mit der Untersuchung der Erzeugung von Rapiditätslücken in Run 2 Daten, die mit dem CMS Experiment bei $\sqrt{s} = 13\,\text{TeV}$ aufgezeichnet wurden. Eine multivariate Analyse Methode, basierend auf "boosted decision trees" wurde entwickelt, um die Wirkungsquerschnitte von einzel- (SD) und doppel- (DD) diffraktiven Ereignissen zu bestimmen. Diffraktive Ereignisse sind durch Rapiditätslücken gekennzeichnet, welches Bereiche im Detektor ohne Teilchenerzeugung sind. Solche Lücken können durch eine Kombination von zentralen Spurdetektoren und Vorwärtskalorimetern wie CASTOR nachgewiesen werden. In hadronischen Kollisionen wird ein Großteil der erzeugten Energie in die Vorwärtsrichtung gelenkt. Dies ist der Grund dafür, dass Vorwärtsdetektoren besonders wichtig sind in der globalen Charakterisierung von Ereignissen. Eine Klassifizierung von Ereignissen wurde entwickelt um inelastische Kollisionen entsprechend einzuordnen. Die Klassifizierung basiert auf Messdaten des zentralen Silizium Spurdetektors, sowie aller Kalorimeter Zellen des CMS Experimentes. Die Charakterisierung verwendet globale Beobachtungen des CMS Experimentes im riesigen Akzeptanzbereich von $-6.6 < \eta < 5.2$ und so nahe wie möglich am Rauschlevel. Ein derart umfassender Einsatz multivariater Analysetechniken wurde in CMS bisher noch nicht verfolgt. Die Arbeit verspricht sich davon einen optimalen Einsatz von CMS Daten für die Klassifizierung von diffraktiven Ereignissen sowie eine hohe Präzision der erzielten Messungen. Ein Ergebnis der Arbeit ist ein Anzeichen für einen nur langsamen Anstieg des einzel-diffraktiven Querschnittes hin zu sehr hohen Energien. Einige Ereignisgeneratoren haben mit dieser Schlussfolgerung Schwierigkeiten. Es könnte sein, dass diese Daten ein erster Hinweis darauf sind, dass zentrale Proton-Proton Kollisionen vollkommen opak werden.

Contents

1 Introduction

Diffractive processes form a significant contribution to the total inelastic cross section and therefore it is very important to understand the mechanism behind them. The aim of this thesis is to develop a selection for single diffractive (SD) and double diffractive (DD) events, and, in addition to this, study some of the properties of these events. Inclusive diffractive interactions cannot be calculated within perturbative quantum chromodynamics (pQCD) [1–4], and traditionally have been described by models based on Regge theory [5]. It is very difficult to understand theoretically [6]. However, very important because of the large cross section and contribution e.g. to the underlying event and pileup in particular also at high luminosity LHC [7]. Furthermore, at ultra-high energies in cosmic ray air showers, diffraction is a major effect with important consequences for the interpretation of cosmic ray data [8]. In this thesis I present the first observation of soft diffractive dissociation in proton-proton collisions of LHC Run 2 at $\sqrt{s} = 13\,\text{TeV}$ using a novel multivariate event classification. It is significantly important to choose a well-motivated parameter set since the performance of the classification method depends on the used variables. I use tracks, energies, and towers from forward hadronic and CASTOR [9] calorimeter as input variables. Several input sets of the classification variables are compared to see the performance using the different simulations such as EPOS [10] and Pythia 8 [11]. Diffraction is classified from the two final state hadronic systems separated by the largest rapidity gap in the event. Runs are selected by requiring that the relevant components of the CMS [12]detector were fully functional, in particular, the CASTOR forward calorimeter, HF, and pixel tracker. The application of multivariate classification on global event properties using all components of the CMS experiment is by itself a big challenge. All aspects of the CMS experiment contribute and must be studied. The thesis provides a basic theoretical introduction needed for the work in Chapter 2. A brief overview of the extensive air showers, cosmic rays, the Standard Model and Quantum Chromodynamics [13] is given.

In the chapter 3, we will take a brief look at experimental methods that were used for this thesis. It also gives a short introduction on multivariate analyses with TMVA and boosted decision tree method [14]. In my thesis as a fundamental part of the cross section measurement, I develop a method to cross-check the CMS luminosity scale. The CMS experiment collected about $35\,nb^{-1}$ of proton-lead collision data in 2013 (see in Chapter 4) In this chapter, I present the analysis of the luminosity determination from ultra-peripheral collisions (UPC) in the proton-lead collision at 5.02 TeV. The cross sections for exclusive $\gamma\gamma \to l^+\,l^-$ production is used [15]. The dilepton is a pure electromagnetic process where the cross section can be calculated very precisely. This is why it was used to check the

existing luminosity scale of CMS in an independent way. I found that the standard Van-der-Meer scan [16] of CMS is consistent with experimental uncertainty with UPC cross check.

Furthermore, to characterize diffractive dissociation the forward detectors are extremely important. In this thesis, I depend on CASTOR for this purpose to a significant degree. In this context, many tasks were carried out to improve the detector performance. I developed the calibration of the CASTOR calorimeter by analyzing beam halo muons events collected during the LHC operation (see in Chapter 4). The CASTOR data proved to be extremely important for my analysis. The main part of the thesis describes the measurement of the diffractive cross section and is given in Chapter 5. This chapter explains how the event selections is done, how rapidity gaps are described, and used for estimating of diffractive fractions in the total inelastic cross section. For this work, the SD from DD processes are redefined into new SD-like and DD-like templates. Specifically the CASTOR detector ($-6.6 < \eta < -5.2$) is crucial to separate SD to DD events, it allows us to detect the hadronic system of the mass M_Y when it escapes the central detector. The rates and a process-specific cross section of SD and DD processes are determined using a multivariate analysis with the boosted decision trees (BDTs) method. The aim of event selection is to determine what kinds of interaction happened given a set of observed variables from the final state. The result of noise study is presented, the identification of rapidity gap signatures relies crucially on the suppression of calorimeter noise contributions. In order to compare gap distributions between MC and data, it is essential to have a good description of the calorimeter noise in MC. Very precisely data-MC validation is studied to optimize agreement, as well as efficiency and acceptance are studied and maximized. These measurements are compared to results from other experiments and to phenomenological predictions. The data were obtained with a field strength of 0 T in the CMS magnet in June 2015. I define the rapidity gaps by pseudorapidity of charged particles from tracks in the pixel detector in combination with calorimeter towers. In the absence of magnetic field, charged particles propagate on straight line trajectories. The yield of primary charged long-lived particles in inelastic proton-proton collisions is determined using the hit-pairs and straight line tracks in the pixel detector. The measurement of this thesis represents the highest energy results on the diffractive cross section so far. The groundbreaking use of multivariate method applied in this work resulted is a more precise analysis, and consequently smaller experimental uncertainties compared to previously published data. The application of multivariate classification on global event properties using all components of the CMS experiment is by itself a big challenge. It is interesting to note that the single diffractive cross section σ_{SD} $6.9\,(-1.4, +1.6)\,(\text{sys})\,\text{mb}$ is smaller than almost all models predict. Some models are severely challenged by that.

The Pierre Auger Observatory [17, 18] studies ultra-high-energy cosmic rays (UHECR), offers a unique environment to search for phenomena of particle physics beyond the reach of particle accelerators. The researchers from astrophysics especially some aspects of the shower phenomenon promise to give new insights on hadronic physics at energies beyond that reached by the LHC. The diffractive cross section is also of big importance for the

simulation of extensive air showers [19]. The measurement of the inelastic proton-proton cross section at $\sqrt{s} = 57\,\text{TeV}$ with the Pierre Auger Observatory identified low-mass single diffraction as one source of significant uncertainty for such analyses. The theory of strong interaction (QCD) is well established but still no predictions can be made for soft particle production with low momentum transfer.

2 Theoretical background

In this chapter, I will introduce a short description of the cosmic rays and extensive air showers, and briefly the theoretical and phenomenological background for the standard model of particle physics. Particle and astroparticle physics are both searching for aspects of the science of particles and their interactions. They have many connections in experimental methods, in particular, some features of the shower phenomenon studies from astrophysics promise to give new opportunities on hadronic physics at energies beyond that reached by the LHC.

2.1 Cosmic rays and extensive air showers

Cosmic ray particles and radiation incident from outside the Earths atmosphere. The cosmic rays nuclei are deflected by galactic and intergalactic magnetic fields and they lose information about their acceleration source. A goal of the studies of the cosmic rays is searching their origin and which processes they undergo on their way, how those particles are accelerated, their mass composition.

2.1.1 Cosmic rays

Cosmic rays can be characterized by their energy, and there are two type cosmic rays which are charged cosmic rays and neutral cosmic rays. Charged cosmic rays consist of electrons and nuclei, while neutral cosmic rays consist of neutrons, neutrinos or photons. A different type of source is responsible for cosmic rays at higher energies, and different sources could have a different maximum energy. Understanding of the mass composition of cosmic rays can be an answer to the question of the origin of the cosmic ray. The mass of the primary particle has to be estimated from detection of the secondary particles. Cosmic rays are mainly atomic nuclei, with energies from less than 100 MeV up to at least a few 100 EeV, of which about 90% are hydrogen nuclei(protons), 9% are helium nuclei and the remaining 1% is composed of heavier nuclei and electrons. These come from primary sources, while there are very small proportions of positrons and antiprotons, which can be of secondary origin and generated by interactions of the primary particles with interstellar gas.

The shape of the energy spectrum of the cosmic ray flux gives information about such processes they undergo on their way during traveling to the Earth. The cosmic ray flux follows the power law:

$$\frac{\mathrm{dN}}{\mathrm{dE}} \propto \mathrm{E}^{-\gamma}. \tag{2.1}$$

N is the number of particles with energy E. The cosmic ray spectra of the highest energy cosmic rays are shown in figure 2.1, are scaled with the energy to the power of 2.5. This scaling reveals the features of the knee and the ankle of the cosmic ray spectrum. The spectrum extends to very high energies and extends from about 10^9 up to 10^{20} eV or more. The index γ changes from 2.7 to 3.1 at about 4×10^{15} eV, which is called the knee region and at about 4×10^{18} eV the spectrum flattens again [20]. This is called the ankle, may be suggestive of an extra-galactic source, since the galactic magnetic field could not contain such particles inside our local galaxy. The region between the knee and the ankle is interpreted as the transition region from galactic to the extragalactic origin of cosmic rays. The composition of sources of the cosmic rays changes in this region and also the flux of cosmic rays. At energies larger than 10^{20} eV a sharp (cut-off) can be seen in figure 2.1, because of the GZK cut-off due to pion production in collisions with the microwave background photons in the following process:

$$\begin{aligned} \gamma_{\mathrm{CMB}} + p \rightarrow & \Delta^+ \rightarrow p + \pi^0 \\ \gamma_{\mathrm{CMB}} + p \rightarrow & \Delta^+ \rightarrow n + \pi^+ . \end{aligned} \tag{2.2}$$

However, origin of these features in the energy spectrum is still unknown. A composition-sensitive measurement is crucial to understand the properties of the cosmic ray accelerators. The maximum energy of the acceleration mechanism should be proportional to the charge Z of the nuclei. Since the rate of different elements changes with energy since energy dependent acceleration and propagation processes. For instance, protons and light nuclei like alpha particles are more abundant in the universe than heavier nuclei, because heavy nuclei have a significant abundance among the cosmic rays only above the maximum energy for protons and helium nuclei.

2.1.2 Physics of extensive air showers

When cosmic rays interact with the Earth's atmosphere particles and produce secondary particles. That plays the same role as a target in an accelerator beam. A cosmic ray persuades extensive air shower which is composed of three components, electromagnetic, muonic and hadronic. The interaction between high-energy cosmic rays and the air produces a correlated cascade of secondary particles. The air shower process starts with the collision of the primary cosmic ray with a nucleus close the top of the atmosphere. The

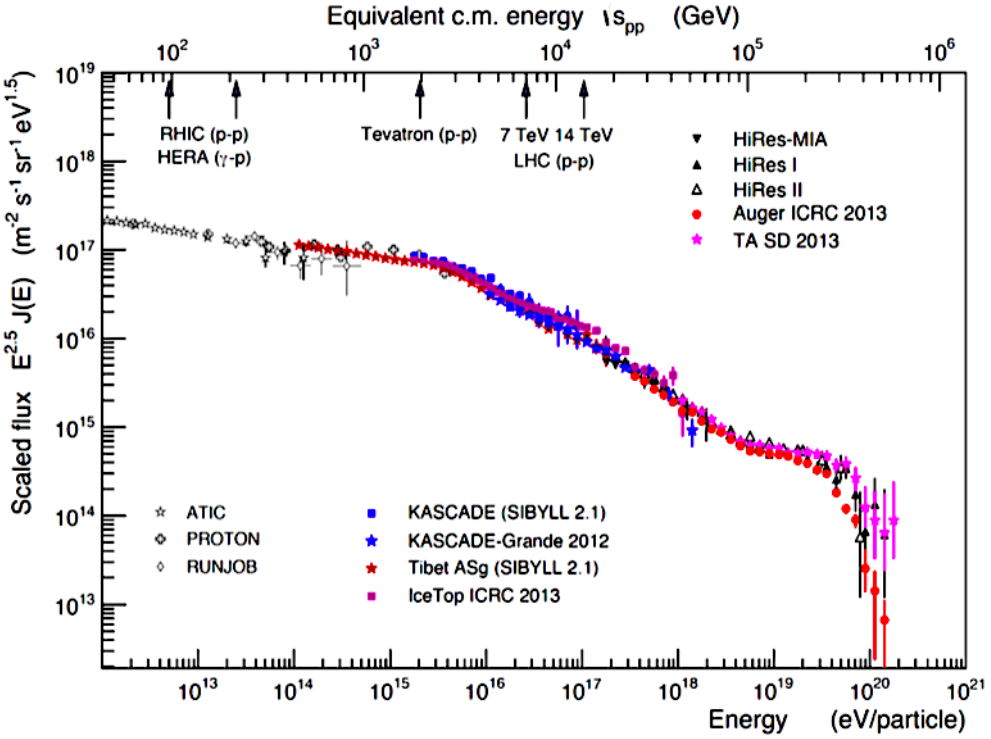

Figure 2.1: Cosmic-ray energy spectrum reconstructed from various air-shower measurements, all-particle energy spectrum of the cosmic rays scaled by $E^{2.5}$. A steeping of the spectrum becomes visible at about 4.10^{15} eV (first knee) and a second one at about 4.10^{17} eV (second knee). A flattening appears at about 4.10^{18} eV (ankle) [20].

schematic view of an extensive air shower developing in the atmosphere can be seen in Fig. 2.2. This first collision produces many unstable secondary particles, mostly pions, and other mesons. All types of pions are produced in the processes when high energy cosmic ray protons and other hadronic cosmic ray components hit matter in the Earth's atmosphere. Three different pions exist, which is positively charged, negatively charged and neutral. The characteristic experimental signature of charged pion is relatively long-lived and they collide with another nucleus before decaying. When charged pions decay, they produce muons and neutrinos, and higher−energy muons can reach deep underground, and for this reason, they are called to feature the hard component of the cosmic radiation. A neutral pion is a short−lived particle produced when cosmic ray protons smash into normal protons. The neutral pion quickly decays into a pair of photons (gamma rays) before interacting with nuclei in the atmosphere, and emission that exhibits a swift and characteristic decline at lower energies [21]. The photons interact with the nuclei in the air to produce electron−positron pairs, which in turn will produce photons via the bremsstrahlung process. The photons from the decay develop electron−photon cascades. This process is called an electromagnetic shower. If the primary particle is a high−energy proton or heavier nucleus, a nuclear cascade will develop through the atmosphere and this process of a cascade of particles which is defined as a hadronic shower. The proton produces mesons in these interactions, and they can, in turn, generate other particles in the next collisions. In the electron−photon shower, the electrons lose the bulk of their energies in a radiation length, but the nucleons can penetrate through several interaction lengths. Both types of processes are called extensive air showers, which is defined as the cascade of ionized particles and electromagnetic radiation produced after the interaction of the primary particle in the Earth's atmosphere.

A maximum value is the number of particles in the shower reaches the highest value, where near to the ground state but it is slightly higher than the energy of the primary particle. In the shower development muons and neutrinos, rates have to be individually understood. In the first aspect, these particles do not contribute to the further shower development, because their interaction probability with the atmosphere is low, and they have a high chance to reach the ground level. Neutrinos are generally invisible to air-shower detectors. The electron number in the shower maximum is a good measurement for the energy of a shower. In the Heitler model prediction, the total number of electrons in the shower maximum is independent of primary energy and the primary mass. However, the model assumption does not match the number of muons. The total number of muons in air shower is large since every hadronic collision produce secondary particles, and each charged hadron produces one muon after they decay. The muon component of the shower is also invisible to most detection methods, except for dedicated particle detectors or for Cherenkov light detection in water or ice. Consequently, the atmospheric depth of the shower maximum and the electron-muon ratio are the two main objects for estimating the type of the primary particle. In the air, shower has the large number of particles undergoing, stochastic interaction processes, and also all secondary particles produced in high and low energy collision. The development of the air shower cannot be practically

approximated. Thus, for analyses and interpretations of measurements, air showers are generated with Monte Carlo event generator. The hadronic interaction models suffer a major systematic uncertainty for the interpretation of any air shower measurement since the center of mass energy in the first interaction exceeds the maximum energy studied at accelerators like LHC at CERN. Interaction forward region, where high pseudo-rapidities, can be important for the modeling of the air shower. Therefore, the hadronic interaction models use extrapolations and postulated assumptions for ultra high energy collisions. Until now, no hadronic interaction model has been able to consistently predict all air shower measurements. The models describe fewer the number of muons on the ground than measured. But, the electromagnetic components of air showers well described for the radio emission.

The detection of cosmic rays has been accomplished by a variety of techniques. It is too different above $\approx 10^{15}$ eV to detect primary particles above the atmosphere before the decay. The ground-based experimental instruments must be used to measure the extensive air shower produced by these primary cosmic rays. The flux of cosmic rays of about 10 MeV to 10 TeV is measure directly because it is high enough for detector area and measurement time. The direct detection of cosmic rays is measured with satellite or balloon experiments. For energies larger 10 TeV the lower flux leads to the ground-based detectors measuring the secondary particles generated in the air shower experiment. From detecting an extensive air shower, a reconstruction is done by estimation the primary particle's energy, composition, and arrival direction. These ground detection detectors sample the charged particles in the shower, tanks containing liquid scintillator or water Cherenkov counters. This technique is also used by the Pierre Auger Observatory which was built to study cosmic rays of ultra-high energy and the steep flux suppression of the highest energy cosmic rays.

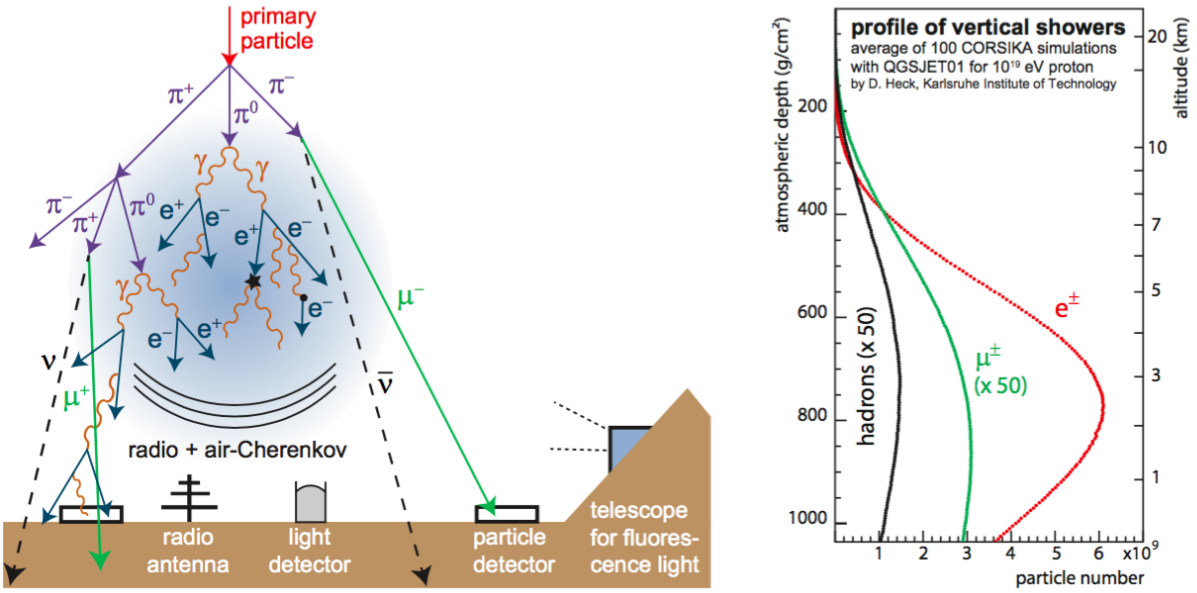

Figure 2.2: Development of cosmic-ray air showers.

2.2 The Standard model of particle physics

The fundamental structure of matter in the universe is made of elementary particles, and governed by four fundamental forces. The standard model is the theory to explain what are the basic building blocks of matter and how the nature of the forces is related to each other. It was formulated in the early 1970*s* and has successfully explained almost all experimental results and precisely predicted a wide variety of phenomena. It incorporated all that is known about subatomic particles at the time and predicted the existence of Higgs boson [22] as well. Additionally, the standard model of particle physics helps to understand the processes transpired in the early Universe before the atoms could form.

The 12 fundamental fermions can be classified leptons and quarks. They are divided into generations depend on their rest mass (energy), angular momentum, spin. There are three generations, and each of generation is essentially identical except their mass. The Dirac equation of relativistic quantum mechanics describes the dynamics of each fermion. One of the results of the Dirac equation is that each of the fermions has an antiparticle state with the same mass but opposite charge. There are the spin-1 gauge bosons of the different interactions, the photon, gluons, and the $W^{+,-}$ and the Z^0. The standard model is completed by spin-0 Higgs boson. The interactions experienced by each particle, as far as we know, there are four fundamental forces, strong, electromagnetic, weak, and gravitational, of this only gravity is not yet described by the standard model. To each of these interactions belong a physical theory. The coupling constants is a quantity to

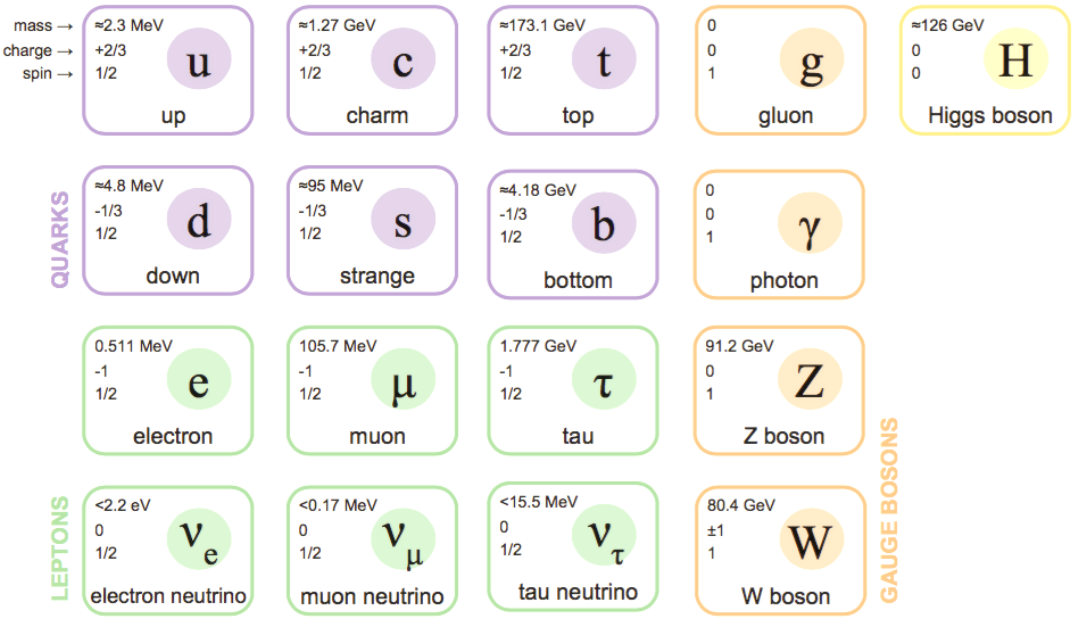

Figure 2.3: The Standard Model of elementary particles with the three generations of matter and gauge bosons.

measure the strength of interaction. It is not constant value, because it is the separation distance between the interacting particles which is called a running coupling constant. It depends on the energies of the particles involved. Gravitational and electromagnetic interactions act on large distances, in contrary weak and strong interactions, are limited to typical distances respectively 10^{-3} and 1 fm.

Quantum electrodynamics (QED) describes the interactions of charged particles, electromagnetic interactions are mediated by photons. The strength of the electromagnetic force is set by the coupling constant, its unit is the fundamental charge. In QED is gauge invariance which is based on elements of a group called U(1), the 'U' indicating for unitary, and the 1 that it refers to a rotation in one dimension. U(1) is related to conservation of the electric charge. All quarks and all leptons experience the weak force. The mediators of weak interactions are the W's (W^+ and W^-) and the Z^0. In contrast to photon and gluons, W's and Z are massive. The weak and electromagnetic interactions are unified. The electroweak model was formulated by Glashow, Weinberg, and Salam. It postulates four massless vector bosons; a triplet W^+, W^- and W^0 belonging to the SU(2) group and b^0 belonging to the U(1) group, that is, a system with SU(2) x U(1) symmetry [23, 24]. The '2' in the SU(2) referring to the dimension of the matrices, the 'U' standing that the transformation is again unitary. The 'S' stands for special SU(2) is based on a subgroup of U(2) in which the matrices are traceless. The SU(2) x U(1) symmetry of the model is broken by the Higgs mechanism, which is that Higgs components are absorbed by the

states W^+, W^- and the Z^0, giving the mass to vector bosons W^+, W^- and the Z^0.

Quantum chromodynamics(QCD) describes the interactions of colored particles, chromodynamic interactions by spin-1 bosons are called gluons. The strength of the chromodynamic force is set by the strong coupling constant colors, which are red (r), blue(b), and green (g). One important property of strong interactions that the forces between the quarks are a long range because the gluons have zero mass, while the forces between hadrons are not long range since hadrons have zero color charges. At the relatively large distances coupling, a constant is big, however, at very short distances (less than the size of a proton) it becomes small. This is known as asymptotic freedom phenomenon, the interaction gets weaker at a short distance (a distance of about 0.1 fm). Furthermore, gluons couple to the particle with non-zero color charges and gluons themselves also have zero charges, gluons couple to other gluons. In this strong interaction regime, the status is very complicated, and the perturbative theory is based on asymptotic freedom, which is limited to the short-distance region [6, 25, 26]. Keep in mind that this is a perturbation theory calculation, valid if the coupling is small. Quarks can't separate from one another when one tries to separate a quark from a hadron, energy builds up between the quarks with the growing distance and when it reaches a critical level, it leads to the production of a quark-anti-quark pair and a new hadron is formed. The quarks have never been seen in isolation [6]. Quarks can carry one of three colors, while anti-quarks carry the anti-color, and they can only exist in the form of colorless combinations. This property is called color confinement. The quark combinations called hadrons don't have color charge. For instance, a baryon (proton or neutron) consists of one red, one blue, and one green quark, the combination is being colorless. Similarly, a meson has a quark of a particular color and an anti-quark of that anti-color, is also colorless. Confinement requires that all naturally occurring particles be colorless. Each gluon carries one unit of color and one of anti-color, and there are nine species of gluons because of the electrically neutral, themselves carry color.

The electroweak theory is unifying the electromagnetic and weak interactions, and this unification is the possibility to unify the fundamental interactions, by incorporating the strong interactions with the electroweak, in which are called grand unified theories-GUTs. The idea behind the theory is that to unify the electroweak symmetry with the symmetry of the strong. The running coupling is one of the challenges for the unification since each the running coupling runs in different ways for the different interactions. Possible unification includes the supersymmetry [27], where each fermion has a supersymmetric boson partner; inversely, for each fundamental boson, there is a fermion partner. Supersymmetry is also formulated for avoiding the hierarchy problem which is about the radiative corrections from bosons and fermions largely cancel. The calculation of radiative corrections involved loops containing virtual fermions and bosons, and in loops lead to divergences in calculating the Standard Model parameters. Supersymmetry shows that the amplitudes for fermion and boson loops have opposite signs. In addition is that above the SUSY (supersymmetry) scale, the unification of the three running couplings is modified and they do come to cross nearly at a point, with a higher unification energy of around 10^{15} GeV. The experimental mass limits for SUSY particles are becoming searched [28, 29]. The mass scale of the

superpartners is less than about 1 TeV, so far there is no direct experimental observe, either for GUTs or for supersymmetry.

Collider physics

This section will describe the kinematics of the colliding particles, and which physics mechanisms and parameters are involved in high energy particle collisions. The collision of hadrons is a complex system contributing many particles, and several other factors must be taken into account.

Reliable predictions for a static property of hadrons and their interactions can be extracted from QCD theory with experimental PDFs results from hadronic interactions. As known, in high-energy particle collisions, the cascades of radiation (a parton shower) produced from QCD [1, 4, 30]. A precise knowledge of the parton distribution functions (PDFs) of the proton is essential in order to make predictions for the Standard Model processes at hadron colliders [31]. The parton density function gives the probability of finding in the proton a parton of a particular flavor, as a function of the x variable, which can be interpreted as the function of proton's longitudinal momentum is carried by parton, in figure 2.4 shows the PDFs from the particle data group [32]. The PDFs have to be determined experimentally. In high energy particle collisions, there are two distinct classes of classified the hadronic processes, soft and hard processes. The soft processes are elastic hadron-hadron scattering and diffractive processes, which are characterized by an energy scale of the hadron size ($1 \approx fm$) and the squared of the momentum transfer is generally small. As shown in figure 2.6, each of the two incoming protons emits a virtual photon. The hard process is deep inelastic scattering (the squared of the momentum transfer is the virtually of the exchanged photon or vector boson). Furthermore, inelastic scattering experiments gave the first clear evidence for scattering from individual quarks in the nucleon, and elastic scattering gave the first measurement of the size of the proton. Before I go into detail about the individual, the following concepts should be clarified.

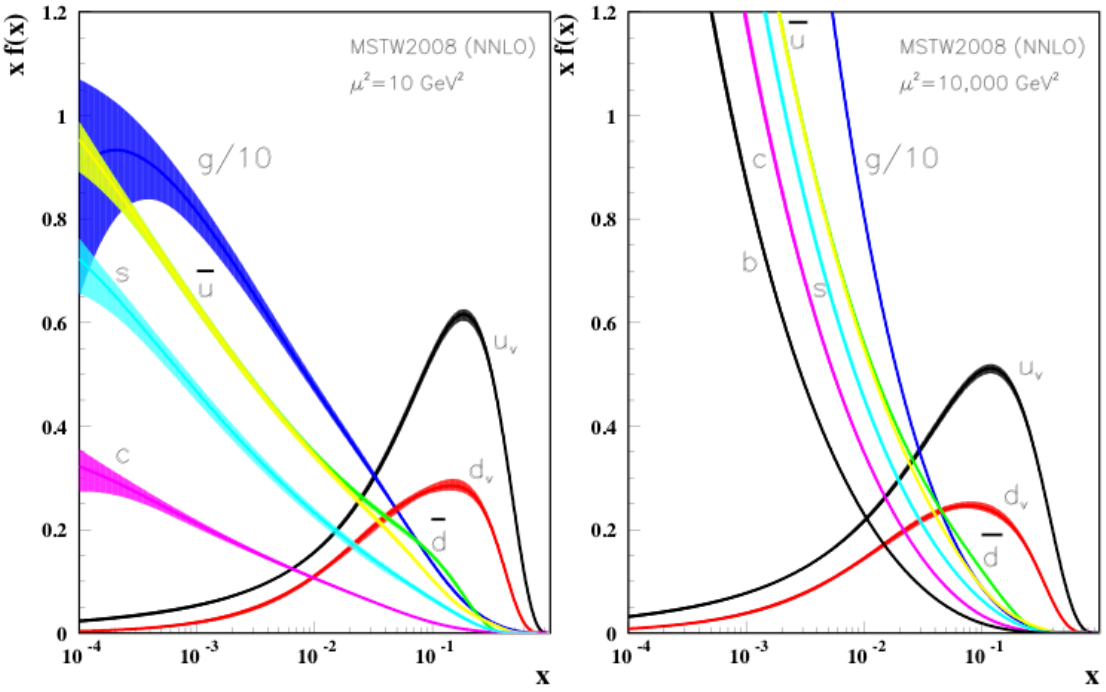

Figure 2.4: Parton distribition functions for protons for $\mu^2 = 10$ GeV^2 [32].

2.3 The kinematics of the colliding particles

The scattering processes are based on the identification of the kinematics. The experimental signatures of diffraction and elastic scatterings have a specific kinematic configuration of the final states. For example, if we want to study on elastic scattering of two hadrons in pp collisions, we have to know its kinematic configuration.

The kinematics of elastic scattering of two-body reactions

$$p_1 + p_2 \rightarrow p_3 + p_4, \qquad (s - channel). \tag{2.3}$$

In pp the protons traveling at relativistic speed, and total energy and momentum is always conserved, while mass is not.

A basic process, shown in figure 2.5, in which two incoming particles with four-momenta p_1, p_2 scatter and produce a final state of two particles with four-momenta p_3 and p_4. In the collisions total energy and momentum conservation can be expressed with four momentum transfer.

$$(p_1 + p_2) = 0. \tag{2.4}$$

These variables belong to the Mandelstam invariants, and two of them s, t are independent variables [33]. The variable of s is the square of the total center-of-mass (CM) energy and

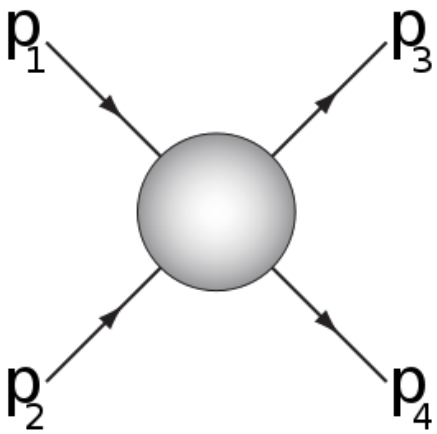

Figure 2.5: Two particles come in with momenta p_1 and p_2, they interact, and then two particles with different momentum (p_3 and p_4) leave.

has threshold value corresponding to the production of two particles of mass (the energy available for particle production). The t is the square momentum transfer which is always negative. The s-channel and t-channel processes are characterized by

$$s = (p_1 + p_2)^2 = E_{cm}^2,$$
$$t = (p_1 - p_3)^2 = (p_2 - p_4)^2. \tag{2.5}$$

As example, for reaction where one particle is kinematically at rest, the center-of-mass energy becomes

$$E_{cm} = \sqrt{s} = (p_1 + p_2)^2 = (p_1^2 + p_1^2 + 2p_1p_2).$$
$$= (m_1^2 + m_2^2 + 2E_1m_2) \approx \sqrt{2E_1m_2}. \tag{2.6}$$

If now we look at the single-diffractive processes

$$1 + 2 \to 3 + X \tag{2.7}$$

It can be described by three independent variables. The invariant mass of the X system is $M^2 = (p_1 + p_2 - p_3)^2$, that X is not a real particle on the mass shell and hence M^2 is not

a fixed number. In the CM system the four momenta of the three particles can be written

$$\begin{aligned} \mathrm{p}_1 &= (E_1, \mathbf{p}) = (E_1, 0, 0, \mathrm{p}_z), \\ \mathrm{p}_2 &= (E_2, \mathbf{p}) = (E_2, 0, 0, -\mathrm{p}_z), \\ \mathrm{p}_3 &= (E_3, -\mathbf{p}') = (E_3, \mathbf{p}_\perp, \mathrm{p}'_z), \end{aligned} \tag{2.8}$$

the asymptotic case when s and M^2 are much larger than the masses of the particles

$$\mid \mathbf{p} \mid = \mathrm{p}_z \simeq \frac{\sqrt{s}}{2}, \qquad E_1, E_2 \simeq \frac{\sqrt{s}}{2}, \tag{2.9}$$

for $s >> m_1^2, m_2^2$, and

$$\mid \mathbf{p}' \mid \simeq \frac{s - M^2}{2\sqrt{s}}, \qquad E_3 \simeq \frac{s - M^2}{2\sqrt{s}}, \tag{2.10}$$

for s, $M^2 >> m_3^2$. From

$$t = (\mathrm{p}_1 + \mathrm{p}_3)^2 = m_1^2 + m_3^2 - 2E_1E_3 + 2 \mid \mathbf{p} \mid\mid \mathbf{p}' \mid \cos\theta, \tag{2.11}$$

using Eqs.(2.9), (2.10) for $s >> m_1^2, m_2^2$ the transverse momentum of the outgoing detected particle is

$$\mathrm{p}_\perp^2 = \mathbf{p}'^2 \sin^2\theta \simeq -t(1 - \frac{M^2}{s}). \tag{2.12}$$

Now we should looked at Feynman's x_F which is defined as

$$x_F \equiv \frac{\mid \mathrm{p}'_z \mid}{\mathrm{p}_z}. \tag{2.13}$$

In hadron scattering the transverse momentum of the produced particle in high energy is small on average, $\mid \mathrm{p}'_z \mid \simeq \mid \mathbf{p}' \mid \simeq \mathrm{p}_z$ and, from (2.10) and (2.12)

$$\begin{aligned} \mid \mathrm{p}'_z \mid \simeq \mid \mathbf{p}' \mid &\simeq \frac{s - M^2}{2\sqrt{s}}, \\ x_F &\simeq 1 - \frac{M^2}{s}, \end{aligned} \tag{2.14}$$

the relations gives

$$t \simeq \frac{\mathbf{p}_\perp{}^2}{x_F}. \tag{2.15}$$

The triplet of the variables $[s, x_F, \mathbf{p}_\perp{}^2]$ defines single diffractive processes, and $\mid \mathrm{p}'_z \mid \simeq 0$, $x_F \simeq 0$ is called central region. The domain where $\mid \mathrm{p}'_z \mid \simeq \mathrm{p_z}$, $x_F \simeq 1$, is the fragmentation region and diffraction processes come into the latter region.

2.3.1 Cross sections

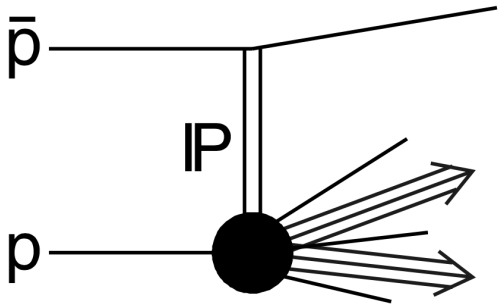

Figure 2.6: Illustration Pomeron exchange diagram for single diffraction Pomeron exchange [34].

The interactions of elementary particles quantitatively clarify in terms of cross sections, which is defined as the probability of an interaction will occur between a projectile particle and a target particle. The measurement of the total cross-section is performed in the following way. A projectile particle traveling towards a stationary target, a proton, will be scattered off the proton by some angle θ. The size of the angle depends on the impact parameter which is denoted by b, which describes the closest distance between the center of the potential interaction, where the particle has not been scattered. If instead, the incoming particle had an impact parameter of $b + db$ the scattering angle would have been $\theta + \mathrm{d}\theta$, if the particle travels through an infinitesimal area $\mathrm{d}\sigma$, it will be scattered by a solid angle of $d\Omega$. In pp collisions, the cross-section can be defined as $(\mathrm{d}\sigma)$ the probability per unit time, per unit flux of the incoming beam and per unit area density of target particles, for scattering the beam out into the solid angle.

The differential scattering cross section can be defined as

$$\frac{\mathrm{d}\sigma}{\mathrm{d}\Omega} = \frac{\mathrm{dN}}{\mathcal{L}\mathrm{d}\Omega}. \tag{2.16}$$

This equation also leads to $\mathrm{N} = \sigma\mathcal{L}$ when all solid angles are considered. The integrated luminosity is used as a measure of the size of collected data. Luminosity is the number of particles passing each other per unit time, per unit area. It is defined as

$$\mathcal{L} = \int \mathrm{Ldt}. \tag{2.17}$$

The cross-section has the same value when measured in the different laboratory systems because the the beam area is unchanged by a Lorentz transformation in the beam direction. The total cross section is the integral of dσ overall solid angles and are related to an observed number of elastic and inelastic events

$$\sigma_{tot} = \sigma_{elastic} + \sigma_{inel}. \tag{2.18}$$

Hadron-Hadron collisions, the interactions are classified by the characteristics of the final states. The interactions can be either elastic or inelastic, or these processes also can be classified as either soft and hard processes. Elastic scattering is defined when exactly the same particles come out after the collision without any exchange of quantum numbers and no multi-particle final state. The final and initial state particles are identical, and both protons emerge intact without the production of other particles, this is a special case of the optical theorem [8]. The only exchanged quantity is the momentum, and the particles do not break up. Later, I will explain the inelastic scattering processes in detail. Firstly, I want to start with the soft processes. In here the soft processes take part since the soft processes are elastic hadron scattering and diffractive processes. The only typical scale for the soft processes is the hadron size (about 1 fm) since they are characterized with energy scale of the hadron size. The momentum transfer squared $|t|$ is small about $1/R^2$ this can correspond few hundred MeV^2. These processes can not calculate theoretically with perturbation QCD, because a large value of R makes the calculations non-perturbative. These processes can be described by phenomenological models based on Regge theory([35]). Now we should look at the Regge theory for soft processes in the detail. Regge theory is the framework for the study of soft OCD processes, that describes high energy scattering at small t. Perturbation QCD is not a good way to describe soft processes, with general QCD jargon the coupling constant gets large enough to make the higher order terms non-negligible, thus making the process non-perturbation. Regge theory belongs to the t-channel models, which describes hadronic processes in terms of the t-channel exchange of a virtual particle called reggeon, which has stated on a reggeon trajectory. More generally, the correlation of the spin of the particle and its mass is used to define a trajectory. The contribution to a given reaction dependent on the quantum numbers and each trajectory has specific quantum numbers. That means each different processes will be contributed by different trajectories.

The t-dependence of the cross section is exponential $d_\sigma/d_t \approx e^{-R^2}|t|$. The cross section is important quantity to understand what is the mechanism undergoing these processes. The ratio σ_{el}/σ_{tot} is quite important observed evidence for physicist. The ratio is well known to decrease at low energies because of rising absolute value of the momentum exchange squared, $|t|$. The Regge theory explains that evidence with existence a forward diffraction peak which is defined by where the pomeron is raising the diffraction peak. The forward peak in the energy physics can be represented by an exponential of the form e$^{B(s)t}$(Fig. 2.7, Fig. 2.8). The slope of the diffraction peak depends on s so the elastics slope parameter B(s) which is t-independent at small t values and is also found to decrease when measured at

$|t|$ values larger than 0.02 GeV^2. Another important quantity is dip which appears around zero with increase energy at larger $|t|$ values. Its position is being roughly proportional to $1/\sigma_{tot}$. Data from TOTEM experiment were collected in proton-proton collisions at $\sqrt{s} = 7$ TeV shows the $|t_{dip}|$ moves to smaller values for high energies. Many theoretical models can describe the structure of the reason of the dip. They describe generally reason for the dip is about the imaginary part of the scattering amplitude, destructive interference between the parts of the amplitude lead to a dip in the elastic cross section.

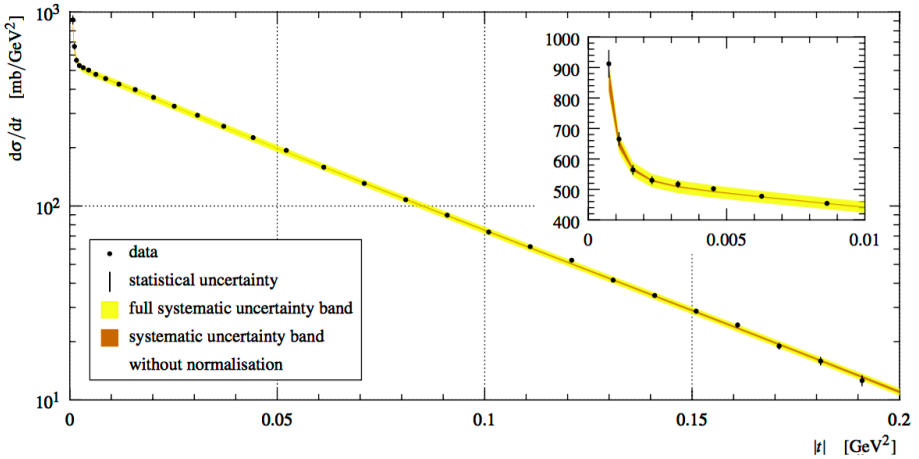

Figure 2.7: Differential cross-section with statistical(bars) and systematic uncertainties (bands). The bands are centred around a data fit including both nuclear and Coulomb components. A low-|t| zoom featuring cross-section rise due to the Coulomb interaction. [36].

Furthermore, antiparticles have a different behavior at small energies. The different behavior of the d_{el}^{pp}/dt and $d_{el}^{p\bar{p}/dt}$ is explained by the soft processes model of Donnachie and Landshoff in the framework of Regge theory with the existence of the three-gluon exchange mechanism [37, 38]. The three gluon exchange is expected to give a vanishing contribution to pp and p$\bar{\text{p}}$ scattering if the proton and antiproton have a quark-diquark structure. The idea behind is that the exchange of three gluons which couple to the valence quarks of the proton(or antiproton). The amplitude of this process has the different sign for these scatterings. Its interpretation with the amplitude of the diffraction peak is destructive in pp scattering, hence producing a dip but for p$\bar{\text{p}}$ case is constructive giving rise only to a break. A relevant way to measure the total cross-section for the soft processes that is large $|t|$ are highly suppressed which is the analogy to the optical theorem. Thus, the measurement is based on the $|t|$ of the elastic cross-section can be done with a luminosity-independent method. Since luminosity is a quantity not very accurately known, it cannot be used to precisely extract σ_{tot}. The TOTEM collaboration is used to the luminosity-independent approach for the measurement of the total cross-section [38]. The total cross-section of the luminosity-independent approach

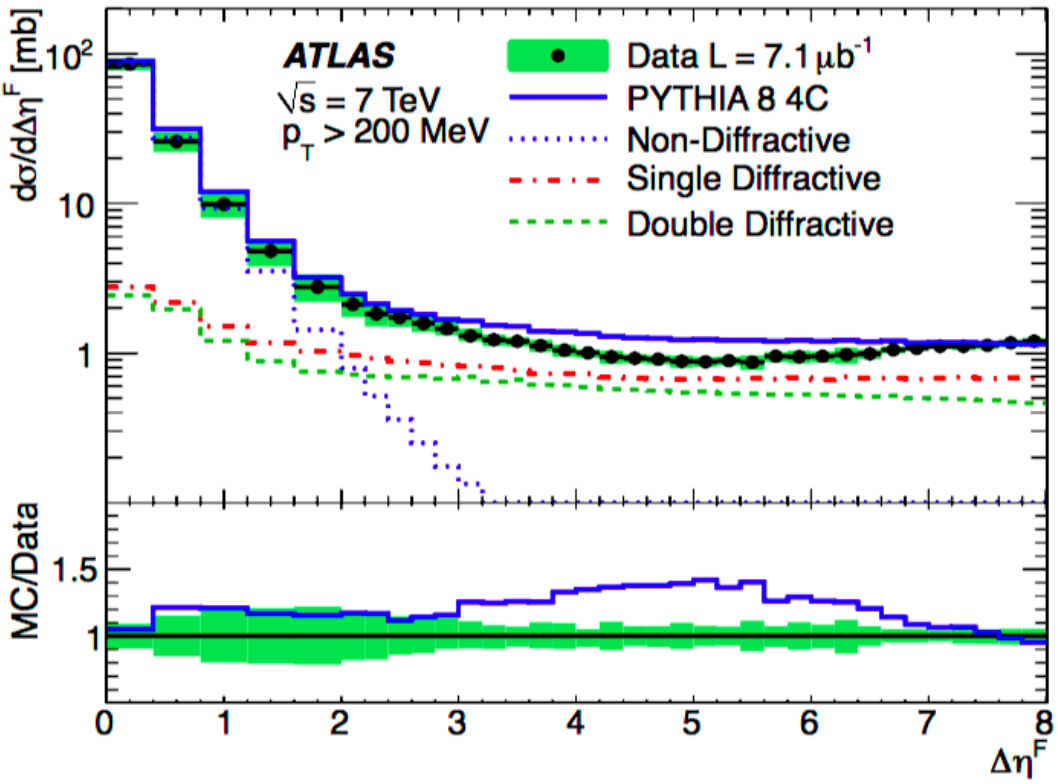

Figure 2.8: Inelastic cross section differential in forward gap size $\delta\eta^F$ at [37]. The shaded bands represent the total uncertainties. The full lines show the predictions pythia8. The dashed lines represent the contributions of the ND, SD and DD components according to the models.

$$\sigma_{tot} = \frac{16\pi}{1+\rho^2}\frac{(dN_{el}/dt)\mid_{t=0}}{N_{el}+N_{in}} \tag{2.19}$$

Where ρ is the ratio of the real to the imaginary forward amplitude. This implies that the real part of the amplitude in the forward direction provides information on the energy dependence of the total cross-section. In the energy region where the total cross-section is first decreasing then rising since ρ has initially a negative value, will rise, going through zero when the cross-section has a minimum and becoming positive at high energy. In addition, there is a limit for the rate of growth with an energy of any total cross-section that is total cross section cannot grow faster than $\ln^2 s$, that is

$$\sigma_{tot} \leq C \ln^2 s, \quad as \quad s \to \infty. \tag{2.20}$$

Where C is constant. The forward part of the amplitude is needed since it corresponds to no momentum transfer between the particles(a scattering angle is 0). By using a Fourier transformation, the scattering amplitude can be converted from a function of A(s,t) to a function of A(s, b). Where b is the absolute value of the impact parameter, which is a distance of the particles perpendicular to their longitudinal direction.

$$\sigma_{tot} = 8\pi \int dbIm(A(s,b))b \tag{2.21}$$

Where, A(s, b) is the profile function which is used to measure the opaqueness of the interacting particles. The scattering wave-like particles have $A(s,b) = 1$, if the impact parameter $0 < b < R_1 + R_2$ which is known as the black disk limit. It means that at the very high energy the effective radius of an interaction of two colliding hadrons would increase as log s and the opacity would also increase. The opaqueness of the colliding particles slowly increases with energy and puts important constraints on the models of high-energy scattering. Among existing models of high-energy collisions, this behavior is most naturally explained. This leads to being the expectation that asymptotically $\sigma_{tot} \sim (\log s)^2$.

Now we should look at the inelastic cross section in detail. In figure 2.10 the detector is sketched for several diffractive event signatures, picturing the empty regions where no particles are deposited. It implies that there is no exchange of quantum numbers between the colliding particles, the two systems are moving apart exchanging a color field with vacuum quantum numbers between them. There are two separate systems, with the same quantum numbers as the two incoming protons, it is required that there is a large, non-exponentially suppressed rapidity gap. This means if we represent by $\Delta\eta$ the final state rapidity gap, the rate of diffractive events is

$$\frac{dN}{d\Delta\eta} \approx constant, \tag{2.22}$$

to be compared with that of non-diffractive events which is

$$\frac{dN}{d\Delta\eta} \approx e^{-\Delta\eta}. \tag{2.23}$$

In order to reject a contribution of non-diffraction events, one has to use the condition of non exponentially suppressed. Diffractive processes can be distinguished only approximately from non-diffraction contributions. The total cross section is a sum of all possible interaction cross sections,

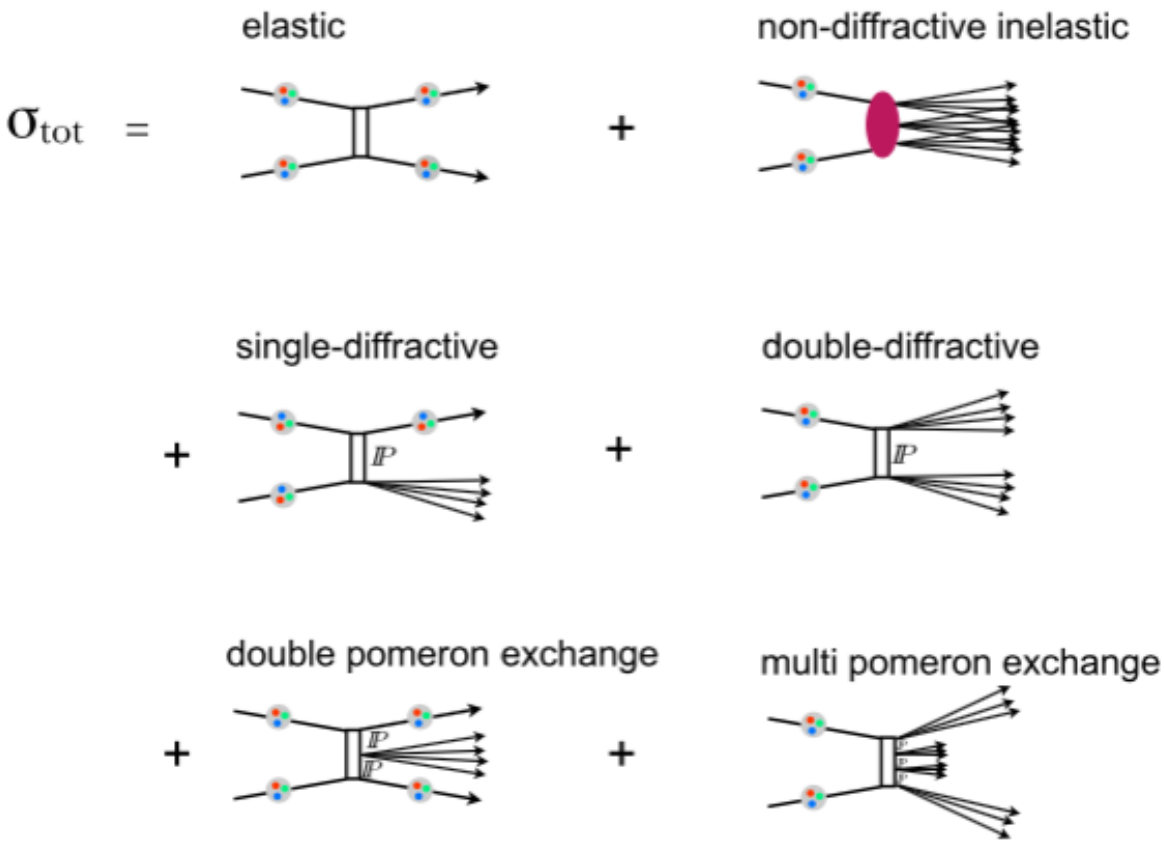

Figure 2.9: Diagrams of the various components of the total proton-proton cross section at the LHC.

$$\sigma_{tot} = \sigma_{ND} + \sigma_{elastic} + \sigma_{SD} + \sigma_{DD} + \sigma_{CD}, \tag{2.24}$$

where σ_{SD} is the single diffractive, σ_{DD} the double diffractive and σ_{CD} the central diffractive, and ND the non-diffractive cross section.

The differential cross-section exhibit a sharp forward peak and production cross-section depend on energy in the reverse the elastic cross-section. The single diffraction processes is shown as $\mathrm{p} + \mathrm{p} \to \bar{\mathrm{p}} + X$, and clear evidence of diffraction is seen experimentally about $M^2/s \sim 0.05$, where M^2 is the mass squared of the remnant of the hadronic X system. The pomeron cross-section M^2, dependence of the single diffraction with $t = 0$ condition is given by

$$\frac{d\sigma^{SD}}{dM^2 dt} \sim \frac{1}{(M^2)^{\alpha(0)}} \sim \begin{cases} \frac{1}{M^2} & \text{if } \alpha(0) = 1 \\ \frac{1}{(M^2)^{1+\epsilon}} & \text{if } \alpha(0) = 1 + \epsilon \end{cases} \tag{2.25}$$

The integrated cross-section of single diffraction is shown in Fig. 2.11, the ratio σ^{SD}/σ_{tot} decreases at high energy. The energy dependence is reverse the Regge theory prediction which gives (with the pomeron intercept $\alpha(0) = 1 + \epsilon$).

$$\sigma_{tot} \sim s^{\epsilon}, \quad \sigma^{SD} \sim s^{2\epsilon}, \quad \frac{\sigma^{SD}}{\sigma_{tot}} \sim s^{\epsilon} \tag{2.26}$$

With the elastic cross-section the Regge theory, expectation which is mentioned above, $\sigma_{el}/\sigma_{tot} \sim s^{\epsilon} \ln s$.

As mentioned before, in the theory description of hadronic interactions at high energies correspond to an exchange of an object rather than a particle, and soft interactions are presumed to be mediated by a color singlet exchange carrying the vacuum quantum numbers, usually referred as Pomeron (IP) exchange. The pomeron can be incorporated since it is considered to have an internal structure. Furthermore, the pomeron trajectory does not correspond to any known particle. Its trajectory has the quantum numbers of the vacuum. A simple way to visualize the parameterizations of the Regge trajectories, is to develop $\alpha(t)$ in power series around $t = 0$, in a linear function $\alpha(t) = \alpha_0 + \alpha' t$. The Regge theory prediction is then obtained by the optical theorem

$$\sigma_{tot} \propto \frac{1}{s} s^{\alpha(t=0)} \propto s^{\alpha_0 - 1} \tag{2.27}$$

The Eq. 2.27 implies that if the reggeon trajectories have $\alpha_0 > 0.5$, that leads to total cross-section decreasing with s of energy, while it is experimentally known the hadronic total cross sections decreases only up to $\sqrt{s} \sim 25-30$ GeV and than $\alpha_0 > 1$ that increase at higher energies. This evidence of the rising cross-section can be explained with the intercept of $\alpha_0 = 1.08$ of the pomeron into the Eq. 2.27. Theoretically aspect assume pomeron has a linear dependence with the condition of $\alpha_0 \leq 1$, $\alpha(t) = 1.08 + (0.25c^2)/\mathrm{GeV}^2$. With an

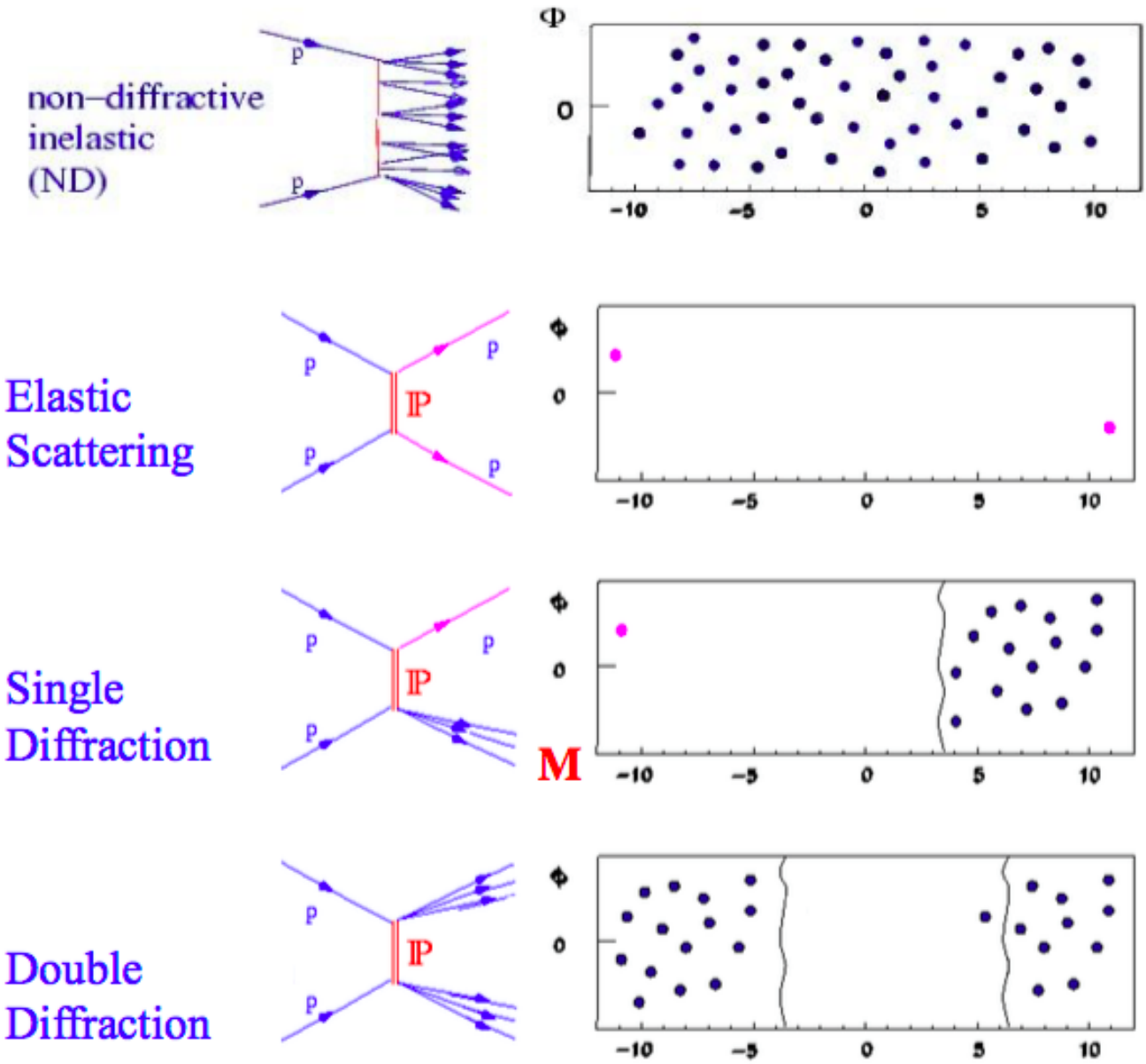

Figure 2.10: Sketch of the $\eta\phi$ detector view for the various diffractive processes in proton-proton scattering at the LHC.

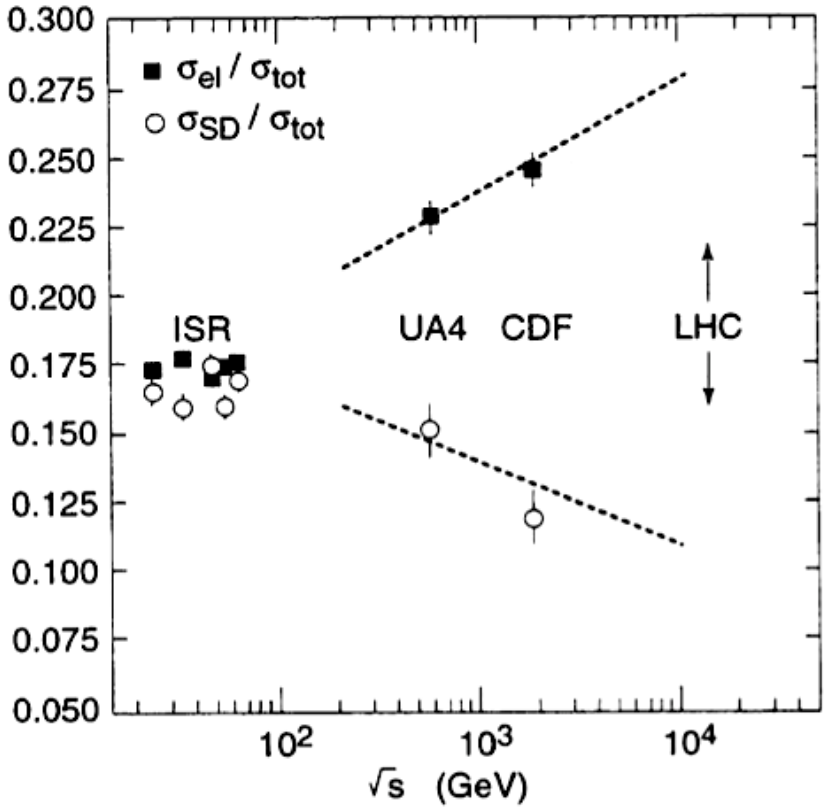

Figure 2.11: The ratio of the single diffraction dissociation to the total cross-section are shown as a function of energy [38].

intercept, $\alpha_0 = 1.08$ is often called soft pomeron. Now we can show the total cross-section in term of the Regge expression with one from pomerons

$$\sigma_{tot}(s) = Xs^{\epsilon} + Ys^{-\eta} \tag{2.28}$$

where the quantities X,ϵ, η can be fitted from data that are used in many parameterizations of the cross-section and well describe LHC energies. Consequently, the fraction of diffractive processes in inelastic collisions were determined from a rapidity gap in charged particle pseudorapidity distribution in this thesis.

2.3.2 Rapidity and rapidity gaps

Another important kinematic variable is the rapidity of a particle which is theoretically well-motivated quantity. The rapidity can be used to measure the energy and the total momentum for highly relativistic particles. The beam axis is to be the z-axis in the LHC experiment. Four momenta of particles and two angles which are the polar angle θ (the z-axis) and the azimuthal angle ϕ (around beam axis) are quantities that describe coordinates of a collision.

The definition of the rapidity of a particle is

$$y \equiv \frac{1}{2} \ln \left(\frac{\mathrm{E} + \mathrm{p}_z}{E - \mathrm{p}_z} \right), \tag{2.29}$$

where E is the energy of the particle and p_z is the momentum in the z direction, the initial direction. Rapidities are so crucial in accelerator physics since rapidity differences are invariant with respect to Lorentz boosts along the beam axis. Energy and three-momentum can change according to Lorentz boosts along the beam axis with respect to the z axis,

$$E' = E\cosh\beta - p_z \sinh\beta, \qquad p_z' = p_z \cosh\beta - E\sinh\beta, \tag{2.30}$$

where β is the boost parameter and then,

$$y = \frac{1}{2}\log\left(\frac{\mathrm{E}' + \mathrm{p}_z{}'}{E' - \mathrm{p}_z{}'}\right) = \frac{1}{2}\log\left(\frac{(E+p_z)(cosh\beta - sinh\beta)}{(E-p_z)(cosh\beta + sinh\beta)}\right) = y + \frac{1}{2}\log\left(\frac{e^{-\beta}}{e^{\beta}}\right) = y - \beta. \tag{2.31}$$

However, the total momentum vector of a particle is hard to get with the rapidity , especially at high values of the rapidity where the z component of the momentum is large. But there is a way of defining a quantity that is almost the same thing as the rapidity which is much easier to measure than y for highly energetic particles. This leads to the concept of pseudorapidity η. Pseudorapidity depends only on the polar angle of the particle's trajectory, and not on the energy of the particle, hence η can be determined purely from geometry even when y can not. Pseudorapidity, is a commonly used spatial coordinate

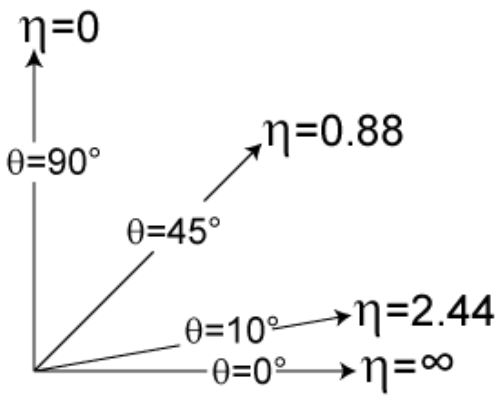

Figure 2.12: The numerical values of pseudorapidity and the corresponding angle between the incoming protons direction and the particle produced.

describing the angle of a particle relative to the beam axis.

$$\eta \equiv -\ln\left[\tan\left(\frac{\theta}{2}\right)\right], \tag{2.32}$$

where θ is the angle between the particle three-momentum $\mathbf{p}$ and the positive direction of the beam axis

$$\theta = 2\arctan\left(e^{-\eta}\right). \tag{2.33}$$

As a function of three-momentum $\mathbf{p}$, pseudorapidity can be written as

$$\eta = \frac{1}{2}\ln\left(\frac{|\mathbf{p}| + p_z}{|\mathbf{p}| - p_z}\right) = \operatorname{arctanh}\left(\frac{p_z}{|\mathbf{p}|}\right). \tag{2.34}$$

Pseudorapidity is particularly useful in hadron colliders such as the LHC. For highly relativistic particles, $y \approx \eta$. The pseudorapidity gives an approximation of the rapidity. Moreover, the equality $y = \eta$ holds for a particle with zero mass, the approximation is very accurate for high energetic particles where the mass of the particle can be neglected. For massless particles ($\mathbf{p} = E$),

$$y = \frac{1}{2}\log\left(\frac{\mathrm{E} + \mathrm{p_z}}{E - \mathrm{p}_z}\right) = \frac{1}{2}\log\left(\frac{(E + Ecos\theta)}{(E - Ecos\theta)}\right) = \log\sqrt{\left[\frac{1 + cos\theta}{1 - cos\theta}\right]} = -\log\tan\frac{\theta}{2}. \tag{2.35}$$

For massive particles, pseudorapidity and rapidity are not identical. The energy, momentum and mass relation this becomes

$$y = \frac{1}{2}\log\sqrt{\frac{E+p_z}{E-p_z}} = \frac{1}{2}\log\frac{E+p_z}{\sqrt{E-p_z}\sqrt{E+p_z}} \tag{2.36}$$

$$y = \frac{1}{2}\log\left(\frac{E+p_z}{\sqrt{E^2-p_z^2}}\right) = \frac{1}{2}\log\left(\frac{E+p_z}{\sqrt{M_T^2}}\right), \tag{2.37}$$

where M_T is the transverse mass. And furthermore the relations

$$y = \frac{1}{2}\log\frac{E+p_z}{E-p_z} \leq \frac{1}{2}\log\frac{E+\sqrt{E^2-m^2}}{E-\sqrt{E^2-m^2}} \tag{2.38}$$

$$= \frac{1}{2}\log\frac{(1+\sqrt{1-m^2/E^2})^2}{m^2/E^2} \leq \frac{1}{2}\log\frac{2E^2}{m^2} = y_{max} \tag{2.39}$$

can be derived. Rapidity and pseudorapidity are important quantities to define the large rapidity gaps for this thesis. It is well known that diffractive processes are identified with the presence of large rapidity gaps. Rapidity gap is angular regions in phase-space, where no particles are produced. An important experimental signature of diffraction is the presence of large rapidity gaps in the final state. For a large gap definition, first, we should consider the single diffraction processes. The maximum rapidity (in absolute value) of the X system is the rapidity of a particle with momentum $\sim \sqrt{s}/2$ and transverse mass m (all particle masses to be equal to m),

$$\mid y_x \mid_{max} \simeq \ln\frac{\sqrt{s}}{m}, \tag{2.40}$$

and the minimum value of $\mid y_x \mid$ correspond to a particle with momentum $\sim (m/M)\sqrt{s}/2$ and mass $\sim M$,

$$\mid y_x \mid_{min} \simeq \ln\frac{m\sqrt{s}}{M^2}. \tag{2.41}$$

Then the final-state rapidity gap between particle and the edge of the rapidity distribution of the X system is roughly given by

$$\Delta y \simeq \ln\frac{\sqrt{s}}{m} + \ln\frac{m\sqrt{s}}{M^2} \simeq \ln\frac{s}{M^2}. \tag{2.42}$$

The particles are produced in the fragmentation of the diffractive X system of mass M_X in a limited rapidity region. For high masses, the average gap width is

$$\Delta y \simeq \ln \frac{s}{M_X^2} = -\ln \xi, \tag{2.43}$$

where $\xi = M_X^2/s$, the fractional momentum loss of the incident proton ξ_X is calculated with the center-of-mass energy $\sqrt{s}$ of the collision and the diffractive X system of mass M_X.

Diffractive processes also take place asymptotically (as the energy increases). Diffractive process is closely related to elastic scattering, where one of the colliding protons is excited to a system X which then decays in a number of stable particles, and the energy transfer between the two interacting protons remains small. In diffraction, interactions are characterized by extended phase-space where momentum is transferal [31]. M_{X} is a crucially important quantity that is known as the diffractive mass of the system. It describes the remnants of the diffractive interaction, which is given by $M_{\mathrm{X}}^2 = (1-x)s$ where x is the momentum of the final state proton p is divided by the beam momentum(p_0). The limit of the diffractive production is given approximately by $M_{\mathrm{X}}^2/s \leq 0.15$. In high energy collision topology diffractive production is different for $M_{\mathrm{X}}^2/s \sim 0.05$. There are three kinds of diffractive events, single-, double- and central-diffractive. Figure 2.9 shows the total pp cross-section including the different final states of diffractive events. Single diffractive (SD) events occur by the exchange of a pomeron, one of the incoming protons remaining intact from the interaction, having lost only a few percents of its energy, whereas the other proton dissociates into a system X of particles with a mass M_{X}. In double diffractive (DD) events both of the incoming protons dissociate into systems of particles. Double diffractive events have two diffractive systems with two diffractive masses, in both hemispheres (the hemispheres are needed as the two sides of the experiment, in the direction of the LHC pipe and with respect to the interaction point). The central diffractive processes in which a central object is produced exclusively accompanied by scattered beam protons only. Those diffractive processes can be separated into categories depending on the definition of a rapidity gap between the proton remnant as I mentioned the rapidity is a distinct experimental signature for diffraction processes.

2.3.3 Modeling of diffraction in MC generators

In this section has an overview of the modeling of diffraction in MC generators in particularly the main physics features of Pythia. MC event generators are frequently used in high-energy physics. An event generator should contain a simulation of several physics aspects since there is multi-particle production in collisions between elementary particles, and hadron collisions are highly complicated processes to interpret. The MC generator program is intended to generate complete events at experimental observables to understand fundamental underlying theory. Generally, an event generator can be used to know what kind of events exist and at what rates one may expect to find them. Typical application strategies on real data for instance, optimizing the signal to background conditions, in

order to extract the true physics signal, or estimating detector acceptance corrections that have to be applied to raw data. The event generator PYTHIA 8 [39] is one of the event generators, widely used in high-energy physics studies. It combines calculations from QCD with phenomenological models in order to provide a complete description of collisions between energetic particles and their antiparticles in various combinations. The evolution of an event may arrange with PYTHIA 8 for those aspects as follows

- First step determines the main characteristics of the event. It starts with two incoming hadrons. In this step, parton distribution is used for particle characterization since each particle is characterized by a set of parton distributions, which defines the partonic substructure in terms of flavor composition and energy sharing. One shower initiator parton from each beam building up an initial-state shower, one incoming parton from each of the two showers enters the hard process, where then a number of outgoing partons are produced. In addition may produce a set of short-lived resonances, whose decay to normal partons. The outgoing partons may branch to build up final-state showers.
- This step is about the fragmentation mechanism. That can be seen as occurring in a set of separate color singlet subsystems at the rest of the final state. When a shower initiator is taken out of a beam particle, a beam remnant is left. This remnant may have an internal structure, and a net color charge that relates to the QCD confinement mechanism.
- The last step is final processes where many of the produced particles are unstable and will continue decaying further. Furthermore it includes a wide range of hard scattering processes of partons with initial and final state radiation corrections.

The branching of the outgoing partons is modeled with a parton shower approach and a string fragmentation model is used for the hadronization to final state particles. Conventionally, only quarks and gluons are counted as partons, while leptons and photons are not. The PYTHIA generator also describes what happens to the partons that remain from the initial proton after the hard scattering. The PYTHIA 8 MBR is used throughout this thesis for generating the soft scattering processes in proton-proton collisions. The PYTHIA 8 MBR predicts the energy dependence of the total, elastic, and inelastic pp cross sections, and fully simulates the main diffractive components of the inelastic cross section: Single diffractive (SD), double diffraction (DD) and centeral diffraction (CD). The diffractive event generation in PYTHIA 8 MBR is based on a phenomenological renormalized-Regge model [11], which is clarified by interpreting the Pomeron flux as the probability for forming a diffractive rapidity gap. Diffractive dissociation is described in a two-channel eikonal model, combining a triple Regge approach to soft processes with the lowest order QCD for processes with parton scattering transverse momenta above 3 GeV. The treatment of particle production in PYTHIA 8 MBR depends on the diffractive mass M. Their main improvements are to enhance the low mass components of the dissociation spectra, to suppress the production of very large masses and, in the DD case, to reduce the probability of the

systems X and Y overlapping in rapidity space. For $M \geq 1\,\text{GeV}$, the system is allowed to decay isotropically into a two-body system. In the case of larger masses, the system is treated as a string with the quantum number of the original proton. In the thesis, EPOS LHC [40] is compared to the PYTHIA 8 generator, which is commonly used to describe hadron-hadron collisions on an event-by-event basis. The EPOS generator is based on Gribov-Regge theory [41], and was developed originally for particle showers produced by cosmic rays. The latest version called EPOS LHC has tuned data to up to 7 TeV measured at the LHC.

2.3.4 Underlying event

The experimental study of the underlying event (UE) is important hadron production in high energy hadron-hadron collisions. It leads to better modeling for Monte Carlo programs that are used in precise measurements of standard model processes. Understanding the UE in terms of particle and energy densities requires a phenomenological description involving parameters that must be tuned with the help of data. In hadron-hadron scattering, UE can be defined the remnants of scattering interactions. The description of the remnant gets complicated since the remnant partons can be subdivided into different subsystems hard(the hadronization of initial- and final-state radiation) and soft processes (interactions with low p_T). The hadronization of partonic constituents, not involved any hadronic activity that cannot be attributed to the particles originating from the hard scattering. The soft processes component is referred to as the UE that has undergone multiple-parton interactions (MPIs) [42] and to the hadronization of beam remnants that did not participate in other scatterings. These interactions cannot be completely described by perturbative quantum chromodynamics (QCD), because describing the hard process and phenomenological models of the soft interactions that explain to simultaneously describe MPIs. Moreover, at the LHC where the protons cross in entire bunches rather than one single proton, the probability for more than one proton colliding event increases with the luminosity. These additional events are called pileup events (PU) and again have an influence on the resulting measurements in the detector. In particular rapiditiy gaps, which are very important to charaterize diffractive events, can be hidden by PU, or MPI.

3 Experimental methods

In this chapter we will take a brief look at experimental methods. This chapter provides an introduction to the LHC accelerator and the CMS detector, as well as a more thorough discussion of the design of the CASTOR calorimeter. The information relevant for this thesis are in particles highlighted. It also gives a very basic overview of the primary research goals of the LHC and CMS.

3.1 The large hadron collider

The Large Hadron Collider(LHC) is a proton-proton collider is located at the European Laboratory for Particle Physics(CERN), where Switzerland and France. The LHC is the largest hadron accelerator (with a circumference of 26.7 km) in the world. That is extremely important experiment to perform precisions measurements of high-energy particle physics. High energies are needed both, to create new and unstable particles, and to explore the structure of hadrons. There are four experiments placed at the interaction points (IP) where beam particles collide. The LHC working principle is based on a colliding-beam experiment which has two rings and superconducting magnets to accelerate and focus the beam bunches. The accelerate design to speed protons up to a kinetic energy of 7 TeV. The stable colliding particles beam bunches traveling in almost opposite directions are made to collide at a small angle (or zero) crossing angle.

The operation of the LHC starts from hydrogen atoms on which electrons have been stripped from protons by using an electric field. The beam particles are not starting with kinetic energy zero, they need to be accelerated in pre-accelerator in smaller rings. The protons are injected into a linear accelerator LINAC2 up to an energy of 50 MeV [16]. The next steps of energy increase for the protons for the BOOSTER (1.4 GeV), the proton synchrotron PS (26 GeV), where all the protons bunches are formed, and the SPS (450 ,GeV). Afterward, they are sufficiently energetic to be injected into the LHC ring. The operation is repeated 24 times, injecting half clockwise and half anti-clockwise. Final acceleration from 450 GeV to TeV analyses in the LHC is performed through a radio-frequency (RF) system consisting of 8 single super-conducting cavities per ring, providing an electrical field of 2 MV/cavity at 400 MHz. The LHC ring, specific optics composed of 1232 dipole magnets and 992 quadruple magnets are used respectively to keep the beam on their paths and to keep it focused. Finally, at four points of the rings, the beams are crossed: ATLAS, CMS are two general-purpose experiments, mainly concentrated on the search for

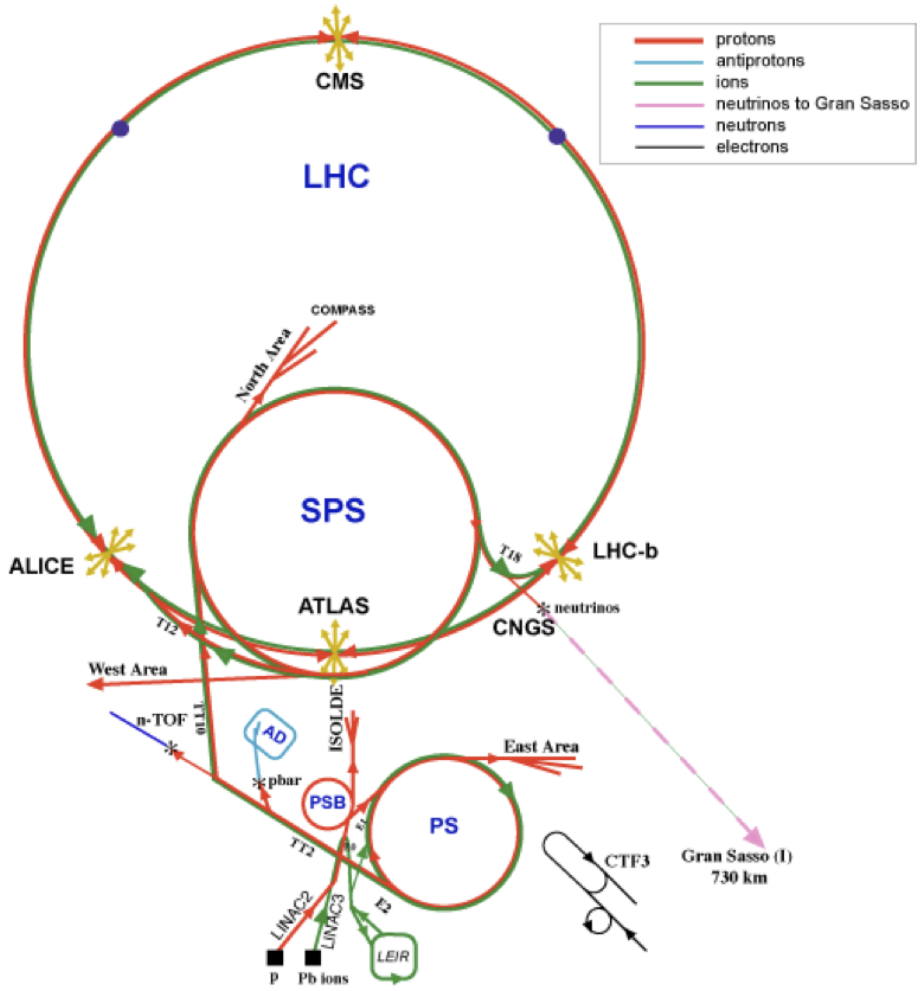

Figure 3.1: Schematic layout of the LHC. The logos of the experiments have been placed at the corresponding interaction points (IP).

Higgs boson and new physics. ALICE is optimal the study of heavy-ion collisions, LHCb is looking for the CP violation in b-quark interactions.

3.2 The CMS experiment

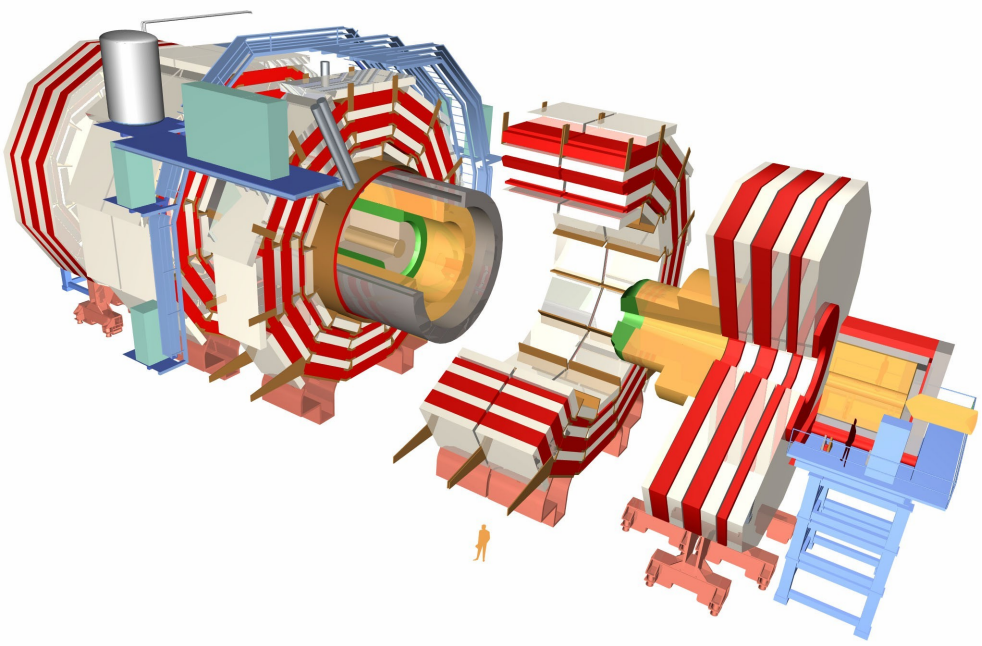

Figure 3.2: Various elements of the CMS detector. The CASTOR calorimeter is the most right detector component and is located on top of the "forward table".

CMS is a multi-purpose large angular coverage detector, with a very high magnetic field (3.8 T) and very compact design, whose detailed description can be found in [43]. It is initially designed to study the physics of high-energy proton collisions, which require a good precision on QCD related probes. It is used to investigate the physics, with its wide coverage, precise calorimetry and good tracking. The acceptance of CMS to high absolute pseodorapidities, and the coverage of the very forward region with CASTOR is of great importance for the study of diffractive interactions in proton-proton collisions performed in this thesis.

CMS uses a right handed coordinate system, as shown in figure 3.3. The z-axis points in the direction of the proton beam, and the x-axis towards the centre of the ring. The polar angle ϕ is measured with respect to the z-axis in the xy plane and is the azimuthal angle. The pseudorapidity is used to define the central and forward regions, and is using the angle θ with respect to the z-axis.

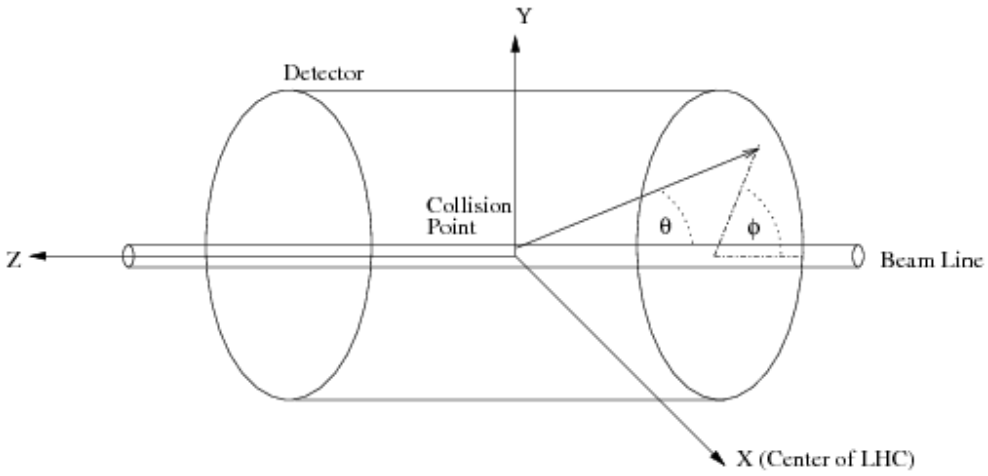

Figure 3.3: CMS coordinate system - Representation of the right-handed coordinate system used at CMS, including the beam directions.

3.2.1 The central instrumentation of the CMS detector

For this thesis also the central pixel tracker is important to detect hadronic collisions activity and to measure central rapidity gaps.

The charged particle tracking system

The CMS tracking system is designed to measure the trajectories of charged particles, emerging from the collisions at the interaction point where covers a range in pseudorapidity of $|\eta| < 2.5$. At the LHC design luminosity of $10^{34}\,\mathrm{cm}^{-2}\,s^{-1}$, the tracker will be traversed by an average of 1000 particles every 25 ns, which results in a hit rate density of $1\,\mathrm{MHz/mm}^2$ at a radius of 4 cm from the interaction point [12]. The detector technologies providing high granularity and fast response are required. The inner tracking system in CMS is composed of two sub-detectors which is the Silicon Pixel Detector, the Silicon Strip detector is surrounding the pixel detector. The pixel detector is the closest detector to the beam and has a very high granularity, which makes it a useful tool for the measurement of primary vertex positions along and transverse to the beam axis, and to identify decays of a long living particle. It consists of three cylindrical layers, barrel and two layers of disks at each side as endcaps, as illustrated in figure 3.14. There are in total 66 million pixels, which can handle the highest multiplicity events achieved in proton-proton runs with high pile-up.

The pixel detector is made of smaller detector units called modules, each containing two rows of 8 read-out chips connected to the active area. The orientation of modules are bended in a way to optimize the charge share between pixels due to Lorentz angle into account, which results in a position resolution of 10 m and 15 m in azimuthal and z directions respectively.

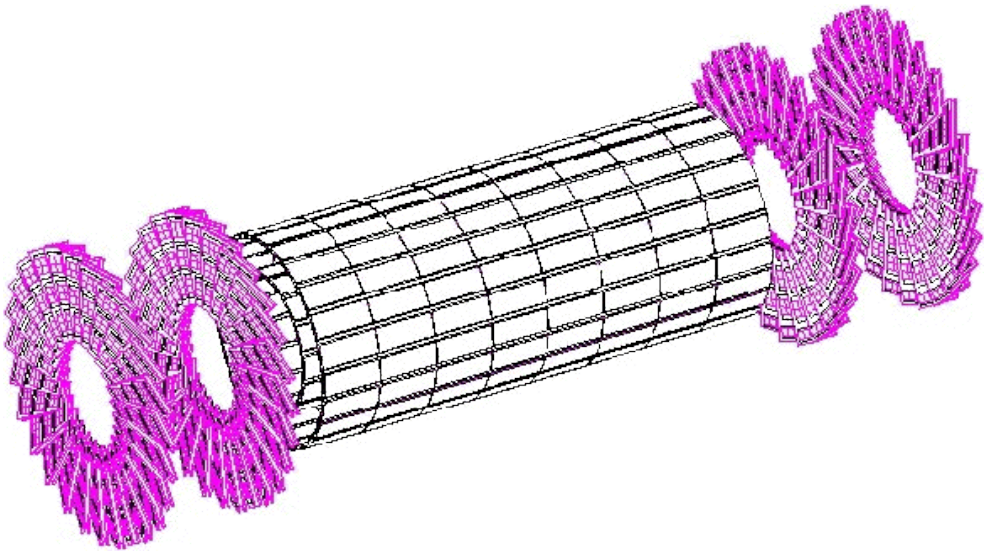

Figure 3.4: Silicon pixel detector with barrel and encap sections.

The Pixel Detector is surrounded by a large ($24\,m^3$) volume of sensors with pixel strips. Different subsystems responsible for different angle of coverage. The subsystems, TIB, TID, TOB and TEC are shown in figure 3.5. The surfaces of the modules, typically 10 cm wide, consist of 80 μm strips. The thickness of the silicon is 320 μm in the inner tracker and 500 μm in the outer layers. The signal is read-out by custom integrated circuits, using optical fibers to transmit signal to the front end driver (FED). A single FED receives data from 96 fibers, with 256 channels per fiber. The pedestal and common-mode noise subtraction are applied to the digitized signal in the off-line reconstruction (and HLT) process.

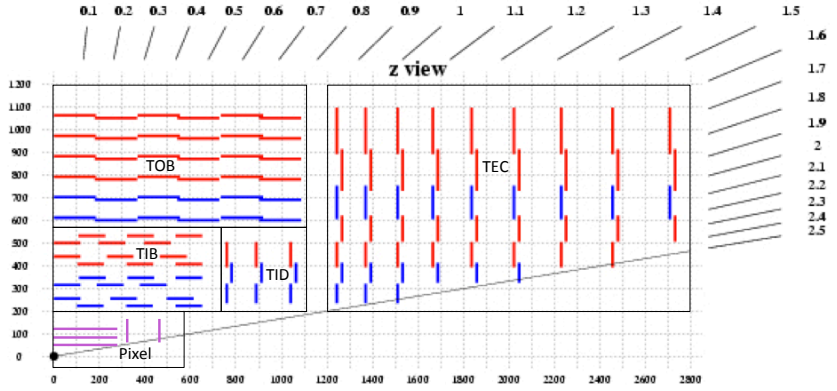

Figure 3.5: Components of the tracker. The red strip layers are single-sided and blue layers are double-sided (stereo) strip layers. The pixel detector is shown in purple.

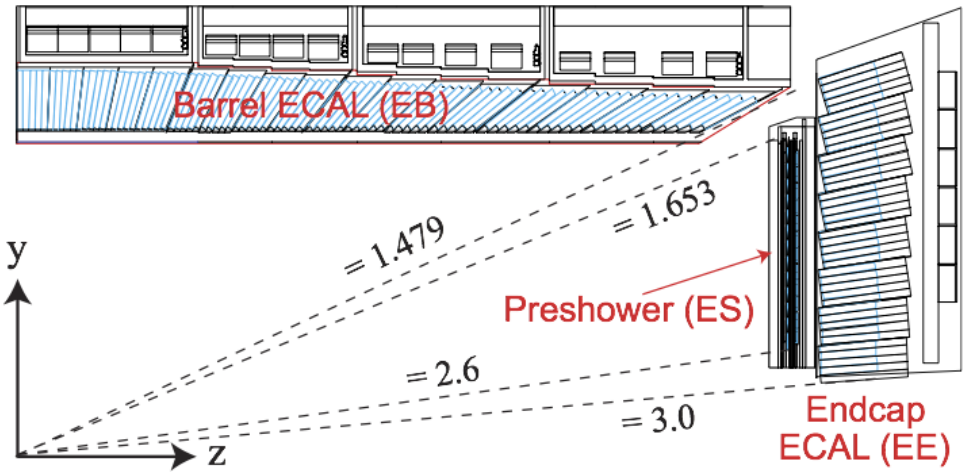

Figure 3.6: Ecal Detector.

The electromagnetic calorimeter

The electromagnetic calorimeter (ECAL) is made of a single homogeneous volume of lead-tungstate ($PbWO_4$) crystals. The requirement to have a fast, radiation resistant detector with a high granularity lead to the usage of the high-density crystals. $PbWO_4$, having a very high density of charge, provides a short radiation length ($X_0 = 0.89\,\text{cm}$) and small Moliere radius (2.2 cm). It measures the electromagnetically interact particle energies, the main importance of the ECAL is to detect photons since they are not seen by the tracking system. A sampling of the scintillation is performed by avalanche photo-diodes (APD) in the barrel, and by vacuum photo-triodes (VPT) in the endcaps. This system provides crucial information on electromagnetically interacting particles, photons, and electrons. The scintillation light produced in the crystals is collected by highly efficient photodetectors placed at the rear. The ECAL Barrel, EB, covers the pseudorapidity range of $|\eta| < 1.479$ and the ECAL endcaps, EE, cover $1.479 < |\eta| < 3$. The pre-shower detector, ES, with is a thin lead sampling calorimeter with silicon sensors, covering the end-caps, which is used to discriminate between direct photon signals.

The energy, position and time resolution of arrays of crystals have been studied at beam tests with no magnetic field, no radiation damage, and no material upstream. The resolution of the ECAL was measured by shooting an electron beam on the central crystal of an array of 3×3 crystals. This operation is repeated with varies electron beam energies. The obtained energy resolution, for central impact

$$(\frac{\sigma}{E})^2 = \frac{S}{\sqrt{E}}^2 + \frac{N}{E}^2 + C^2 \tag{3.1}$$

where S is stochastic, 2.8%, N is noise (pileup), 0.12, and C is a constant (calibration

errors), 0.3%, terms are where E measured in GeV. The constant term is dominated by the longitudinal non-uniformity of light collection. Material of ECAL can be result in photon conversion and electron bremsstrahlung that can both affect all terms in the energy resolution. The energy resolution is between 0.9% at low energies around 20 GeVand for higher energies is the 0.4%.

The hadronic calorimeter

The next stage for traveling particles which pass through the ECAL, they will be absorbed by the hadronic calorimeter (HCAL) which is the outer most detector inside the magnetic coil and it surrounds the ECAL and the tracking system. It is designed to measure the energies of the strongly interacting particles (hadrons). The purpose of the HCAL is to measure the particles that survive the ECAL material and are particularly important for the measurement of jets. It also measures the total visible transverse and missing transverse energy due to almost hermetic coverage. Its system is a combination of different components. In the mid-rapidity region, a hybrid absorber scintillator calorimeter is used, and in the forward region plastic scintillators (Cherenkov radiation-based system) are used to measure the energy of hadrons.

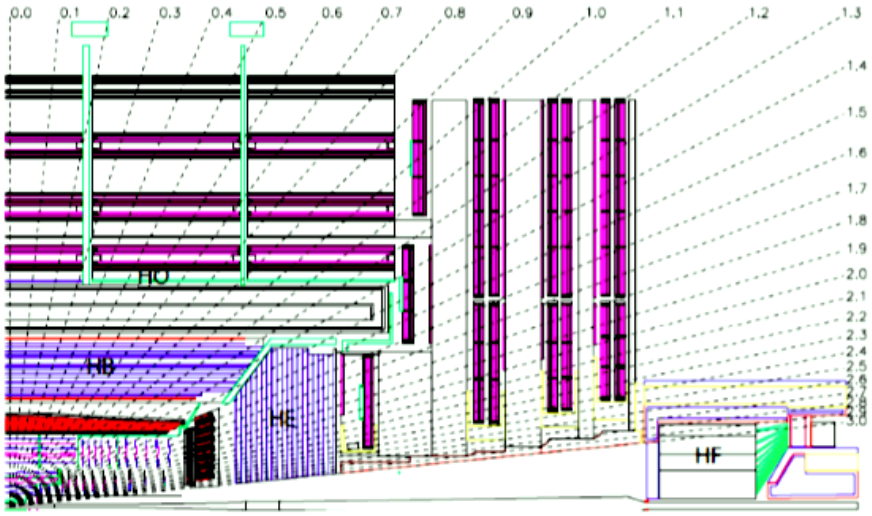

Figure 3.7: Longitudinal sketch of the hadronic calorimeter. Transverse section through the HCAL, showing the geometrical configuration of the hadronic barrel (HB), hadronic endcap (HE), hadronic outer (HO) and hadronic forward (HF) calorimeters. The numbers denote pseudorapidity.

There are two subsystems, HCAL barrel, covering $|\eta| < 1.3$ and HCAL Endcap for $1.3 < |\eta| < 3$. The towers of radially stacked brass and scintillator plates have a granularity of 0.087×0.087 in $\eta \times \phi$ in the barrel and 0.17×0.17 in the endcap. The aim of HBHE is to

absorb all energy from charged and neutral hadrons, to determine the missing transverse energy (MET) when combined with the information from ECAL and tracker. The outer hadron calorimeter (HO) within $|\eta| < 1.3$ that uses the coil of the solenoid as an additional absorber. HO is an extension to the barrel calorimeter, an additional layer of absorber and scintillator located outside the magnet coil, with towers of 0.17×0.17 granularity in $\eta \times \phi$. HO mostly aims to distinguish hadronic residual from muon signal in the outer muon tracker, and it is not primarily used in the studies discussed in this thesis. Energy resolution for hadronic calorimeter is at lower energies

$$\frac{\sigma_E}{E} \geq \frac{50\%}{\sqrt{E}} \tag{3.2}$$

3.2.2 Forward instrumentation of the CMS detector

The Forward instrumentation of the CMS detector is used in this thesis to detect collisions activity in the largest possible acceptance. Rapidity gap can be measured up to almost 12 units in pseudorapidity.

Forward hadronic calorimeter (HF)

The forward hadronic calorimeter (HF) is a system of quartz fibers placed behind a lead absorber which is located at a distance of 11 meters from the interaction point to extend the coverage up to $\eta < 5$. This pseudorapidity region is also important for Higgs, SUSY and low-x QCD effects in forward-jet production searches. The calorimeter is mainly sensitive to the electromagnetic cascades and the electromagnetic core of hadronic showers. HF calorimeter is based on the detection of Cherenkov radiation [44, 45] which is emitted by a charged particle traversing a quartz fiber with a velocity greater than the speed of light in quartz. When a charged particle with v velocity traverses a dielectric medium with a refractive index n ($n = n(\lambda)$), it polarized the molecules in the medium. After its passage, the molecules return to the unpolarized state through the emission of the photon.

$$\beta > \beta_{threshold} = \frac{1}{n}. \tag{3.3}$$

If $\mathrm{v} > c/n$, constructive interference occurs and Cerenkov radiation is emitted as a coherent wavefront at a fixed angle θ to the trajectory of the charged particle.

The Cherenkov radiation in the fibers is guided to the PMTs which are placed close to the detector in order to achieve a fast response. The HF consists of two units which have a cylindrical shape, one at each end of CMS detector. Each unit has an active radius of 1.4 m away is located, 11 m away from the interaction point. The beam pipe passes the

central cylindrical axis. The absorber is made of iron and divided into 18 wedges covering 20 degrees. The iron absorber length (1.65 m) corresponds 10 nuclear interaction lengths. Several mm wide holes are drilled into the wedges parallel to the beam, and 600 micron thick plastic clad quartz fibers are inserted into these holes as the sensitive material in the calorimeter. The fibers exist in two different lengths. The longer fibers provide light from electromagnetic and hadronic showers in the absorber and the shorter fibers only measure the hadronic showers. Each wedge is divided into 24 towers. The short and long fibers from a specific tower are bundled separately. Each bundle is attached to its own phototube through a 42 cm long air-core light guide.

CASTOR calorimeter

The CASTOR detector is a quartz-tungsten calorimeter located at a distance of 14.4 m from the interaction point. It is installed at the CMS experiment around the beam and covers the forward pseudorapidity range of $-6.6 < \eta < -5.2$ [9]. The detector is aligned parallel to the beam along z, is very close to the LHC beam pipe, is only 1 cm to 2 cm away from the beam pipe. The conditions in the detector, require a compact detector design, radiation-hard materials, a fast response and acceptable operation in a magnetic field. This has been achieved by using plates of tungsten as an absorber, a combination with quartz as sensitive material. The detectors segmentation in ϕ is provided by 16 sectors and together with 14 longitudinal modules, thus the 1.6 m long detector is divided into 224 readout channels.

The first two modules represent the electromagnetic (EM) calorimeter part of CASTOR. Their tungsten plates have a thickness of 5 mm and their quartz plates have a thickness of 2 mm. This corresponds to a module depth of 10.05 radiation lengths X_0 and 0.385 nuclear interaction lengths. The other 12 modules form the hadronic (HAD) part of CASTOR. All modules combined, amount to material corresponding to about 10 nuclear interaction lengths. The energy deposited by particles after they initiated particle cascades is measured in these modules. The detector is shielded from the magnetic field of 3.8 T from the central CMS solenoid but stray magnetic fields of less than 0.2 T penetrate the shielding and have an impact on the readout of the central modules. Most channels of modules 6 to 8 are suffering from the magnetic field and modules 9 to 14 collecting only a small fraction of hadronic showers.

3.2.3 Trigger system

The trigger system is essential as the bunch crossing rate at the LHC is ≈ 31.6 MHz, a rate is providing more data that can be written to tape. Since only about 10^3 events per second can be archived, CMS reduces the rate using a two-level trigger system. The trigger is designed to ensure that high efficiency as much as possible within the limitations of the detector. The first level (L1) triggers the readout of the detector at a hardware level, is based on information from the calorimeters and muon detectors to select the most

interesting events. The high-level trigger (HLT) processor decreases the event rate in order to have a small enough amount of output data that can be stored. HLT is a typical CMS software process, an HLT process is seeded by a given L1 bit, and it can run any type of off-line reconstruction on the event in order to perform the decision. Bunch crossings are identified by a coincidence of the BPTX signals on both sides of the experiment called the zero bias trigger. The BPTX devices are capacitive beam current pickup sensors are located up- and down-stream of CMS. They are used to measure the presence and timing of individual LHC bunches. Furthermore, the minimum bias trigger required at least one signal above the noise on each side of the interaction point in one of the HF detectors. For this thesis, the zero bias trigger is used. This is of crucial importance since it is the only unbiased trigger of CMS and at the same time has the largest possible acceptance.

3.2.4 Simulations

The Monte-Carlo (MC) models are important to understand the physical processes. High energy collisions can be simulated by different event generators depending on the colliding system and the studied physics process. Generators usually provides the final state particles with their decay history for each event. Furthermore, all physical regions (detector, support structure, etc.) of the detector simulated, and the magnetic fields effects on the detector response are also modeled. After events producing by these MC generators, they needed to propagated through the detector by GEANT4 [46, 47] simulations which are an MC-based simulation toolkit which simulates detector response and output signals. Through the accurate simulation of particle interactions with various materials and detector geometry, results from event generators become comparable to actual data.

All simulations are performed with the CMS software (CMSSW) [48]. Particles from the final state produced by the event generators are decayed according to their branching ratios and kinematics. As these particles pass through the detector, the interaction of the particles with the detector material is computed. Detector noise and digitalization steps are applied by each sub-detector and also included in the simulation. Finally, a full emulation of the L1 trigger and HLT is added. The interaction of particles with the material is modeled and parametrized using test beam data for the individual subsystems. Deviations between data and simulation are minimized by tuning the simulations to collision data. The tracker software, a precise and correct implementation of the CASTOR geometry is crucial to have a simulation that can be validated with data and subsequently used for efficiency and acceptance corrections. The configuration of the materials at CASTOR, the tungsten absorber, and active quartz plates is important since it has a significant effect on the shower development. During the simulation of the particle showers with GEANT4 [47], the code calculates the number of Cherenkov photons that is emitted in the quartz plates. The next process is the conversion of those Cherenkov photons into a number of photo-electrons that are produced inside the photo-multiplier tubes when the former hit the cathode. The resulting number of photo-electrons in the PMT then produce a current that

is read-out by the electronics. This is simulated in the software by producing a charge (in units of fC) distribution utilizing the PMT gain factor. At the same time, the code also reproduces the pulse shape and stores the collected charge in time slices of 25 ns. The last step in the simulation chain then converts this analog signal into a discretized digital one according to the properties of the read-out electronics. The resulting ADC counts distribution (still in 25 ns time slices) is stored into the raw data format.

3.3 Multivariate event classification

To use of multivariate analysis method (TMVA) [49] has become commonplace in particle physics. It is a statistical tool can be used for every type of data classification in analysis selection criteria. The most common usage of the classifier boosted decision trees (BDTs) is in classifying candidate as a signal or as background, or to define physics objects.

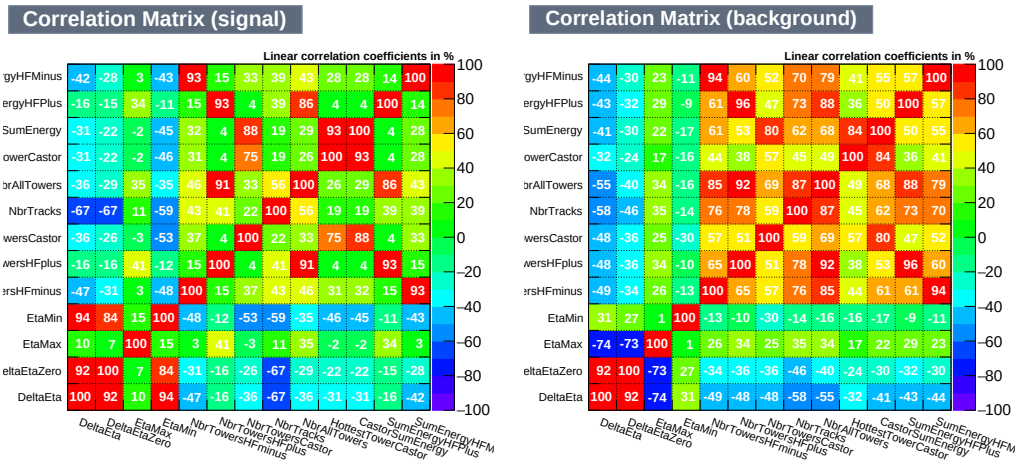

(a) Signal (b) Background

Figure 3.8: Correlation between input variables in PYTHIA 8 MBR samples in the training. For diffractive events classification: (a) the signal type is chosen as "SD1" in the training phase for this example, and (b) "background" is the rest of all events such as DD, SD2 and rest.

Generally speaking, the main goal of this thesis is to discriminate between signal events from the background events. Optimal discrimination of signal is done with considerable success in using multivariate analysis techniques in this thesis. Pre-processing of data or variable selection is the first step since the performance of the classifier is based on training the characteristics of interest that are observed on each of the selected units in the sample. The training variables as technical indicators must represent reasonable physics-motivated variables, and selection of the variables is based on which give the maximum

signal/background discrimination, is not necessarily the best choice. For example in this thesis, detector response is characterized by several variables such as multiplicities and rapidity gaps, which are used as input variables to the multivariate analysis, and they give a reasonable separation between signal and background events. An understanding of these variables is fundamental to the use of multivariate analysis. The variables are gathered as vectors, where each event corresponds to a vector of observed variables. After selecting the variables there are checked for any linear correlations between them which are shown in Fig. 5.17. In addition, dimensionality reduction of the feature space and simplification can be done by reducing the number of variables. The extremely correlated variables in general, anything over 90% are less useful. Adding poorly discriminating or highly correlated variables can lead to an underperformance of some methods. Another disadvantage is for a training with many variables which it needs more time. When having selected a set of variables, multivariate analysis techniques can be applied to transform to the variables into a representation of the data that gives certain target properties. The processing could be simple scaling of the variables or mathematical transformations such as decorrelation or in combination with others to construct physics-motivated variables. The user can define each transformation as the event class (signal, background or both; for classification typically only one event class is defined) which is taken as the basis for the calculation of the transformation.

3.3.1 Training phase and application phase

The multivariate analysis provides the ability to exploit the available information from the observables most efficiently to separate data into signal and background. The performance of multivariate analysis methods depends on the subject of an analysis and the correlation between the variables. In this work, I use the ROOT analysis framework [50]. The data samples are split into a training and a test sample. Here I use the same numbers of the events in both samples. Both must not exceed the entries of the input datasets. This guarantees a statistically independent evolution for two samples. Train (build), test and evaluate classifiers using data samples with a known signal and background events.

The training is done inclusively with the total background and one signal type. The multivariate analysis method, boosted decision trees (BDTs) is used in this thesis and in the next section it will be introduced. As mentioned before a classifier optimizes the signal and background separation cuts using the power of multiple variables and optimizes it. We need to find the best variables and to decide how many variables to give for the training phase. There is a way to a quick check of the variable performance training multivariate analysis by checking the ranking of the variables used during the training. The ranking of variables depend on the used variable set and the used method, the ranked variables of this analysis are shown in Tab. 3.1(variables will be introduced in the chapter of data analysis).

The ranking is an indication if a variable is a good input variable for the given method. The

Table 3.1: Ranking input variables from PYTHIA 8 MBR samples in the training. For diffractive events classification, the signal type is chosen as "SD1" in the training phase for this example. Ranking result, top variable is best ranked for signal type SD1.

Rank: Variable	Separation
1: The total number of towers in the CASTOR calorimeter	0.75
2: η_{min}	0.70
3: The hottest towers in the CASTOR calorimeter	0.66
4: The sum of energy in the CASTOR calorimeter	0.62
5: $\Delta\eta$	0.47
6: The total number of towers in the HF calorimeter($-\eta$ side)	0.461
7: The total number of towers in all CMS calorimeters	0.460
8: The sum of energy in the HF calorimeter ($-\eta$ side)	0.34
9: The total number of tracks	0.29
10: The size of the rapidity gap $\Delta\eta^0$	0.28
11: The total number of towers in the HF calorimeter($+\eta$ side)	0.17
12: The sum of energy in the HF calorimeter (($+\eta$ side))	0.15
13: η_{max}	0.052

variable set obtained from the ranking does not have to be the optimal one. The optimal selection of the MVA output can be calculated with the signal and background selection efficiencies, and the number of the signal and background events, S or B respectively. After running the training phase, a weight file is created, containing all needed information for the application phase like the analysis type, the method, and input variables. During the application phase, a reader object is used for interpreting the weight files. Also, a ROOT output file is created containing all important information from the training. For example, histograms which show the characteristic distributions for the signal and the background.

Furthermore figure 3.9 illustrates the example of an gaussianisation transformation of input variables.

The classification corresponds to a mapping from the N-dimensional phase space of the N input variables to one dimension. A further mapping to the signal and background class completes the classification:

$$\mathbb{R}^{\mathbf{N}} \rightarrow \mathbb{R} \rightarrow \mathbf{C}_{signal}, \mathbf{C}_{background}. \tag{3.4}$$

For event selection based on simple cuts, the mapping from $\mathbb{R}^{\mathbf{N}}$ to the signal and background classes is done directly, without the intermediate step to $\mathbb{R}$ [14]. During the application phase, with the weight file from the training, the MVA output can be calculated for the whole data sample. The multivariate analysis computes a number of benchmark quantities that evaluates the performance of the methods on the independent sample. For

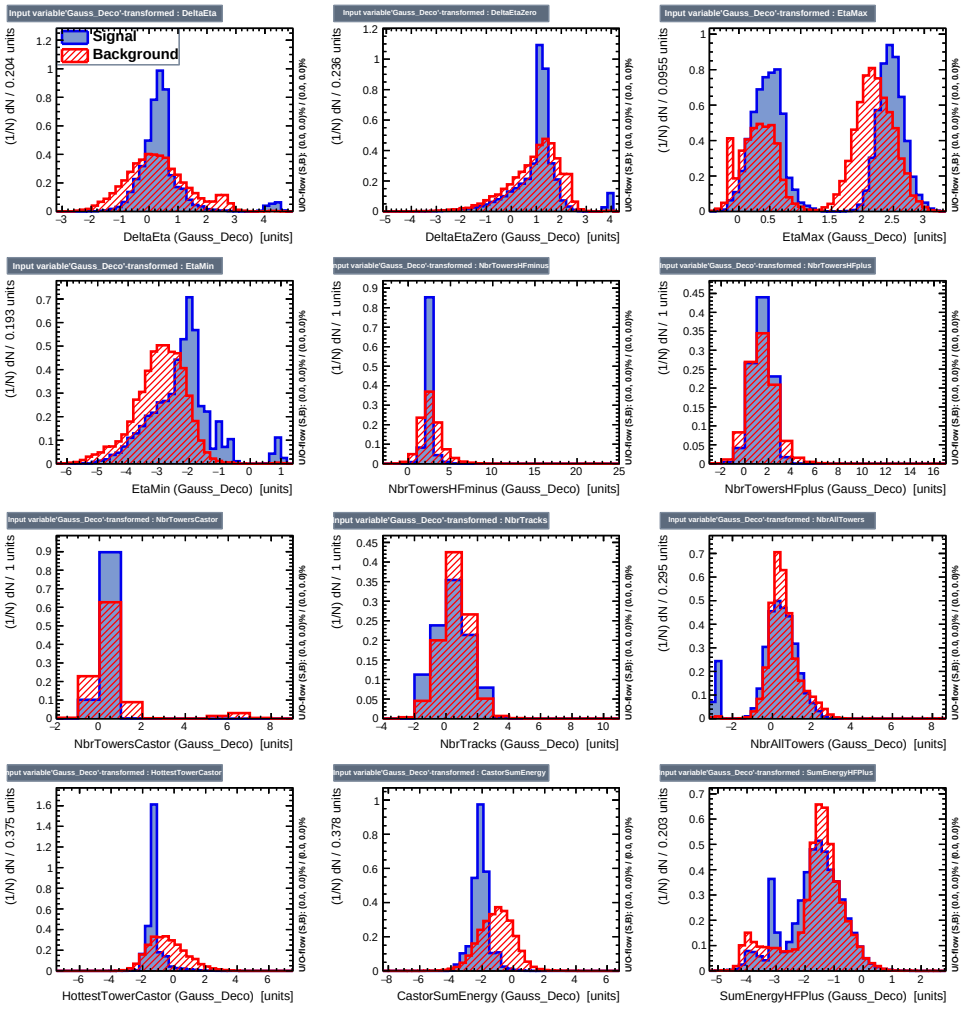

Figure 3.9: Gaussianisation transformation of input variables which are trained with boosted decision trees the final response in PYTHIA 8 MBR samples, the signal type is chosen as "SD1" in the training phase for this example

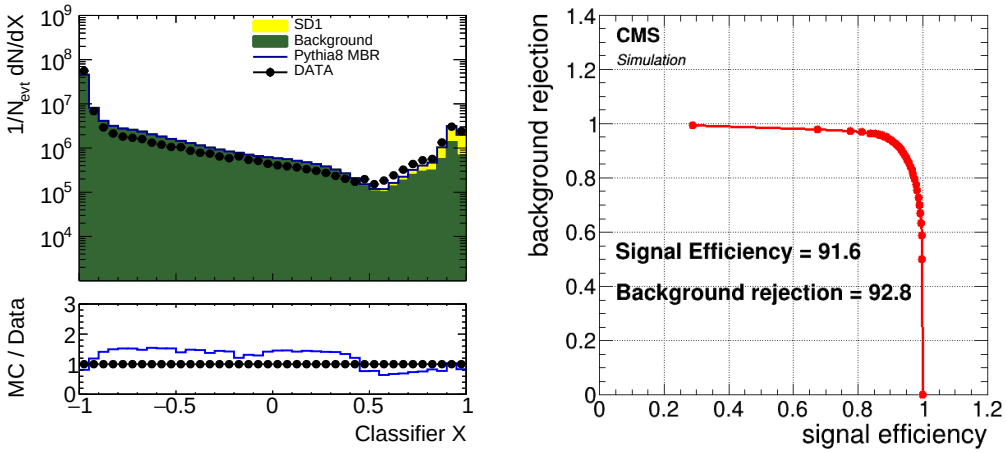

(a) (b)

Figure 3.10: Example of classifaction output for signal/background training data (a). The predictions between signal selection efficiency and background rejection is shown in (b).

optimal signal discrimination classification relate the separation of a classifier output y, the signal efficiency, and background rejection efficiencies. The separation of a classifier y is defined by the signal and background PDFs of y. It derives from the input variables (observables) a classifier output where signal-(background-) like events have values close to 1 (0). In figure 3.10 the classification output y is shown. For each method, a classifier y is computed. During the training, the true class of the event (signal/background) is known, the classification output y is plotted for both classes independently. The number of background and signal events and the corresponding statistical significance and the number of events can be classified correctly or wrongly as signal or background, thus the signal efficiency and background efficiencies are needed to be calculated. They are computed for a set of cuts on the classifier output. From the sets of the signal efficiency $\epsilon_{sig,eff}$, and purity, background rejections (1 - $\epsilon_{eff,background}$) calculated by the cuts on y the receiver operating characteristics (ROC) curve is obtained (see Figure 3.10(b)). Which point on the ROC curve the user should choose as working point (i.e. which signal efficiency and which background rejection) depends on the type of analysis the user wants to perform. In figure 3.11 (a) several exemplary ROC curves with different classification performances are shown. The larger the area below the curve, the better the separation of signal and background that is achieved.

The multivariate analysis can be optimized so that way a higher statistical significance is achieved. The selection of signal is optimal then the statistical significance is maximal,

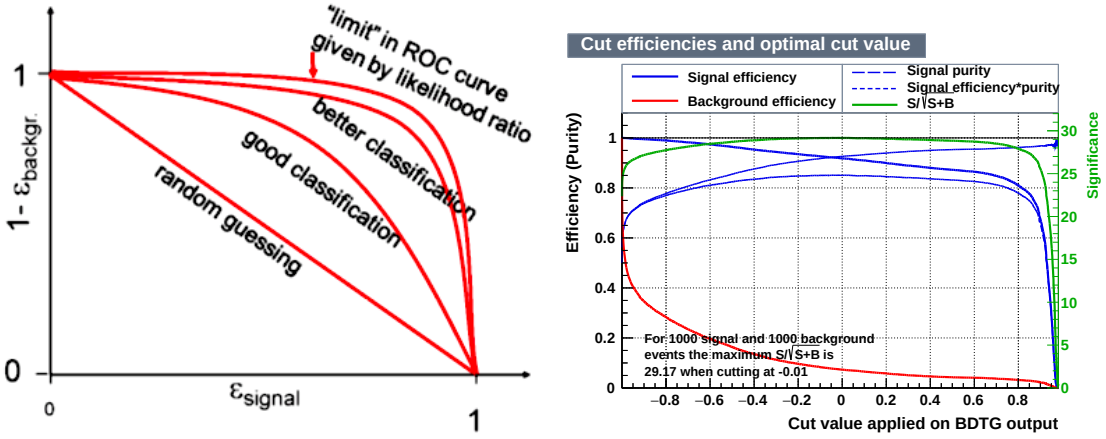

Figure 3.11: The ROC curve (a) shows the relationship between signal efficiency ($\epsilon_{eff,signal}$) and background rejection ($1 - \epsilon_{eff,background}$). In figure ($b$), the significance, the purity and the efficiencies for signal and background as well as the signal efficiency multiplied with the purity are shown.

$$\frac{S}{\sqrt{S+B}} \tag{3.5}$$

where S is the number of signal events and B is the number of background events. For a signal search, the best cut is where $S/\sqrt{S+B}$ has a maximum. Given the event yields, TMVA calculates significances, purities and efficiencies and proposes an optimal cut (the best cut) value to get the best performance in figure 3.11 (b), the output of this tool is shown which computes those values as a function of the cut on the classifier output. All events with a classifier output larger than the best cut value are classified as a signal, all events below the cut are classified as background ($y > y_{cut}$). Finally for precision measurements one aims for a high purity.

3.3.2 Boosted decision trees

The multivariate classifier boosted decision trees (BDTs) is now commonly used in data analysis. Boosted decision trees (BDT) are boosted classifiers. Boosting at a series of classifiers of decision trees is technique in which the classifiers are not made independently, but sequentially. A series of classifiers are trained to enhance the performance. This technique applies the idea in which the classifiers learn from the mistakes of the previous classifiers. As I mentioned before the decision algorithm starts with root node in which the entire training data set containing signal and background events (see Fig. 3.12). The phase space is split into many regions as signal or background depending on training events.

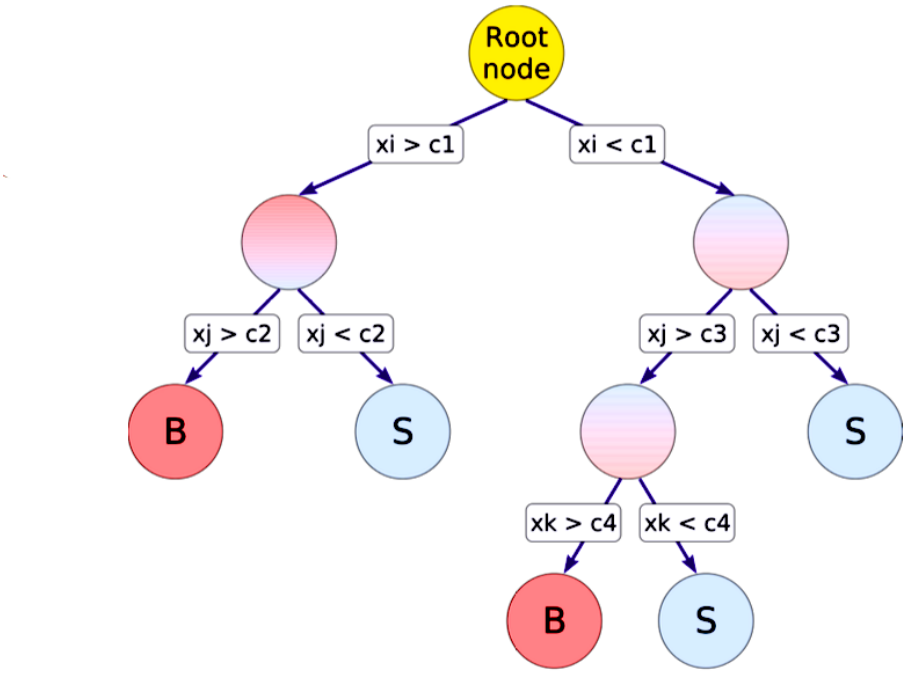

Figure 3.12: Schematic view how boosted trees method works.

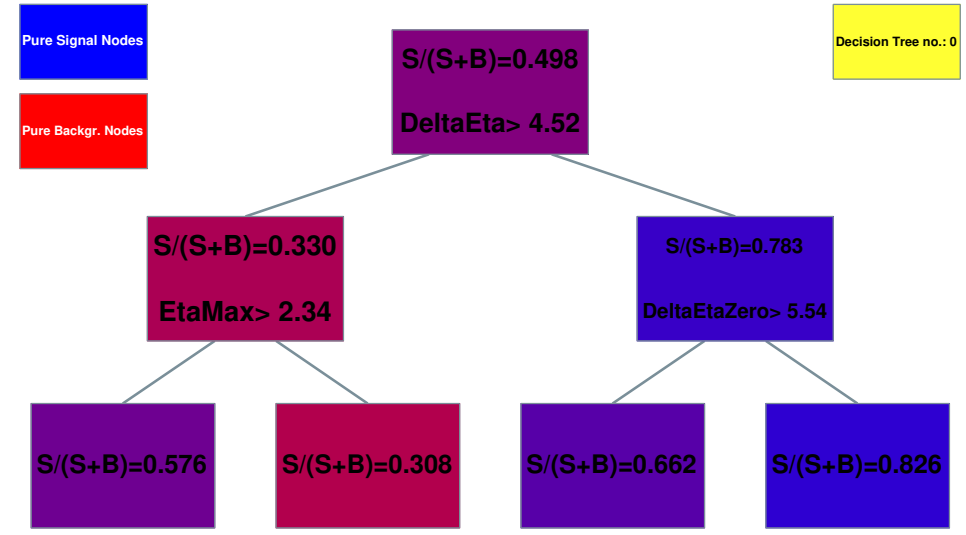

(a)

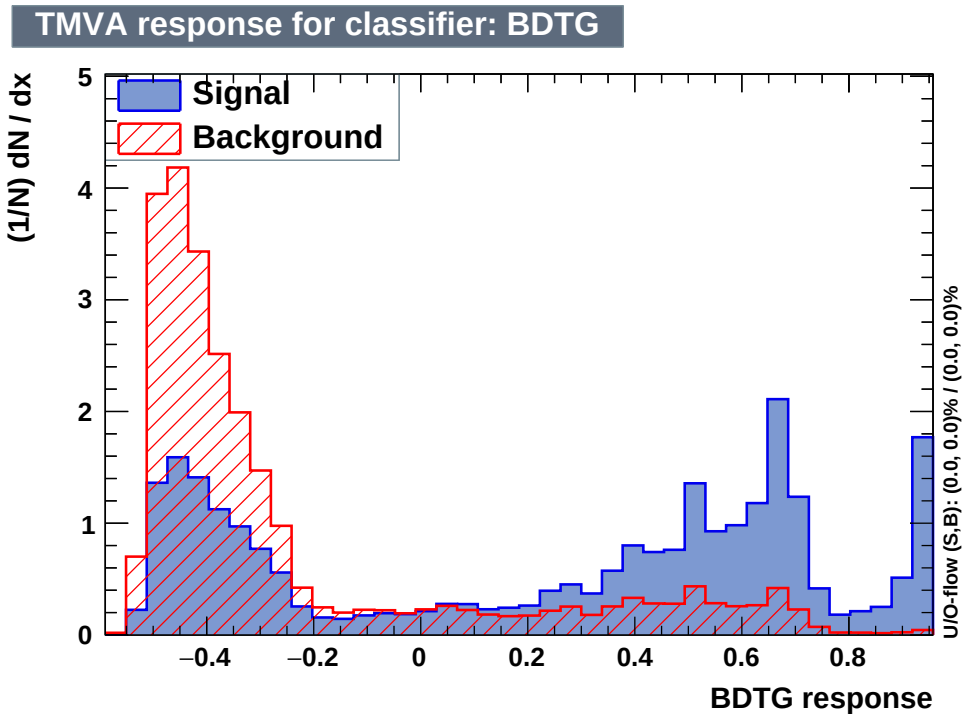

(b)

Figure 3.13: a.) A tree in boosted decision trees , b) boosted decision trees the final response in PYTHIA 8 MBR samples, the signal type is chosen as "DD" in the training phase for this example.

At each step in the sequence, cut optimization is searched with the variables which give the best separation of signal and background events, and used to split these processes is continued recursively on resulting partitions until a stop criterion is fulfilled. In the algorithm, each node is searching for the best cut for each variable, and individual cut sequences lead to the different leaf nodes. After finding the best cut for each variable, the data is split by the best cut hence forming the branching nodes (see Fig. 3.13(b)). It repeats until one splitting no further possible reduction in impurity that leads to a more stable response with respect to statistical fluctuations. Furthermore, the stopping criteria carefully have to be chosen since that could lead to overtraining on training data. The quantity of impurity is the Gini index, which is given by,

$$Gini = (s+b)P(1-P) = \frac{sb}{s+b}, \tag{3.6}$$

Where $P = s/(s+b)$ is the signal purity and s and b are the signal and background rates in the processes. The splitting at a branch node is processed until the impurity is not reduced further after splitting. And then node becomes as leaf and which is assigned to leaf with an output response, $s/(s/b)$. It builds and combines a forest of randomly different decision trees, and each tree attempts to correct errors from the previous stage. The key idea behind boosting is that they build a series of trees which each tree makes a sequence of classifiers. Instead of searching which tree has higher performance classifier, looking for a boosted performance which is collectively an ensemble of classifiers see in Fig. 3.13(b). For the prediction of the final classifier for an ensemble of D classifiers,

$$y(x) = \sum_{i=1}^{D} \alpha_i y_i(x, w_i), \tag{3.7}$$

where w_i are the parameters of the i^{th} classifier. The weighting coefficients α_i of being weighted count how often a variable is used to split a node and determined differently in each algorithm. The weight is given by the squared separation gained and the number of events in the given node.

Gradient boosted tree method is used in this thesis, which weak leaner built in a non-random way that makes fewer and fewer mistakes when more trees are added. In addition to gradient boosted decision tree, the predictions are fast and do not use a lot of memory. The learning rate (shrinkage) is an important parameter which controls performance of gradient boost how the tree algorithms build a series of trees. When the learning rate set with high values, each tree strongly correcting the mistakes of its predecessor. With smaller values of the learning rate, there is less emphasis on correcting the errors of the previous step.

3.4 Event reconstruction and software

3.4.1 Introducing software

After events have been selected by the L1 and HLT triggers, the data needs to be reconstructed properly and with high detail. This is done with CMSSW software for the CMS experiment. Analysis of reconstructed events is done with ROOT, a CERN designed C++ based program that is the necessary classes to perform statistical analysis and visualization of results. CMSSW software provides an implementation of all data taking conditions and to transform the information coming from the various subdetectors into other subdetectors. The software consists of a large number of classes and objects, information in the sub-detectors. For example, the Data of CASTOR can be combined with data from other CMS subdetectors. A new framework, common small-x OCD physics framework (CFF) has been developed for RUN2. This framework has tools to produce small files sizes on the complex data files produced by data reconstruction. The produced tree-like files provide only specific events knowledge for different type data analysis. Each data analysis is chosen event information in the files which are relevant for analysis strategy. Thus, not using all knowledge in the files make faster processing time than with complex reconstruction files. The event objects from the CASTOR is used in the CFF.

The CMSSW software has to be applied to Monte Carlo simulations. Combining MC software packages allows the physicist to create a simulated event that can be processed with CMSSW software. The CFF is not only used for data reconstruction, also is used for Monte Carlo simulations. Monte Carlo samples are used to validate the data, and to correct it to generated level. Also, the samples are obtained from systematic uncertainties. Monte Carlo software such as Pythia can simulate the physical side of a bunch crossing (the matrix element, the hard scattering. The use of the CFF. Simulating the detector response is an essential part of the research, software packages, such as GEANT4, can simulate the CMS detector.

3.4.2 Track and vertex reconstruction

The CMS detector is designed in a way to handle not only single proton-proton collisions but also high track multiplicity in many proton-proton interactions. This is many proton-proton interactions happening simultaneously called *pile-up*. The charges accumulated in the detector that should be clustered to locate the exact position of all the tracks. The integrated of the charge in a cluster is a measurment of the energy that the particle has deposited in the active part of detector, which is needed for particle identification via dE/dx method [51]. The reconstructed tracks of charged particles are among the most fundamental objects such as electrons, muons, and jets that are used in physics analysis. When a track traverses a piece of active tracker layer, the excited electron-hole pairs spread in a larger area than a single pixel.

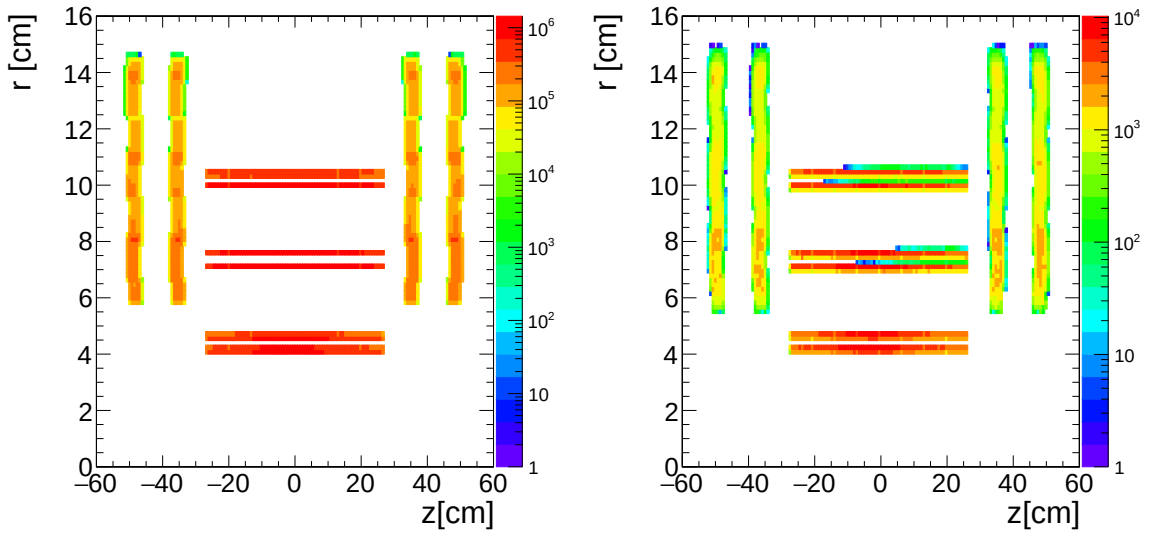

Figure 3.14: Position distribution of hits in the CMS pixel detector, z and radius are plotted, using 10 k hits from data. The aspect ratio of the plot is distorted.

The tracking system can go further and reconstruct tracks in even proton-proton collisions with the zero-magnetic field. Due to the absence of a magnetic field, a particle traveling in the central tracker of CMS are not curved but are straight lines. The standard track reconstruction can be processed in the extreme condition. The CMS pixel detector provides information of charged particle tracks when it traverses in the detector layers. Since the pixel hits alone are very clean and enough to properly reconstruct tracks with high precision and purity, its $150\,\mu m \times 100\,\mu m$ pixels are an excellent position resolution 3.14, also its layers are very close to the beam-line. Hence charged particles are measured as tracks traveling approximately as a straight line, but their direction is slightly altered at each layer-crossing due to multiple Coulomb scattering. In the data used here with no magnetic field (B = 0) the particle trajectories are simply straight lines. The collisions of the beams happen in a finite region in the center of the detector, which is very small in the transverse direction (a few μm), since the beams themselves are very narrow; however very wide in the z-direction (10-20 cm), the luminosity region is very extent in z-direction. The parameters that describe the region of possible collisions, is called the *beam-spot*. The beam spot is calibrated both in real-time during the data-taking, and off-line before data processing (with better precision). Since the beam-spot is wide in the z direction, in order to reconstruct the primary tracks in a given event, it is important to determine, event-by-event, the exact position of the collision, named the *event vertex*.

3.4.3 ECAL and HCAL towers energy reconstruction

The ECAL is located in front of the HCAL. Each tower of HCAL is combined with five ECAL towers. The fine granularity of ECAL is needed to precisely reconstruct photons and electrons. The ECAL and HCAL candidates are constructed by clusters of crystals. The energy within the smallest $\eta \times \phi$ unit of the detector, (combining all layers of the detector in HB, HE, and different-length fibers in HF) is summed up to form the *RecHits*. When the HCAL energy is also summed up with the corresponding 5×5 group of ECAL crystals, the candidates representing the total energy in that unit cell are called *CaloTowers*. For this thesis HCAL, only towers are used.

3.4.4 CASTOR tower reconstruction

CASTOR is a calorimeter and as such the reconstruction process will convert the electrical signals measured by the detector into measures of energy. This is done by transforming all digital signals from the read-out electronics into a charge (in fC) using a digital-to-analog converter (DAC); subtracting the average noise from the charge distribution; integrating the signal over a number of time slices; multiplying the resulting charge with a calibration factor into an energy value (in GeV). After this process, each of the 224 channels in CASTOR will have an energy deposit, with the exception of channels labeled as "bad" and channels with energy below the threshold value. Channels within the same sector are clustered together in a CASTOR tower with a fixed $\eta = -5.9$ value, corresponding to the central η value of the calorimeter. Towers in Castor calorimeter contain information from the hadronic and electromagnetic part of the detector. If the tower energy drops below 600 MeV - $\sqrt{N_{channels}}$ the particular tower is zero-suppressed since it is very close to the noise level.

4 Performance improvements studies

An interesting tool is to check the existing luminosity scale of CMS in an independent way based on a physics process. The dilepton is a pure electromagnetic process where presumably the cross-section can be calculated very precisely. An important aspect of the thesis is dedicated studies as predictions for the main data analysis project. The luminosity determination in ultra-peripheral collisions (UPC) in the proton-lead collision at 5.02 TeV analyses and CASTOR calibration will be described in this section.

4.1 The luminosity determination in ultra-peripheral collisions in proton-lead collisions

Exclusive photoproduction of dileptons and vector mesons at very high center-of-mass energies can be studied in ultraperipheral collisions (UPC). In protons and ions collisions that than more the prediction of vector mesons occurs through γp or γPb interaction via the exchange of two-gluons with no net color transfer and thus, at the LO, hence the cross section is proportional to the square of the gluon density in the target proton or ion [25]. The main requirement for a collision to be determined as a UPC is the existence of strong electromagnetic fields with the simultaneous suppression of hadronic processes mediated by the strong interaction. Such events are collected by selecting collisions with impact parameter larger than the sum of radii of the interacting particles. This study was presented in a poster session at the Quark Matter conference in Darmstadt(Germany) [52]

The situation is visualized in figure 4.1, where the two relativistically nuclei of charge Ze and radii $R_{1,2}$ are passing each other at the impact parameter b [53, 54]. The electromagnetic fields are concentrated in the direction perpendicular to the direction of movement and can be considered as a flux of virtual photons. The photoproduction process on a proton target may leave the proton intact in the so-called elastic interaction, or the proton may interact with a low-mass system, or the proton may break with a transfer of color in the inelastic collision reaction. UPC interaction between two hadrons, the final state can be produced in the interaction of a photon and a hadron interaction (see in figure 4.4) [55]. Here, this measurement is presented in di-muon decay channel in ultraperipheral collisions of protons and heavy ions (pPb) at $\sqrt{s} = 5.02$ TeV. The available an integrated luminosity of for Pbp collisions $L_{int} = 14.0\,nb^{-1}$, pPb collisions $L_{int} = 20.6\,nb^{-1}$ and total collisions $L_{int}= 34.6\,nb^{-1}$. The luminosity corresponds to the beam delivered by LHC.

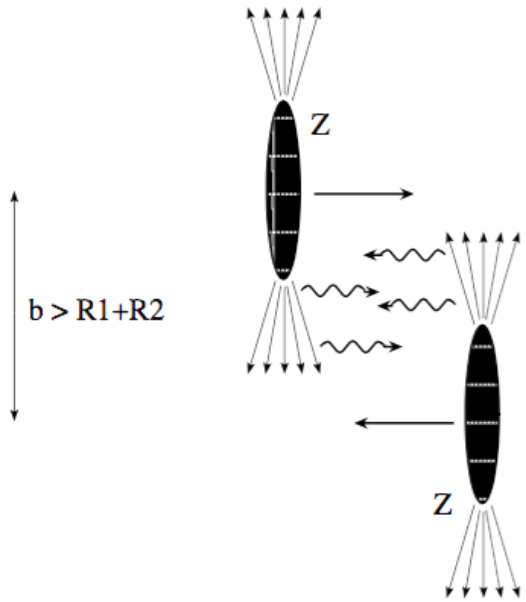

Figure 4.1: Schematic view of an ultra-peripheral collision of relativistic nuclei.

4.2 Proton-lead collisions

In September 2012, LHC physicists were colliding beams made of two different particles heavy ions with the less massive protons [48]. With proton-lead collisions can be studied for quark-gluon plasma, and to study its evolution into the kind of matter that makes up the Universe today. Lead ions started from lead atoms, which have an atomic nucleus containing 82 protons and between 122 and 126 neutrons, surrounded by a cloud of 82 electrons.

The LHC only accelerated one type, or isotope (Pb-208), of lead that contains 126 neutrons. Since protons and neutrons have approximately the same mass, an LHC lead ion weighs roughly 208 times more than a proton. An atom of lead became an ion of lead when some or all of its electrons were stripped away, leaving the remaining portion of the atom positively charged. The LHC acceleration process gradually striped away all of the lead atoms electrons, leaving a beam composed only of lead nuclei.

4.2.1 Starlight event generation

Starlight can be used for a wide number of UPC analyses since it is able to generate various mesons in photon-proton or coherent, incoherent interactions and also a two-photon production of mesons or dimuon pairs, all of these under arbitrarily defined colliding beams. In order to validate the generator not precisely predict the analysis of real data should

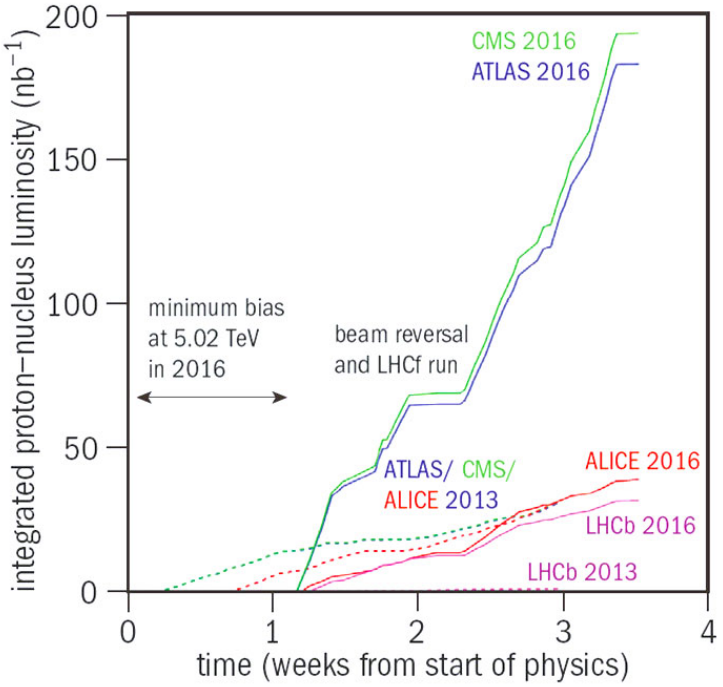

Figure 4.2: Collisions in LHC.

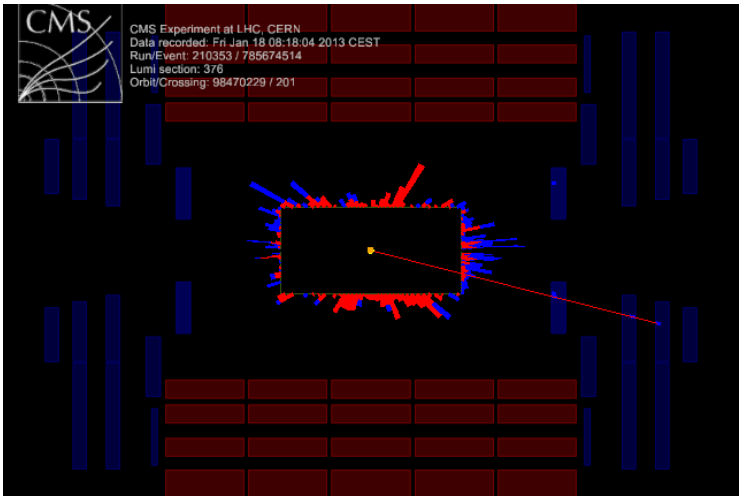

Figure 4.3: A proton-lead collision at a centre-of-mass energy of 45 TeV per nucleon. In this side-on view, the proton beam enters from the right side of the image and leaves on the left; the lead beam travels in the opposite direction. The event was selected requiring a muon trigger, and the muon (red line) was reconstructed in the CSC detectors.

be model-independent. The generator described data can be tested by comparing the distributions of kinematic and technical parameters obtained from the MC. The simulation samples are used in this to study for a baseline for acceptance and efficiency corrections or as the source of samples of elemental processes contributing to the signal from real data.

The MC generated sample is reconstructed in CMS software CMSSW_5_3 version with global tag START_53_V10::All. Ten million events for different mass range samples of QED dimuon from the two-photon process were generated with the Starlight event generator. As mentioned before, the Starlight event generator, which gives inputs to the Monte-Carlo (MC) simulations of various photoproduction processes. There are two contributions in exclusive photoproduction in pPb collisions, photoproduction from γp process where nucleus acts as the source and the proton as a target but there is also a non-negligible contribution from γPb process where proton as the source of photon and Pb as a target. Due to QED $\gamma\gamma \to l^+ l^-$ processes which are theoretically clean process [56]. The full QED calculation of the process would require to treat the photons as virtual, but at high energy, the virtuality can be neglected and the equivalent photon approach can be used. Several invariant mass ranges in the two-photon QED background were generated with Starlight event generator. The whole invariant mass spectrum of the di-muon system is included in this study. The aim is to scan a wide range of invariant masses, and the yields of selected di-muon events are compared to high precision theoretical calculations of electromagnetic particle production from photon-photon collisions in the very periphery of the colliding nuclei [57]. The cross section for lepton pair production, $\gamma\gamma \to l^+ l^-$, where l indicates e, μ or τ, is determined by the Breit-Wheeler formula [58]. The formula provides the cross section for a pair with given mass in the final state when there was a two-photon pair of a given center-of-mass energy in the initial state. As each of the nuclei is the source of virtual photons, the two-photon luminosity is given by the convolution of photon fluxes of the two nuclei.

4.2.2 The kinematical description of the dimuon process

The exclusive two-photon production of lepton pairs referred to as exclusive $\gamma\gamma \to l^+l^-$ can be calculated in the framework of quantum electrodynamics (QED) [55]. These processes have a very clean experimental signature that only involves the detection and reconstruction of simple objects such as leptons and photons. The dilepton production in photon-photon collisions is a benchmark process that allows for precise determination of the luminosity at the LHC. The kinematical description of the dimuon process is provided by the square of the center-of-mass energy of proton and lead ion, the center-of-mass energy of photon and proton $W_\gamma p$, the absolute value of the four-momentum transfer squared at the $Pb-\gamma$ vertex Q^2, and the four-momentum transfer squared of the proton t. The rapidity variable y can be calculated using the four-momentum p as:

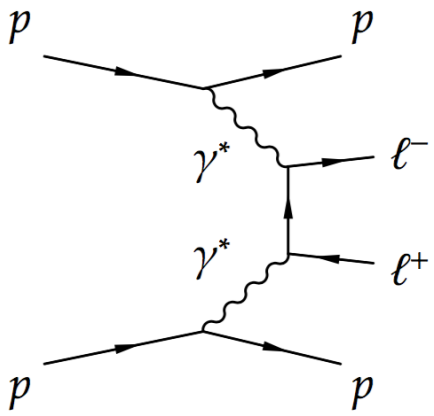

Figure 4.4: Diagrams representing exclusive two photon exchange in pPb collisions.

$$y \equiv \ln\left(\frac{p_0 + p_z}{p_0 - p_z}\right). \tag{4.1}$$

For any particle in the high-energy limit $p \approx m$ where m is the rest mass of the particle, the rapidity of such a particle becomes equal to the pseudorapidity $\eta \equiv -\ln\left[\tan\left(\frac{\theta}{2}\right)\right]$, where θ is the polar angle relative to the axis of the beam. UPC production has a distinctive signature -two oppositely charged tracks with small net p_T.

There are only two identified muons in the selected dimuon events, without any other activity in the central detectors, and the leptons are back-to-back in azimuthal angle. The data sample was skimmed of requesting dedicated HLT UPC trigger bits and for events with two tracker muons which pass the soft muon ID selection with an invariant mass more than $2\,\mathrm{GeV/c^2}$ and The invariant mass range $8\,\mathrm{GeV/c^2} < m(\mu\mu) < 12\,\mathrm{GeV/c^2}$ is excluded to restrict the background from υ decays. The muon ID selection used in this analysis [15] and the details of Muon ID are given below:

- The number of valid tracker layers > 5 which indicates the quality of inner tracks;
- The distance between the event vertex and the muon track in the transverse plane, $Dxy < 3.0$ mm, and the longitudinal plane, $Dz < 30.0\,\mathrm{mm}$, which indicates if the muon comes from a decay in flight or is a prompt muon, and removes cosmic muons;
- The number of pixel layers with valid hits > 1, to remove the muon tracks with 0 pixel layer hits;
- The probability of two tracks to belong to the same decay vertex $\approx 1\%$, opposite sign muons.

In order to look at the high mass regions in the dimuon decay channel, the $\gamma^+\gamma^-$ pair is required to have an invariant mass $4.5\,\mathrm{GeV/c^2} < m(\mu^+\mu^-) < 99.5\,\mathrm{GeV/c^2}$ and to restrict the background from upsilon decays, excluding $8\,\mathrm{GeV/c^2} < m(\mu^+\mu^-) < 12\,\mathrm{GeV/c^2}$.

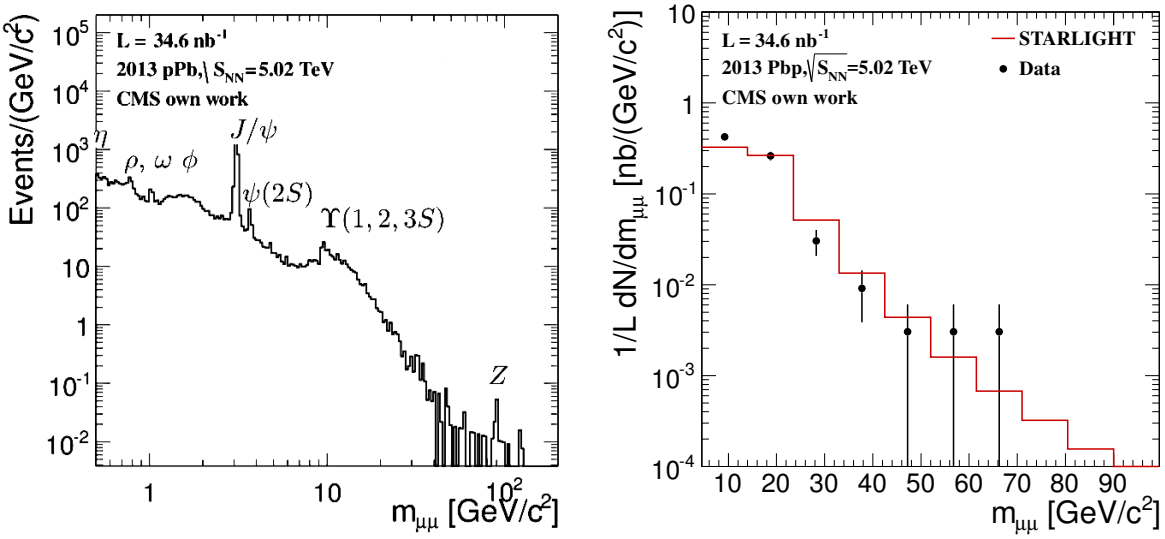

(a) (b)

Figure 4.5: (The invariant mass spectrum of dimuon in pPb collisions: (a) the inclusive spectrum, (b) data-MC comparison of the distribution of invariant mass of exclusive opposite sign dimuon systems for the events passing all selection criteria.

In figure 4.5 shown the invariant mass for dimuons in the mass range of $4.5\,\mathrm{GeV/c^2} < m(\mu^+\mu-) < 99.5\,\mathrm{GeV/c^2}$.

4.2.3 Exclusive collection

The exclusivity condition is requiring an absence of detectable energy deposition in both the central system and the array of the forward calorimeters. The high η coverage, allowed to hold a light on this rapidity gap and ensure a direct tagging. The track-based condition is using the reconstruct the tracks and vertices in each event. To identify such objects, single tracks with a transverse momentum in a range starting at a few hundred of MeV can be used as seeds to a primary vertex. The most important condition, the number of tracks should be identical to two, which is used to efficiently reduce the background of non-exclusive events (background from proton dissociation etc.). And only two tracks are originating from a single primary vertex and that the two tracks are associated to a higher-level (electron or muon) object, one can define an exclusivity selection ensuring a lower contamination by inclusive production processes. Thus the exclusivity selection is performed to keep only events with a vertex having no extra tracks other than those from two muons and no activity above the noise threshold in the calorimeters. A high-rate trigger path requiring at least two muons, with asymmetric constraints on their minimal transverse momentum is used. In order to supress background events, the muon pair is required to

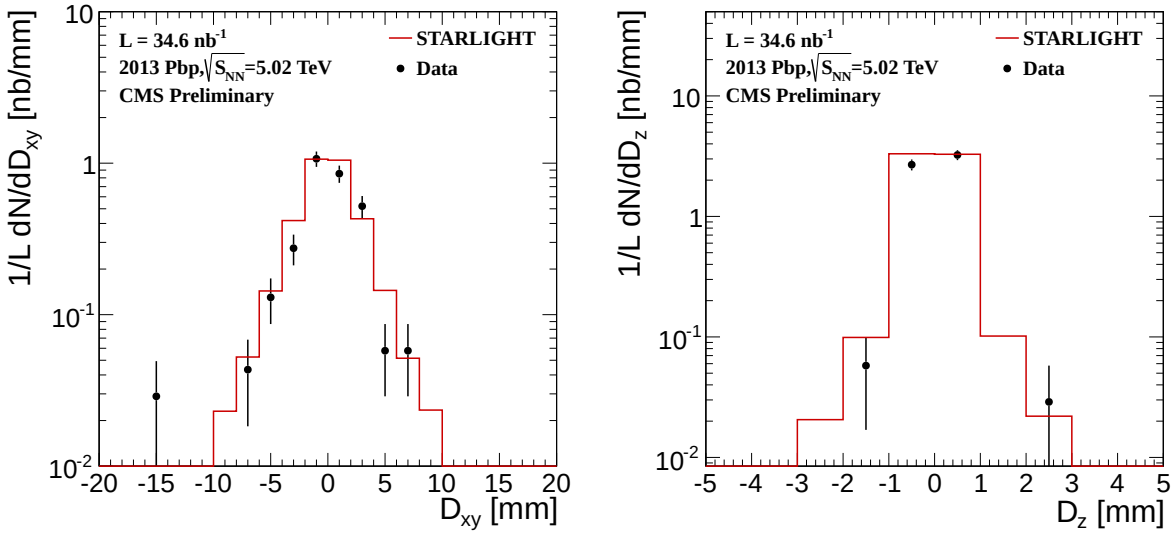

(a) Dxy (b) Dz

Figure 4.6: Data-MC comparison of the distribution of Dxy which is the distance between the accepted event vertex and muon track in the transverse plane and Dz which is the distance between the accepted event vertex and muon track in the longitudinal plane.

be back-to-back in the azimuthal angle $|\Delta\phi(\mu^+\mu^-)| > 2.8$ and balanced in the p_T of the two muons $|\Delta p_T(\mu^+\mu^-)| < 1.0\,\mathrm{GeV/c}$ [59]. Any charged or neutral hadronic contribution is removed by exclusivity requirements. In order to minimize the systematic uncertainties effected to the knowledge of the low-pT muon efficiencies muons with $p_T > 3\,\mathrm{GeV/c}$ are selected. The single muon distributions show in figure 4.8. In addition to reduce the contamination from non-exclusive events, events with pair muon $0.05 < p_T < 0.3$ GeV/c are only being considered. At high p_T there are indications from beam dissociation, which are not modeled precisely by the STARLIGHT generator.

Figure 4.7 shows the distribution of p_T, η and ϕ of dimuon (upper panel). All control distributions are showing a good agreement in the observations with the theoretical predictions. Calorimeter exclusivity criteria are done by rejecting any activity in calorimeter contributed to the dimuon events. There should not be any additional towers in calorimeters (EB, EE, HB, HE and HF). An additional tower is defined as tower above the noise threshold and outside a region of $\Delta r = (\Delta\eta)^2 + (\Delta\phi)^2 < 0.3$ around either muon. The noise thresholds are determined from the leading tower energy distributions comparison of data with Starlight events (signal + QED background) where we exclude the region of $\Delta r < 0.3$ from the muon tracks. The noise levels have no beam measured in data taken will no collisions.

4.2.4 Correction for acceptance and efficiency

The acceptance and efficiency ϵ in the cross section is the probability that the UPC created in the collision is successfully reconstructed in the detector. The correction can be determined using a Monte Carlo (MC) simulations, where the events of the process are generated by a software generator of the process, then folded by a detailed detector simulation, and finally analyzed applying the same requirements as were the basis for the determination of the number of measured events.

The analysis of the simulation provides the number of successfully reconstructed events. To determine the efficiency of detecting a dimuon system with an invariant mass $m_{\mu\mu}$, the Starlight Monte Carlo samples generated level is folded with the CMS detector simulation (Reco) using the CMSSW framework. In figure 4.9 the number of events N per luminosity L over the invariant mass is shown for both distributions. The right panel illustrates the analysis efficiency based on this study. Both trigger efficiency and acceptance are important contributions here. The efficiency:

$$\epsilon = \frac{\mathrm{N}^{\mu\mu}_{Reco}}{\mathrm{N}^{\mu\mu}_{Gen}} \tag{4.2}$$

is in the range $0, 1, ..., 0, 5$. Due to the very low p_T of muons the detection efficiency is limited to some extent. It is a fact, that CMS can only see a small fraction of the full cross-section because a) the limited reach in rapidity of the trackers, and b) the magnetic cutoff of tracks at low p_T. Both of these strongly limit the "visible" dilepton cross-section. Thus, I decided to calculate the "visible" cross-section and call this "acceptance" of CMS:

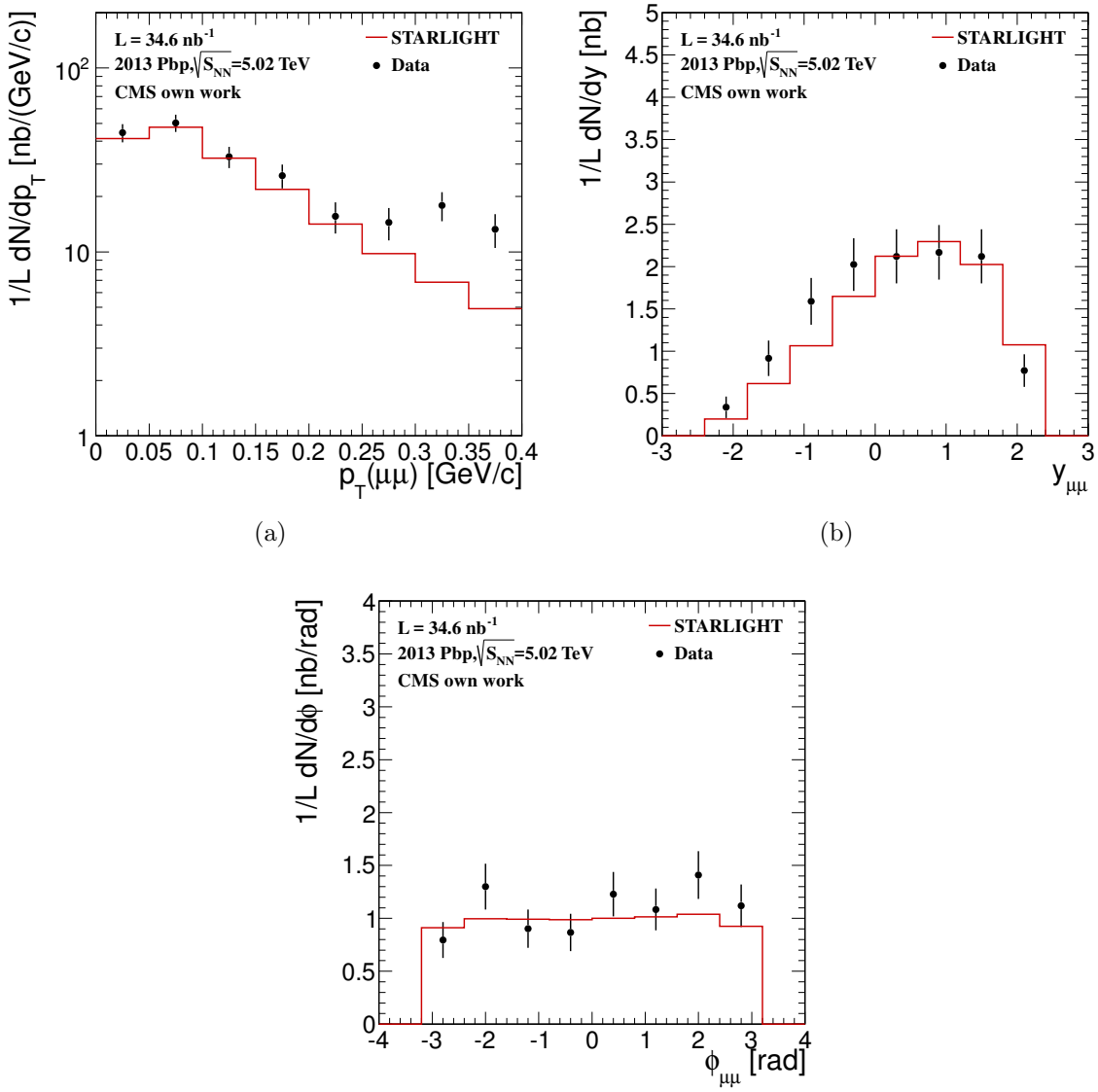

(a) (b)

(c)

Figure 4.7: Data-MC comparison of the distribution: (a) p_T with $0.05\,\mathrm{GeV/c} < p_T < 0.3\,\mathrm{GeV/c}$, (b) $y_{\mu\mu}$, (c) the $\phi_{\mu\mu}$of opposite sign dimuon systems for the events passing all selection criteria.

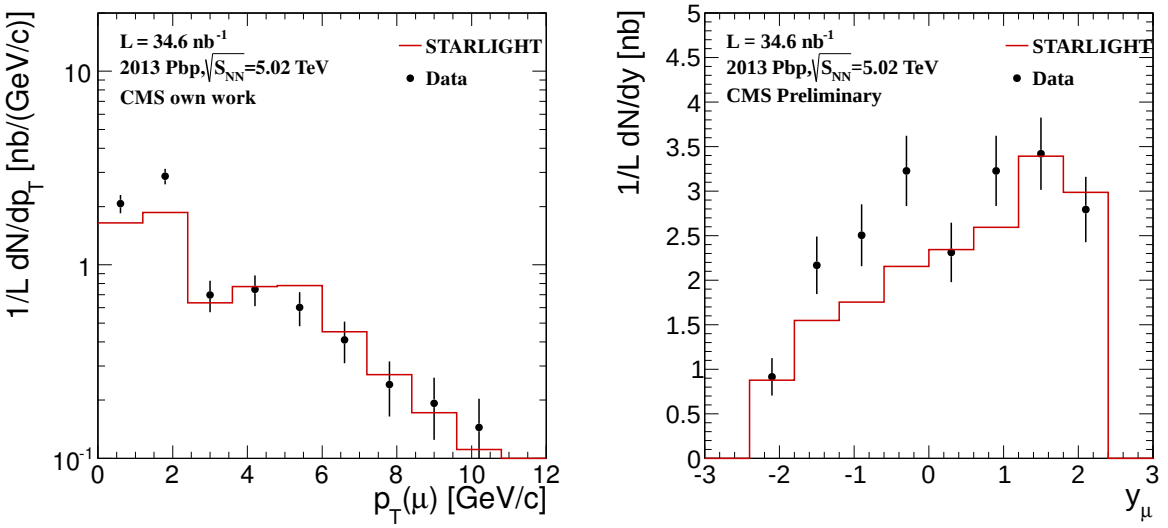

(a) p_T (b) y_μ

Figure 4.8: Data-MC comparison of the single muon p_T and the single muon rapidity y_μ.

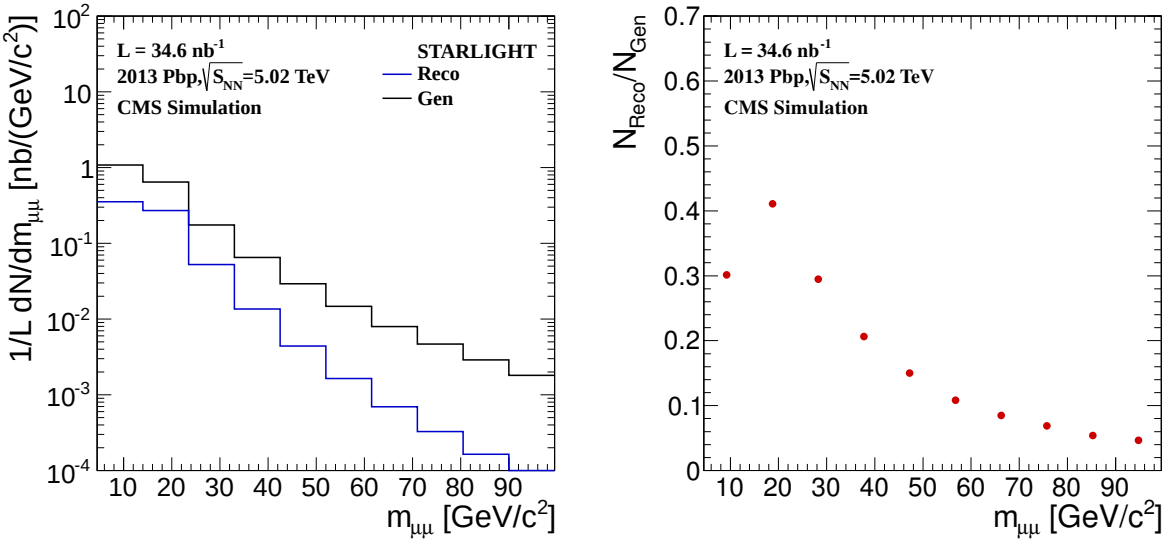

Figure 4.9: Comparison of the Starlight Monte Carlo on generated level sample (Gen) and (Reco) using the CMSSW framework. The invariant mass is shown for both distributions. On the right, the ratio distribution of Reco and Gen is shown.

$$\alpha = \frac{\mathrm{N}^{\mu\mu}_{Gen}(\mid y^{\mu\mu} \mid < 2, p_T^{\mu\mu} > 3\,GeV)}{\mathrm{N}^{\mu\mu}_{Gen}} \tag{4.3}$$

Table 4.1: The MC production from Starlight generator for p-Pb collisions; invariant masses and cross-sections are given below for each sample

QED-background	Mass range GeV/c^2	σ nb
$\gamma\gamma \to \mu + \mu$	4-10	1290
$\gamma\gamma \to \mu + \mu$	10-25	126
$\gamma\gamma \to \mu + \mu$	25-50	8.9
$\gamma\gamma \to \mu + \mu$	50-100	1.0

Thus STARLIGHT generator is successfully used in the analysis to determine exclusive photonproduction in p-Pb UPC collisions. MC productions related to the UPC measurement in p-Pb UPC, fully managed by the author, cover almost 10 million simulated events.

4.2.5 Luminosity cross-check

The experimental determination of the cross section is based on counting the number of occurrences of the process in question with simultaneous knowledge of the efficiency to detect its occurrence and the parameters of the beams whose collisions produce the process. The differential cross sections for exclusive photon production by the STARLIGHT generator are shown in the table 5.1. The luminosity at the LHC is defined using the revolution frequency f of circulating bunches, the number of bunch crossings nb at the interaction point, the average number of interactions in one bunch crossing and the total inelastic cross-section. In the CMS experiment, a procedure to measure a visible cross section σ_{vis} is implemented using Van-der-Meer scans technique [16]. The advantage is that there is no need to know as the detail of the luminosity in physics process. In continuing to this standard method here I use a precisely known physics process. The visible cross-section is the fraction of events which can be seen by a given acceptance condition. However, the σ_{vis} of the reference process is known, the luminosity is given by the measured rate of the reference process divided by the corresponding visible cross section. It is the strength of the Van-der-Meer scan technique technique [16] that the knowledge of the fraction of σ_{vis} to σ_{inel} is not necessary.

The integrated luminosity $\mathscr{L}$ of a given UPC trigger is derived by dividing the efficiency-corrected number of selected dimuon events by the predicted cross-section of starlight as a function of the dimuon mass:

$$\mathscr{L} = \int L\,\mathrm{d}t = \frac{N^{\mu\mu}_{Data}}{\epsilon^{\mu\mu} \times \sigma_{\gamma\gamma\to\mu\mu}} = (36.0 \pm 2.24(stat.) \pm 3.6(syst.))\,nb^{-1} \tag{4.4}$$

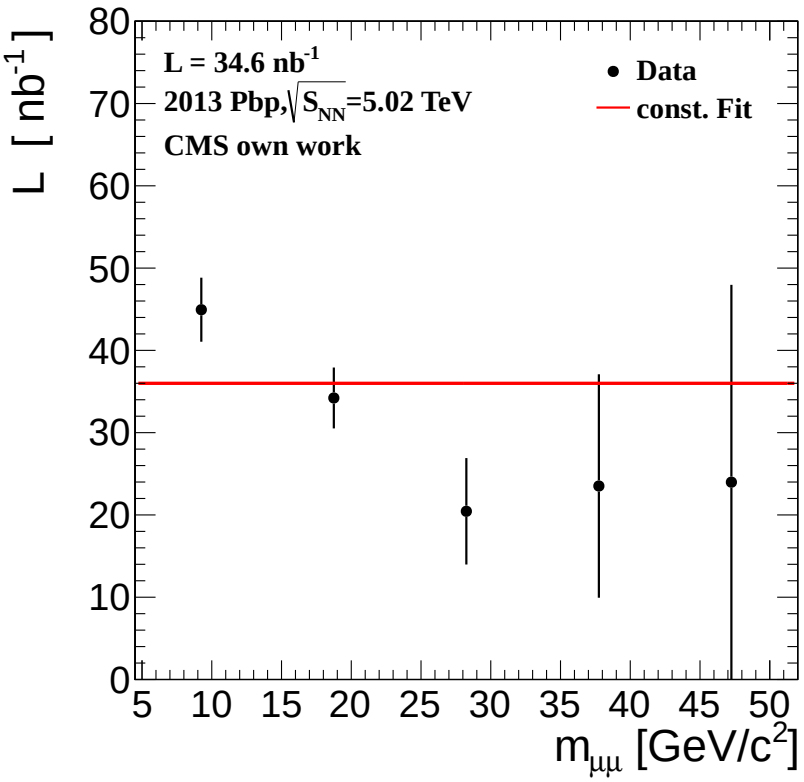

Figure 4.10: Consistency of luminosity measurement as a function of di-muon mass.

Where $N^{\mu\mu}_{Data}$ is the number of selected dimuons events, $\epsilon^{\mu\mu}$ is efficiency from simulation(Eq. 4.2), $\sigma_{\gamma\gamma}$ is the cross-section from STARLIGHT(Tab. 5.1).

Furthermore systematic uncertainties are estimated by variying the di-muon p_T selection. The lower boundary was changed from 0.05 GeV/c and upper boundary from 0.3 GeV/c. Also the calorimeter thresholds here changed in systematic studies. In the figure 4.10, the red line is a constant fit to the data from this measurement. With a χ^2/ndf of 3.64, the luminosity is shown to be independent of the dimuon mass in good approximation. The fit yields luminosity of 36.4 nb^{-1} with a statistical uncertainty of 2.24 nb^{-1}. Please note that the luminosity given in the legend ($L = 34.6\,\mathrm{nb}^{-1}$) refers to the luminosity determination by Van der Meer scans. The number is compatible with this result within the combined statistical and systematical uncertainties. It turned aout the that the measurement of exclusive dimuons events in pPb data statistically limited to about 10% precision.

4.3 Inter-calibration of CASTOR calorimeter

We will take a detailed look at the Centauro And Strange Object Research (CASTOR) detector which is one of the main objectives of this thesis. I have been taking part in the calibration, the monitoring, and the performance analysis for CASTOR. These study results are presented in this section.

4.3.1 CASTOR calorimeter

The CASTOR calorimeter is a non-compensating cylindrical Cherenkov calorimeter. The main features of the CASTOR calorimeter are its very forward position at 14 m at the minus z-side from the interaction point in CMS, where it covers the pseudorapidity range $-6.6 < \eta < -5.2$ as illustrated in figure 4.11. Because of constraints, the forward region of CMS requires a compact detector design, radiation-hard materials, a fast response and reliable operation in a magnetic field.

Many technical challenges exist for the CASTOR detector due to its position in the high $|\eta|$ region, because it is aligned parallel to the beam along the z axis, it is very close to the LHC beam, only 1 cm to 2 cm from the beam pipe. The detector is shielded from the magnetic field of 3.8 T from the central CMS solenoid but still there is a significant magnetic field is about 0.2 T present in the CASTOR volume. The detector is made up of layers of tungsten plates (the absorber) as an absorber quartz and fused silica plates as a sensitive active medium. The detector segmentation in ϕ is provided by 16 sectors together with 14 longitudinal modules. A schematic drawing is shown in figure 4.12. The detection technique is based on measuring Cherenkov light produced by charged particles traversing the calorimeter. Cherenkov light is produced by charged particles of secondary showers passing through the quartz. In order to maximize the amount of Cerenkov light captured,

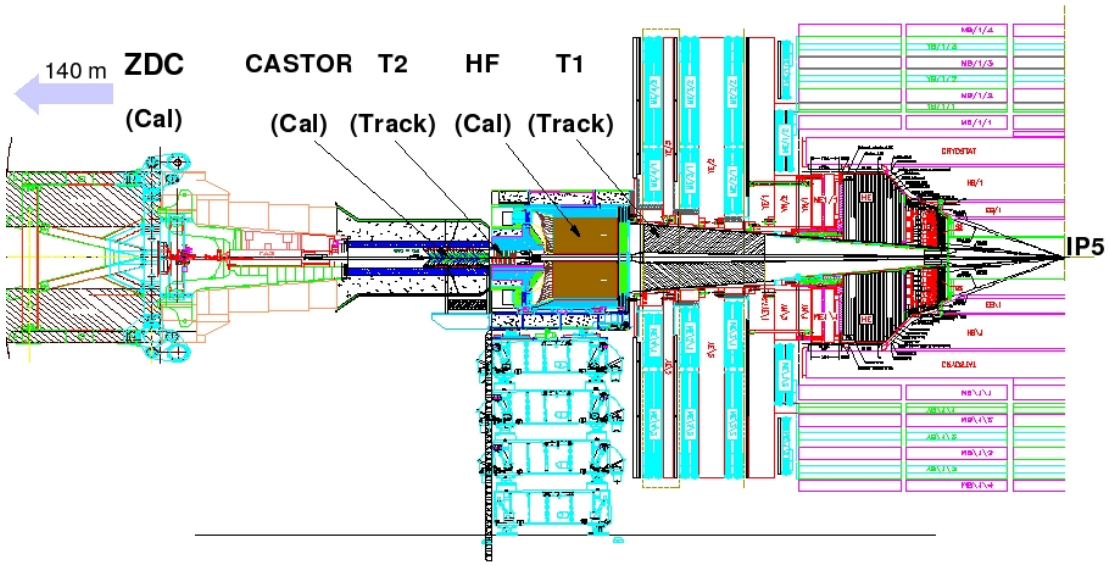

Figure 4.11: The position of CASTOR in CMS, as seen from inside the LHC ring. Also shown are the T1 and T2 trackers of the independent TOTEM experiment, the Hadron Forward (HF) calorimeter and the position of the Zero Degree Counters (ZDC) 140 m further away.

the plates are tilted to an angle of 45° with respect to the beam pipe. Air-core light-guides collect the light emitted by the quartz plates and transfer it to photomultiplier tubes (PMT) of type Hamamatsu R5505, where it is amplified and converted to an electrical signal. The fine-meshed PMTs are used since these PMTs work under the extreme magnetic fields.

Figure 4.13 shows a description of the CASTOR geometry with respect to the CMS coordinate system. Here the module configuration along z is clearly indicated the effect of magnetic field, with the first module closest to the CMS interaction point. The 1.6 m long detector is divided into 224 readout channels. Each channel is connected to a readout unit, which in itself consist of 5 sampling units. A sampling unit is made of a pair of tungsten and quartz plates. The tungsten plates in the electromagnetic channels are 5 mm thick and the quartz plates are 2 mm thick. Each channel corresponds to 0.385 λ_I, the total electromagnetic section corresponds to 0.77 λ_I. and the hadronic section has total depth 9.24 λ_I.

4.3.2 Inter-calibration

A calibration scheme for CASTOR absolutely necessary. The Cerenkov radiation is propagated only for light at an angle greater than the critical angle for our quartz, and most of the energy loss of the showers occur due to interactions with the tungsten absorber, only a specific fraction of the critical energy is transmitted. Thus, there will be energy loss

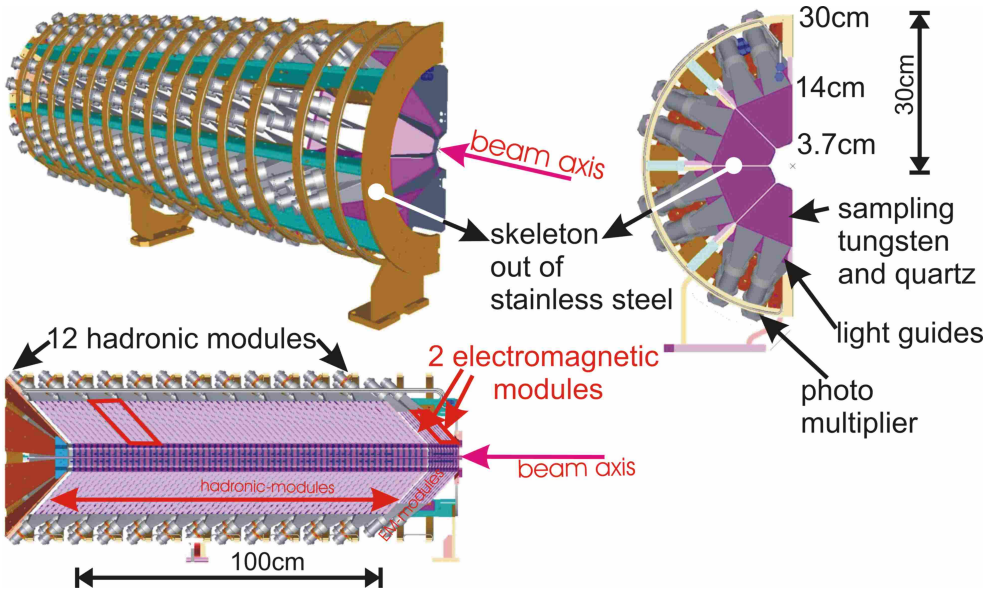

Figure 4.12: CASTOR illustrated.

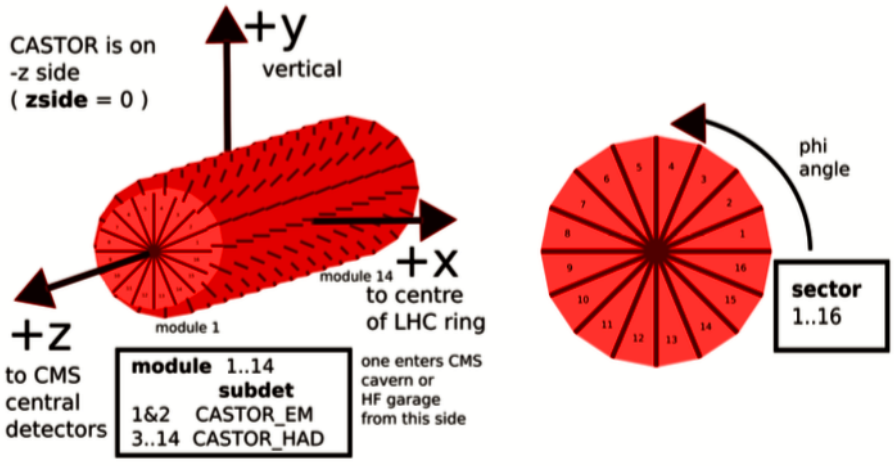

Figure 4.13: CASTOR geometry definitions and numbering

for which we need to compensate. In addition, the calorimeter works under the extreme magnetic fields also the calibration of CASTOR is needed to equalize gains of the different PMTs responses. Furthermore, test beam cannot be the case since any calibration outside of magnetic field is a rough approximation because the scintillator and a sandwich calorimeter response depend on magnetic field value and its orientation. The inter-calibration must be performed to achieve to understand the absolute energy scale, and the detector response and the uniformity.

The calibration of the CASTOR calorimeter is performed in situ by analyzing beam halo muons events collected during the LHC operation. Basically, that is to perfor inter-calibration events with equal energy deposition in each CASTOR channel. Each CASTOR channel is characterized by the PMT gain, quantum efficiency and by the efficiency of a light guide. An acquired signal or response is proportional to these constants which are individual for every channel. Hence the channel response is the most important step towards the full calibration of the detector. The inter-calibration constants are defined as the inverse of the ratio of each channel response to a corresponding response of a chosen reference channel. Reference channel is obtained previous the CASTOR calibration analysis, hence for comparison it is needed to be used the same channel. After calculating the inter-calibration constants for each channel which are used to correct for variations in the channel response within the detector. However, the calibration of the calorimeter is significantly complicated because of many technical challenges as mentioned above. Due to these technical challenges, in *situ-calibration* procedures to be developed mainly to account for the effect of the magnetic field. CASTOR is shielded against radiation and magnetic field but the iron shielding in the forward region of CMS has poorly shielded narrow gaps. In the region around the gaps, the high voltage applied to the PMTs is increased to compensate for the gain loss. Some of the calorimeter channels are still affected by the stray magnetic field varies both in magnitude and direction. Calibration of a longitudinally segmented calorimeter is known to be a non-trivial task. Several classes of events are considered to perform the equalization of channel responses (inter-calibration):

- Zero bias and minimum bias LHC beam collected in special runs during injection and ramp up, and beam splash events.

- Beam halo muons are products of proton interactions with a collimator material or beam gas.

  Muons are used because they are very penetrating particles due to their low chance of interacting which create a clear and easily identifiable signature in CASTOR. These types of muons are generally considered as sources of background, but they can be a very good candidate for the study of detector alignment, calibration, and detector performance validation. It is an advantage that in a wide energy range muon energy loss is similar to the energy loss by a minimum ionizing particle. Thus a halo muon penetrating CASTOR deposits an equal amount of energy in every module. It has a clear signature in the calorimeter and can be easily identified.

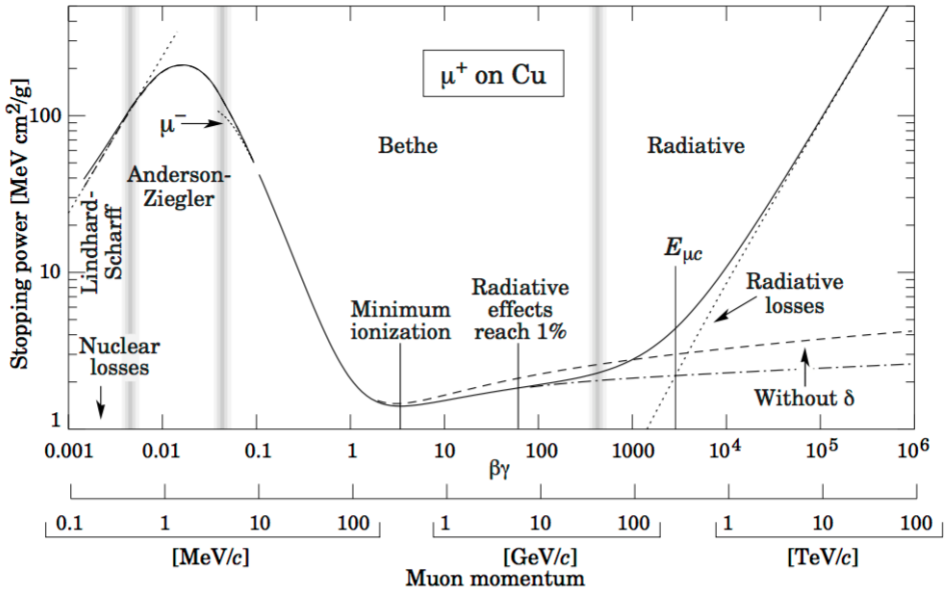

Figure 4.14: Stopping power for positive muons in copper as a function of muon momentum. Solid curves indicate the total stopping power.

But there is a disadvantage the use of muons for these tasks, which is about the muon energy loss since they generate electromagnetic showers, but this will only happen at the highest energies. There are the different contributions to the muon energy loss, this can be seen in figure 4.14, which shows the muon energy loss (stopping power) in Cu as a function of the muon momentum. Radiative processes start to dominate after 1 TeV. Below that the muon will only lose a small fraction of its energy via ionizing. This is why muons are characteristically called minimum ionizing particles (MIP) in this energy region, and only above energies of 1 TeV the loss is dominated by radiative processes.

4.3.3 Channel by channel inter-calibration

The relative inter-calibration of channels is based on the *in-situ* successful observation and selection of beam halo muons [60]. Most of the halo muons are produced $50 - 148$ m from the interaction point. Thus the halo of muons which reach the CMS area are almost parallel to the beam axis and is most intense close to the beam axis, where CASTOR is located. Since muons are very penetrating particles they have a clear signature in the calorimeter and can be easily identified in a suited data set. Muons lose only about 10 GeV of energy traversing CASTOR. For high energy muons of the beam halo, this energy loss of muons in CASTOR is negligible. Radiative energy losses are an important contribution at these energies, but on average they contribute equally to all channels of the calorimeter.

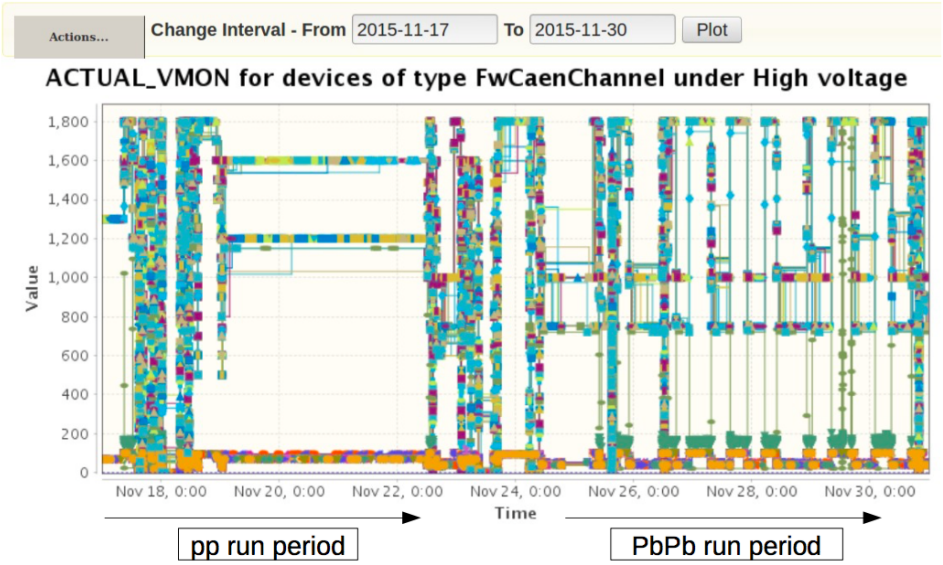

Figure 4.15: Example for runs from 2015 CMS data taking the LHC "interfill-" and "circulating-" beam periods for proton-proton and proton-lead. Shown are LHC high voltage setting in the calorimeter. The intervals of proton-proton and HI data taking can be identified.

Almost all halo muons used to calibrate CASTOR are taken during the period when LHC is filled with new protons at a constant beam energy of 450 GeV. For this reason, halo muons are a particular stable probe for the relative calibration of CASTOR. Muons are recorded with regular CMS data taking during the LHC "interfill-" and "circulating-" beam periods (see in figure 4.15). A dedicated hardware trigger is used for the LHC interfill and circulating-beam runs in CASTOR to trigger the CMS experiment. This trigger is routinely operated by CMS during these runs. In order to most reliably detect muons, the high voltage is typically increased during dedicated halo muon runs. However, in some occasions, muon data is also taken at physics high voltage in order to check the gain correction factors.

For a precise inter-calibration it is the aim to collect about 1000 muons per sector (see figure 4.17). In reality, the number of good muon candidate events depends on a significant factor also on the sector number. To obtain an event sample which is both statistically relevant and sufficiently pure, it is indispensable to use dedicated hardware muon trigger and combine it with sophisticated event selection. Since the needed thresholds are very close to the calorimeter noise level, the noise characterization is very important. Each azimuthal sector contains 12 hadronic channels, which are grouped in four groups of three channels (triplets). In each azimuthal sector, the 4 triplets are considered for the trigger. At least 3 triplets in one sector must have one channel (two channels in 2015/2016) above the noise level in at least three of these groups, and no further channel above noise level

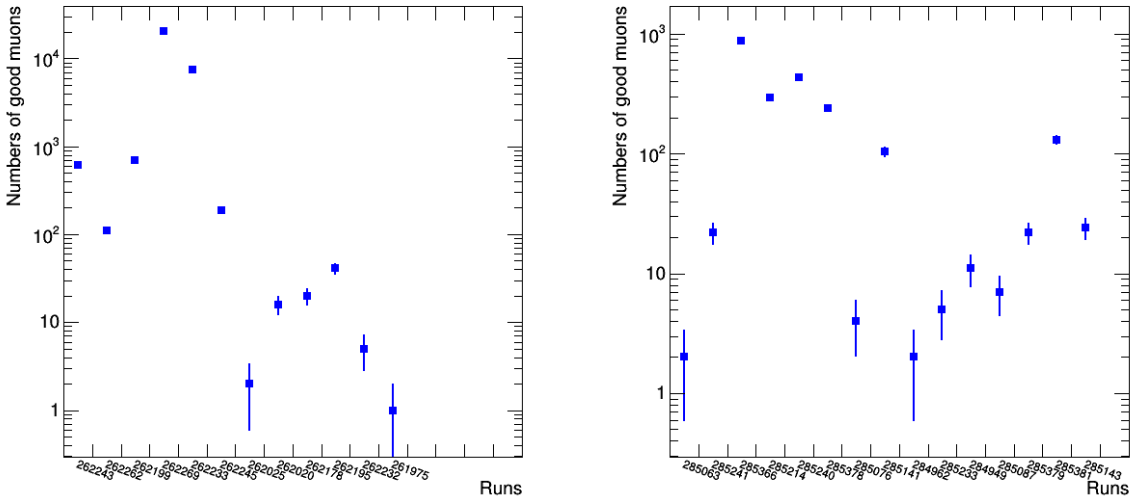

(a) 2015 (b) 2016

Figure 4.16: Example for runs which have good muons from 2015 and 2016 CMS data taking the LHC "interfill-" and "circulating-" beam periods.

anywhere else in the calorimeter for the trigger to fire.

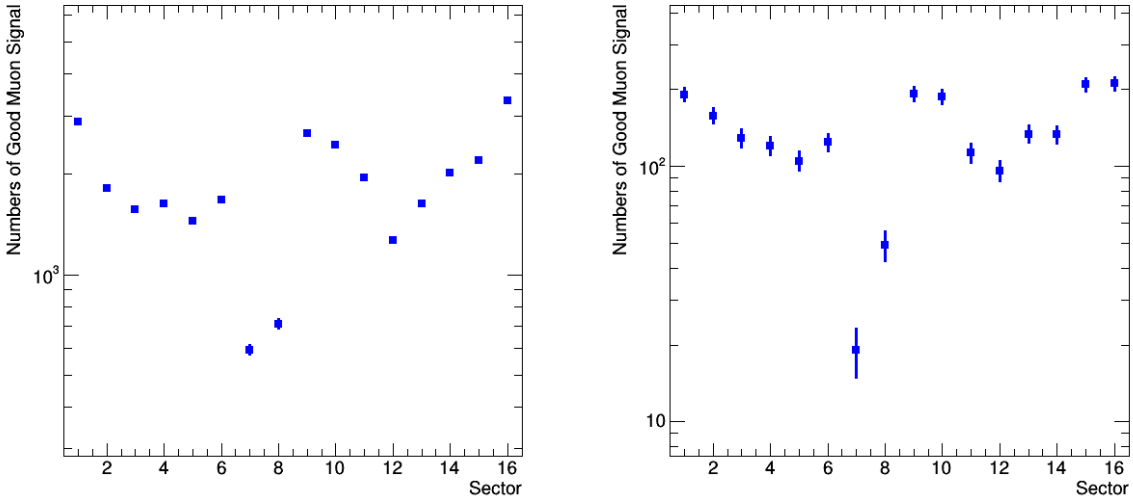

(a) 2015 (b) 2016

Figure 4.17: Example for good muons events per sector from 2015 and 2016 CMS data taking the LHC "interfill-" and "circulating-" beam periods.

The typical trigger rate of this configuration is around 10 to 100 Hz depending on the number of protons in LHC. The triggering and accurate measurement of minute beam halo muon signals are very sensitive to precise channel-by-channel estimates of the noise level and baseline to separate the signal from noise. In figure 4.18 the average signals in each channel are shown. Note that in 2015 has the higher gain because high-voltage was used while in 2016 it was the normal physics high voltage. In order to most reliably detect muons, the high voltage is typically increased during dedicated halo muon runs. The dedicated muon high voltage menu is 1600 V for all PMTs. However, in many occasion muon data is also taken at specific physics high voltage for cross checks. A detailed offline event analysis is required to prepare the collected data for inter-calibration. For this purpose for each of the 224 channels, the no-beam noise thresholds are determined for the exact same data taking periods as analyzed.

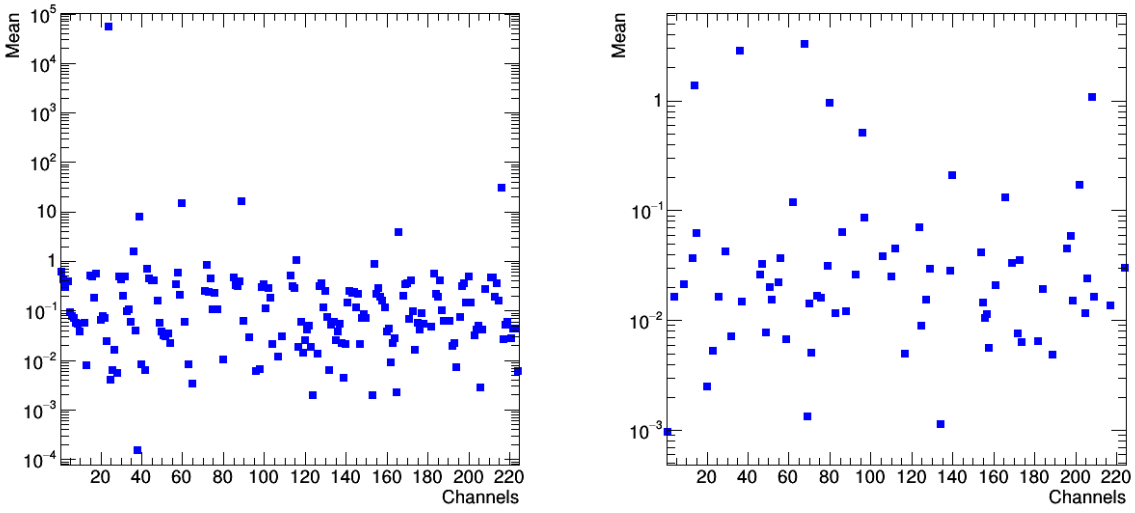

(a) 2015 (b) 2016

Figure 4.18: Example for average muon signal in the 224 channels from CMS data taking the LHC at 3.8 T in the proton-proton run period in 2015 and 2016.

With this information, an offline zero-suppression of the data is conducted at $2\,\sigma$ noise level. A high-quality exclusive muon candidate is then found if there is one single tower with more than 5 non-zero-suppressed channels, and not more than 5 non-zero-suppressed channels all over the rest of CASTOR. Furthermore, the muon-tower must fulfill to have one channel in each of these three longitudinal regions: module 1 to 4, module 5 to 9 and module 10 to 14. This requirement is sensitive to the penetrating nature of muons and will reject low-energy pions that do not reach to the back of the calorimeter.

In figure 4.19 as example of the result of the on-line and offline muon selection the first 64 muon candidates are shown. This data was taken with the CMS magnet at 3.8 T in the

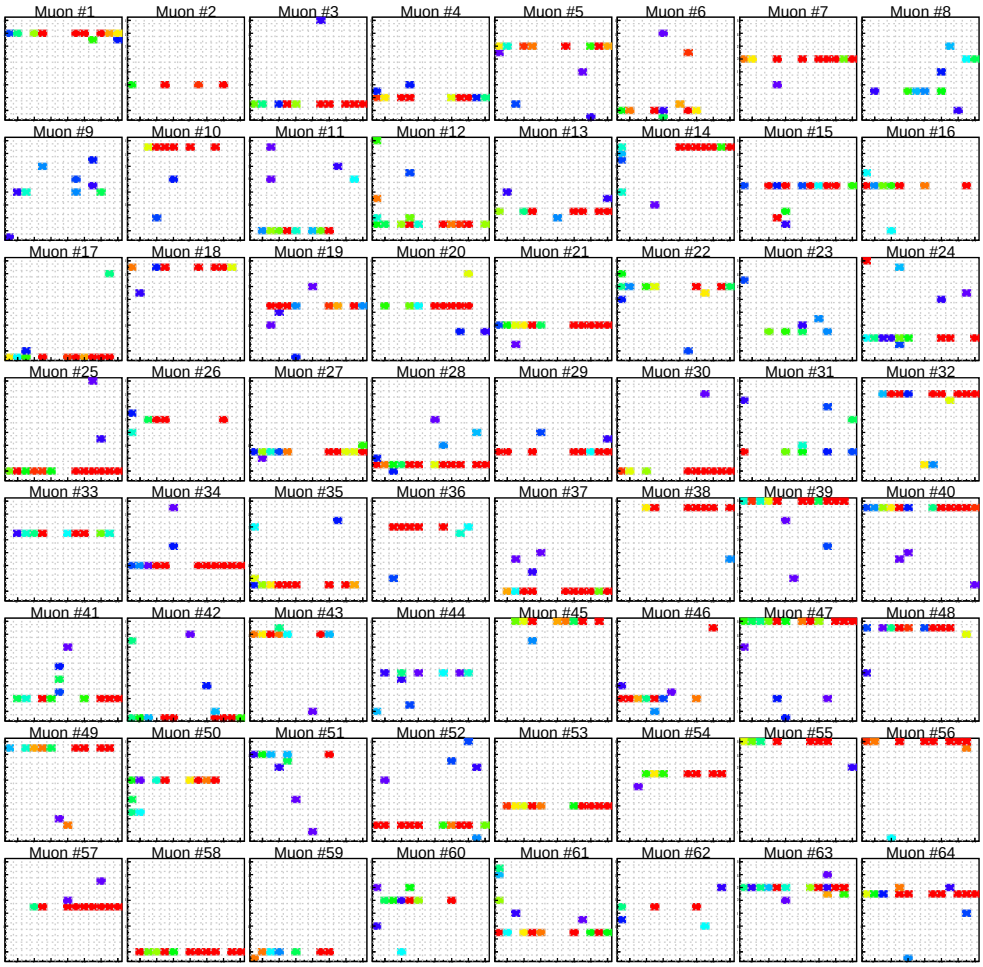

Figure 4.19: Typical halo muon events in CASTOR recorded during the proton-lead run period in 2016. Shown are the first 100 continuously selected muon candidate events after the full offline event selection. For each event the towers (y-axis) and modules (x-axis) of CASTOR are indicated with a grid. The z-axis is identical for all events and has a maximum of 60 fC.

proton-lead run period in 2016 which can be seen since many of the modules at depth 7 to 9 are yielding no signal.

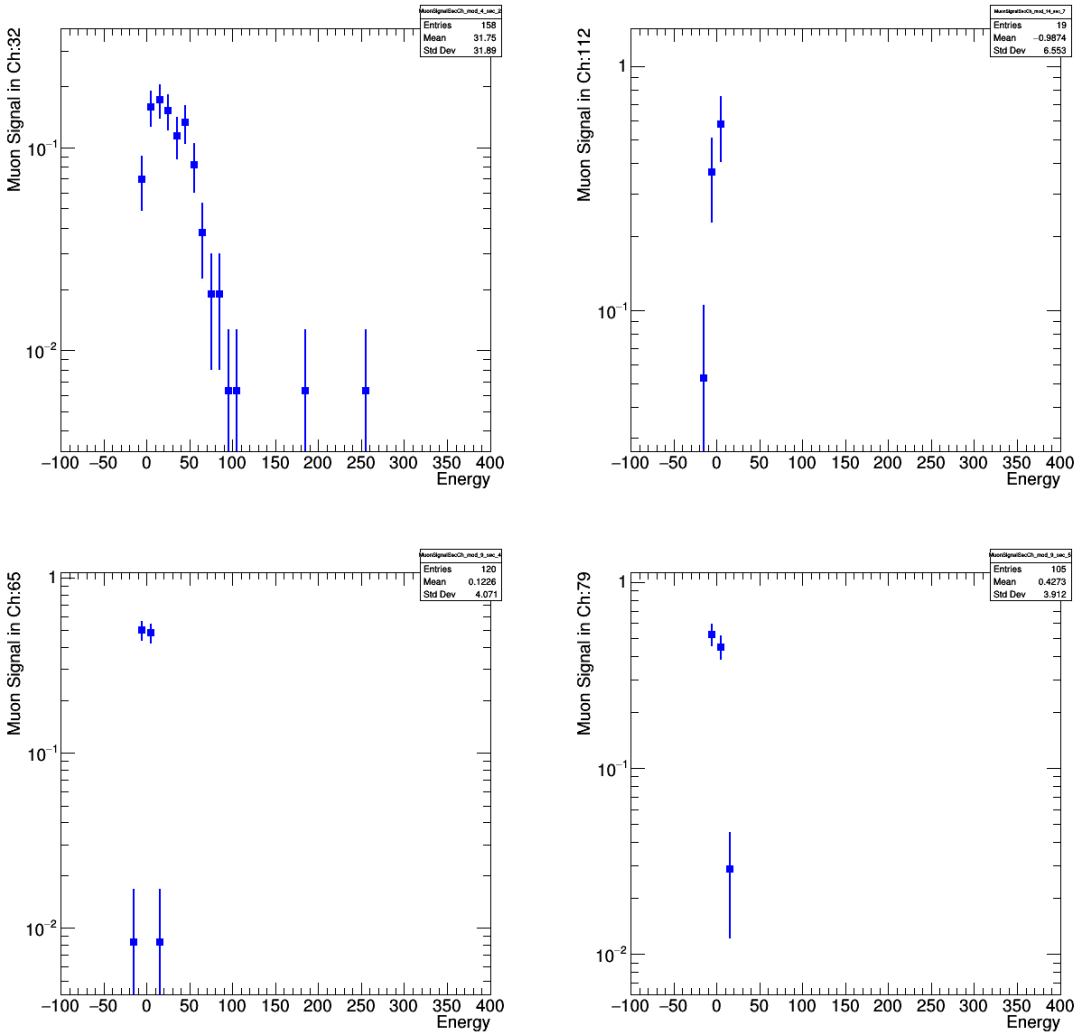

Figure 4.20: Example for channels that have low muon signal at 3.8 T in the proton-proton run period in 2015.

And some channels with very low muon signal which are also included in the bad channel lists. Some channels with low muon signal are shown in figure 4.20. In Figure 4.21 the signal and noise spectrum after the offline selection are displayed for a particular channel together with a simplified fine-mesh PMT model tuned to the data. The model assumes constant amplification per dynode including Poissonian fluctuations. It is important for the used fine-mesh PMT to consider the probability of electrons to miss a particular dynode, p_{miss}.

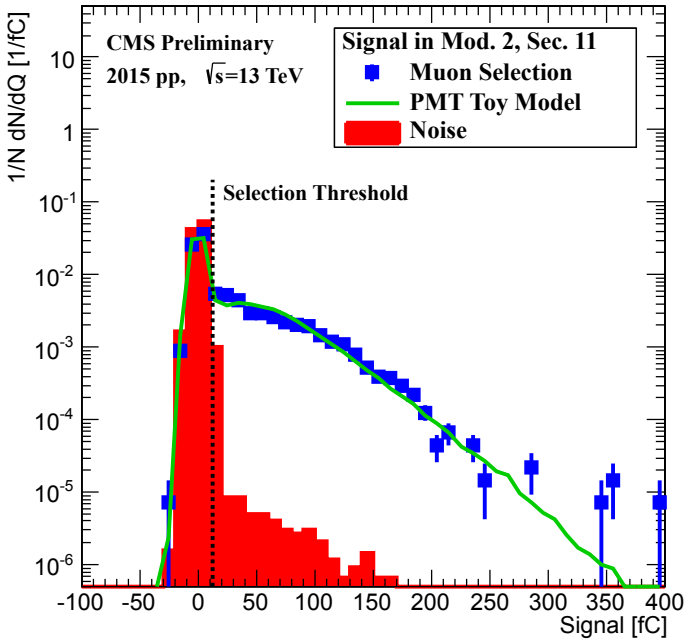

Figure 4.21: Signal spectrum for a typical CASTOR channel after an off-line isolated muon event selection. The data is recorded in June 2015 with proton beams and CMS magnet at 0 T. The dedicated muon high-voltage menu is used. The overlaid noise distribution is measured from non-colliding bunch data. The model line corresponds to a simplified mesh-type PMT model with 15 dynodes, amplification/dynode of 2.65 and dynode-miss probability of 0.21, for an average number of photoelectrons $\langle N_{\text{p.e.}} \rangle$ of 0.58.

The relatively low-energy resolution of fine-mesh PMTS and is important to understand the recorded muon data. While the muons are clearly seen above the noise level, there is no obvious muon peak produced. These muon data are a very powerful probe of the stability of the calorimeter over time. If we consider the collected muons during 2013 (Run 1) as the reference, we can compare channel-by-channel how the calorimeter evolves over time. The 2013 data are shown in figure 4.22. This is of paramount importance also to transport the energy scale from 2011 up to 2016 data. The most precise and direct comparison can be performed for periods of time where the same high voltage menu, as well as magnetic field setting of CMS, was used. The absolute stability of CASTOR is within 4% and the spread of channels can be quite well described by Gaussian distributions. The observed differences are corrected for with the inter-calibration. The response to muons is considered as an absolute reference scale. A further detailed off-line analysis is required to prepare the collected data for inter-calibration. For this purpose for each of the 224 channels, the no-beam noise thresholds are determined for the exact same data taking period.

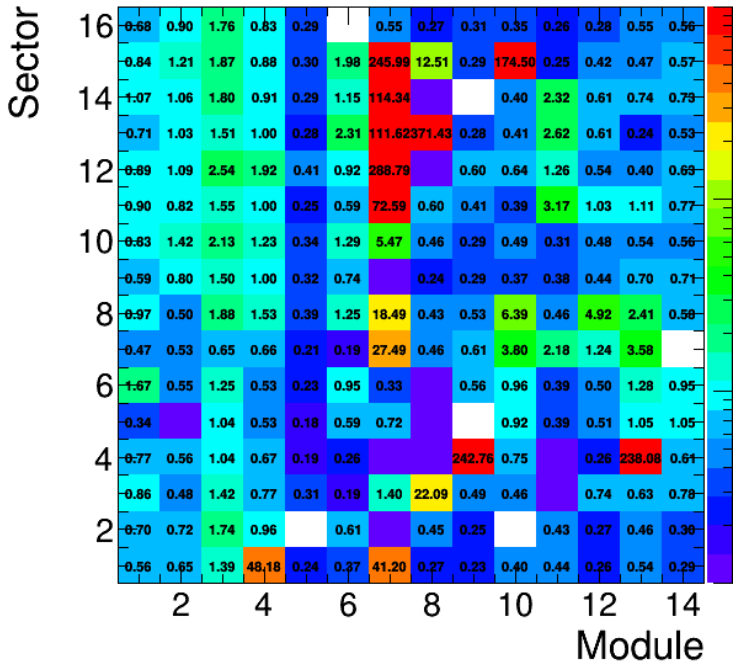

Figure 4.22: The average of muon signal in 224 channels for 2013 (Run 1) as the reference run.

This is of paramount importance also to transport the energy scale from 2011 up to 2016 data. The most precise and direct comparison can be performed for periods of time where the same high-voltage menu, as well as magnetic field setting of CMS, was used. The absolute stability of CASTOR is within 4% and the spread of channels can be quite well described by Gaussian distributions. The observed differences are corrected for with the

inter-calibration. Thus, the inter-calibration takes care of location of channels in the calorimeter as well as a location in time. The response to muons is considered as an absolute quantity. Figure 4.23 shows the difference of muons recorded from 2013 with and 2016. The right-hand side illustrates the stability of muons collected at muon high voltage. With a bootstrapping method, it was found that the statistical uncertainties on the inter-calibration constants are ≈ 10 to 15% in each channel.

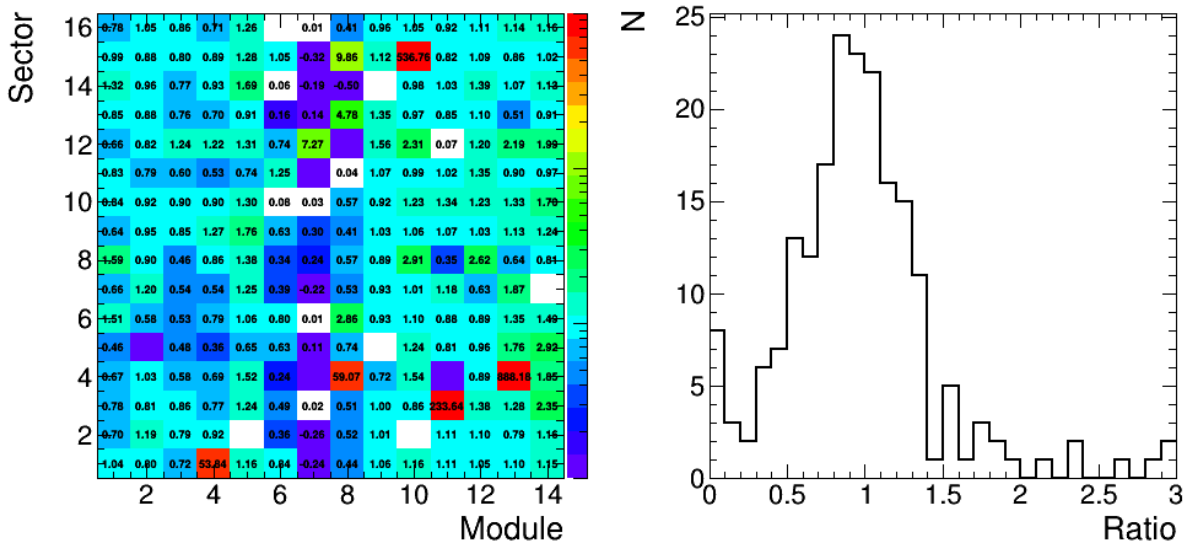

Figure 4.23: The difference of muons in 224 channels from 2013 with and 2016. The right hand side illustrates the stability of muons collected at muon high voltage.

4.3.4 Absolute energy scale

The aim of the absolute calibration is to measure which energy deposit in the calorimeter, in units of GeV, results in a specific output of the electronics measured in fC. A first estimate of the absolute calibration is performed by cross-calibrating to HF. There are data on the pseudo-rapidity dependence of the deposited energy in the HF calorimeter, which can be used for this task [61]. The approach consists in extrapolating the measured η-dependence of energy deposit in HF to the CASTOR η range. The η-dependence in HF is approximately linear in log scale, therefore an exponential extrapolation is applied by fitting a straight line to the log of the data. Since all models indicate an overestimation of this exponential approximation for CASTOR, a correction for this effect is applied. The overestimation is calculated for all model predictions. The correction factor is calculated by $E^{\text{log-linear}}_{\text{CASTOR}} / E^{\text{HE-model}}_{\text{CASTOR}}$, and find an average of 1.309 with an RMS of about 6 %. This RMS is taken as an estimate of the uncertainty of the extrapolation. Also, the uncertainty of the absolute calibration of HF with ≈ 3 % (for the long fibers) and the uncertainty of

the HF hadron level correction, which is $< 10,\%$, contribute to the total uncertainty of this extrapolation of energy deposit to CASTOR,

$$\Delta_{\mathrm{tot}} = \sqrt{(6\,\%)^2 + (3\,\%)^2 + (10\,\%)^2} \approx 12\,\%. \tag{4.5}$$

The inter-calibration of CASTOR adds $\sim 20\,\%$ of uncertainty to this measurement. The fact that only the front modules of the calorimeter are used means that $25\,\%$ of the hadronic energy is not observed. The composition of the used minimumbias data in terms of hadrons and electromagnetic particles is estimated with the above mentioned 9 different event generators and a correction factor relative to a pure electron beam is derived using the ratio of energy deposit of pions to electrons measured at the test beam

$$R_{\mathrm{minbias/e}} = \frac{\sum E_\gamma + 0.75 \sum E_{\mathrm{h}} \cdot R_{\pi/e}(E_{\mathrm{h}})}{\sum E_\gamma + \sum E_{\mathrm{h}}}. \tag{4.6}$$

This calculation runs overall photons and hadrons entering CASTOR, $R_{\pi/e}(E_{\mathrm{h}})$ is the π/e ratio measured at the test beam, and the coefficient 0.75 accounts for the fact that in measurement only the first 5 modules were used and thus $\sim 25\,\%$ of the average hadronic shower profile is not observed. Due to different energy spectra of produced particles and different electromagnetic/hadronic energy sharing in different generators $R_{\mathrm{minbias/e}}$ differs for different generators.

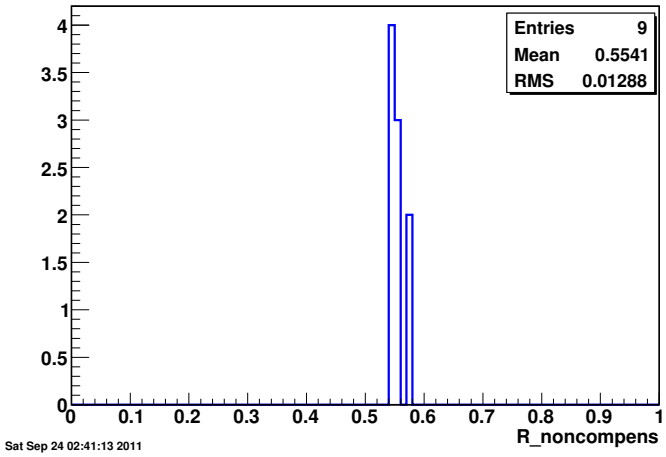

Figure 4.24: Distribution of factor of correction for non-compensation for 9 generators.

Figure 4.24 shows the distribution of this factor obtained from using the 9 event generators. We find an average value of 0.55 with an RMS of $\sim 2\,\%$. Thus the final value of the absolute calibration factor is

$$k_{\mathrm{cal,e}} = \frac{581\,\mathrm{GeV}}{20960\,\mathrm{fC}} \cdot 0.55 = 0.015\,\mathrm{GeV/fC} \tag{4.7}$$

where the total uncertainty of the approach is ∼30 %, which is dominated by the CASTOR inter-calibration and hadron-level correction. The uncertainty will be reduced in the near future with an update of the CASTOR detector simulation. The overall hadron level correction uncertainty for CASTOR is estimated from these studies, which is essentially related to the performance of the detector simulation, to be 5%. Thus the final value of the absolute calibration factor is

$$k_{\mathrm{cal,e}} = \frac{665\,\mathrm{GeV}}{20960\,\mathrm{fC}1.978} = 0.0160\,\mathrm{GeV/fC}. \tag{4.8}$$

Since the position of CASTOR in CMS is subject to small changes the corresponding hadron level correction can also be affected. With improved detector alignment techniques, this effect was reduced to contribute about 16% to the uncertainty. The total uncertainty of the absolute energy determination taking all factors into account is 22%. The obtained calibration constant is compatible within uncertainties with the value that is determined from the test beam measurements.

5 Data analysis

Observation of soft diffractive dissociation in proton-proton collisions of LHC Run2 at $\sqrt{s} = 13\,\text{TeV}$ is presented in this chapter. Diffractive processes form a significant contribution to the total inelastic cross-section and therefore it is very important to study the mechanism behind them since they are non-perturbation OCD processes. The main object of this work is to study properties of the diffractive processes. The aim of this study is to measure the cross-section of the soft diffractive dissociation in proton-proton collisions such as single diffraction (SD), and double diffractive (DD). All the relevant processes are illustrated in figure 5.1. Single diffraction (SD, $p+p \to p+\text{X}$), processes in which one proton dissociates into a system which carries quantum numbers of the proton and the second proton remain intact and the rapidity gap is produced in the forward region separating the diffractive proton and the dissociated system. Double diffraction (DD, $p + p \to \text{X} + \text{Y}$) are events in which both protons are broken. Each dissociated system carries the quantum numbers of the protons and they are separated by a central rapidity gap. Furthermore central diffraction (CD, $p + p \to p + \text{X}p$), is class of processes in which both protons remain intact and system with quantum numbers of vacuum is produced in the central region. I focus particularly on the cross-section measurement of single diffraction (SD) and double diffraction (DD) events and their characteristic properties. Also, the comparison with non-diffractive (ND) processes is included.

The final state hadronic system is separated by the largest rapidity gap in the event. Well-defined rapidity gaps are crucially important for classification of the diffractive processes. One important aspect of the work is the measurements of the rapidity gap distributions corrections for detector effects to the level of stable final particles are required in order to compare the experimental results with the theory. If the probability of particle detection is low, large model dependent corrections are introduced to the experimental result. Thus, events for classification and for diffractive mass measurement are selected in order to have enough information to make classification or calculation of diffractive mass feasible. Another important aspect is the rapidity gaps are defined here by pseudorapidity of charged hadrons from tracks in the pixel detector because the information from the strip tracker system cannot be used for technical reasons. The yield of primary charged long-lived hadrons in inelastic proton-proton collisions is determined using hit-pairs and straight line tracks in the pixel detector [51]. Because of the CMS pixel detector, with it's $150\,\mu m \times 100\,\mu\text{m}$ pixels, has an excellent position resolution. Its layers are very close to the beam-line. Hence, charged particles are measured as tracks, since they traveling approximately as straight lines (perturbed by multiple Coulomb scattering and energy loss)

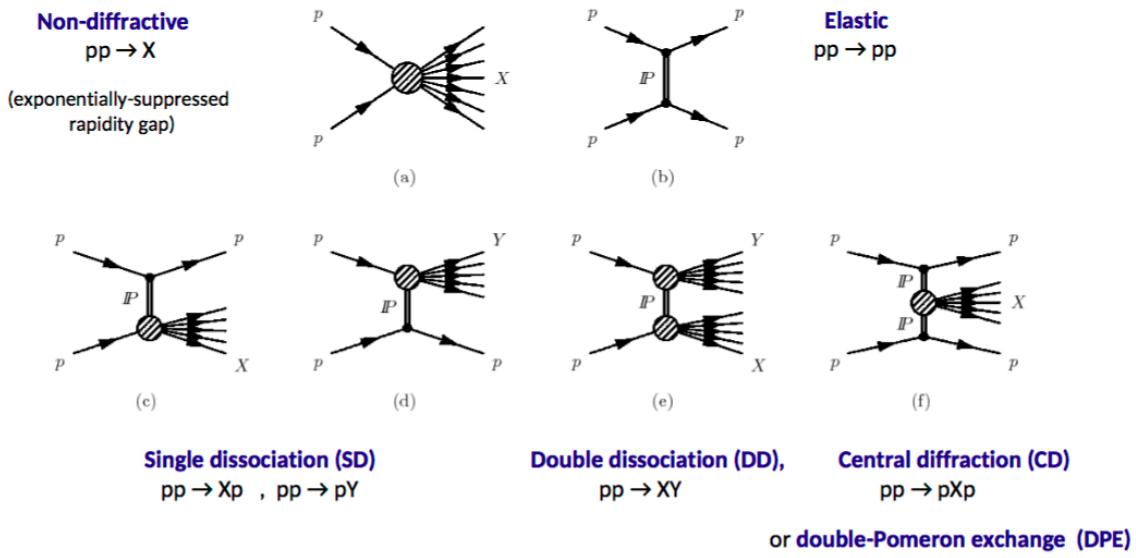

Figure 5.1: Schematic diagrams of inelastic events.

the pixel hits alone are very clean and are trial to reconstruct tracks and vertices with high precision and purity. In Fig. 5.4 illustrate the pixel hits in $\phi - \eta$ phases, and in Fig. 5.6 the performance of the pixel tracking of the data is compared to simulation. The track events selection cut is required by using events with the number of track ≥ 1.

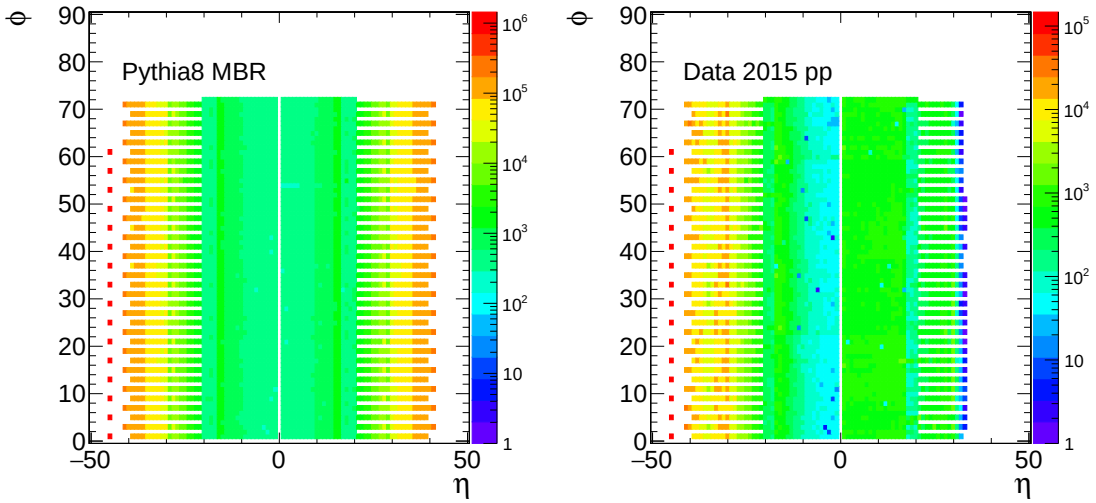

Figure 5.2: The pixel hits on $\phi - \eta$ phases.

5.1 LHC run 2

A shut-down period for the LHC occurred during 2013 and 2014, where upgrades and technical improvements have been performed in order to reach the designed instantaneous luminosity and center of mass-energy. On March 21st 2015 the first proton-proton collisions at $\sqrt{s} = 13\,\text{TeV}$ have been obtained, at a new record-breaking energy [62]. A number of bunches per beam up to 2244 at the CMS experiment have been reached for the first time in 2015. The first part of this run 2 proton-proton operation ended on November 2015 with a total delivered integrated luminosity of 4.22 fb^{-1} [63]. The luminosity of 2015 is shown in figure 5.3.

CMS has been taking zerobias data at 13 TeV since 3rd of June. During this period, the CMS magnet has been kept off due to an issue with the cooling system, this is the technical reason for not using the strip tracker system for particle identification. These the data collected with zero magnetic fields are used in this thesis. The issue with the magnet cooling system was found feeds liquid helium to the CMS superconducting magnet. The problem was later diagnosed to be due to oil, which is used in the initial compression stages, reaching the so-called "cold-box" of the cryogenic system.

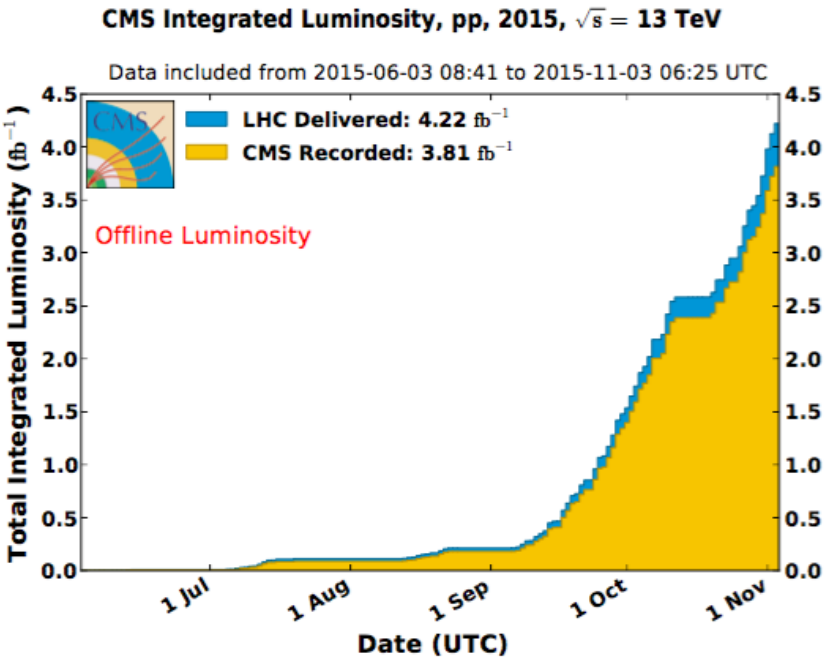

Figure 5.3: Cumulative luminosity versus day delivered by LHC (blue) in 2015; the offline luminosity recorded by the CMS experiment is also reported (orange) [63].

Low luminosity runs

Runs are selected by requiring that the relevant components of the CMS detector were fully functional, in particular, the CASTOR forward calorimeter, HF, and pixel tracker. The three runs (247324, 247920, and 247934) were obtained with a field strength of 0 T in June 2015. Run 247324 is 7 very low-intensity bunches, has an interaction probability of about 5%, and other one has bunch with a higher intensity [64].

Table 5.1: Overview of the runs magnetic field of 0 T and the CASTOR forward calorimeter is installed, as used in this analysis.

	Run	Approx. pileup	Initial Lumi section selection	Integrated Luminosity μ b^{-1}	L1×HLT pre-scale	Effective luminosity μ b^{-1}	Luminosity source
	247324	5%	97 – 311	186	240	0.38	bcm1fv1
	247920	30%	1 – 771	26740	1644	130	hfocv1
	247934	30%	26 – 607	18051	1644	91.35	hfocv1

The runs 247920 and 247934 were taken towards the end of the low luminosity operations. Both loose an interaction probability of about 30% and around 40 colliding bunches. These runs are summarized in table 5.1. Furthermore for those runs have to be removed from some bad towers, because they have a technical problem on the energy scale of the HF at η minus. In figure 5.4 illustrate the pixel hits in $\phi - \eta$ phases, on the b plane shows after removing problematic towers.

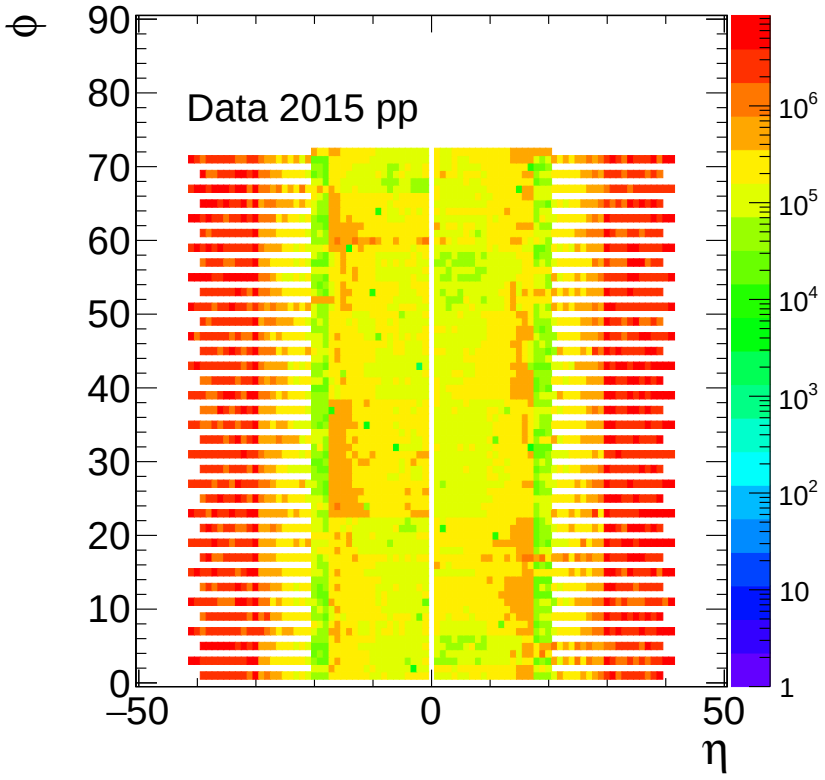

(a)

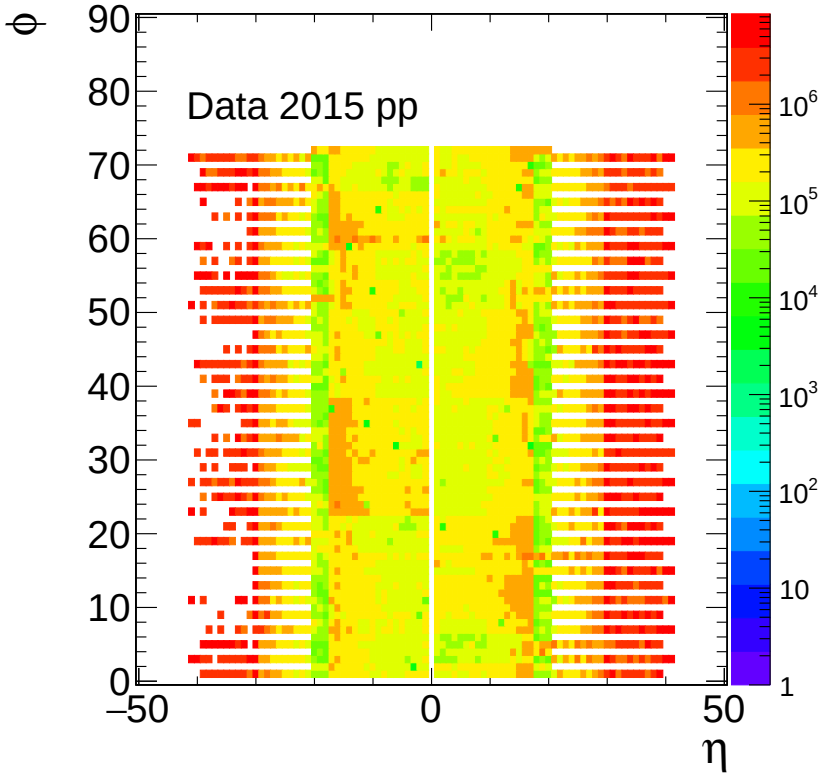

(b)

Figure 5.4: The pixel hits on $\phi - \eta$ phases (a). Noisy towers are removed (b).

5.2 Event selection

At trigger level, diffractive interactions are recorded with an unbiassed trigger. Pre-selected events are required to be accepted by the BPTX-based zerobias event trigger. Such datasets contain events that are selected without possible selection bias, to ensure that the sample of hadronic collisions is as inclusive as possible. The term unbiassed is an experimental term, and mostly corresponds to a set of basic detector selection cuts that make sure one really selects hadronic collisions. These selection cuts can be e.g. interaction vertex requirements, hit coincidence triggers, bunch crossing triggers, minimal detector activity, etc. In this analysis, we further impose a stricter off-line requirement to identify actual collision events. A suppression of non-collision events is achieved by requiring a reconstructed primary interaction vertex in the event with more than two tracks associated, or one single calorimeter tower above noise level within $-6.6 < \eta < -5.2$. The event is accepted if there is not more than one vertex or two vertices very close to each other. The latter is to accept the few percents of high-multiplicity events, where the vertex reconstruction by mistake finds two separate vertices. Figure 5.5 shows the vertex Δz distribution, where

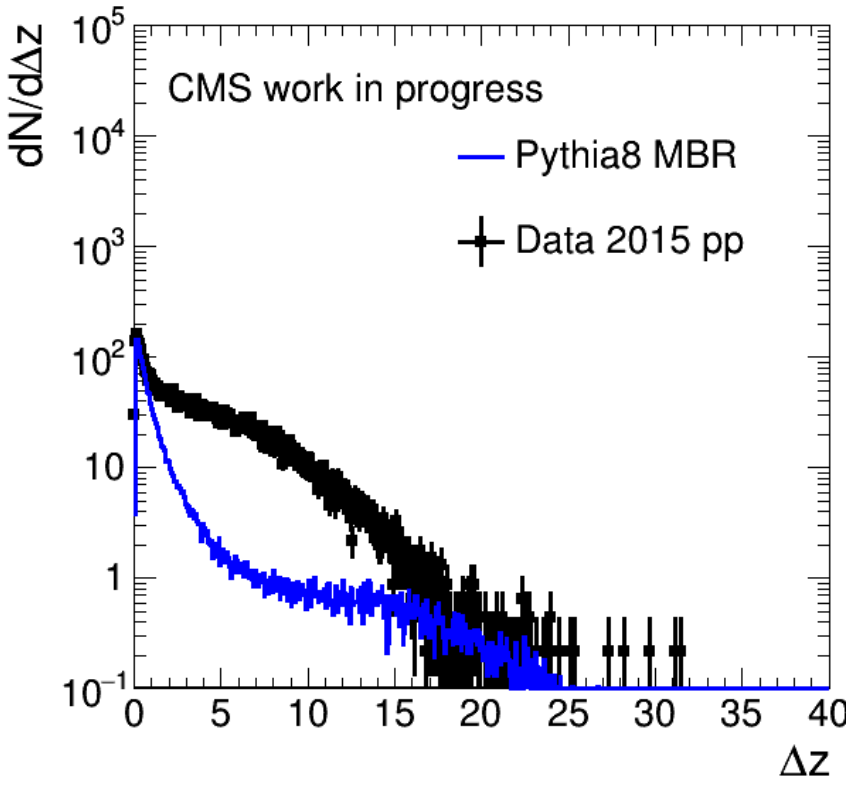

Figure 5.5: The vertex Δz distribution, where Δz is the longitudinal distance between two vertices in the same event.

Δz is the longitudinal distance between two vertices in the same event. By comparing to MC, very low pileup data it was decided to split vertices close than 0.5. Finally, tracks are required to be located within $|\eta| < 2.5$ and are reconstructed from the pixel detector. This selection is keeping the efficiency for event selection high.

The identification of rapidity gap signatures relies crucially on the suppression of calorimeter noise contributions. In order to compare gap distributions between MC and data, it is essential to have a good description of the calorimeter noise in MC. The η-dependent significance cut established in order to remove calorimeter noise also remove a small quantity of physics signal. This is taken into account in the analysis. The noise levels are individually in the following regions: barrel:$|\eta| < 1.4$, end-cap-forward transition: $1.4 < |\eta| < 2.8$, HF minus: $-5.2 < \eta < -3.2$, HF plus: $3.2 < \eta < 5.2$, and CASTOR: $-6.6 < \eta < -5.2$. Rapidity gaps in the calorimeter, in that analysis both the forward calorimeter parts and the center detectors, are used to find the gap. For example, the use of the CASTOR calorimeter system for measurement of rapidity gaps with, its large toward coverage $-6.6 < \eta < -5.2$ that allows us to detect the hadronic system of the mass M_Y when it escapes the central detector. Thus, the activity (or lack of it) in CASTOR enables to distinguish an SD event from a DD event very efficiently. Therefore, one of the crucial steps of the work is to precisely study the calorimeter noise levels in all calorimeter towers of CMS. This is done using dedicated random trigger events taken at the same period where the cross section measurement is performed. From the random triggers, only these events are studied that are outside of the LHC bunch filling scheme and for this reason not contain any collisions signals. These events are used to characterize the calorimeter noise levels on tower level. In figure 5.7 these data are compared to pure noise MC simulation. The tower noise thresholds are chosen where the probability to have more energetic towers per event drops 0.1%. The read-out electronics of the CASTOR calorimeter yield a mean noise per channel of 1 ADC count, which corresponds to a change of 2.6 fC. Using the absolute calibration factor of 0.02 GeV/fC, this would then lead to a mean noise signal per channel of about 60 MeV, when the signal is integrated over two-time slices (50 ns), to reconstruct the signal. However, after applying the channel inter-calibration constants, which equalize the channel gains the variance of inter-calibration adds to the noise level. Furthermore, in zero-bias data, typically a tower signal threshold of at least several n times mean the mean noise level is used. The final threshold that will be applied uniformly to data at all center-of-mass energies is the one corresponding to the 4σ-cut with a value of 1.5 GeV.

And the HF calorimeter is also needed to be taken account to define the rapidity gaps. Activity in HF is identified by the presence of a reconstructed calorimeter tower considering all the towers except for two rings of HF closest to the endcap region [65]. Those rings are shadowed by the endcap calorimetry and can thus not be modeled with sufficient precision for the analyses. In the soft inclusive inelastic events a calorimeter tower energy threshold of 5 GeV is used.

Track and vertex selections are also used to reduce background and noise events. A track selection is applied to select only tracks which are considered good, tracking data is very

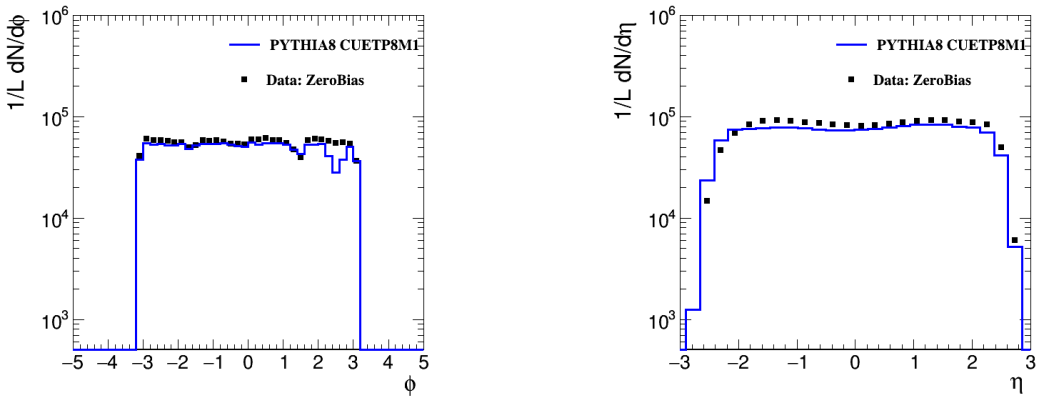

(a) ϕ (b) η

(c) Number of vertex (d) Number of tracks

Figure 5.6: The performance of the pixel tracking of the data is compared to simulation. (a) ϕ-plot. (b)η-plot. (c) Number of vertcies. (d) Number of tracks.

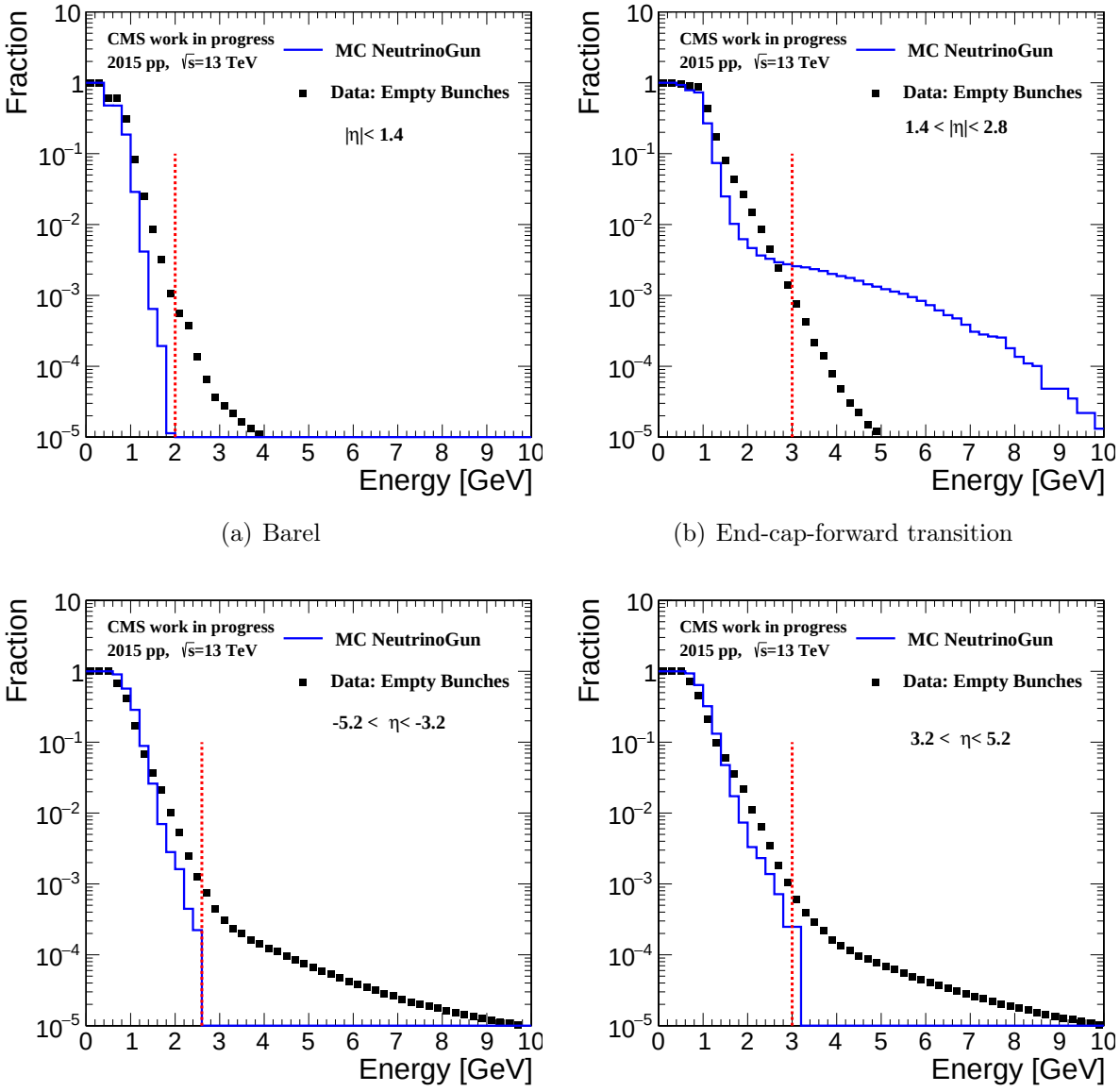

(a) Barel

(b) End-cap-forward transition

(c) HF minus

(d) HF plus

Figure 5.7: Detector-level distributions of the energy from all intervals: (a) Barel: $|\eta| < 1.4$, (b)end-cap-forward transition: $1.4 < |\eta| < 2.8$, (c) HF minus: $-5.2 < \eta < -3.2$, and (d) HF plus: $3.2 < \eta < 5.2$ for noise study. The empty bunch trigger is used for data and simulations are produced by neutrino gun, normalized to the number of events. The red line denotes the noise threshold.

important since it increases the acceptance of the analysis. The reconstruction of collision vertices only handles to remove rare events with multiple simultaneous collisions in the event (pileup).

All data are processed using CMSSW release 7_5_4 with global tag "75XdataRun2v2" and updated HCAL conditions (HcalRespCorrs v5.0 off-line). This also includes a reprocessing of data using updated pedestals, calibration conditions and a bad channel list for the CASTOR detector [66]. Events are selected on detector level if there is either at last single track that is compatible with originating from LHC beam, or one single calorimeter tower. To be as inclusive as possible the presence of a reconstructed vertex is not required. However, to exclude pileup, events with two or more vertices that were further separated from 0.5 cm in ΔZ are rejected.

5.3 Rapidity gap definition

In this section is defined by how the rapidity gaps are devoted. Experimental rapidity gaps are defined by using all information of sub-detectors of the CMS detector (Fig. 5.8). It has previously been mentioned that the presence of a rapidity gap is the experimental signature of diffractive events. A precise experimental determination of rapidity gaps is required either to separate single diffractive, double diffraction, and non-diffractive events and to measure cross sections. Rapidity gaps are created in non-diffractive processes due to fluctuation in hadronization process, although they are exponentially suppressed with a size of the gap, in contrary to diffractive events. In addition, it is called rapidity gap but in fact, pseudorapidity gap instead of rapidity gap is measured events at the detector level. As was already mentioned, this does not introduce large difference and is corrected for with simulations. Pseudorapidity is experimentally well measurable observable. At the stable-particle level, the true rapidity is used. In the following text, the rapidity gap means a pseudorapidity region without particle activity The PYTHIA 8 MBR and EPOS-LHC simulation are used, which describe the data well, to extrapolate the measured cross section into the low-mass region.

Two kinds of variables which are related to the rapidity gaps are η_{max} and η_{min}. They are defined based on the reconstructed track and calorimeter tower, pseudorapidities, or particles on generator level, which are sorted in the entire η space of CMS detector coverages. Generator level a particle is required to be $p_T > 900\,MeV$. In each event, particles are first ordered in η. An example of an event with rapidity gap is shown in figure 5.8. The smallest and largest values of the all pseudorapidities particles in each event are defined as η_{min} and η_{max}. And the two rapidities closest to, η^0_{max} and η^0_{min}, and are used to define the central gap $\Delta\eta^0 = \eta^0_{max} - \eta^0_{min}$. The largest rapidity gap in the event is denoted $\Delta\eta$. The distance of η_{min} and η_{max} from the border of the detector acceptance are the forward gaps. The largest forward gap the event is $\Delta\eta^f = max(\Delta\eta^f_+, \Delta\eta^f_-)$. The rapidity gap distributions show in (Fig. 5.9) for the (a) η_{max}, (b) η_{min}, and (c) $\Delta\eta^0 = \eta^0_{max} - \eta^0_{min}$ variables measured

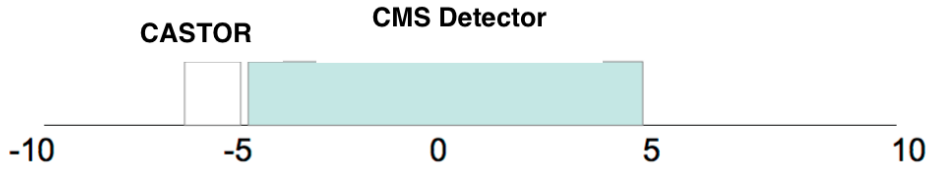

(a)

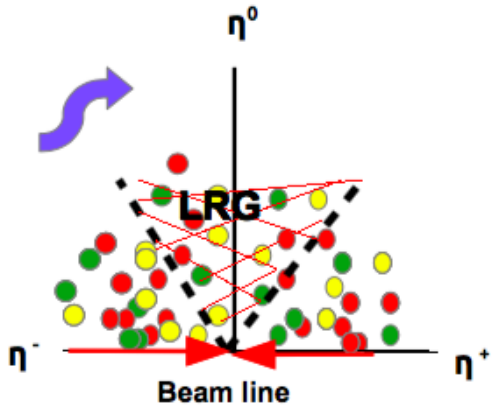

(b)

Figure 5.8: (a) Detector coverage for rapidity gap definitions. (b) On the right, colored dots indicate the final state particles, which are sorted in pseudorapidity to define η^0_{max} and η^0_{min}.

in the zero bias sample, compared to predictions of the PYTHIA 8 MBR [39] and EPOS [40] simulation normalized to the integrated luminosity of the data sample (run 247934). All MC plots presented here are on a detector level. After defining the rapidity gaps, the system X is separated from the forward proton up to the large rapidity gap. The system Y contains all particles where the large rapidity gap. If both interacting protons are broken they are called the double diffraction (DD). Two final state hadronic systems X and Y, both carrying quantum numbers of the original protons, are created and a rapidity gap separates them. The third class of diffractive events is the central diffraction (CD) composed of double pomeron exchange (DPE) and central exclusive production (CEP) where both protons remain intact and a system X with quantum numbers of vacuum is created in the central region, separated by a rapidity gap from each of the re-scattered protons [8]. However, CS is not explicitly used further in this analysis.

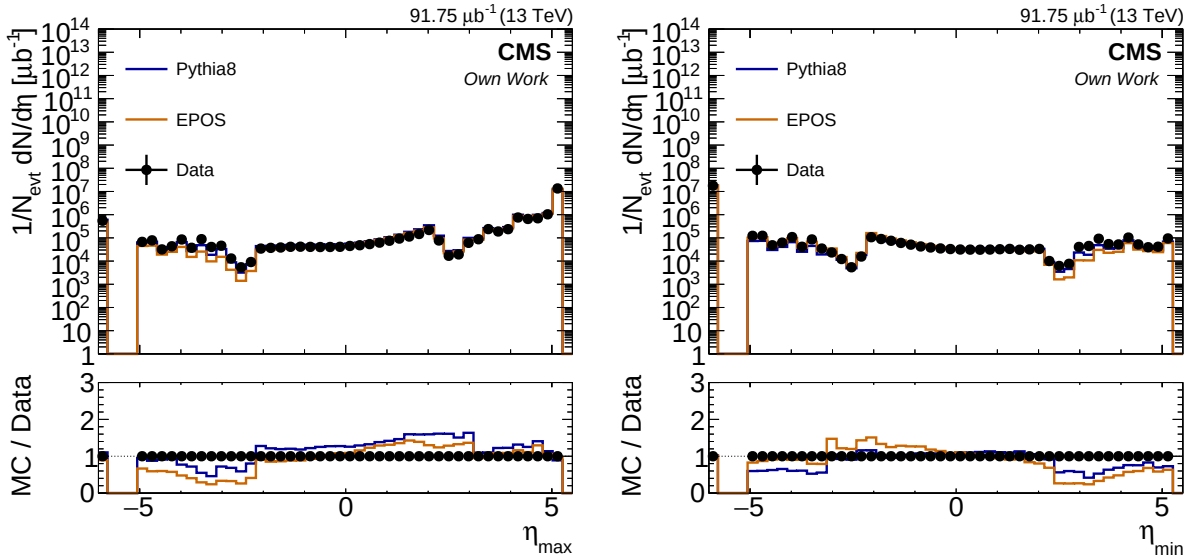

(a)

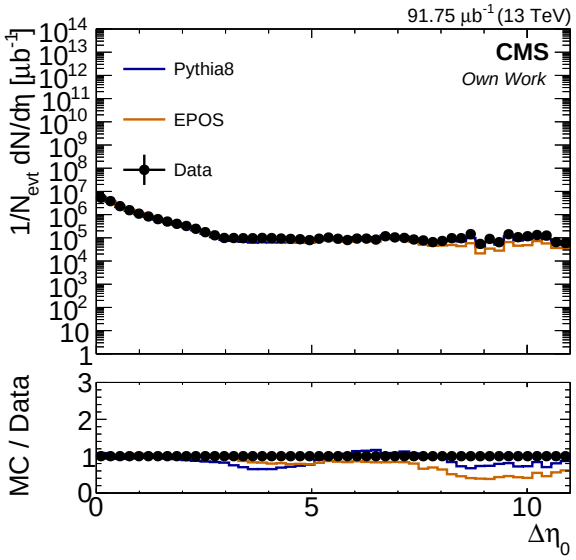

(b)

Figure 5.9: Generator-level distributions for the (a) η_{max}, η_{min}, and (b) $\Delta\eta^0$ variables measured in the zero bias sample, compared to predictions of the PYTHIA 8 MBR and EPOS simulation normalized to the integrated luminosity of the data sample (run 247934).

5.4 The kinematics of the diffractive process

Rapidity gaps are important for understanding of what type of diffraction interactions in each event represents. This requires very precise measurement of the rapidity gap, which is often not possible due to limited η acceptance. The rapidity gaps define the biggest gap between any two particles (event by event the particle list is ordered in pseudorapidity) is located from the rest of the final state and assuming that they are closely related to the kinematics of the diffractive processes. After defining the rapidity gaps, the rest of the final state can be separated by the widest pseudorapidity gap. The collection of stable final state particles(generated level) or tracks(detector level) is divided into two systems, X, and Y, using the mean rapidity of the two particles separated by the largest rapidity gap in the event. All particles to the positive side of the largest gap are assigned to the system X, while the particles at the negative side are assigned to the system Y. After separation of the final systems into X and Y, a calculation of the mass of a diffractive system can perform. Invariant mass M_X or M_Y of the dissociation system is one of the common variables describing diffraction, the largest invariant mass of the system of particles which can be obtained from the momentum of the final state proton when the energies of the initial state protons are known. For calculation, the invariant mass, M_X, M_Y in this study, for each system is calculated using the four-momenta of the individual particles or calorimeter towers and their ratio to the total center-of-mass energy.

$$\xi_x^{\mp} = \frac{\sum_i (E^i \mp p_z^i)}{\sqrt{s}}. \tag{5.1}$$

where E_i is the energy of particle i and p_z^i is the longitudinal momentum of the ith particle. The sign $\mp$ indicate whether the dissociated system is on $\mp z$ side of the detector [65]. In my calculation, I accept only particles with $-6.6 < \eta < 5.2$, I include only the particles are within the acceptance of the CASTOR detector. There is also another way to obtain the invariant mass of the system in the diffractive event. Using the center-of-mass energy $\sqrt{s}$ of the collision and the fractional momentum loss of the incident proton ξ_X, it is defined as

$$\xi_X = \frac{M_X^2}{s}, \tag{5.2}$$

and for ξ_Y

$$\xi_Y = \frac{M_Y^2}{s}. \tag{5.3}$$

The number of charged particles is rather a global quantity but it is very widely used in particle physics and often compared with theory calculations, which is why it is listed in our set of examined variables. The diffractive mass distribution is calculated for the simulated sample of diffractive events. At detector level, the rapidity gap is defined by using the track information from the pixel detector. The final state is then separated into

system X and Y, which populate the regions on the positive and negative side of the largest rapidity gap, and the corresponding masses M_X and M_Y (see in figure 5.10) are calculated from the energy of every calorimeter towers. Furthermore, on detector level M_X essentially

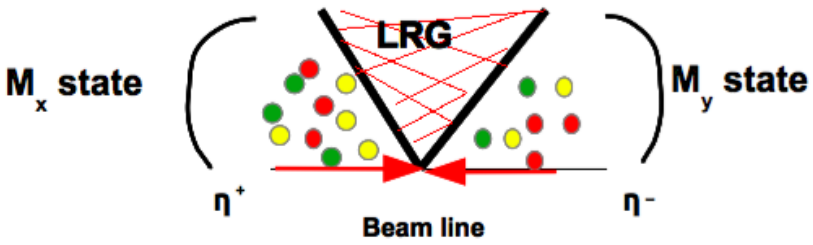

Figure 5.10: The diffractive masses M_X and M_Y. Colored dots indicate the final state particles, which are sorted in pseudorapidity to define η_{max} and η_{min}.

corresponds to the final system that can be detected in the central detector, insensitive to low-mass diffraction. The CASTOR calorimeter allows the detection of the hadronic system Y when it escapes the central detector.

Figure 5.11 shows the two-dimensional distributions of generated level ξ_X, ξ_Y values for the events in the ND events, DD, SD1 and SD2, where SD1 is single diffraction with proton dissociation on the positive η hemisphere and SD2 the geometrically inverse process. Samples obtained with the PYTHIA 8 MBR simulation. For the ND events ξ_x and ξ_y are not so clearly defined and in the plot it is shown that ND covers a very wide phase-space with a significant enhancement of small values. The DD sample has the characteristic almost uniform coverage of the entire phase-space down to very low values of ξ. The two SD samples are inverted with respect to each other. The point out that there is always one proton surviving on one side, and the other proton dissociates.

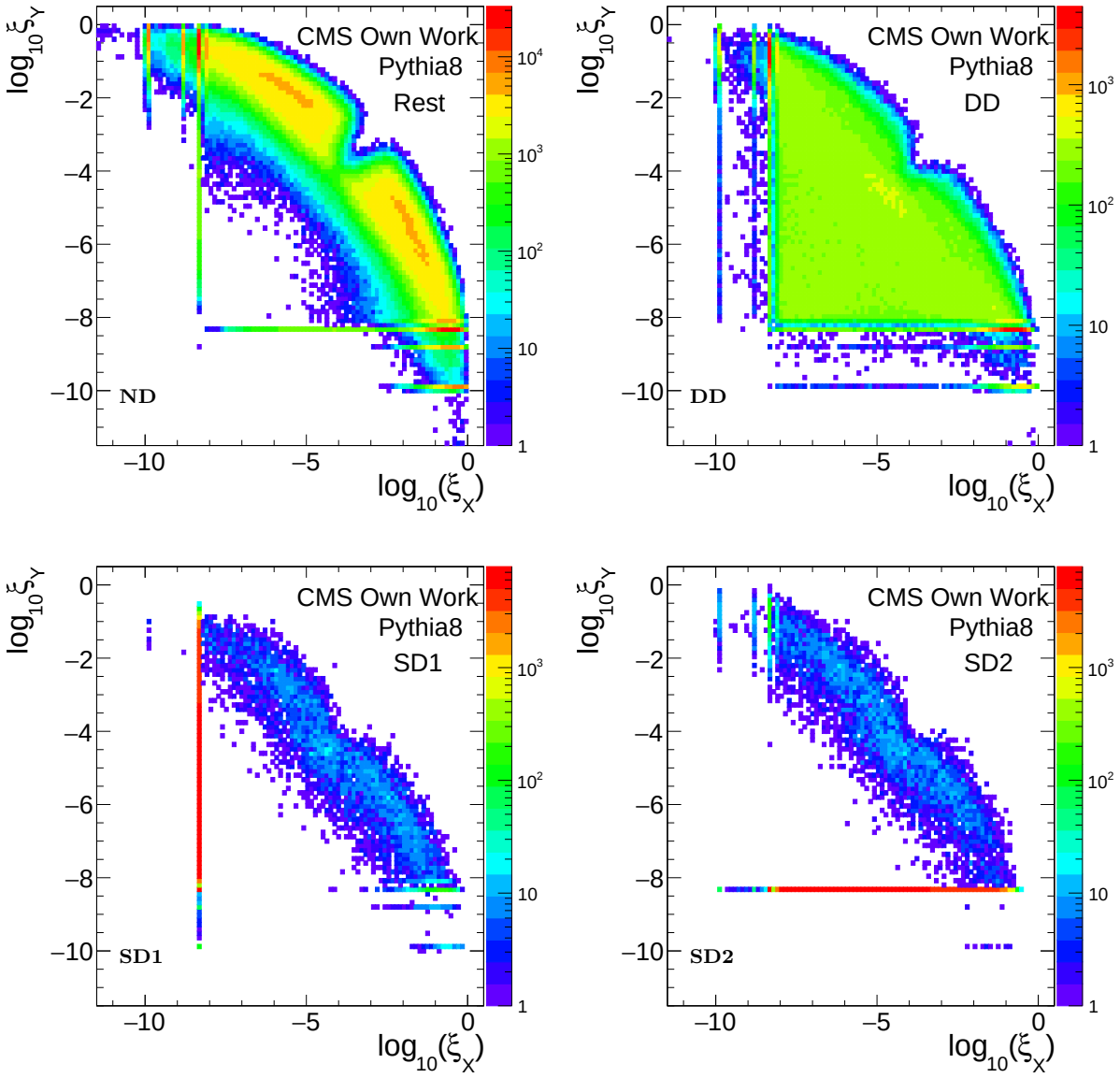

Figure 5.11: Two-dimensional distribution of generated level ξ_X, ξ_Y values for the events in the ND events, DD, SD1 and SD2. Samples obtained with the PYTHIA 8 MBR simulation.

5.5 Diffractive processes identification

The multivariate classification is used to determine diffractive process rates. In training phase of the multivariate analysis, a certain signal type sample is trained to obtain the clear definition of signal and background characteristics. Diffractive events classification is done on event generated level for using as training sample in the multivariate analysis. The diffractive classification cuts have to be chosen as model-independent since EPOS and PYTHIA 8 MBR event generators are used in the training phase. Characteristics features of diffractive signals are obtained from EPOS and PYTHIA 8 MBR predictions. From figure 5.11 shows that in particular, DD events have a clear signature in the central region, and DD always has a large overlap with ND, but ND events are more common than DD events. Single diffraction (SD) is the most frequent of them and also the easiest one to detect, always one of the protons remain intact and is only rescattered in the forward direction (i.e. with large η) and the other proton dissociates into a hadronic system X carrying the quantum numbers of the original proton. From figure 5.11 is also shown that entirely clear that a full ambiguous separation of the event classes is not possible. Furthermore, even a perfect ξ reconstruction has a negligible impact on the separation of DD from ND events, as shown in figure 5.11. That was the case to use multivariate analysis for optimal discrimination of diffractive processes. We decided to use ξ for diffractive processes identification. The PYTHIA 8 MBR simulation process predictions are shown in Fig. 5.12, which shows ξ distribution for proton momentum fraction loss ξ_X at the positive direction of the detector (in the diffractive system X). Moreover, the ξ also not reconstructed well from the mass of dissociated systems due to the limited CMS detector coverage. In Figure 5.13 the acceptance to low mass diffraction on the negative and positive η side is shown. The limited acceptance of CMS is already considered here. It can be seen that the one side presence of CASTOR reduces the threshold by about are orders of magnitude. Here it is visible that above $\xi > 0.1$ the non-diffractive dominate the distribution. In similar way figure 5.14 illustrates that non-diffractive events dominate the data a rapidity gap size of $\Delta\eta < 4$.

It is clearly obvious that in the low $\Delta\eta$ values non-diffractive processes form the main contribution to the section and single diffractive and double diffractive contributions are rather negligible. However, with increasing $\Delta\eta$ the rest contribution falls exponentially and for large $\Delta\eta$ it is insignificant when compared to SD and DD. This behavior is in agreement with observations made where EPOS was used. The double diffractive contribution to the inelastic cross-section seems to be very similar to the one in the EPOS. However, the single diffractive contribution is much smaller which is caused by the choice of pomeron flux. Combining all these results, we conclude that very good definition for visible diffractive final states is given by:

- For DD event selection cut: $\Delta\eta > 4$ and $\log_{10}\xi_Y > -6$ or $\log_{10}\xi_X > -7$.
- For SD1 event selection cut: $\log_{10}\xi_Y > -6$ and $\log_{10}\xi_Y < -1$, in combination with intact proton on minus side.

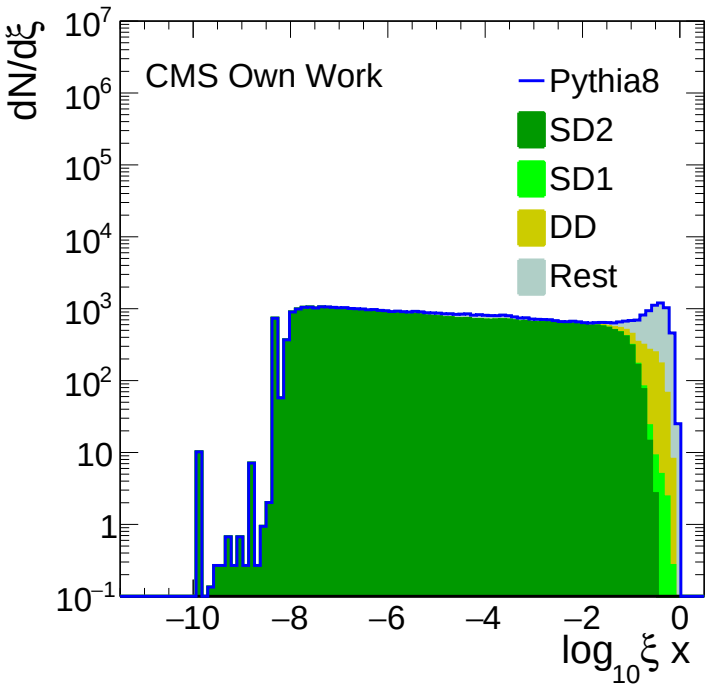

Figure 5.12: The distribution of generated level ξ in logarithmic scale for the events in the DD events, SD1, SD2 and rest events. Samples obtained with the PYTHIA 8 MBR simulation.

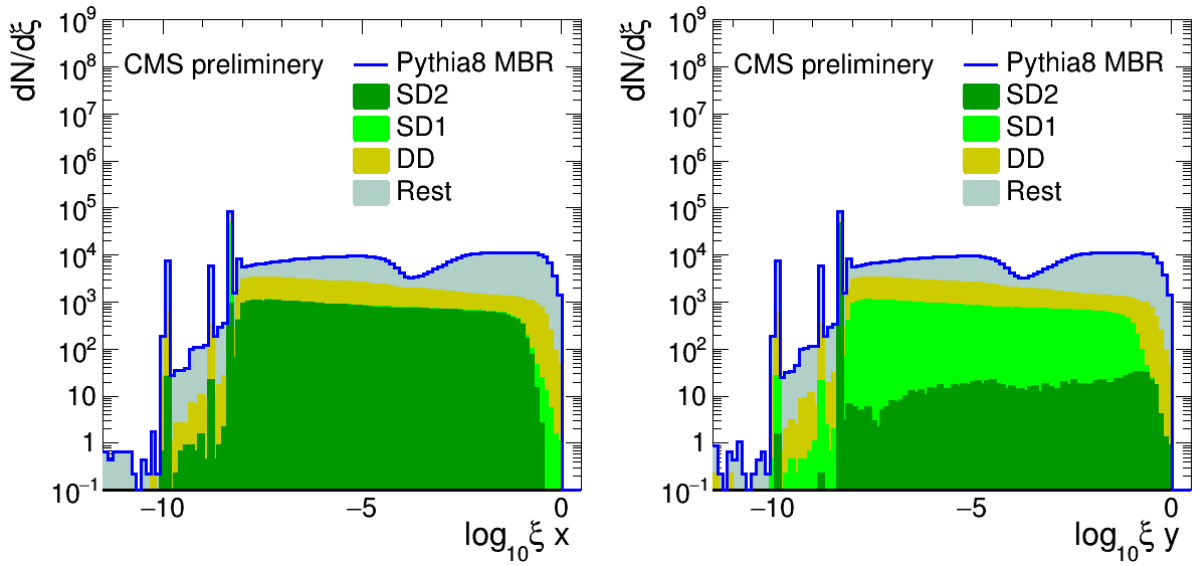

Figure 5.13: The acceptance to low mass diffraction on the negative and positive η side.

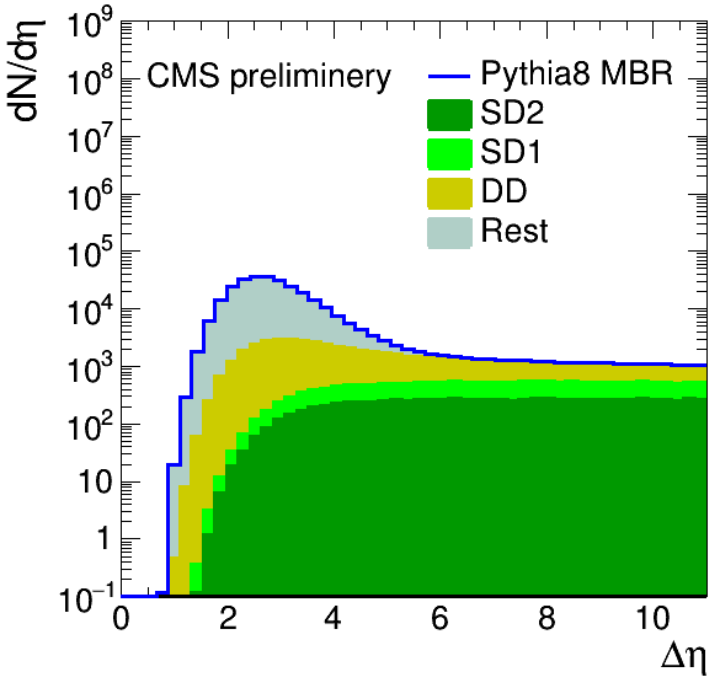

Figure 5.14: The distribution of generated level $\Delta\eta$ values for the events in the DD events, SD1, SD2 and the rest events. Samples obtained with the PYTHIA 8 MBR simulation.

- For SD2 event selection cut: is $\log_{10}\xi_X > -7$ and $\log_{10}\xi_X < -1$, in combining with intact proton on plus side.

For ND is indicated by "the rest" which is the rest of the events after selecting SD and DD events.

In the rest at this work diffractive processes are separated by using the event selection based on the ξ as introduced here. It is the remaining task of this thesis to assign data to these classes. Double diffractive events have a clear rapidity gap in the central region. ND events are more common than diffractive events. Single diffraction (SD), one of the protons remain intact and is only rescattered in the forward direction (i.e. with large η) and the other proton dissociates into a hadronic system X carrying the quantum numbers of the original proton. Thus, single diffraction is characterized by large forward rapidity gaps, which correspond to the widest pseudorapidity gap adjacent to the edge of the detector.

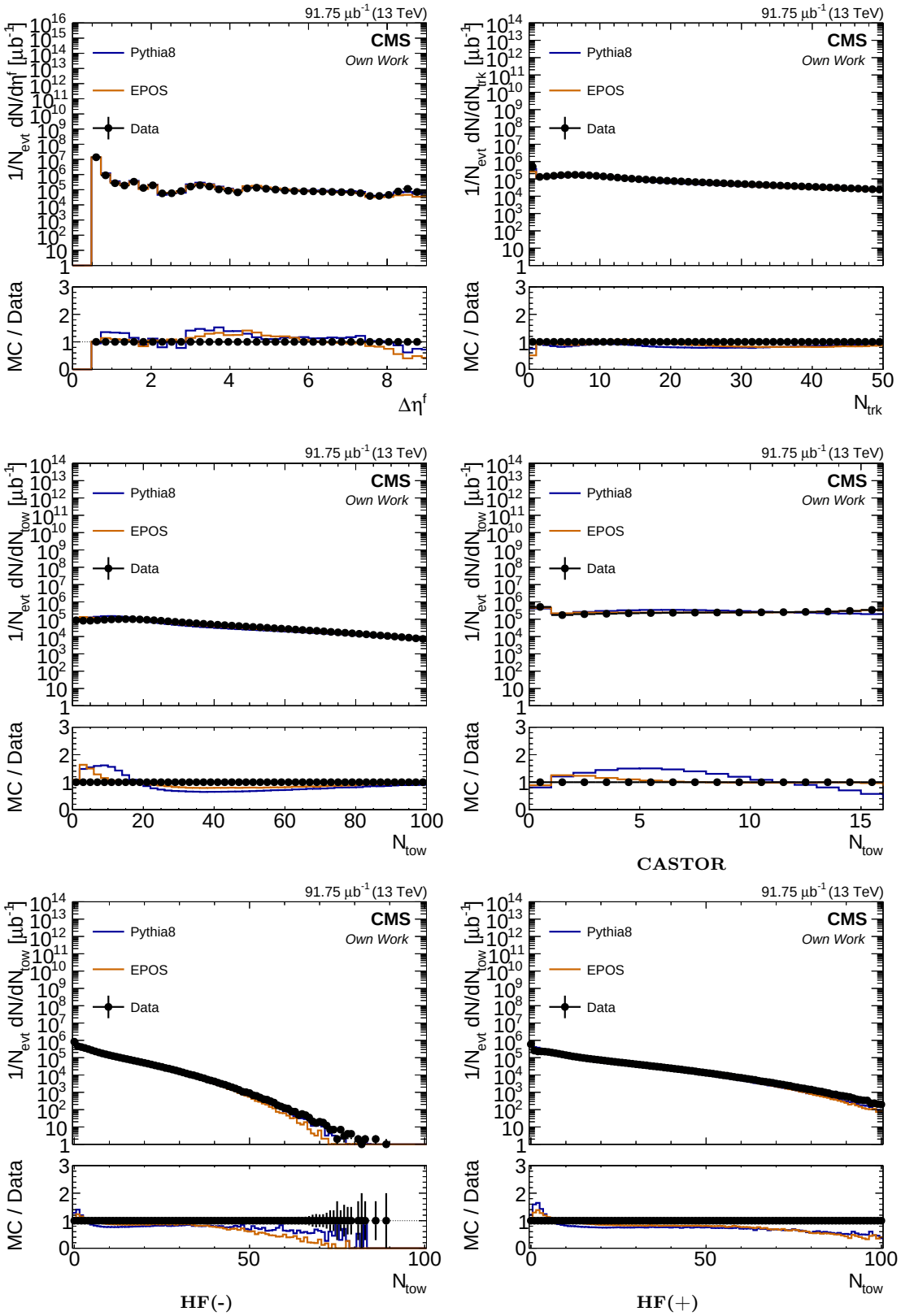

Figure 5.15: Detector-level distributions for the $\Delta\eta^f$, number of tracks, total number of towers in calorimeters, number of towers of CASTOR, number of towers of HF at plus side and HF at minus side variables, are shown. They are measured in the zero bias sample. Diffractive processes are separated by using the event selection is based on the ξ, compared to predictions of the PYTHIA 8 MBR and EPOS simulation normalized to the integrated luminosity of the data sample (run 247934).

5.6 Multivariate analysis

TMVA provides a multitude of evaluation outputs which help to decide on the best classifier to choose for a particular classification problem. Boosted decision trees (BDTs) method is used and the training phase is done exclusively with the total background and particular signal class. This is repeated for all signal classes out of DD, SD1, and SD2 individually.

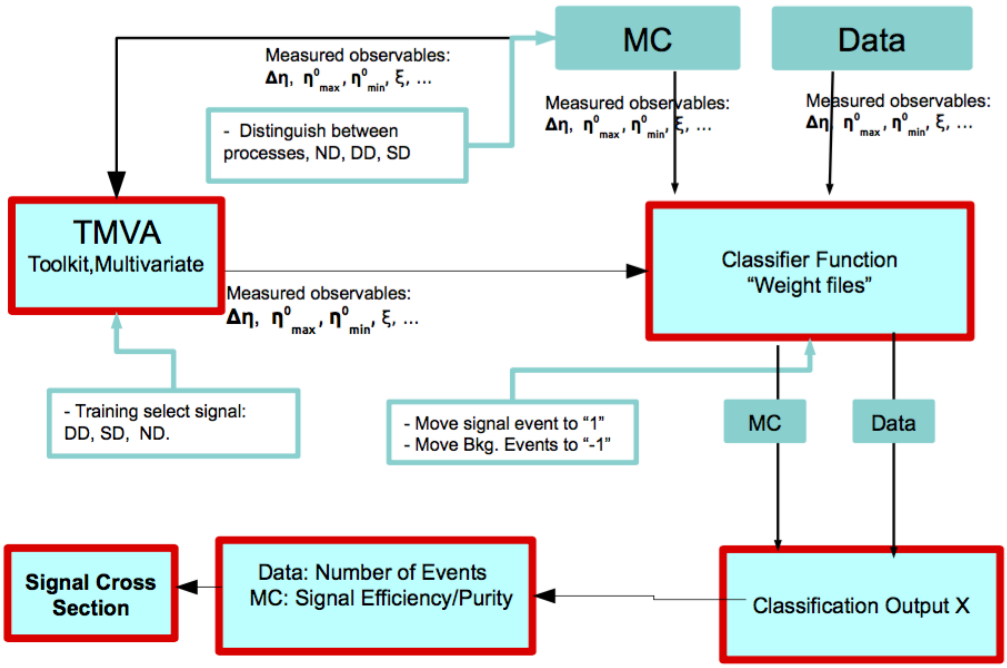

Figure 5.16: Work flow of analysis.

The training starts with the root node. For the training signal and background events are just taken from in section 5.5, the influence of the event selection on the training is studied in this section. An example in Fig. 5.17, the signal type is chosen as SD and rest of all events is defined as "background". Event selection based on a simple cut is able to select only one region of phase space, the decision tree is able to split the phase space into a large number of region phase space, each of which is identified as either "signal-like" or "background-like". Leaf node represents an individual cut sequence. At each node, the split is determined by finding the variable and corresponding cut value that provides the best separation between signal and background. The splitting criterion is always a cut on a single variable, the training procedure selects the variable and cut value that optimizes. The split results in two subsets of training events that each goes through the same algorithm of determining the next splitting iteration. This procedure is repeated until the whole tree is built. And boosting improves the performance and stabilizes response with respect to fluctuations in the training sample compared to using a single tree, and

extends the concept from one tree to several trees, which together form a forest.

Performance learning algorithm to classify events as signal or background is only based on the available variables. It is significantly important to choose a well-motivated variable set since the performance of the methods depends on the used variables. Discriminating variables are also needed to further reduce the background. For Training phase these variables are used:

- The smallest and largest values of η value in the final states, η_{max} and η_{min}.
- The size of the rapidity gap around $\eta = 0$, $\Delta\eta^0 = \eta^0_{max} - \eta^0_{min}$.
- The over all largest rapidity gap between and object in the final states, $\Delta\eta$.
- The total number of towers in all CMS calorimeters above noise level.
- The total number of towers in the forward hadronic calorimeter at plus η side.
- The total number of towers in the forward hadronic calorimeter at minus η side.
- The sum of energy in the forward hadronic calorimeter at plus η side.
- The sum of energy in the forward hadronic calorimeter at minus η side.
- The total number of towers in the CASTOR calorimeter.
- The sum of energy in electromagnetic and hadronic parts of the CASTOR calorimeter.
- The hottest towers in the CASTOR calorimeter.
- The number of tracks which are reconstructed from the pixel detector.

The classifier is using all input variables to indicate the best cuts to separate events into signal and background. Some of these variables obviously have a corrected response, but there still is an additional information in all of them. All input sets of the classification variables were compared to see the performance using the different simulations such as EPOS and Pythia 8 MBR has similar correlations and reasonable agreement with data (in figure 5.17). The event selection has an influence on the shape of the variable distribution. The selection of the BDT response is optimized to yield maximal significance for the training. The absolute comparison of cross section distributions of all input variables is shown in figures 5.18 and 5.21. That is also compared EPOS and Pythia 8 MBR simulations. The sensibility to the event class is illustrated by the color coding that is based on Pythia 8 MBR event classes as introduced before.

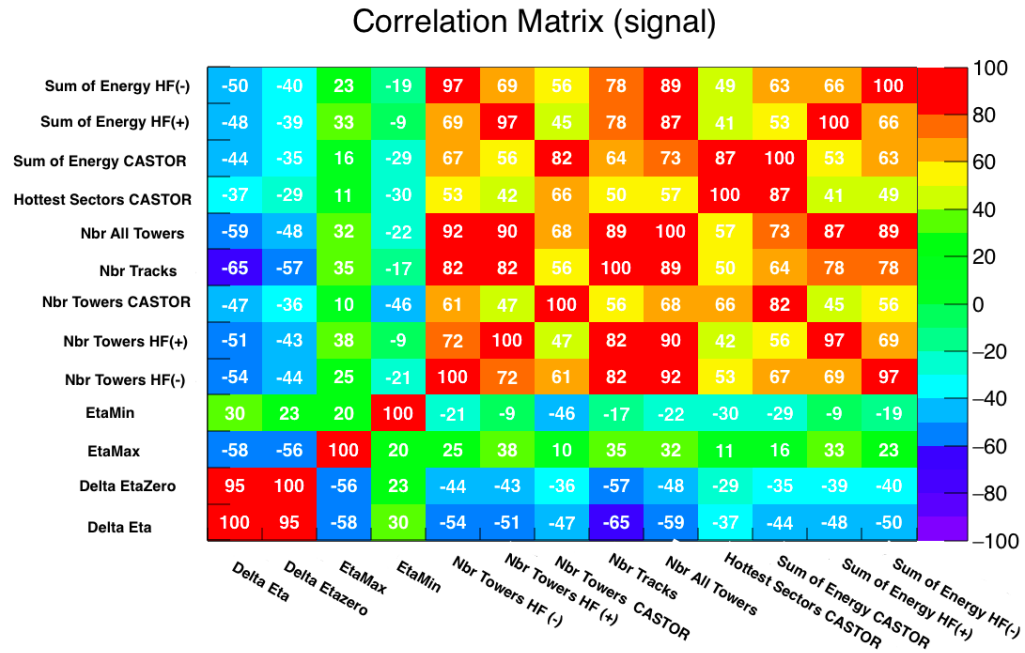

(a) Signal

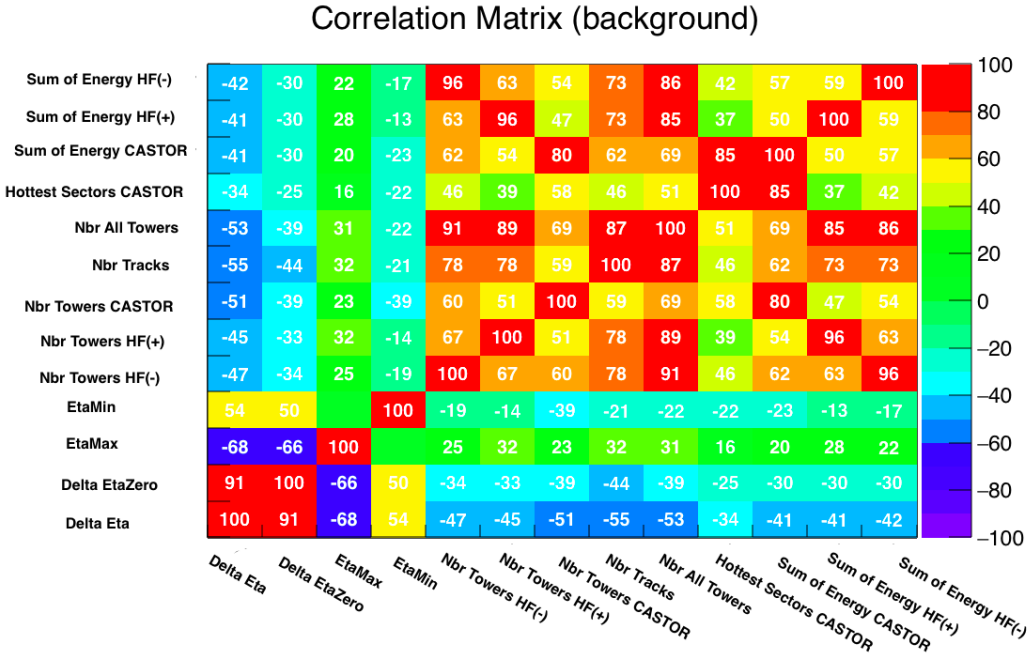

(b) Background

Figure 5.17: Correlation between input variables in PYTHIA 8 MBR samples in the training. For diffractive events classification: (a) the signal type is chosen as "DD" in the training phase for this example, and (b) "background" is the rest of all events such as SD1, SD2 and rest.

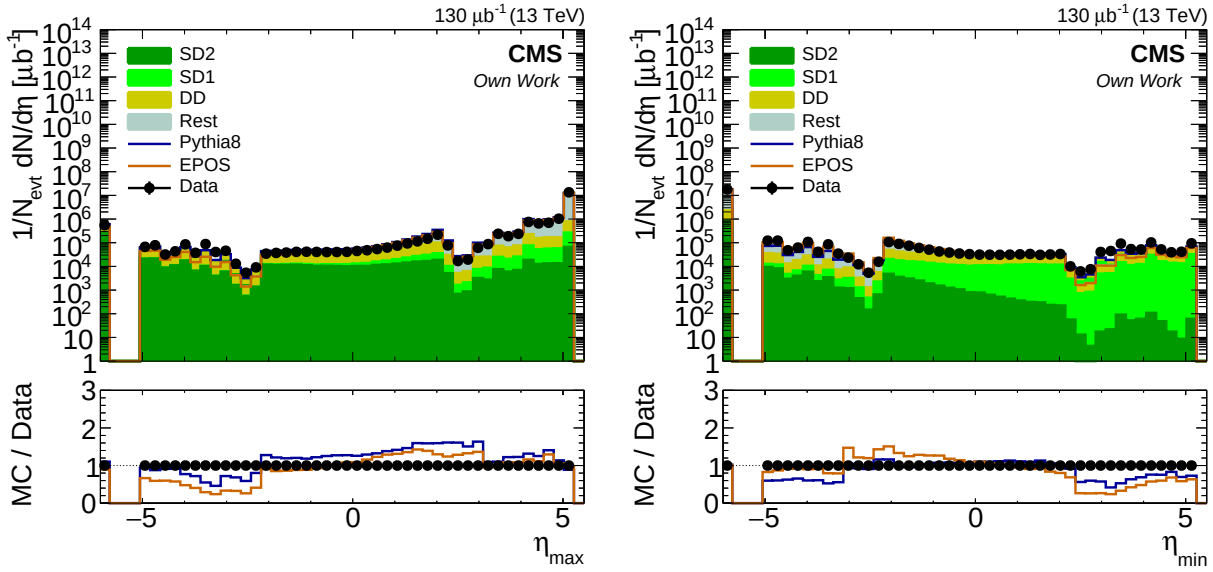

(a)

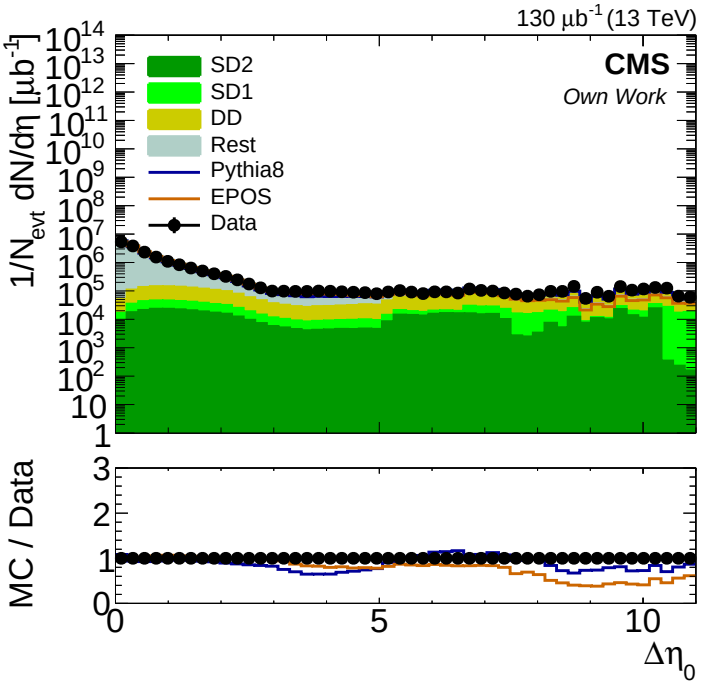

(b)

Figure 5.18: Detector-level distributions: (a) η_{max} and η_{min}, and (c) $\Delta\eta^0$ variables measured in the zero bias sample, compared to predictions of the PYTHIA 8 MBR and EPOS simulation normalized to the integrated luminosity of the data sample (run 247934).

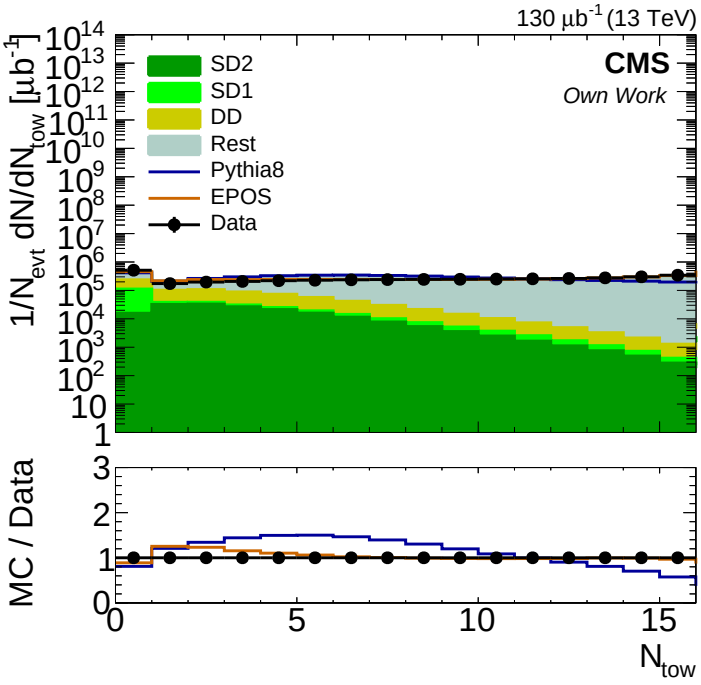

(a) The number of CASTOR towers.

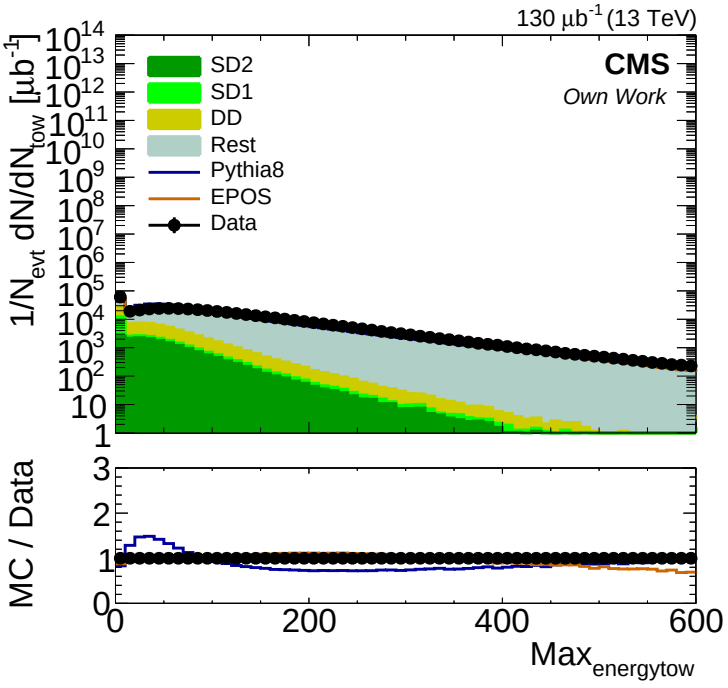

(b) The hottest CASTOR towers.

Figure 5.19: Detector-level distributions for the number of CASTOR towers and the hottest CASTOR towers, variables measured in the zero bias sample, compared to predictions of the PYTHIA 8 MBR and EPOS simulation normalized to the integrated luminosity of the data sample (run 247934).

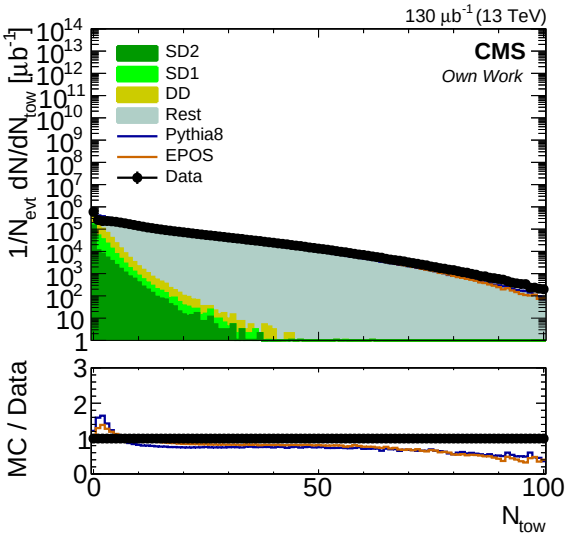

(a) The number towers of HF(+).

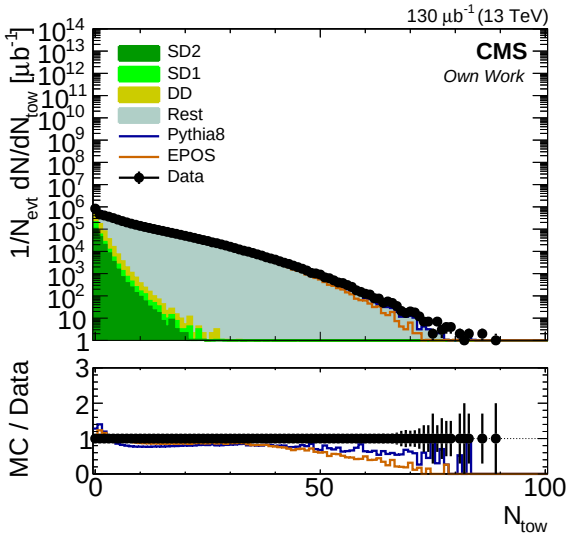

(b) The number towers of HF(-).

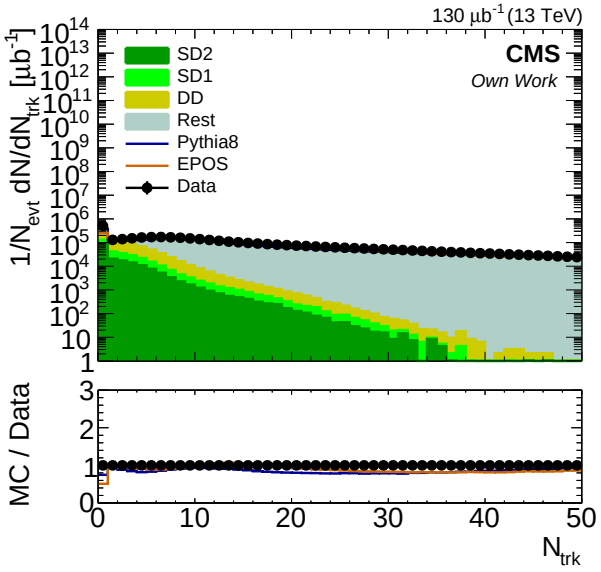

(c) The number tracks.

Figure 5.20: Detector-level distributions for the number towers of HF and HF minus, and the number of tracks variables measured in the zero bias sample, compared to predictions of the PYTHIA 8 MBR and EPOS simulation normalized to the integrated luminosity of the data sample (run 247934).

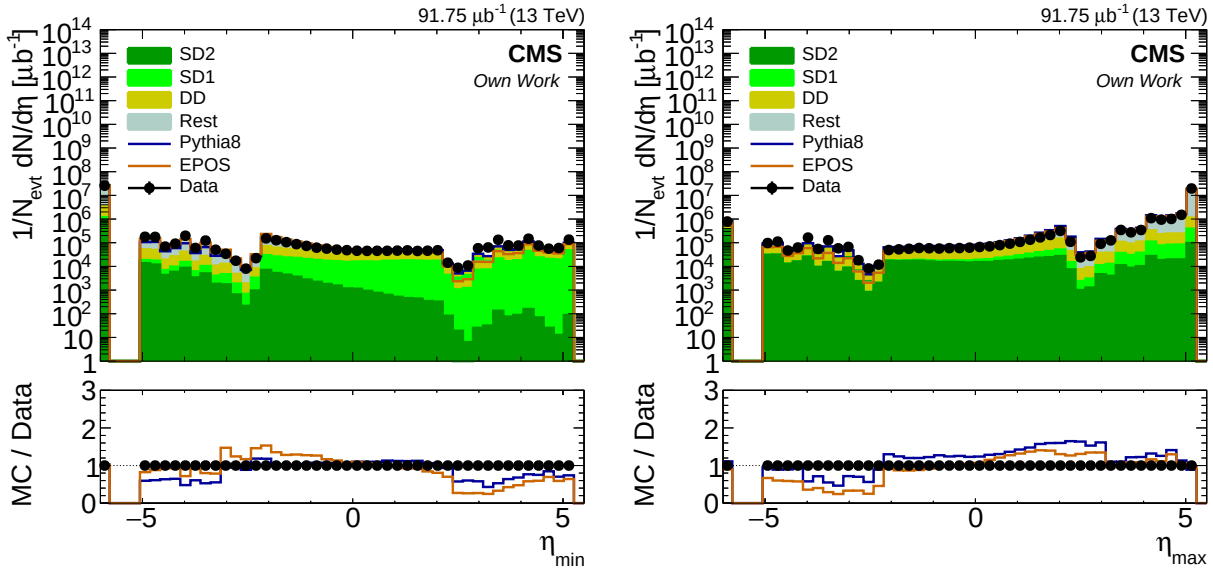

(a)

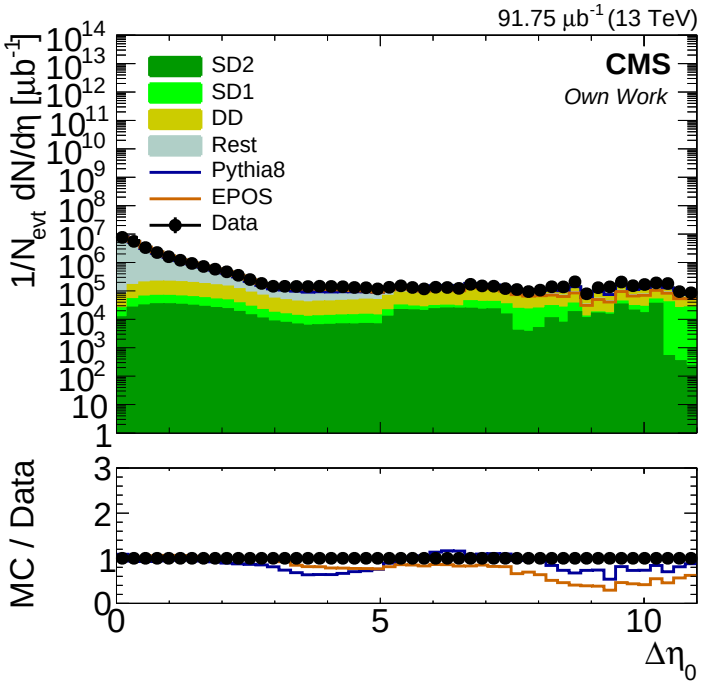

(b)

Figure 5.21: Detector-level distributions for the (a) η_{max}, and η_{min} and (c) $\Delta\eta^0$ variables, measured in the zero bias sample, compared to predictions of the PYTHIA 8 MBR and EPOS simulation normalized to the integrated luminosity of the data sample (run 247920).

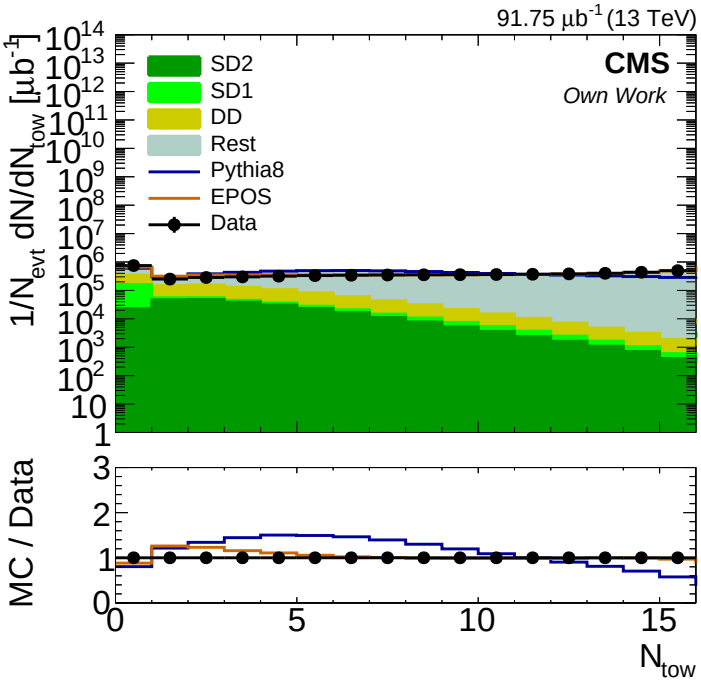

(a) The number of CASTOR towers.

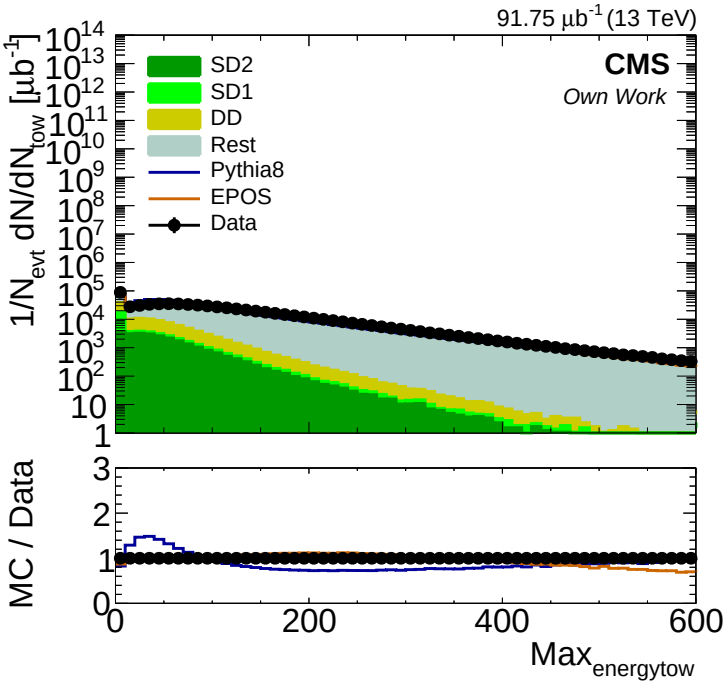

(b) The hottest CASTOR towers.

Figure 5.22: Detector-level distributions for the number of CASTOR towers and the hottest CASTOR towers variables measured in the zero bias sample, compared to predictions of the PYTHIA 8 MBR and EPOS simulation normalized to the integrated luminosity of the data sample (run 247920).

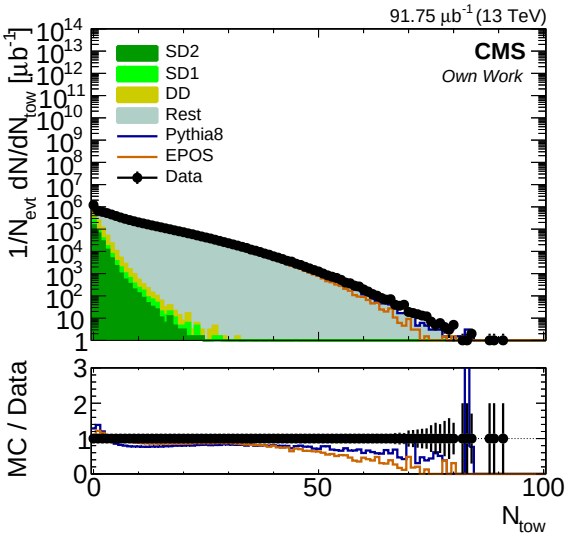

(a) The number towers of HF(-).

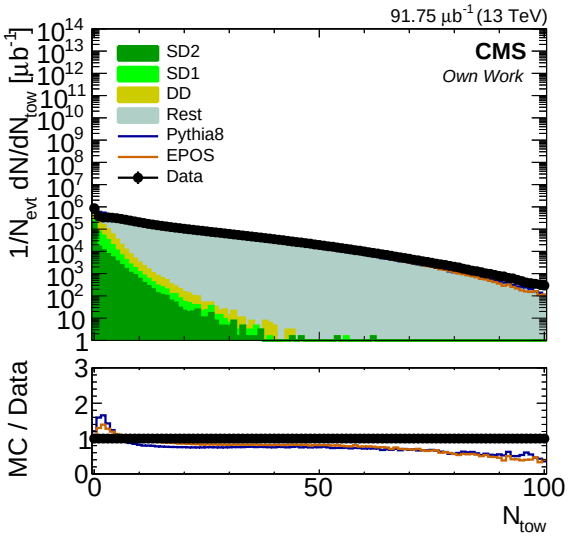

(b) The number towers of HF(+).

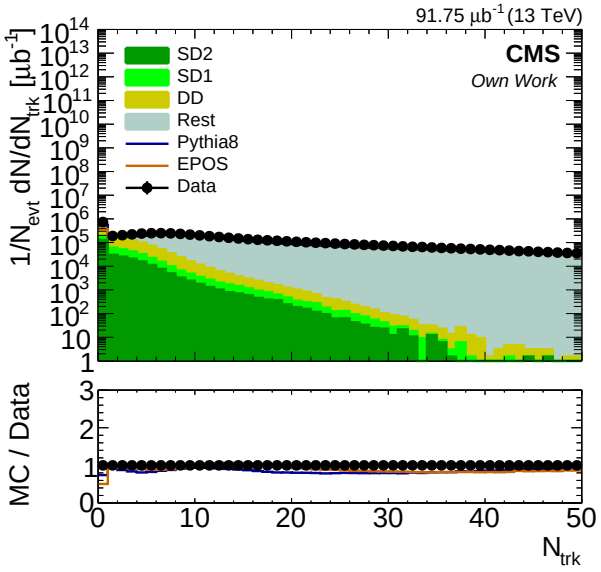

(c) The number of tracks

Figure 5.23: Detector-level distributions for the number towers of HF plus and HF minus, and the number of tracks variables measured in the zero bias sample, compared to predictions of the PYTHIA 8 MBR and EPOS simulation normalized to the integrated luminosity of the data sample (run 247920).

5.7 Classifier response

The classification in TMVA derive from the input variables (observables), are illustrated in figure 5.24 and 5.25. Figures show the classifier outputs for events are trained with the PYTHIA 8 MBR and EPOS simulation. "BDT" method is used for training for two runs (247934 and 247920). Signal type is DD, SD1, and SD2 tested and trained. One can see both simulations give a different response because the performance of the BDT with a cut optimization depends on the MC model.

In addition, overlap matrices are derived for signal and background that determine the fractions of signal and background events that are equally classified by each pair of classifiers. This is useful when two classifiers have similar performance, but a significant fraction of non-overlapping events. Overtraining occurs when a classifier models signal/background differences that are specific to the particular training sample used. Overtraining have to be checked out, because a decision tree can be overtrained since it can be very sensitive to statistical fluctuations in the training sample. For example, a single sample is training with deep decision tree with no minimum number of events per node. For the events in its training sample, it would give perfect signal/background separation, however, we could not expect that it would also give perfect separation for a separate testing sample. This classifier would be overtrained. There are two common types of overtraining which training sample overtraining, and data/Monte Carlo overtraining. Training sample overtraining can be detected by comparing distributions of the training and testing samples for both signal and background. The Kolmogorov Smirnov (KS) test [67] is a very efficient way to determine if two samples are different from each other. The statistical probability that two samples are plotted from the same distribution, is shown in Fig 5.26, the Kolmogorov Smirnov test provides a p p value equal to the statistical probability that two samples are plotted from the same distribution. Classification should be as similar between the training sample results and testing sample results as statistical fluctuations permit. However the training and testing samples will never be identical, a very small degree of overtraining may be unavoidable. It is recommended to try to reduce overtraining if KS ≤ 0.01, especially if the separation is visibly poorer for the testing samples than for the training samples. In some applications, real data may be used as background for training Applications training on MC for signal but data for background are subject to data/Monte Carlo overtraining. This case is not for this work. Signal and background efficiencies are computed for a set of cuts on the classifier output. All events with a classifier output larger than the cut value are classified as a signal, all events below the cut are classified as background. From the number of events which are classified right or wrongly as signal or background, the efficiencies are calculated.

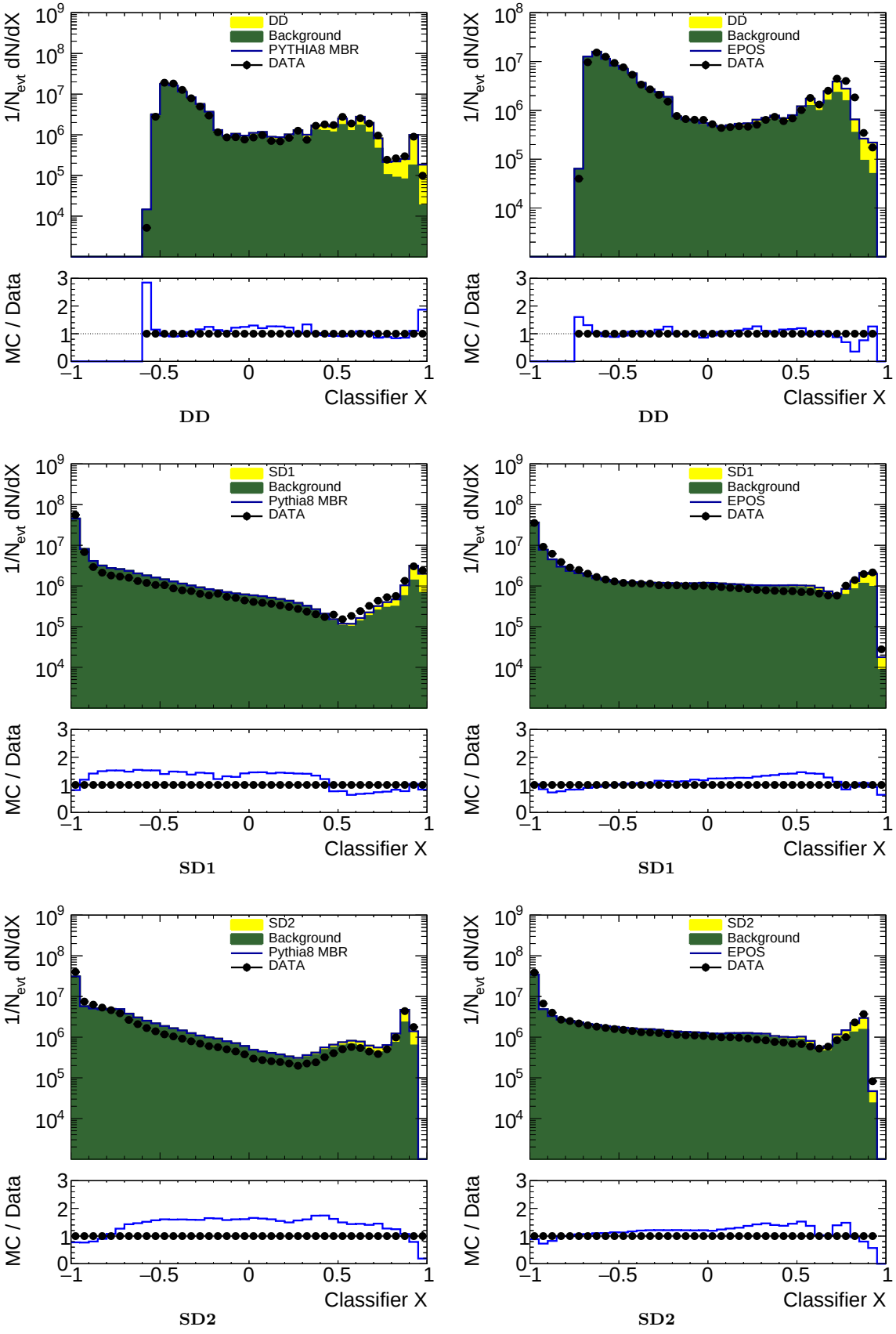

Figure 5.24: Classifier outputs for events are trained with the PYTHIA 8 MBR, and EPOS simulation into signal DD, SD1, and SD2. They are normalized to the number of events. BDT method is used (run 247934)

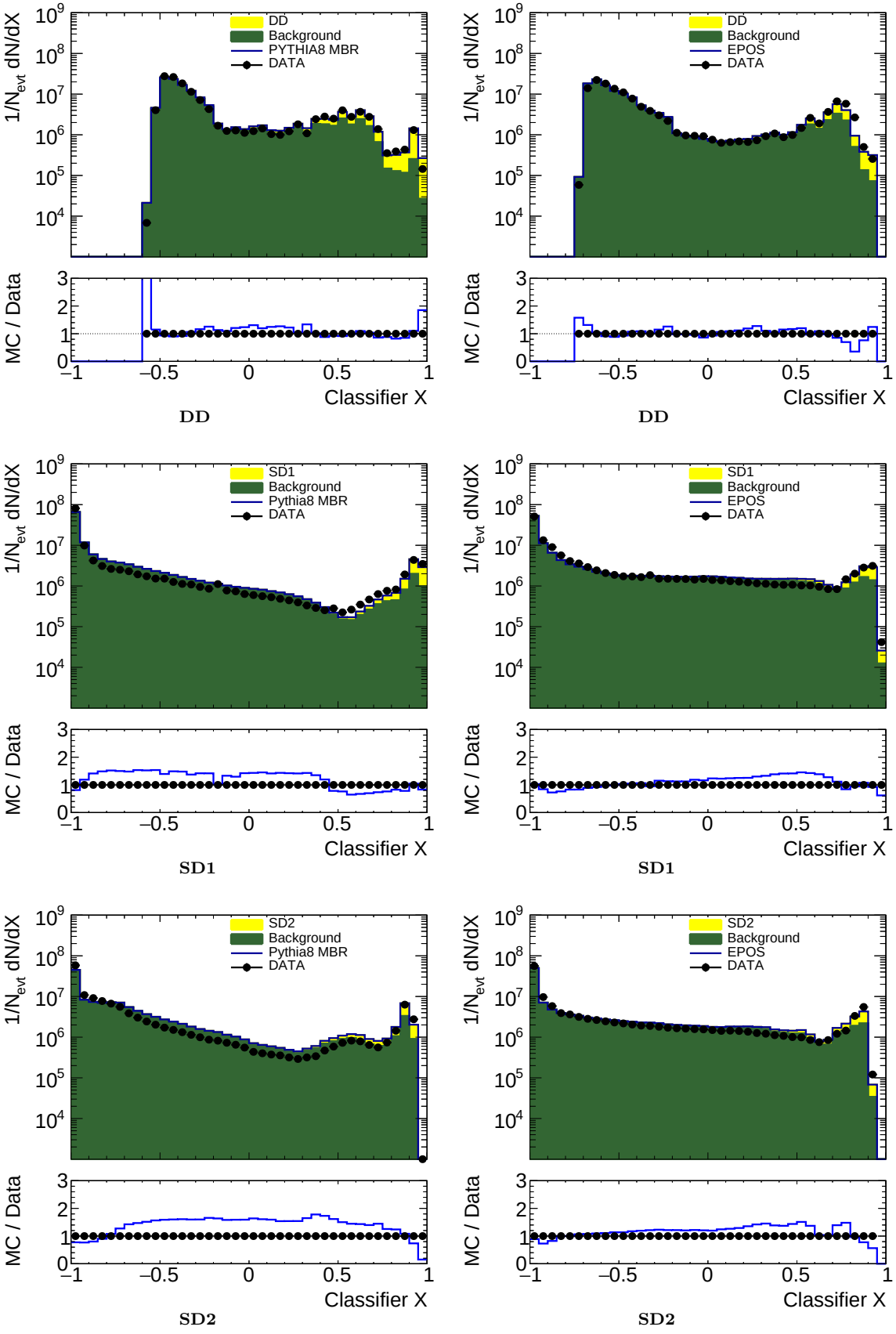

Figure 5.25: Classifier outputs for events are trained with the PYTHIA 8 MBR, and EPOS simulation into signal DD, SD1, and SD2 (respectively). They are normalized to the number of events. BDT method is used (run 247920).

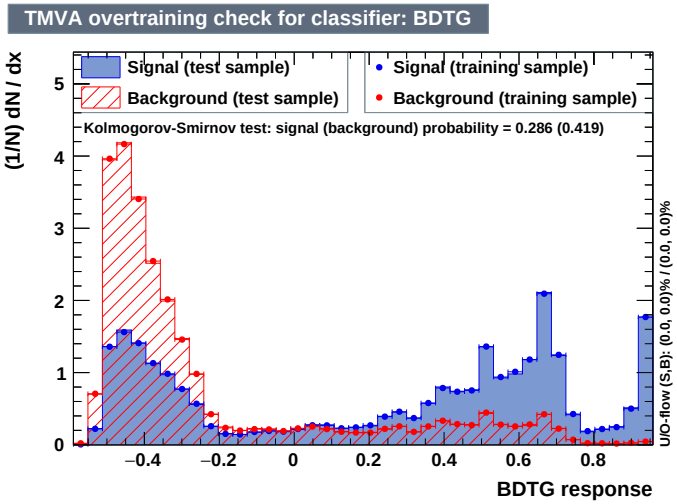

(a) signal is DD

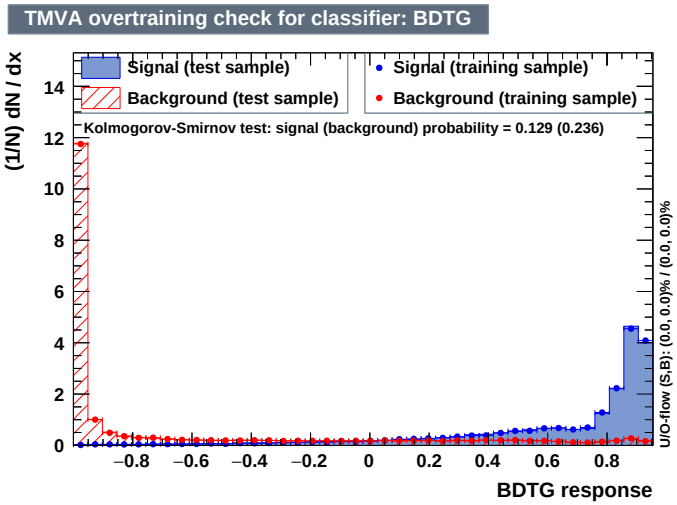

(b) signal is SD1

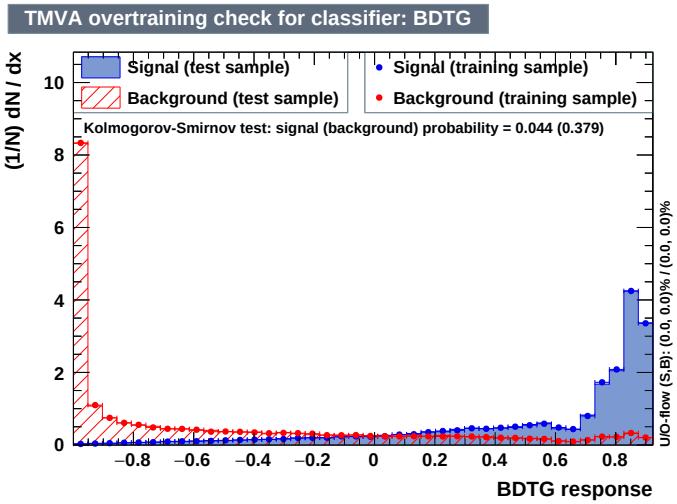

(c) signal is SD2

Figure 5.26: The statistical probability that two samples are drawn from the same distribution. The Kolmogorov Smirnov test provides a p p value equal to the statistical probability that two samples.

5.8 Integrated cross section DD and SD

The rate of SD to DD events is used to determine the efficiency and purity of the event selection. An advantage of the method is a possibility of separation of SD and DD events. Due to small pseudorapidity coverage of the detector, a large fraction of DD events mimics the SD event topology and their corresponding templates differ only slightly. Moreover, wider rapidity coverage of the calorimeter should make the measurement less model dependent. This is motivated by the fact that SD events should create gaps starting from the edge of the detector while a large fraction of DD produces gaps in the central region. The DD template contains a large fraction of events having gap starting from the $\eta = -5.2$. Specifically the CASTOR detector ($-6.6 < \eta < -5.2$) is crucial to separate SD to DD events, allows us to detect the hadronic system of the mass M_Y when it escapes the central detector. The obtained separation of these redefined templates strongly depends on the MC model, therefore, the result is interpreted as tuning of fractions in the MC generators. The fraction of DD events for which both diffractive masses M_X and M_Y are sufficiently large and tend to produce large rapidity gaps in the central region of the detector. For the comparison of the performance of the BDT with a cut optimization, the variable set has to be changed because the classification depends on fluctuations in the training samples and depends on the MC model. The performance of the BDT illustrates with the receiver operating characteristic(ROC) curve, which describes the relationship between the false positive fraction and true negative fraction associated with a diagnostic test as a function of the test threshold defining the boundary between background and signal. This entry describes how the ROC curve is derived from data and reviews summary indicates that may represent its performance. The "ROC" Curves are a good way to illustrate the performance of given classifier:

- Shows the background rejection over the signal efficiency of the remaining sample,
- Best classifier can be identified by the largest AUC (Area under curve).

As before mentioned, all events with a classifier output larger than the cut value are classified as a signal, all events below the cut are classified as background and a classifier output where signal-(background-) like events have values close to 1 (0). For a decision of the best cut from a selected signal is done by estimation of the signal (S) and background (B)efficiencies, which are obtained from cutting on the classifier outputs, versus the cut value. Green a classifier distribution and a cut value y_{cut}, the number of signal events at $y > y_{cut}$ are N_S and the number of background events there are N_B. That is the total number of signal events with no cut in y is $N_{All}(S)$. We define $\epsilon_{sig,eff} = N_S/N_{All}(S)$ and $\epsilon_{bkg,eff} = N_B/N_{All(B)}$. From the sets of signal efficiencies and background rejections $(1 - \epsilon_{bgk,eff})$ defined by the cuts on classifier output, the receiver operating characteristics (ROC) curve are plotted for SD1, SD2, and DD. Which point on the ROC curve the user should choose as a working point, depends on the type of analysis the user wants to perform. Several exemplary ROC curves with different classification performances are shown. The larger the area below the curve, the better the separation of signal and

background then is achieved. The signal and background class are done by defining all events with a classifier output $y > y_{cut}$ as signal and all other events as background. For each cut value y_{cut} the signal efficiency $\epsilon_{sig,eff}$, purity and background rejection $(1 - \epsilon_{bkg,eff})$ are calculated. Also shown are the signal purity and the signal efficiency times signal purity corresponding to the expected number of signal and background events before cutting (numbers given by the user). The optimal cuts according to the best significance are printed on standard output. Figure 5.27 a) compares the receiver operating characteristic (ROC curve) showing the background rejection for a given signal efficiency of the BDT. The efficiencies are obtained by cutting the classifier outputs. The best cut is chosen by good background rejection combined with high signal efficiency. Background rejection, or background efficiency, versus signal efficiency for the classifiers. For the given example the best cut or maximum significance separation of signal and background is then found at -0.1 classifier output values for DD signal events (background is selected SD1, SD2, and the rest events) for PYTHIA 8 MBR (in figure 5.28). The cut ensemble leading to maximum significance corresponds to a particular working point on the efficiency curve. Here this working point corresponds to -0.1 and the optimal efficiency and purity value are shown in figure 5.27 (a). On the bottom, it is shown how the performance of selection changes as a function of cut.

The figure 5.28 shows the cut optimization. The cut optimization for classifier threshold which is estimated with the total variable set and the classifier threshold which are estimated with the total variable set and the classifier thresholds depend on fluctuations in the training samples. The cut optimized reflects the sensitivity of the result on the choice of significance threshold.

The cross-section of a given DD events is derived with these parameters:

$$\epsilon_{Sig} = \frac{\mathrm{N}_S / F_{Split}}{\mathrm{N}_{All(S)}}, \tag{5.4}$$

where ϵ_{Sig} is the signal efficiency, and F_{Split} is split-vertex correction factor derived from MC samples which derives:

$$F_{Split} = 1 - \frac{(Event\,rejected\,by\,vertex\,cut)}{All\,events}. \tag{5.5}$$

The pile-up efficiency or vertex correction factor for data samples is derived:

$$\epsilon_{Pileup} = \frac{All\,selected\,events}{(Event\,rejected\,by\,vertex\,selection)}, \tag{5.6}$$

$$\mathrm{P}(S) = \frac{\mathrm{N}_S}{\mathrm{N}_S + \mathrm{N}_B}, \tag{5.7}$$

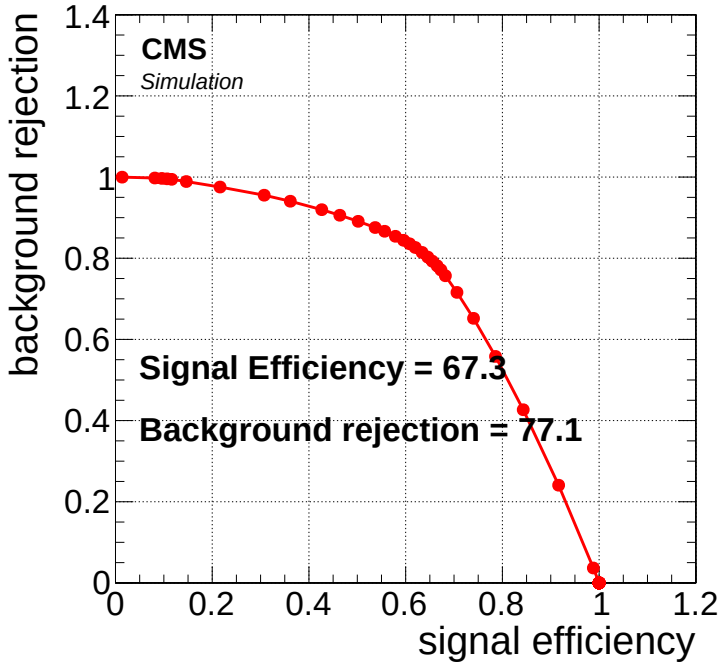

(a)

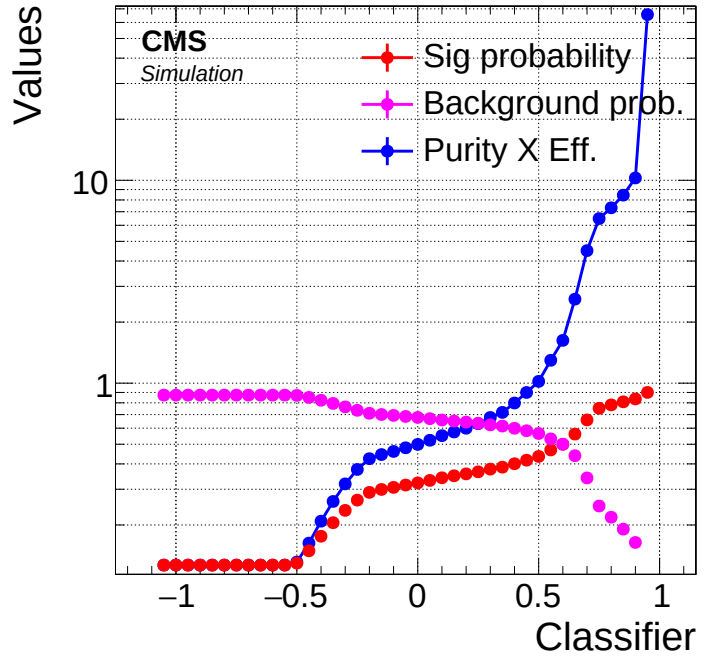

(b)

Figure 5.27: a) The background rejection versus signal efficiency ("ROC curve") obtained by cutting on the classifier outputs for the events with signal selected DD, and b) signal efficiency (run is 247934).

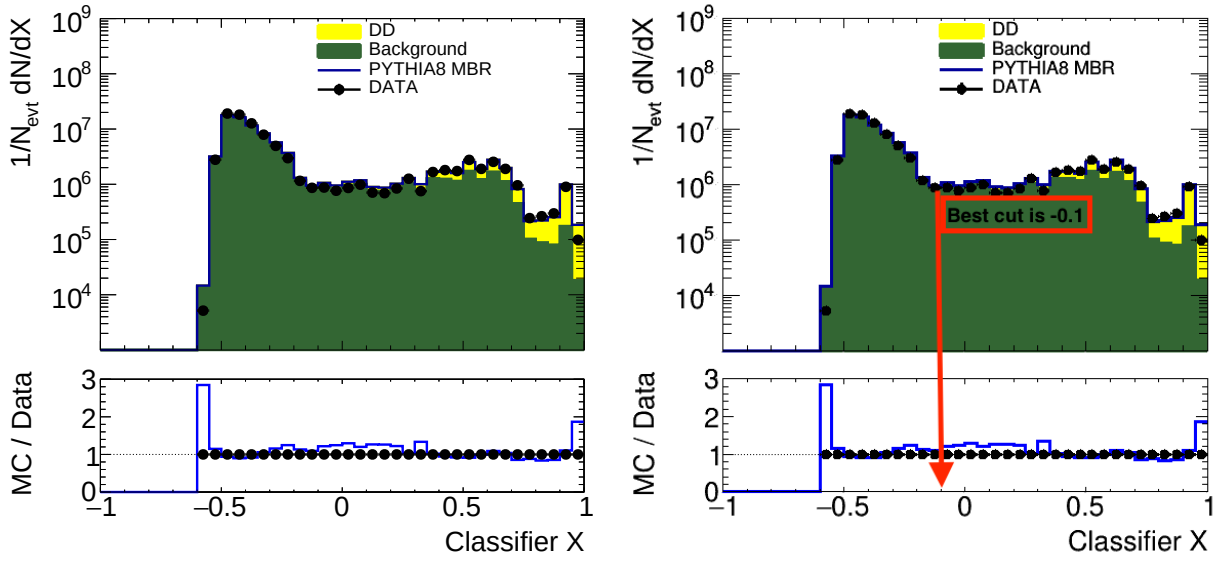

(a)

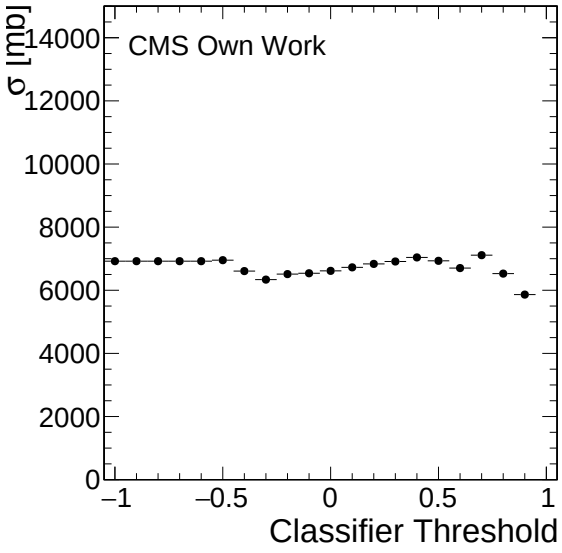

(b)

Figure 5.28: Classifier output (a) and cut optimization (b) distributions for events are trained with the PYTHIA 8 MBR signal type is "DD", on right side cut optimization(run 247934). BDT method is used.

and then the cross-section L of a given DD events is derived:

$$\sigma = N(y > y_{cut})\, events \times \mathrm{P}(S) \times \frac{1}{Lumi} \times \epsilon_{Pileup}, \tag{5.8}$$

where luminosity is the integrated luminosity which is 22.98 $\mu\mathrm{b}^{-1}$ from run 247934.

Table 5.2: Measured diffractive cross sections for SD and DD. It shows which MC model uses in TMVA training phase and which run uses in the TMVA application phase.

	TMVA trained MC model	Data	$\sigma_{SD}(\,mb)$	$\sigma_{DD}(\,mb)$
	PYTHIA 8 MBR	247920	5.6	6.7
	PYTHIA 8 MBR	247934	5.3	6.5
	EPOS	247920	5.1	5.9
	EPOS	247934	4.9	5.7
	Mean(Averaged Value)		5.2	6.2

The measurements rely on the used MC generators. The comparison of the performances show the BDT with a cut optimization, the variable set has to be changed because the classification depends on the MC model and on fluctuations in the training samples. The cut optimization reflects the sensitivity of the result on the choice of significance threshold. It is important to note that the cross section for DD is very insensitive against changes in y_{cut} for PYTHIA 8 MBR, while it is very insensitive for SD events when EPOS is used. In any case y_{cut} variation is a considered one source of systematic uncertainty. These efficiency and purity corrections are made using the MC generators and introduce some model dependence into the final result. All results are shown in table 5.7 which shows the diffractive cross sections for SD and DD and it shows which MC model uses in TMVA training phase and which run uses in the TMVA application phase. The PYTHIA 8 MBR tune(using a Pomeron trajectory with $\xi = 0.08$) and EPOS describe the data well, and is subsequently used to extract the diffractive cross sections. The purpose of these tests is the selection of the generator with the best description of the data that will be used for the data corrections. The cross sections obtained from the average of a cross-section of EPOS and PYTHIA 8 MBR. I compare the measured visible cross sections with result of other experiments. I generated one million events at $\sqrt{s} = 13\,\mathrm{TeV}$ for EPOS LHC [40], SIBYLL 2.3 [68], QGSJET-II 0.4 [69], PYTHIA 8 MBR. In addition, PYTHIA 8 MBR simulations with values of $\alpha\prime$ and ξ changed to $\alpha\prime = 0.125\ \mathrm{GeV}^{-2}$, $\xi = 0.007, 0.104$ (one parameter changed at a time) are also included to provide a scale for their effect on the cross sections.

The diffractive final states are used these definitions which defined as

- For DD event selection cut: $\Delta\eta > 3$.

- For SD, $\xi < 0.05$.

Table 5.3: Measured diffractive cross sections for SD, DD, $SD^{visible}$ and $DD^{visible}$ (unit is mb).

	MC Model	$\sigma_{SD}^{visible}$	$\sigma_{DD}^{visible}$	σ_{SD}	σ_{DD}
	EPOS LHC	8.2	5.2	12.3	9.2
	Sibyll 2.3	14.52	6.91	15.4	12.1
	QGSJET-II 0.3	10.9	1.2	14.6	2.5
	QGSJET-II 0.4	8.1	2.44	12.6	4.7
	Pythia 8 MBR ($\xi = 0.08$)	8.4	5.4	10.4	7.7
	Pythia 8 MBR ($\xi = 0.07$)	8.2	4.9	10	7.1
	Pythia 8 MBR ($\xi = 0.104$)	8.8	6.6	11.6	9.3
	Pythia 8 MBR ($\alpha\prime = 0.125$)	8.4	6.7	11.3	9.4

All results are shown in table 5.3 which MC model uses, and the diffractive and the visible diffractive cross sections for SD and DD. Furthermore, the visible diffractive final states are used the same definitions which defined above.

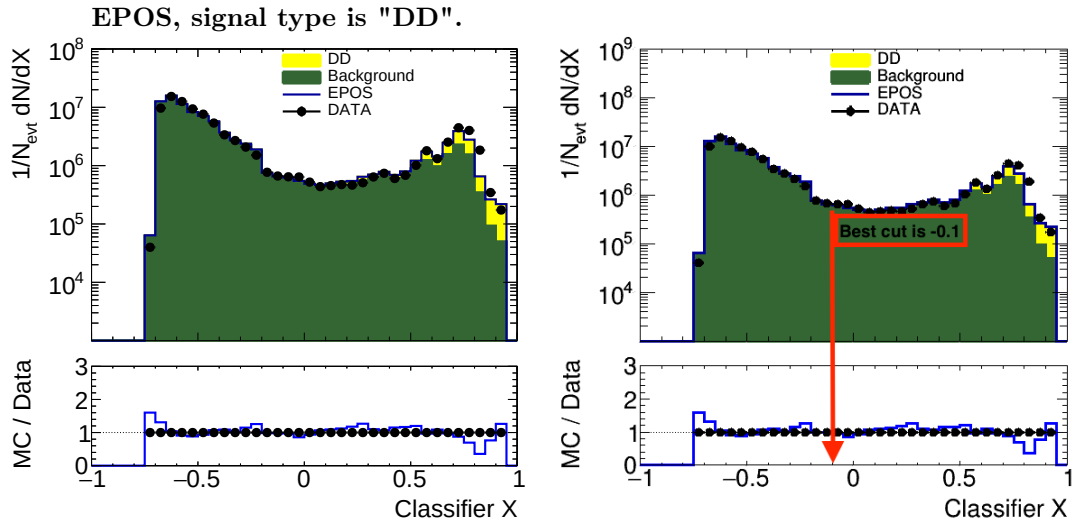

(a)

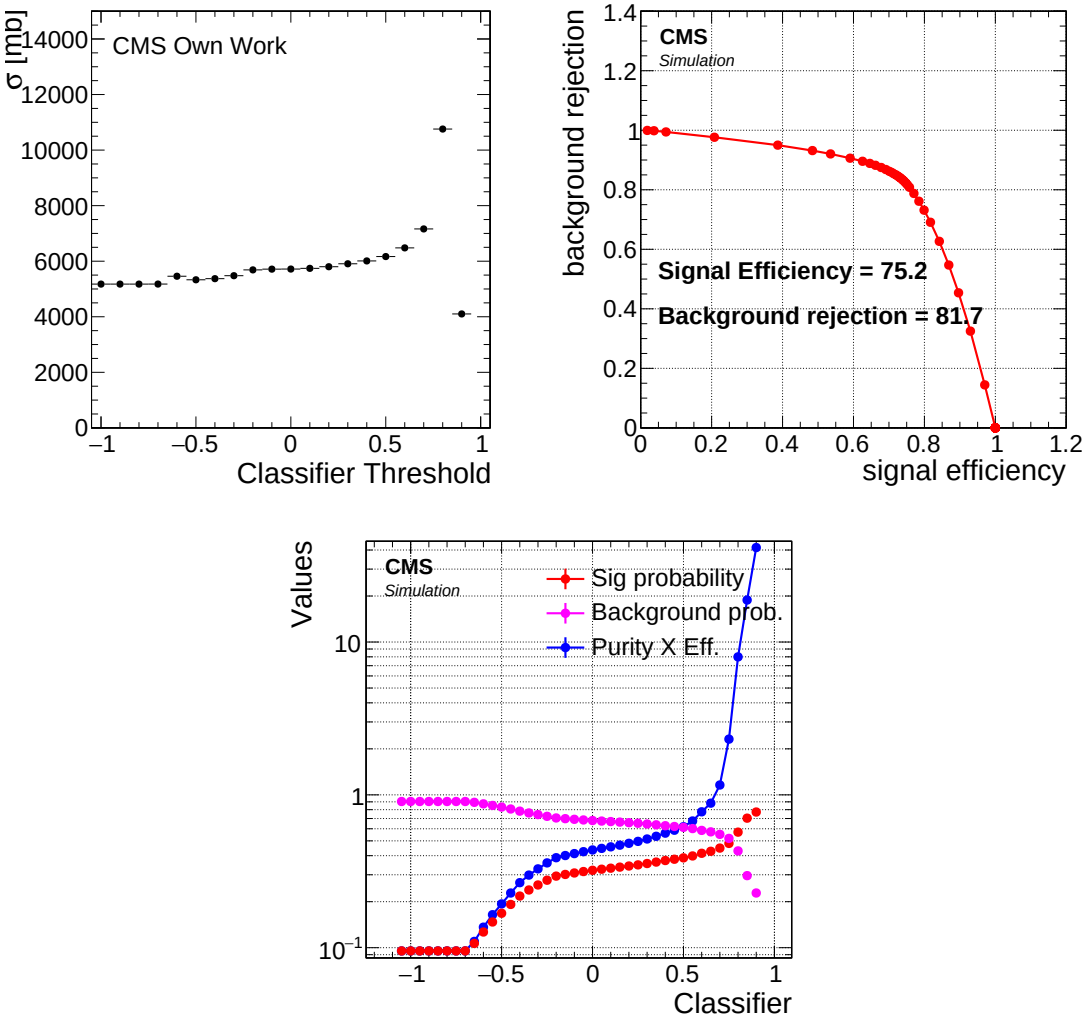

(b)

Figure 5.29: a) Classifier output for events are trained with the EPOS signal type is "DD", on right side cut optimization, b) cut optimizations from classifier threshold, the background rejection versus signal efficiency ("ROC curve") obtained by cutting on the classifier outputs for the events with signal selected "DD", and optimal signal efficiency (run is 247934).

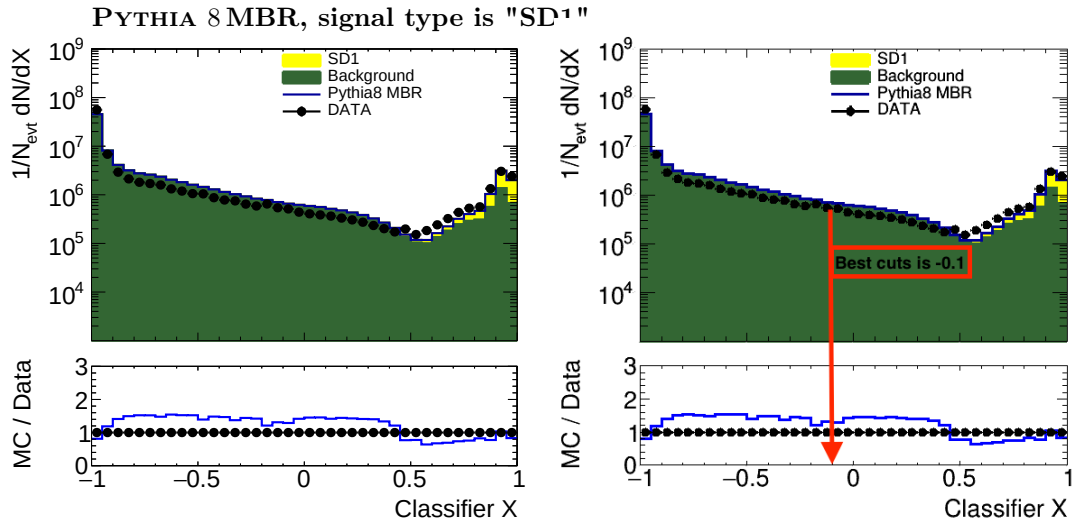

(a)

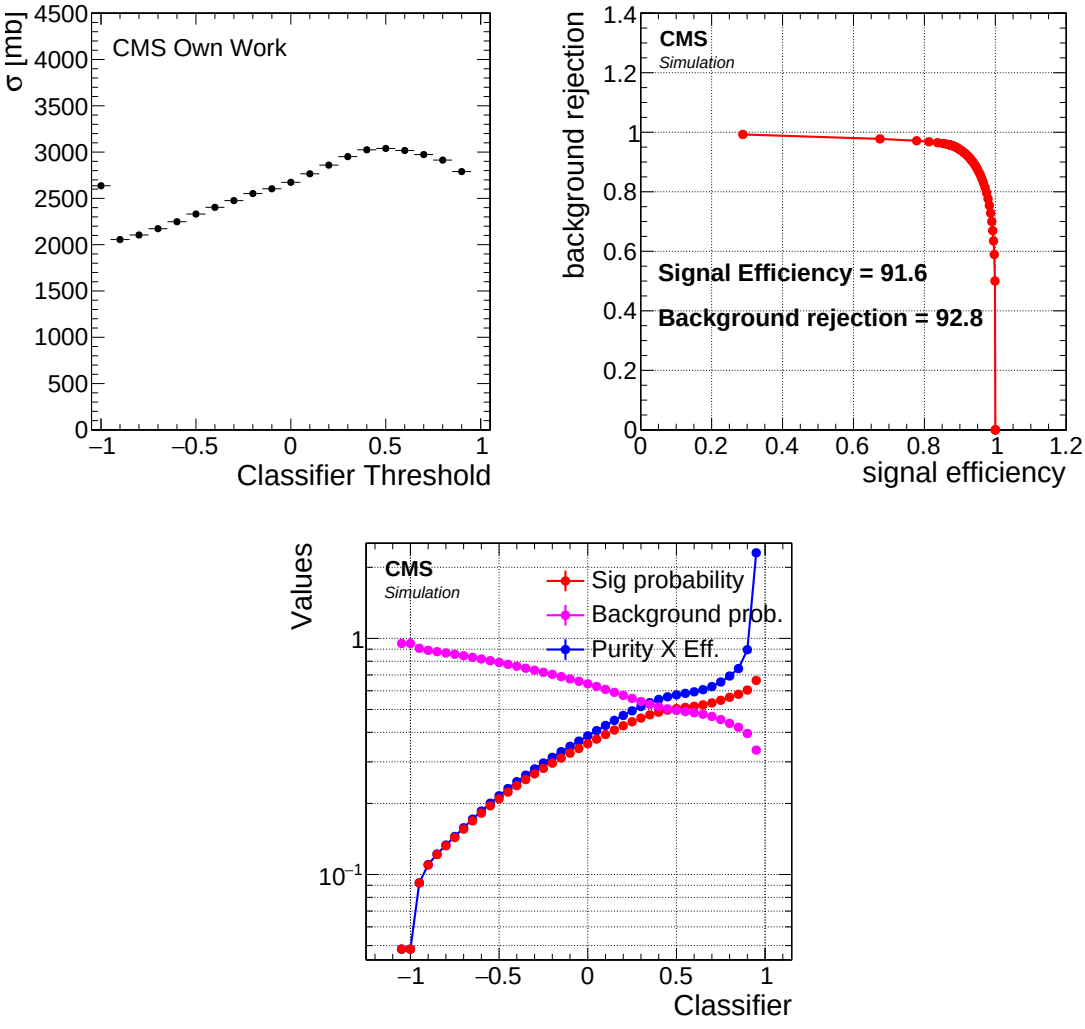

(b)

Figure 5.30: a) Classifier output for events are trained with the PYTHIA 8 MBR signal type is "SD1", b) cut optimization, the background rejection versus signal efficiency ("ROC curve"), and optimal signal efficiency (run 247934).

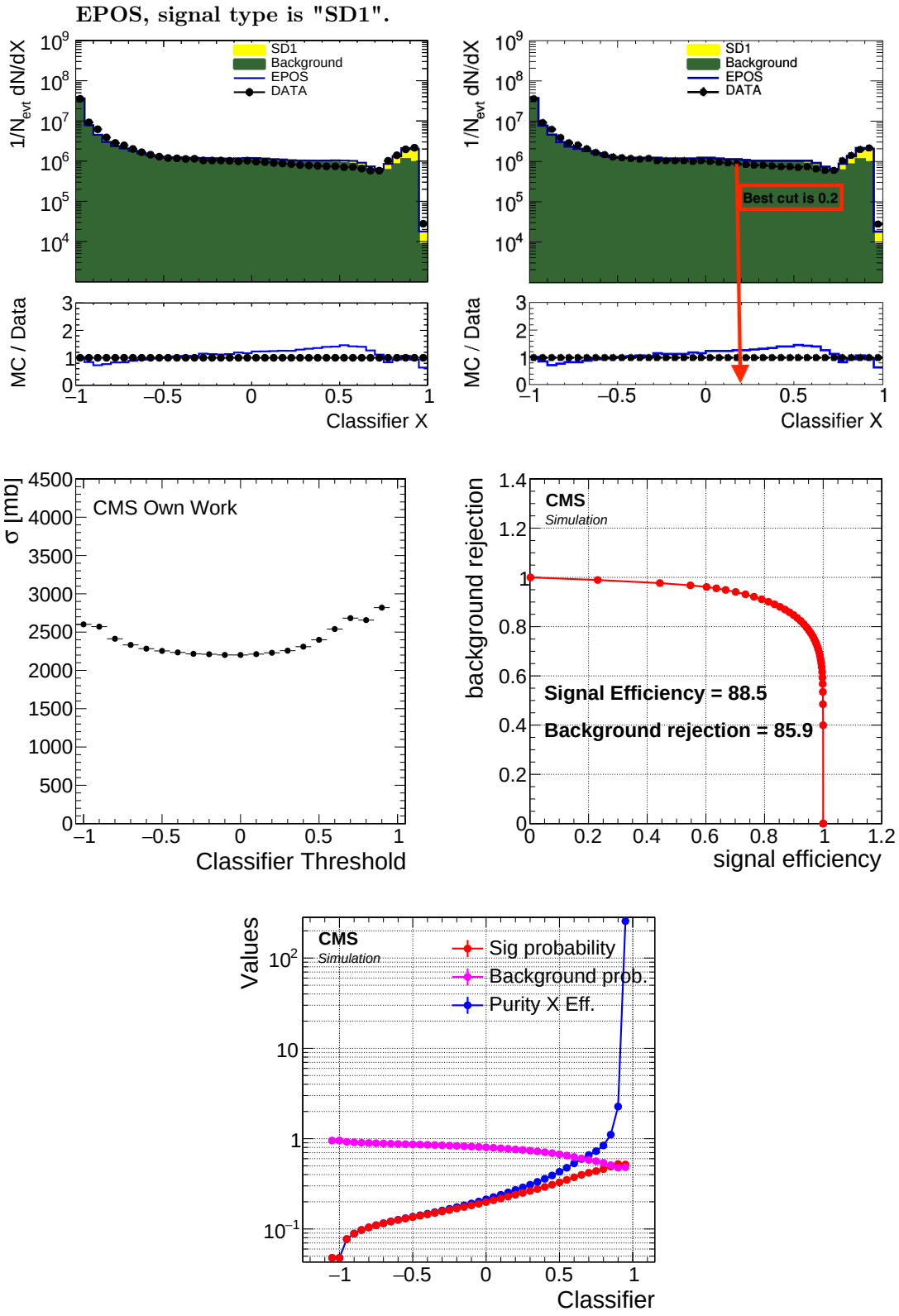

(b)

Figure 5.31: a) Classifier output for events are trained with the EPOS signal is SD1, b) cut optimization, the background rejection versus signal efficiency ("ROC curve"), optimal signal efficiency (run 247934).

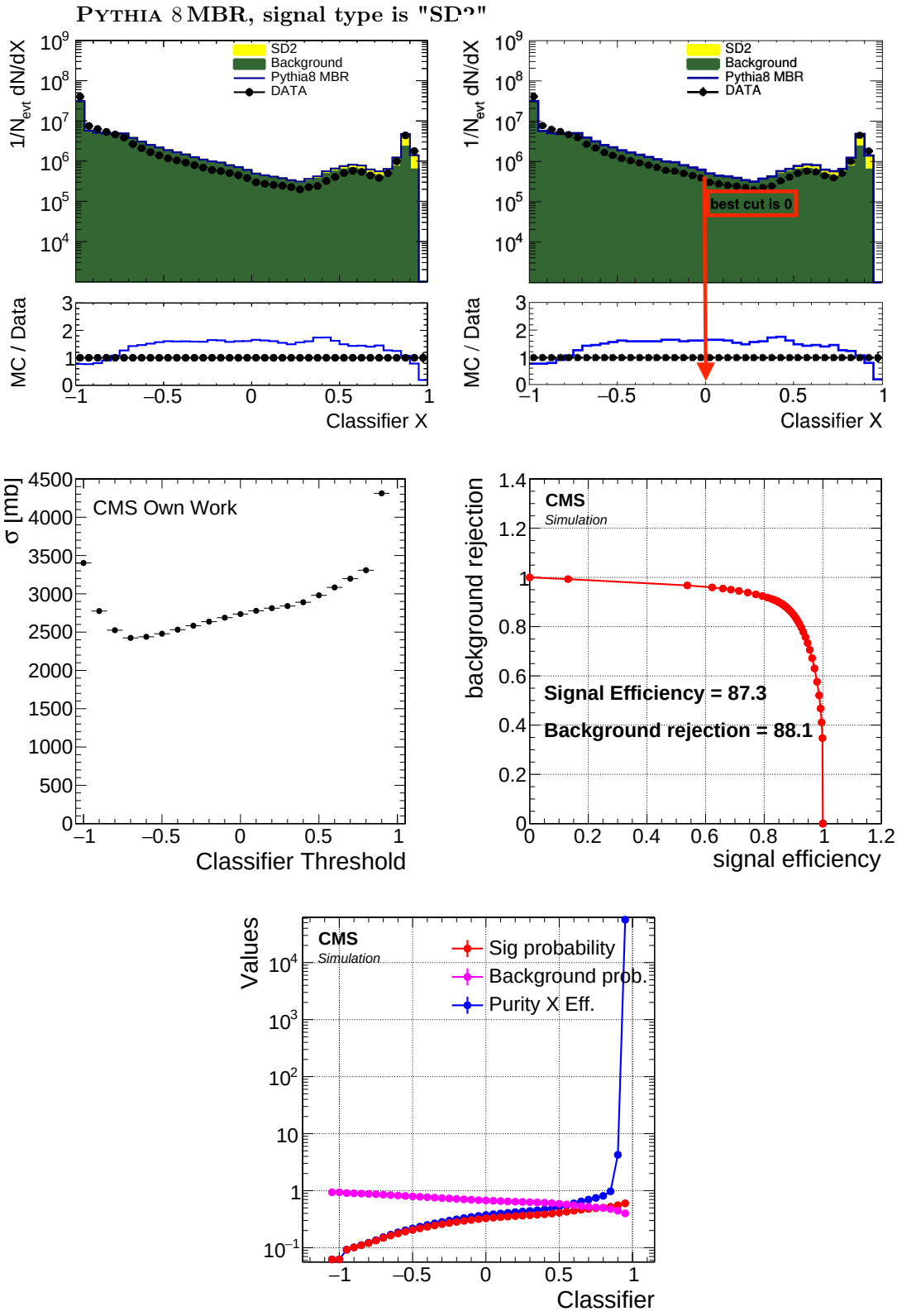

(b)

Figure 5.32: a) Classifier output for events are trained with the PYTHIA 8 MBR signal type is "SD2", b) cut optimization, the background rejection versus signal efficiency ("ROC curve"), optimal signal efficiency (run is 247934).

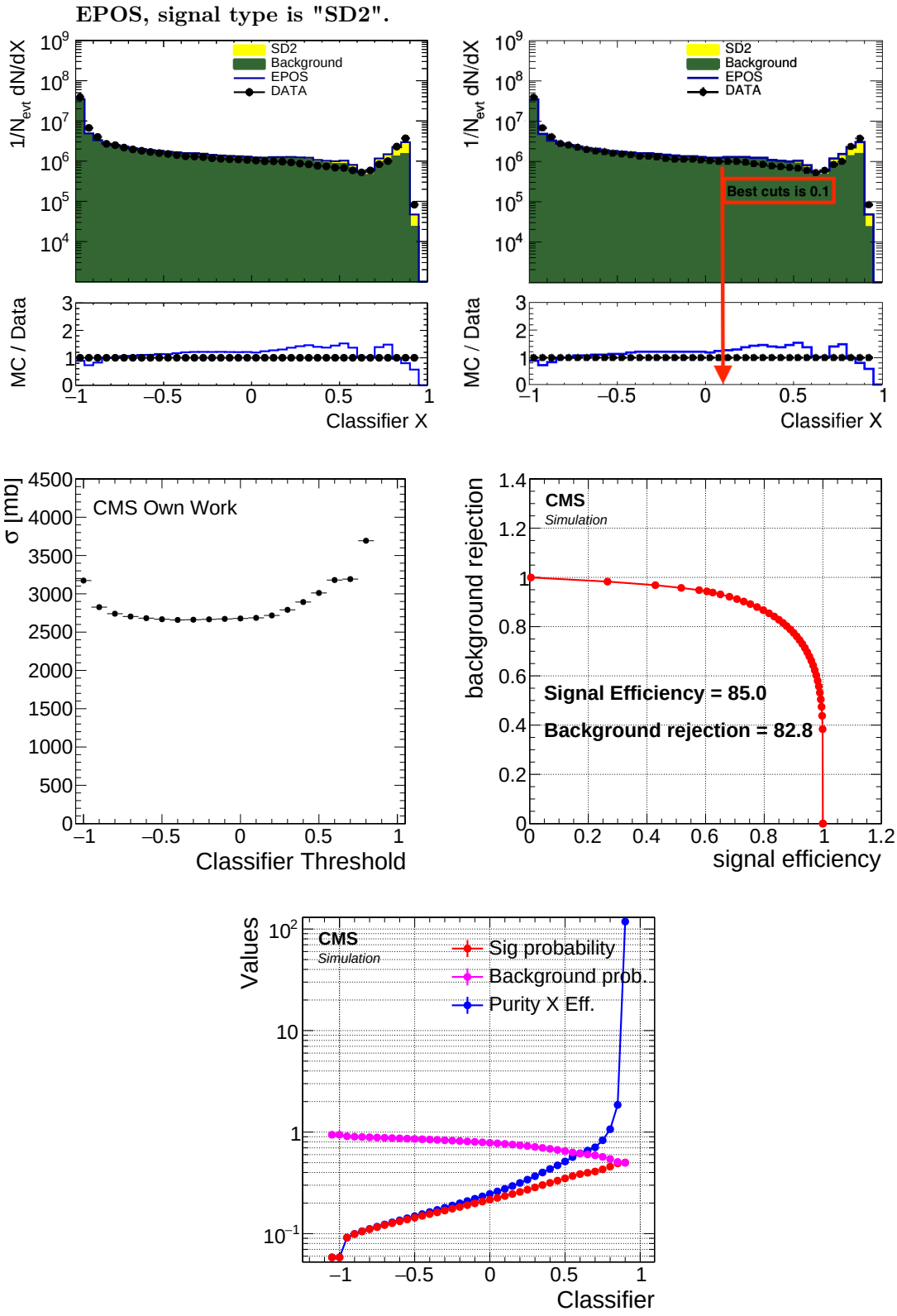

(b)

Figure 5.33: a) Classifier output for events are trained with the EPOS signal is SD2, b) cut optimization, the background rejection versus signal efficiency ("ROC curve"), optimal signal efficiency (run is 247934).

5.9 The Influence of the variable selection on the training

To make sure that the cross sections obtained are not biased by a particular classification variable, the classification was repeated excluding different sets of variables. It was done excluding multiplicities, proton momentum losses or rapidity gap based variables. The results are shown in table 5.4. From the results, it is seen that the results obtained with all the different sets of variables are compatible with the result obtained in the main analysis and with each other. It is also observed that the single diffractive classification suffers when the number of towers from HF and CASTOR are excluded, and multiplicity based variables are not enough to assure symmetry between the left and right configurations (proton momentum losses). A BDT was trained with the baseline sample and the five discriminating variables groups.

- For first group these variables are used in training phase: The smallest and largest values of η separation in the final states, $\Delta\eta^0$, $\Delta\eta = \eta_{max} - \eta_{min}$, the total number of towers in the forward and central regions subdetectors, the total number of towers in the forward hadronic calorimeter at the positive η side, the total number of towers in the forward hadronic calorimeter at the minus η side, the sum of energy in the forward hadronic calorimeter at the positive η side, the sum of energy in the forward hadronic calorimeter at the minus η side.
- In the second group ξ_X and ξ_Y variables are included from the first group.
- For the third group the sum of energy from CASTOR variable is included from the first group.
- For the fourth group the sum of energy from HF at the positive side variable is included from the third group.
- For the 5th group the sum of energy from HF at the minus side variable is included from the third group.
- For the 6th group the sum of energy from HF at the minus side variable and the positive side are included from the third group.

The purpose of these tests to check the choice of optimal selection variables obtained by comparison the number of signal and background events and the significances after baseline and BDT selection. The best cut for measuring the cross section is where $S/\sqrt{S+B}$ has a maximum. for precision measurement one aims for a high purity. Figures are above illustrated the BDT response for the training and the different variables group are trained. In Figure 5.38 shows Results for the second group variables, one can see in classifier output distributions, data and MC are not matching well. Table 5.4 is seen the cross section of σ_{SD} and σ_{DD} from all groups. The smallest σ_{SD} and σ_{DD} values are measured with the second group variables. ξ_X and ξ_X are not used the selected variables in TMVA training

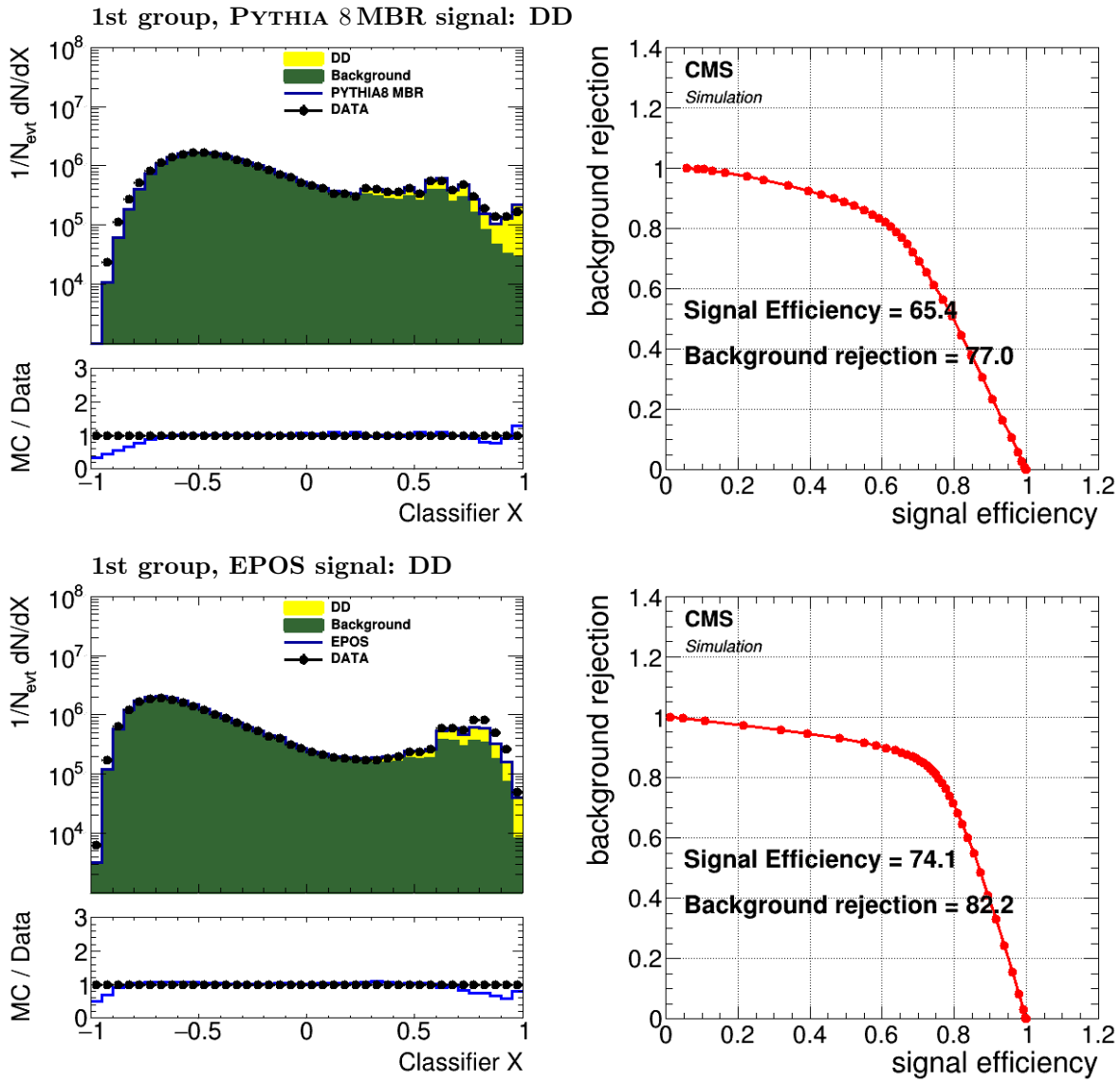

Figure 5.34: Results for 1st group variables. On the top, classifier output for events are trained with the PYTHIA 8 MBR with the signal type is DD. It shows the classifier output, the background rejection versus signal efficiency ("ROC curve"), and on right side signal efficiency (run 247934). At the bottom the same plots for EPOS simulation.

phase. It is concluded from this study that the standard choice of variables is well suited for classification. No surprising effects are found.

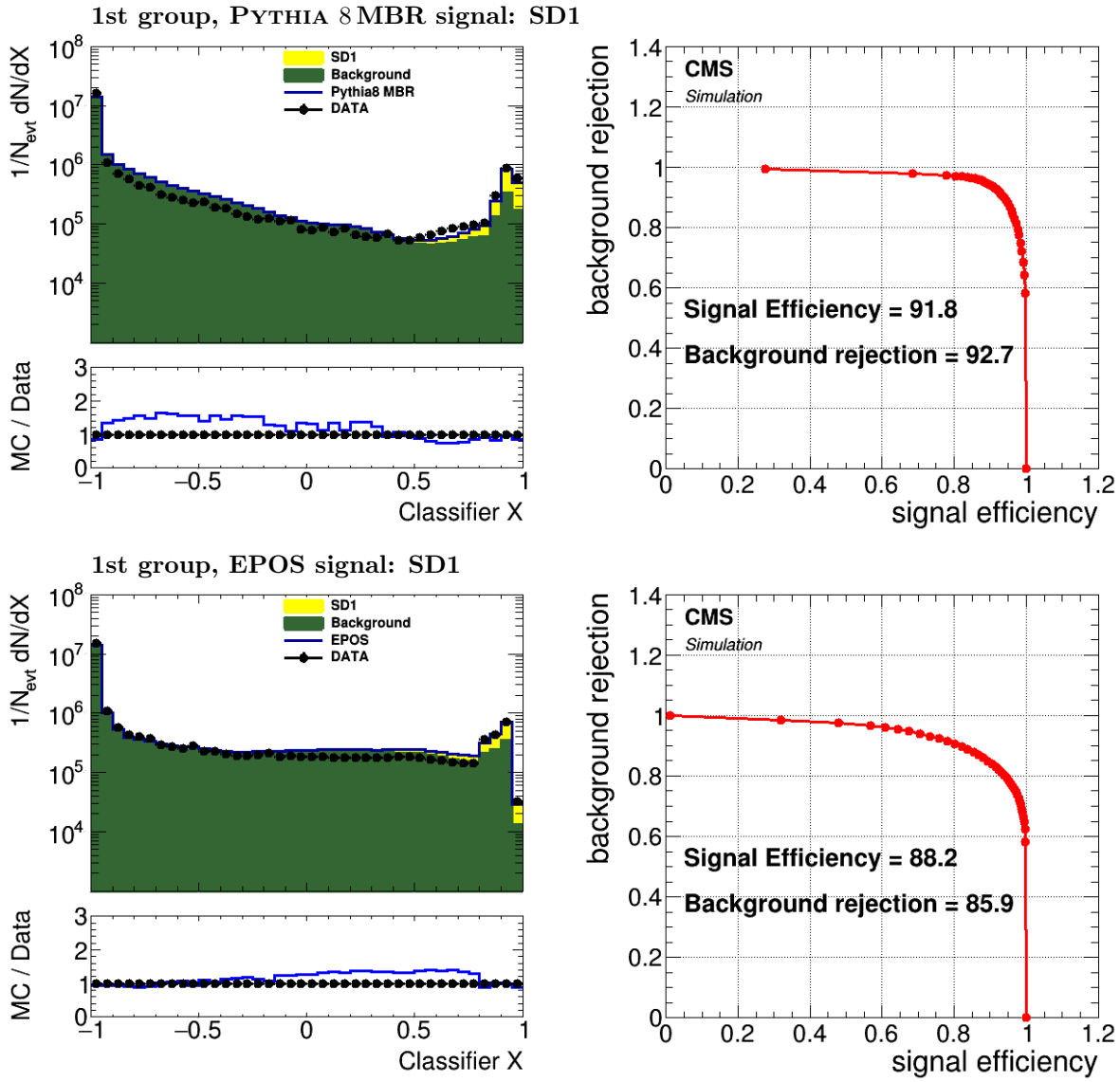

Figure 5.35: Results for 1st group variables. On the top, classifier output for events are trained with the PYTHIA 8 MBR with the signal type is SD1. It shows the classifier output, the background rejection versus signal efficiency ("ROC curve"), and on right side signal efficiency (run 247934). At the bottom the same plots for EPOS simulation.

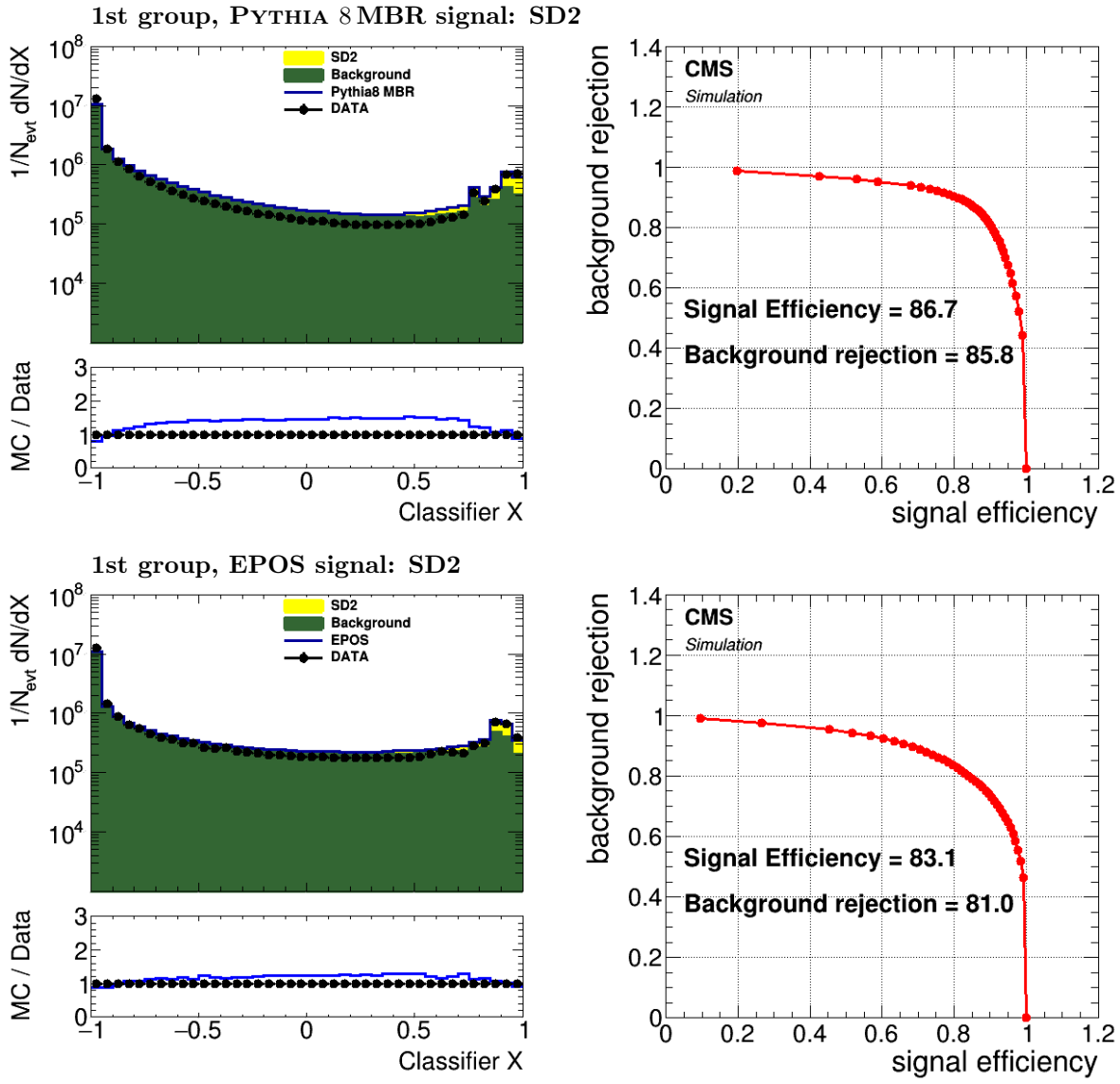

Figure 5.36: Results for 1st group variables. On the top; classifier output for events are trained with the PYTHIA 8 MBR with the signal type is SD2. It shows the classifier output, the background rejection versus signal efficiency ("ROC curve"), and on right side signal efficiency (run 247934). At the bottom the same plots for EPOS simulation.

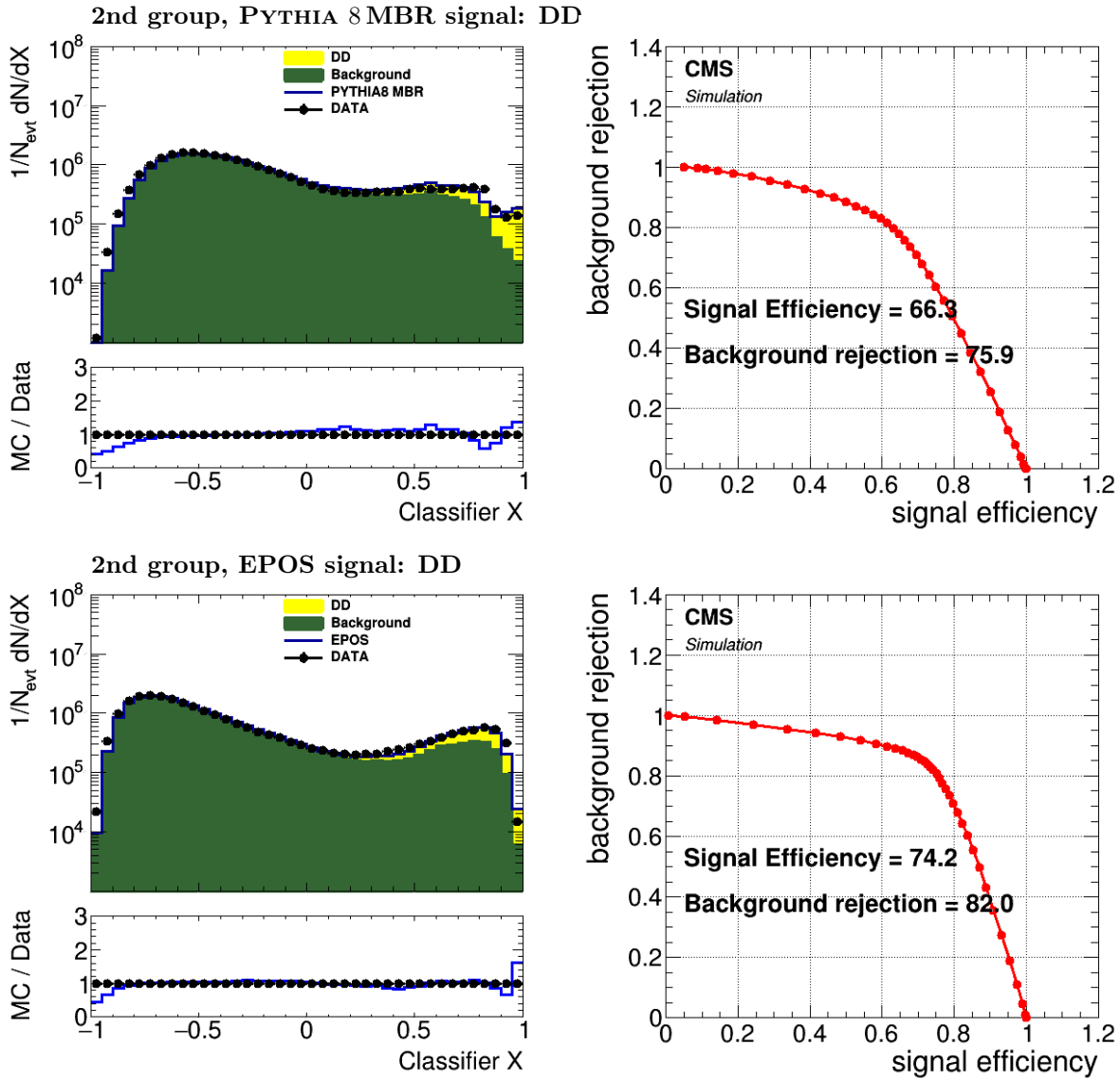

Figure 5.37: Results for 2nd group variables. On the top; classifier output for events are trained with the PYTHIA 8 MBR with the signal type is DD. It shows the classifier output, the background rejection versus signal efficiency ("ROC curve"), and on right side signal efficiency (run 247934). At the bottom the same plots for EPOS simulation.

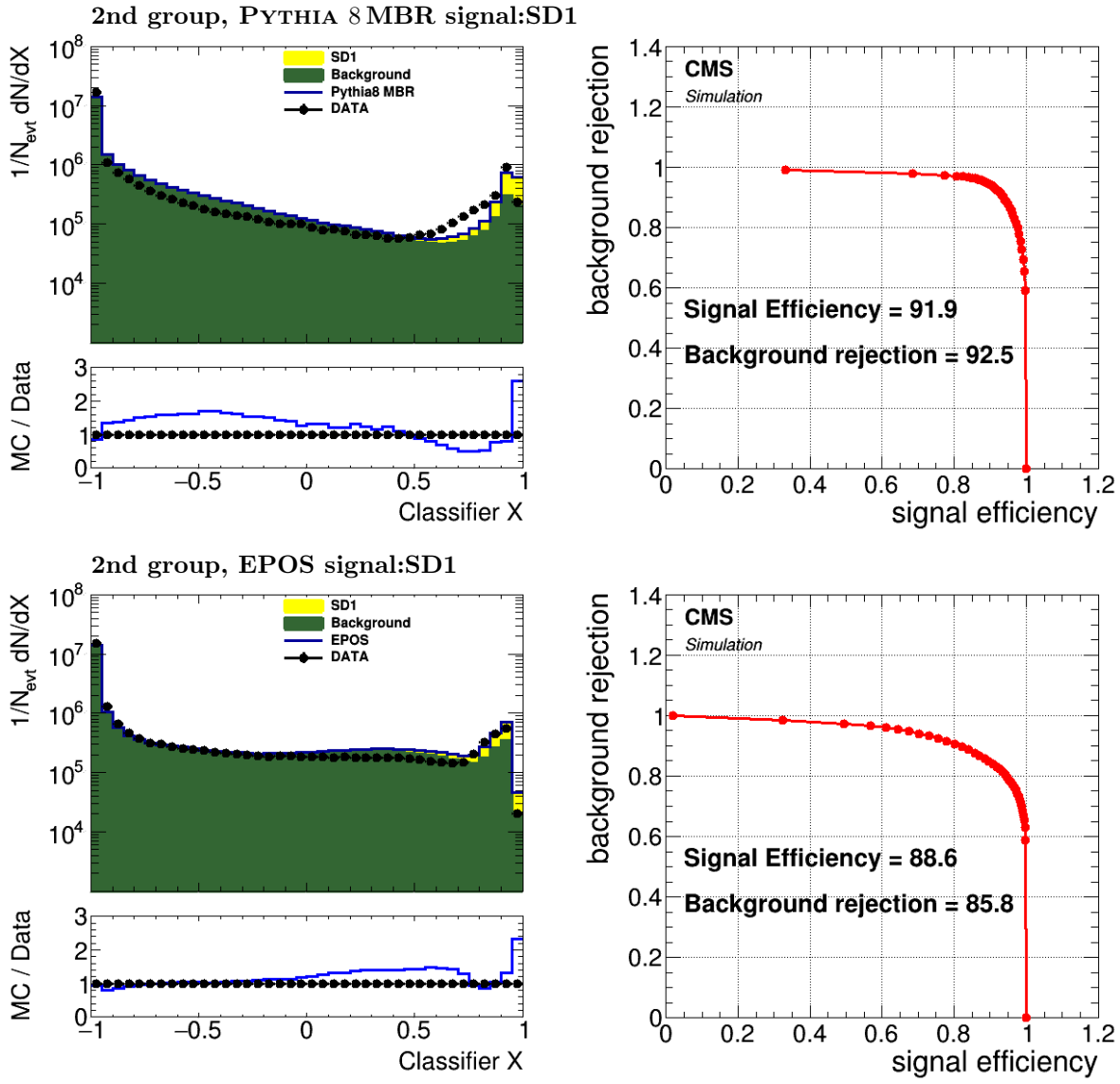

Figure 5.38: Results for 2nd group variables. On the top, classifier output for events are trained with the PYTHIA 8 MBR with the signal type is SD1. It shows the classifier output, the background rejection versus signal efficiency ("ROC curve"), and on right side signal efficiency (run 247934). At the bottom the same plots for EPOS simulation

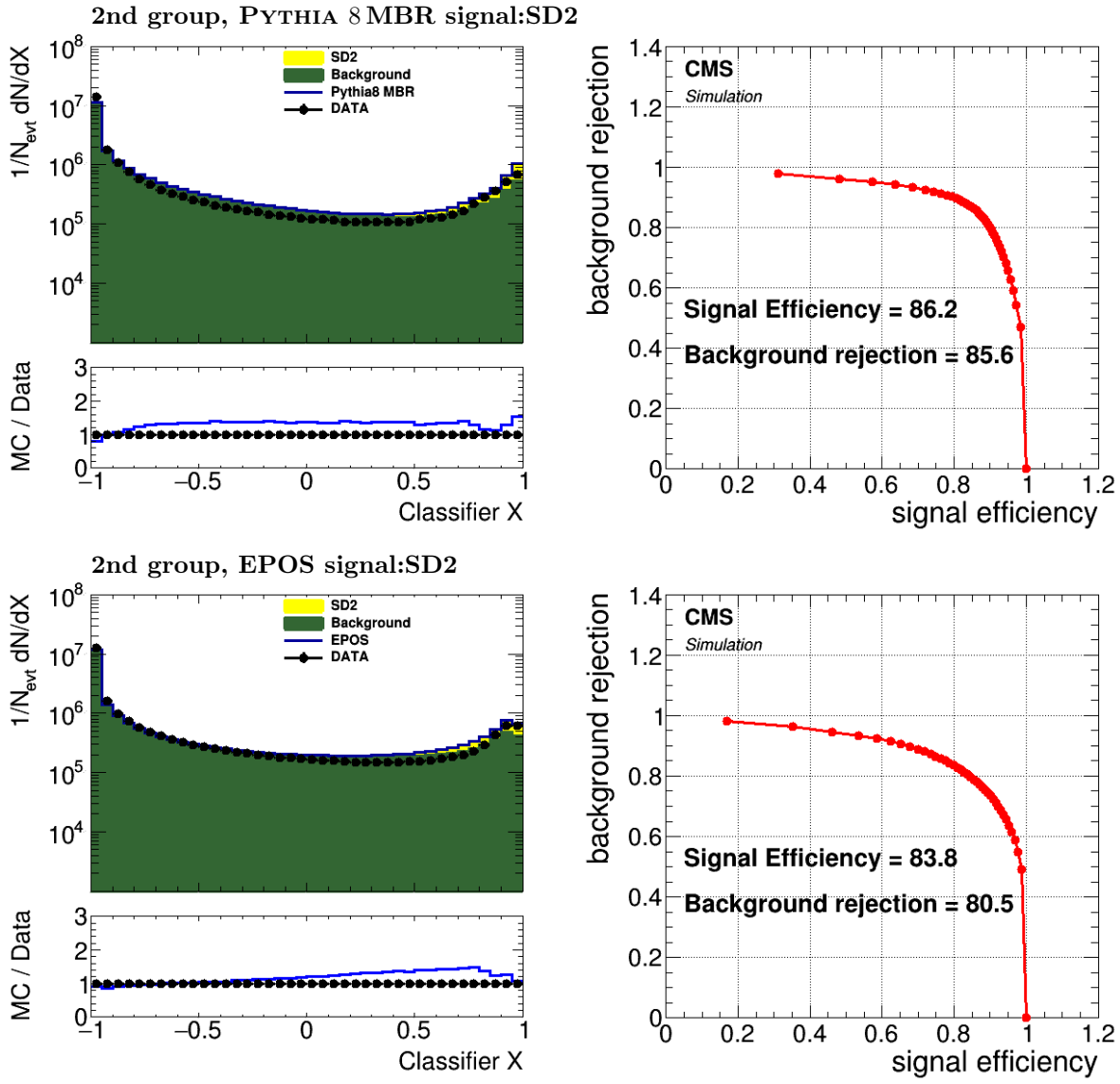

Figure 5.39: Results for 2nd group variables. On the top; classifier output for events are trained with the PYTHIA 8 MBR with the signal type is SD2. It shows the classifier output, the background rejection versus signal efficiency ("ROC curve"), and on right side signal efficiency (run 247934). At the bottom the same plots for EPOS simulation

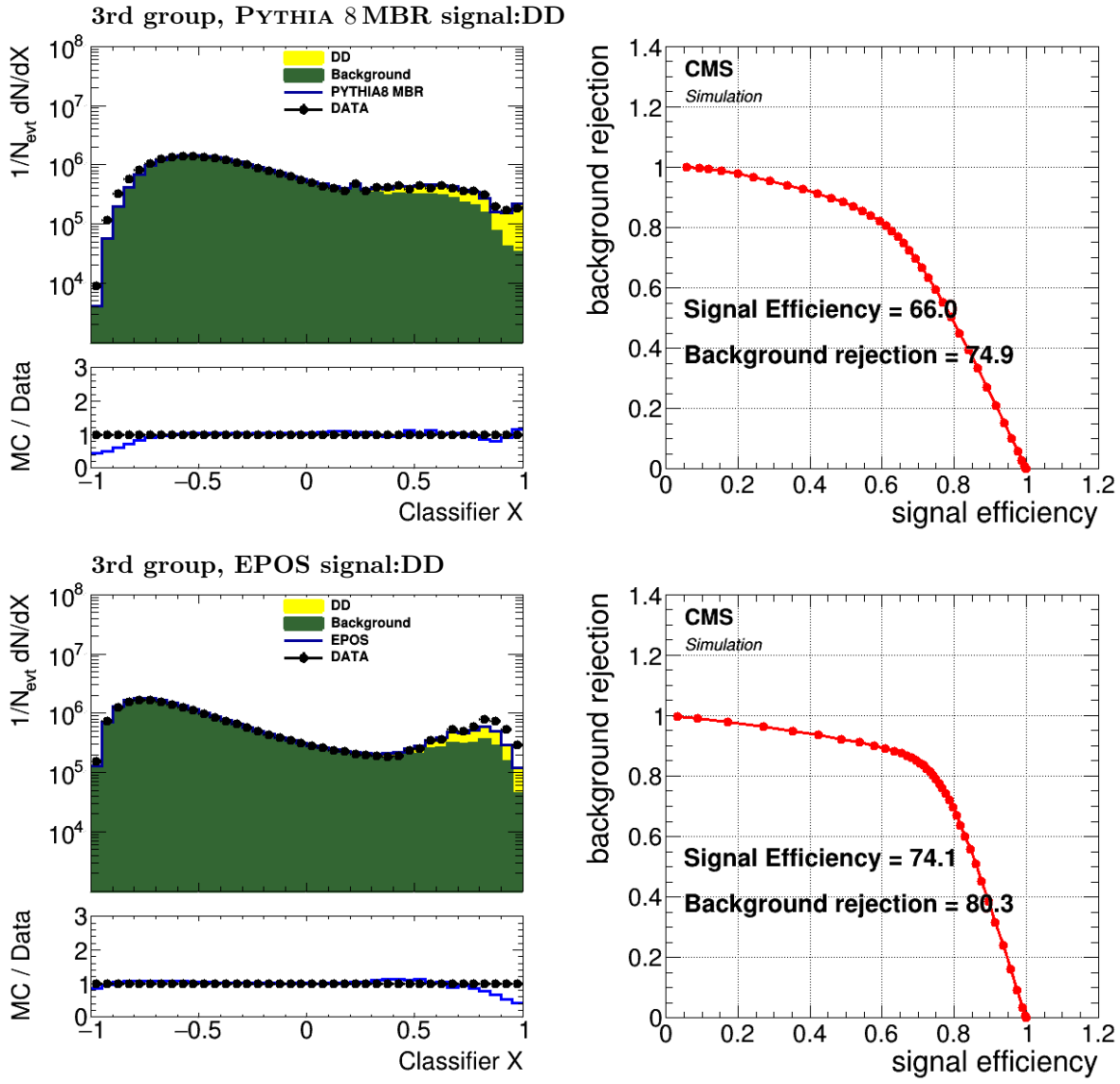

Figure 5.40: Results for 3rd group variables. On the top, classifier output for events are trained with the PYTHIA 8 MBR with the signal type is DD. It shows the classifier output, the background rejection versus signal efficiency ("ROC curve"), and on right side signal efficiency (run 247934). At the bottom the same plots for EPOS simulation

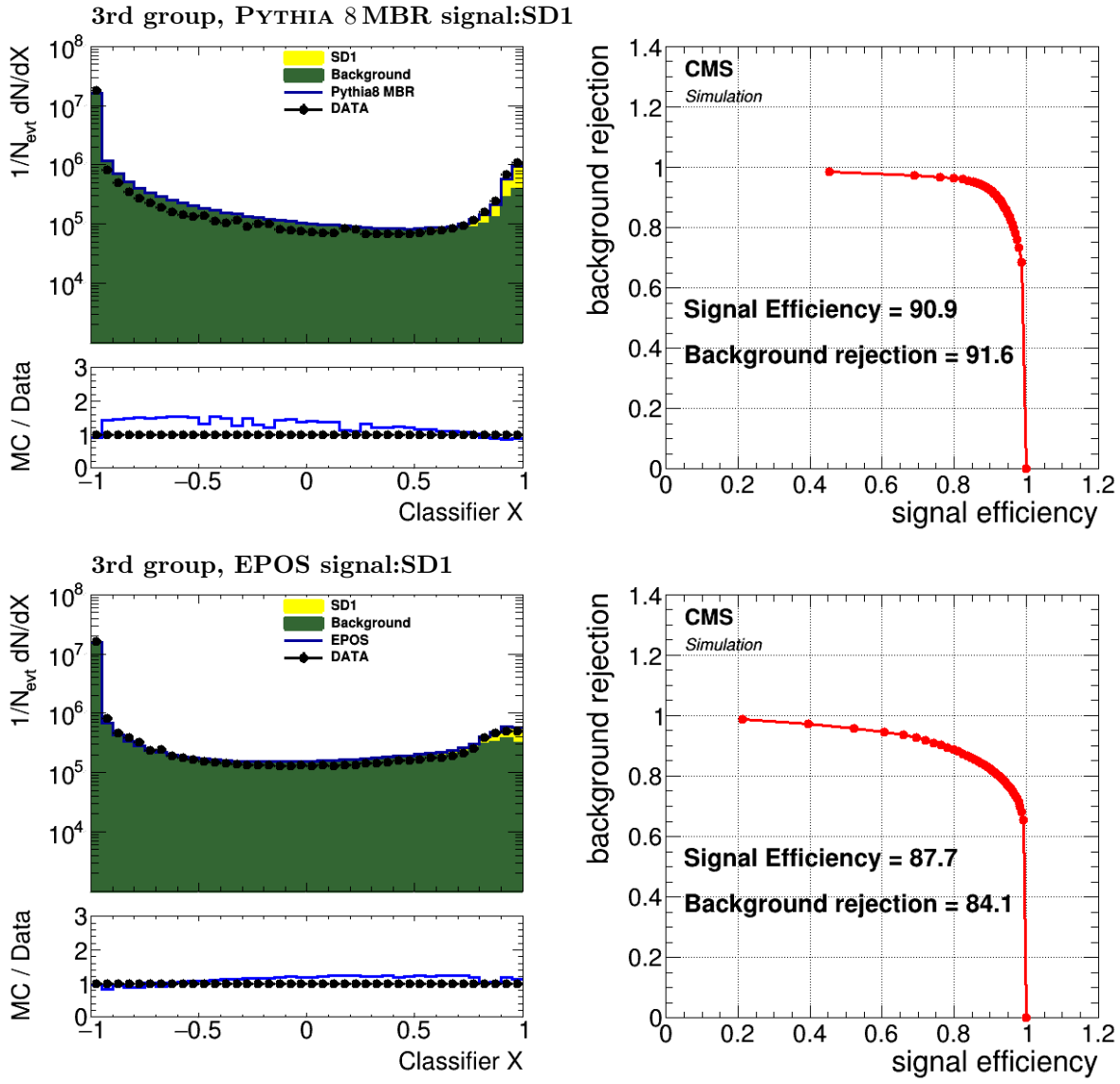

Figure 5.41: Results for 3rd group variables. On the top; classifier output for events are trained with the PYTHIA 8 MBR with the signal type is SD1. It shows the classifier output, the background rejection versus signal efficiency ("ROC curve"), and on right side signal efficiency (run 247934). At the bottom the same plots for EPOS simulation.

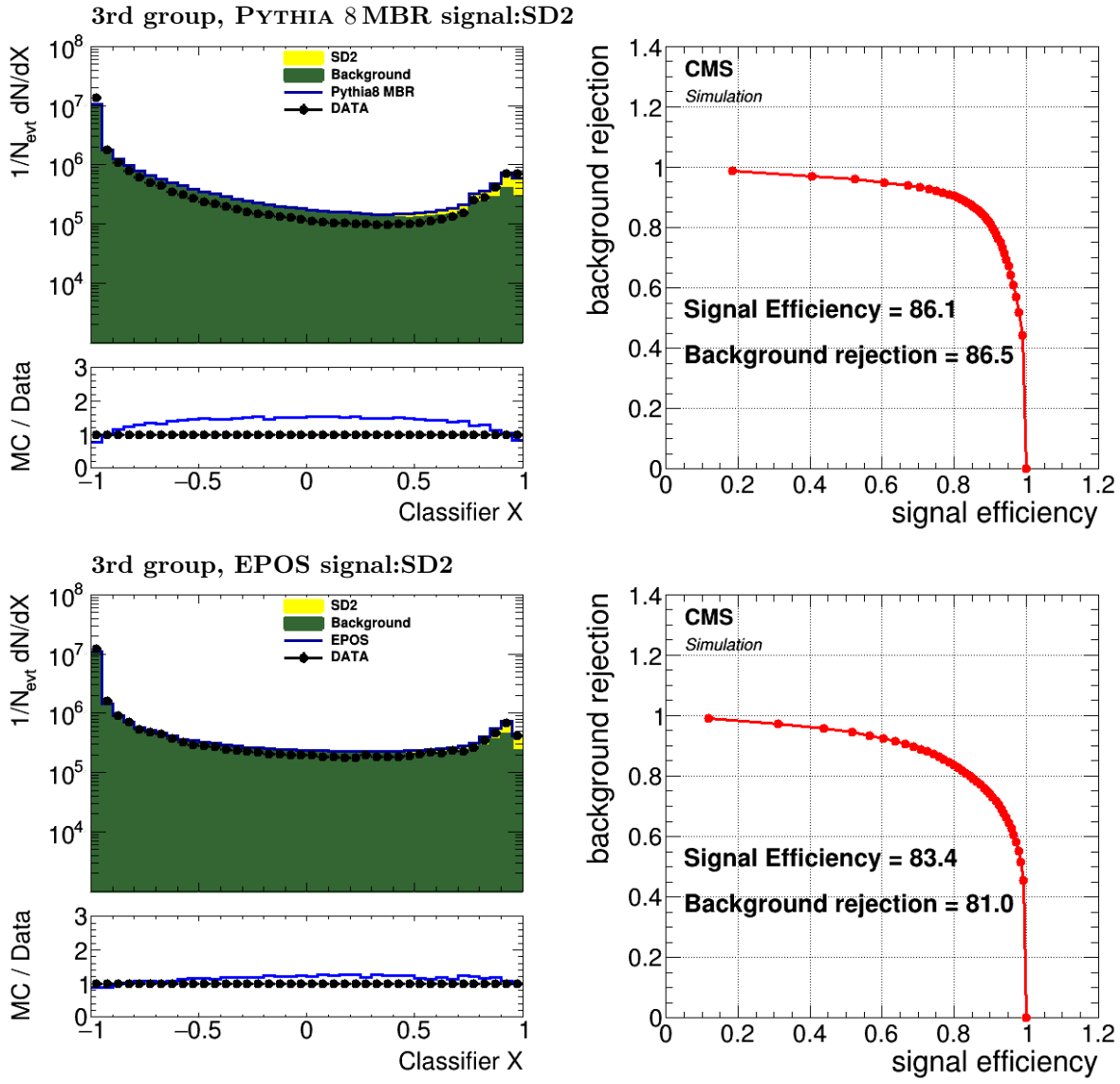

Figure 5.42: Results for 3rd group variables. On the top, classifier output for events are trained with the PYTHIA 8 MBR with the signal type is SD2. It shows the classifier output, the background rejection versus signal efficiency ("ROC curve"), and on right side signal efficiency (run 247934). At the bottom the same plots for EPOS simulation.

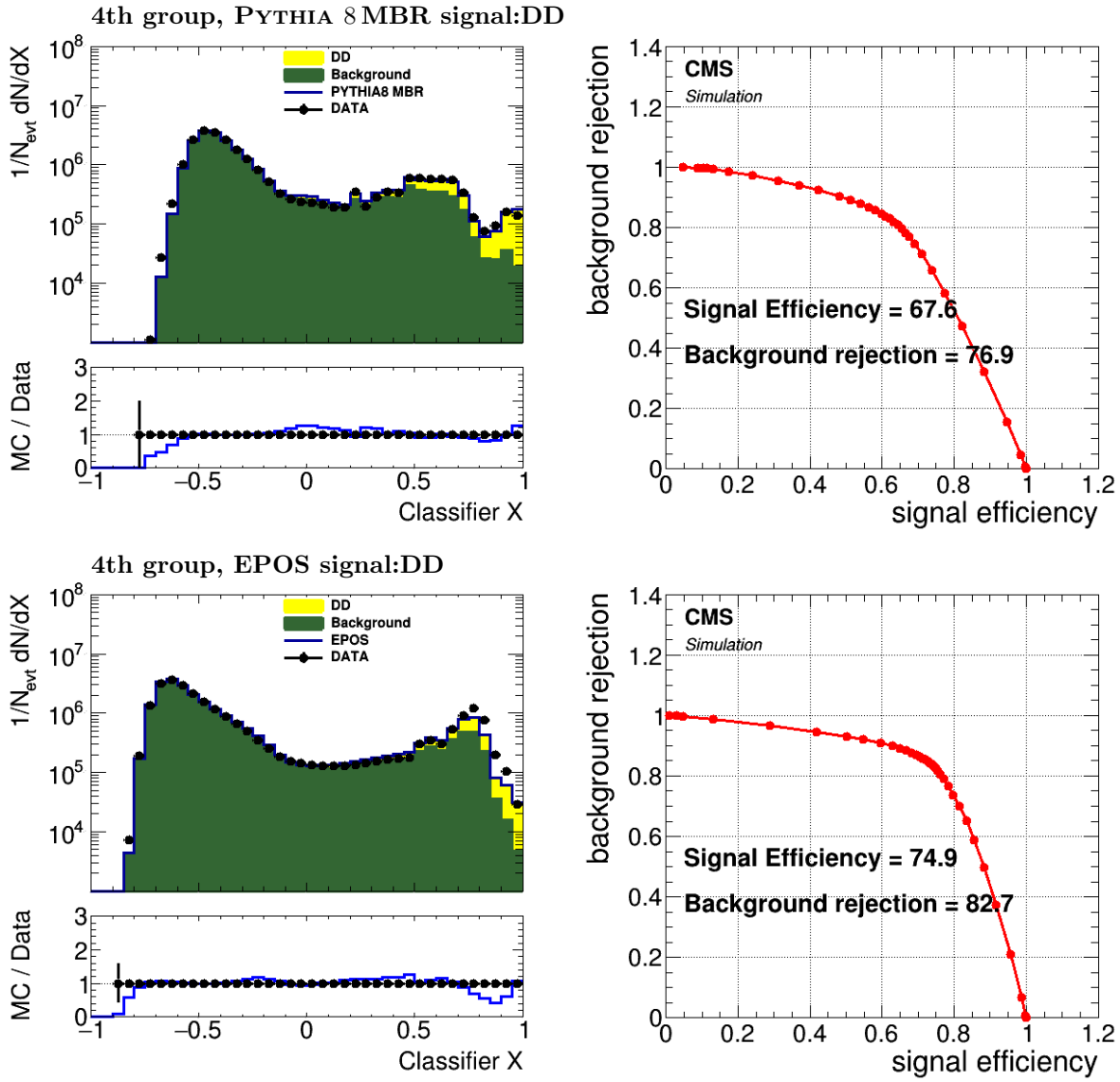

Figure 5.43: Results for 4th group variables. On the top, classifier output for events are trained with the PYTHIA 8 MBR with the signal type is DD. It shows the classifier output, the background rejection versus signal efficiency ("ROC curve"), and on right side signal efficiency (run 247934). At the bottom the same plots for EPOS simulation.

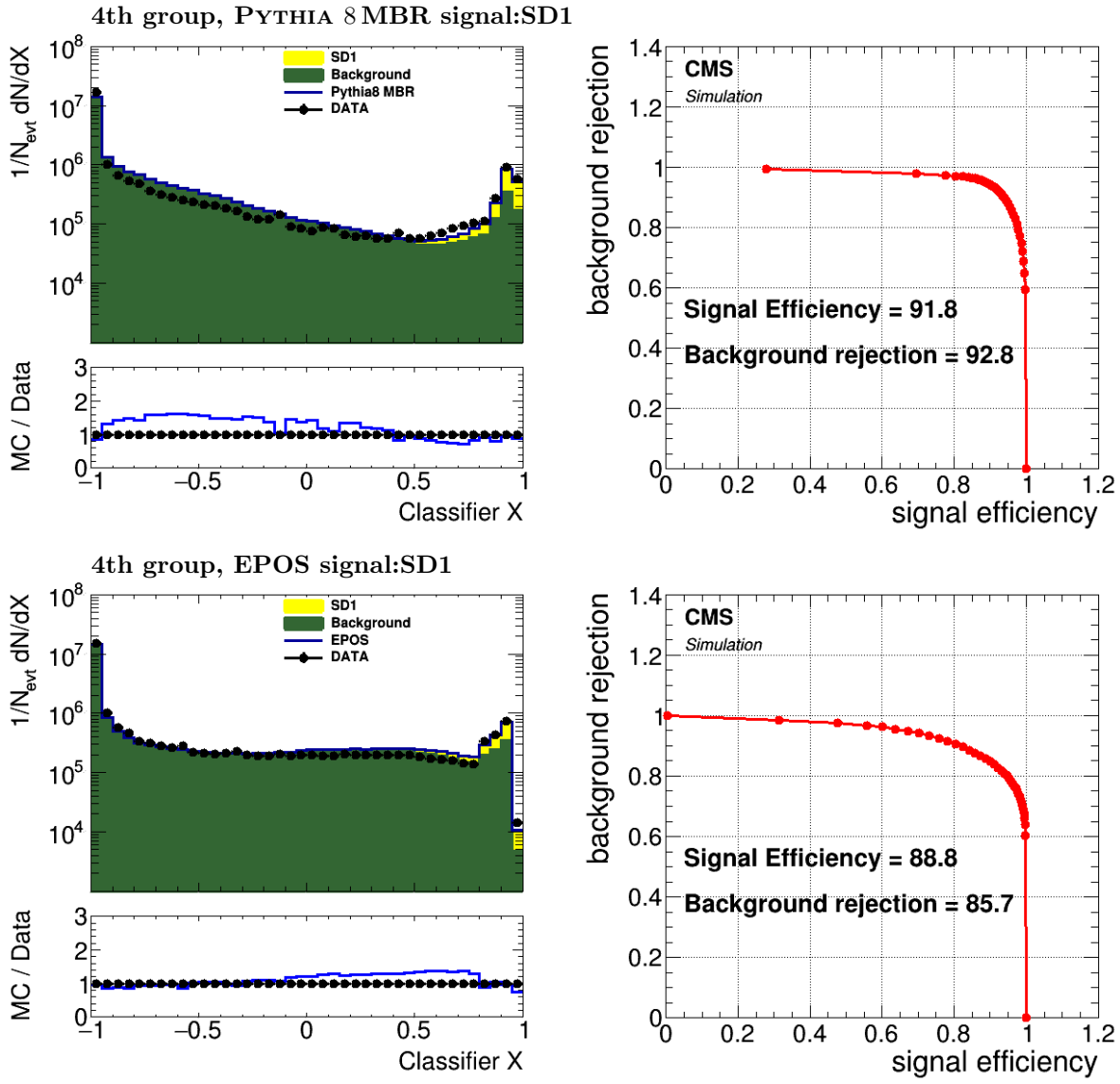

Figure 5.44: Results for 4th group variables. On the top; classifier output for events are trained with the PYTHIA 8 MBR with the signal type is SD1. It shows the classifier output, the background rejection versus signal efficiency ("ROC curve"), and on right side signal efficiency (run 247934). At the bottom the same plots for EPOS simulation.

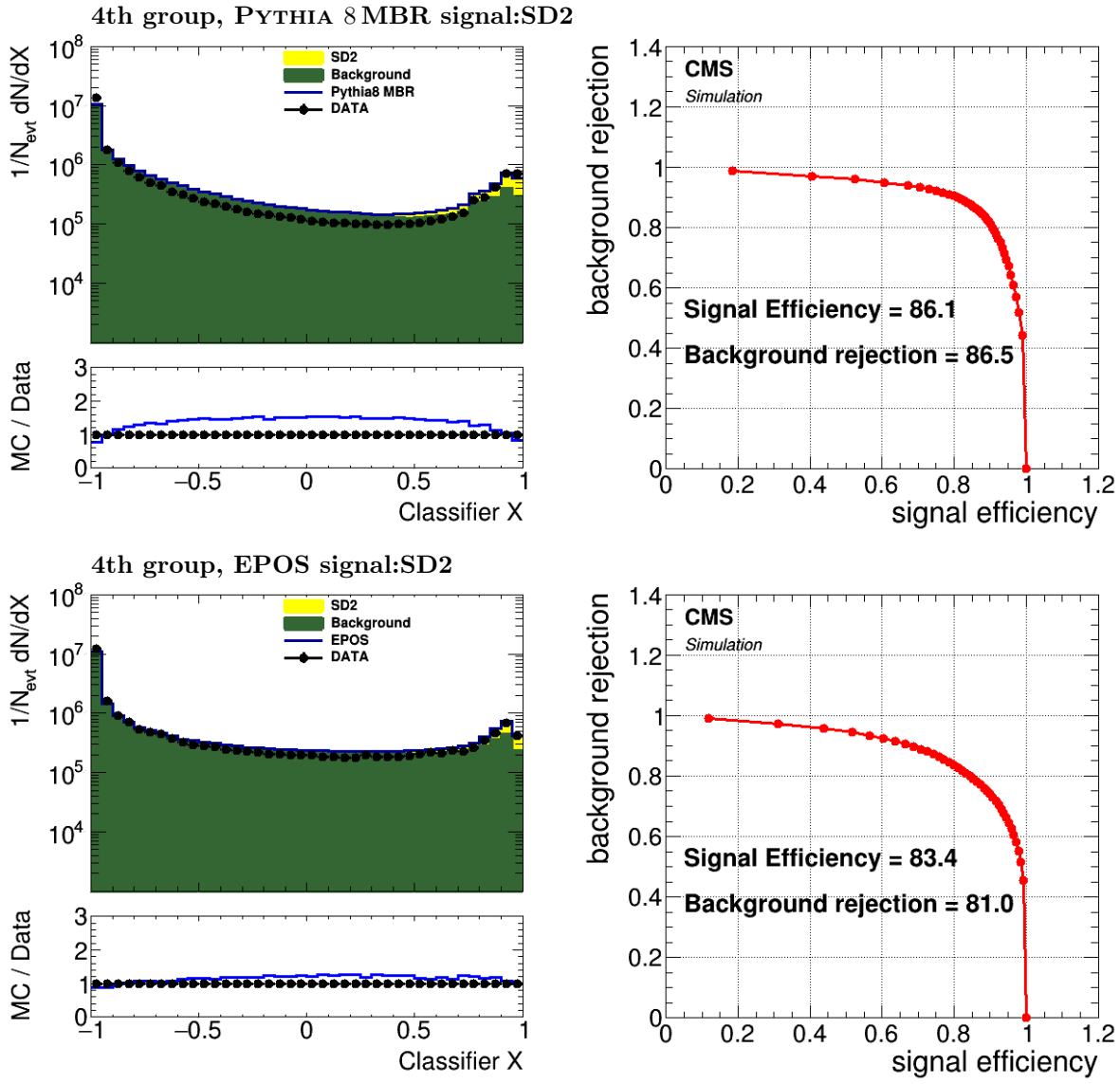

Figure 5.45: Results for 4th group variables. On the top; classifier output for events are trained with the PYTHIA 8 MBR with the signal type is SD2. It shows the classifier output, the background rejection versus signal efficiency ("ROC curve"), and on right side signal efficiency (run 247934). At the bottom the same plots for EPOS simulation.

Table 5.4: Different variable groups are tested for to figure out which variable group is the best using as input variables in TMVA training for optimally to get classified the events.

	Group	$\sigma_{SD}\,[mb]$	$\sigma_{DD}\,[mb]$
	1st	5.1	6.2
	2nd	4.8	5.7
	3rd	5.1	6.2
	4th	5.1	6.1
	5th	5.2	6.1
	6th	5.2	6.0

5.10 Extrapolation of the visible SD and DD cross sections

The measurement based on the central CMS detector is insensitive to low mass part of diffractive dissociation. Therefore, in order to compare the measured visible cross sections with results of other experiments and theoretical models we need to use additional extrapolation corrections. To calculate extrapolation factors 1.000.000 events are generated at $\sqrt{s} = 13\,\text{TeV}$ for EPOS LHC, SIBYLL 2.3, QGSJET-II 0.4, PYTHIA 8 MBR. Extrapolation factors are related to diffractive cross section and the visible part of the total SD and DD cross sections. The extrapolation factors are defined as

$$f^{SD} = \sigma_{SD}/\sigma_{SD}^{visible}, \tag{5.9}$$

where σ_{SD} is defined as $\xi_X < 0.05$, and $\sigma_{SD}^{visible}$ is combination of SD1 and SD2. The SD1 event selection cut: $\log_{10}\xi_Y > -6$ and $\log_{10}\xi_Y < -1$, in combination with intact proton on minus side. For SD2 event selection cut: is $\log_{10}\xi_X > -7$ and $\log_{10}\xi_X < -1$, in combining with intact proton on plus side.

The extrapolation factors are the DD case

$$f^{DD} = \sigma_{DD}/\sigma_{DD}^{visible}, \tag{5.10}$$

where σ_{DD} is defined as $\Delta\eta > 3$, and $\sigma_{DD}^{visible}$ is defined with $\Delta\eta > 4$ and $\log_{10}\xi_Y > -6$ or $\log_{10}\xi_X > -7$.

Table 5.5: Extrapolation factors f^{SD} and f^{DD}.

	MC Model	f^{SD}	f^{DD}
	EPOS LHC	1.51	1.78
	SIBYLL 2.3	1.06	1.75
	QGSJET-II 0.3	1.33	2.20
	QGSJET-II 0.4	1.56	1.91
	PYTHIA 8 MBR ($\xi = 0.08$)	1.25	1.43
	PYTHIA 8 MBR ($\xi = 0.07$)	1.22	1.45
	PYTHIA 8 MBR ($\xi = 0.104$)	1.32	1.4
	PYTHIA 8 MBR ($\alpha\prime = 0.125$)	1.35	1.4
	Mean(Averaged Value)	$1.33 \mp 0.27, 0.24$	$1.66 \mp 0.27, 0.53$

The extrapolation factors for SD and DD cross sections are shown in table 5.5 for each of the MC models. Table 5.5 shows the extrapolation factor, f^{SD} and f^{DD} for the SIBYLL 2.3, QGSJET-II 0.3, QGSJET-II 0.4, and EPOS simulations, compared to the

PYTHIA 8 MBR simulation. In addition, PYTHIA 8 MBR simulations with values of $\alpha\prime$ and ξ changed to $\alpha\prime = 0.125$ GeV^{-2}, $\xi = 0.007, 0.104$ (one parameter changed at a time) are also included to provide a scale for their effect on the cross sections. Those are the parameters of the pomeron trajectories that determines the very low-mass cross-section in PYTHIA. The cross section of SD and DD are corrected with the extrapolation factors. The cross section of SD and DD are corrected with the extrapolation factors. The final values are illustrated in table 5.6. The spread in the exrapolation factors is used for the systematic uncertainaties.

Table 5.6: It shows average of diffractive cross sections for SD and DD. These values are corrected with extrapolation factors.

	TMVA trained MC model	Data	$\sigma_{SD}\,[mb]$	$\sigma_{DD}\,[mb]$
	Mean(Averaged Value(PYTHIA 8 MBR, EPOS)	247920	7.1	10.5
	Mean(Averaged Value (PYTHIA 8 MBR, EPOS)	247934	6.8	10.2

5.11 Systematic uncertainties

Systematic uncertainties are obtained by varying the selection criteria and modifying the analysis. To calculate each systematic effect, the full analysis is repeated and the differences in the final data points are added in quadrature to obtain the total systematic error. The following sources of uncertainty, summarized in table 5.7, are found to have effects on the

- HF and CASTOR energy scale: Though the noise threshold is well determined using zero bias events, the noise thresholds are subject to energy scale uncertainty. Since an increase in the threshold would remove more noise and signal in calorimeters, the effect of such a variation is estimated. The HF energy scale is varied in the data by $\mp 20\%$ for both sides of HF. To gauge the possible influence of a change in the CASTOR energy scale, the noise threshold applied to CASTOR towers is changed by $\mp 15\%$, corresponding to the uncertainty in the absolute calibration factor.
- Model dependence: Modeling of the diffractive interaction and the hadronization process, the hadronization parameters in the nominal PYTHIA 8 MBR MC sample are tuned diffractive systems in proton-proton collisions at much lower energies. Note that the two generator offers a very good overall description of the data. Each model describes different aspects of the distributions. In total, EPOS offers a slightly better general agreement with the data. A comparison of predictions from the two event generators helps, estimate the possible impact of proper diffractive modeling.
- The uncertainty in the integrated luminosity measurement is 2.3%.

- The influence of tracking efficiency on gap reconstruction was studied. The number of the track is changed by 5% by randomly tracks from data.
- The effect of pile-up was investigated by calculating the ratio which is estimated by the number of events with vertex and the number of events without vertex cut in data and MC. The pile-up correction to on cross-section. The selection required two or more tracks associated to the primary vertex, thereby keeping the efficiency for event selection high and the fake-rate manageable.

A detailed description of the systematic uncertainties considered in the measurement is presented in this section. The effect of HF energy scale is illustrated in figure 5.46. The CASTOR energy scale impact is shown in figure 5.48, and the tracking impaction 5.47.

Table 5.7: Systematic uncertainties for the measurement of the SD, DD.

	Source	$\sigma_{SD}\,[mb]$	$\sigma_{DD}\,[mb]$
	CASTOR energy scale	0.12	0.1
	HF energy scale	0.2	0.1
	Track efficiency	0.01	0.03
	Run dependence	0.01	0.09
	Different modeling	0.36	0.68
	Extrapolation	$-1.33, +1.52$	$-1.74, +3.49$
	Luminosity	0.16	0.24
	Total systematic error	$-1.4, +1.6$	$-1.9, +3.6$
	Statiscal uncertainty	0.009	0.06

In Figure 5.49 and 5.50 show the classifier outputs for events are trained with the PYTHIA 8 MBR and EPOS simulations into DD, SD1, SD2(respectively). Comparison of different data which they are corrected by the systematic corrections. Data is represented by the black line. The red blue and pink lines indicate for HF energy scale which is varied in the data by $\mp 15\%$ for both sides of HF. The red and yellow lines are CASTOR energy scale, is changed by $\mp 20\%$, the uncertainty in the absolute calibration factor. The green line is for the influence of tracking efficiency.

SD1 and SD2 give slightly different results for the systematic uncertainties study. The SD2 distribution shows large statistical uncertainties and fluctuations because of the different beam directions. The Y system has to extend over the full detector, including CASTOR, and thus a high efficiency is again reached for large M_Y and Y. The total systematic uncertainty is obtained by summing all individual uncertainties in quadrature, separately for the positive and negative deviations from the nominal cross-section values. Table 5.7 presents the summary of the systematic uncertainties for the measurement of the σ_{SD}, σ_{DD}.

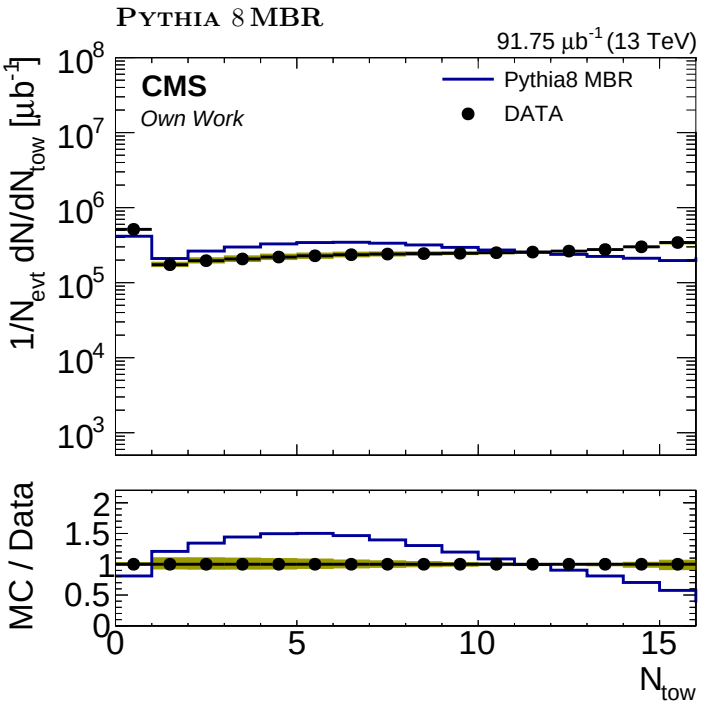

(a) The hottest CASTOR towers.

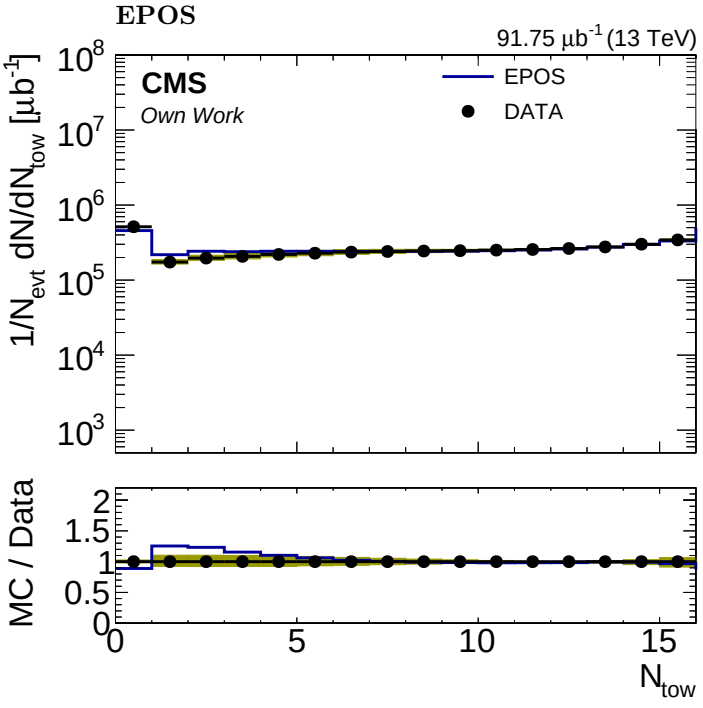

(b) The hottest CASTOR towers.

Figure 5.46: The number of towers towers from CASTOR, and PYTHIA 8 MBR and EPOS are compared to data. CASTOR energy scale is changed in the simulation by $\mp 15\%$, to reflect the estimated energy scale uncertainty for the data.

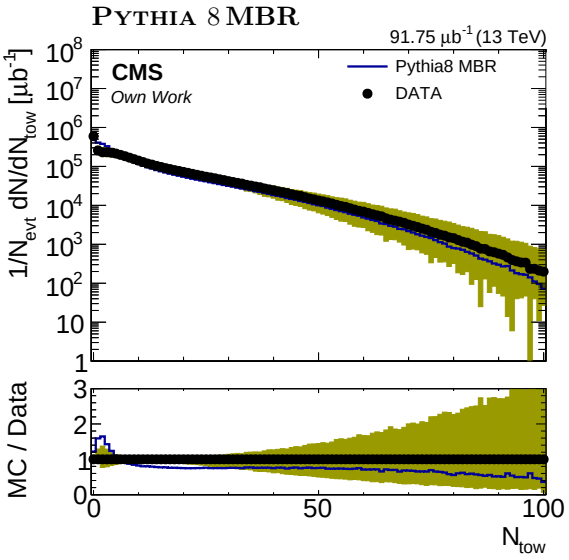

(a) The number HF(+) towers.

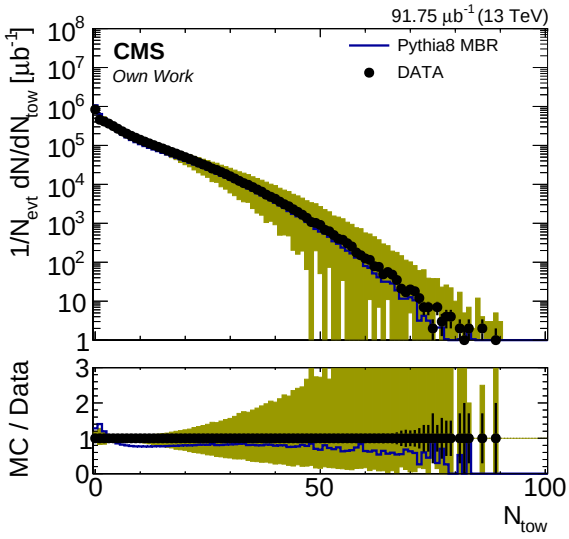

(b) The number HF(-) towers.

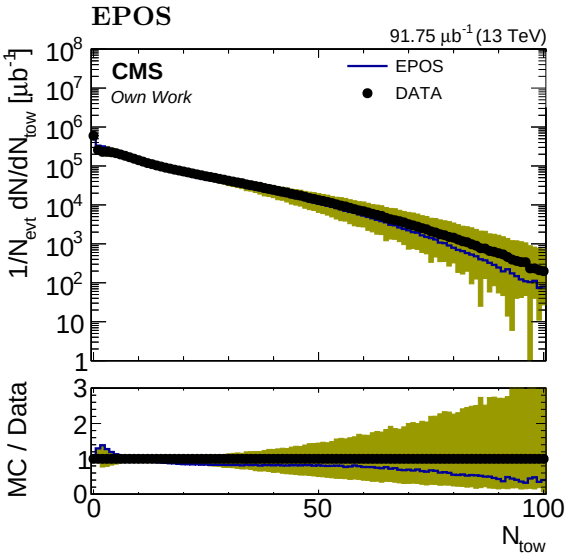

(c) The number HF(+) towers.

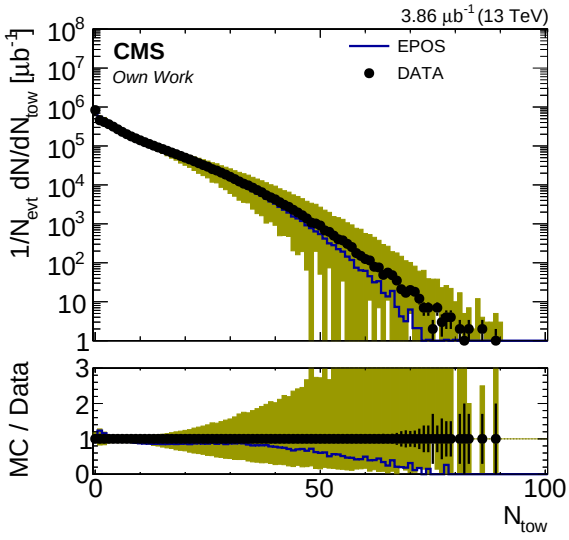

(d) The number HF(-) towers.

Figure 5.47: The number of towers from HF(+) and HF(-), and PYTHIA 8 MBR and EPOS are compared to data. HF energy scale is varied in data by $\mp 10\%$, to reflect the energy scale uncertainty estimated for the data.

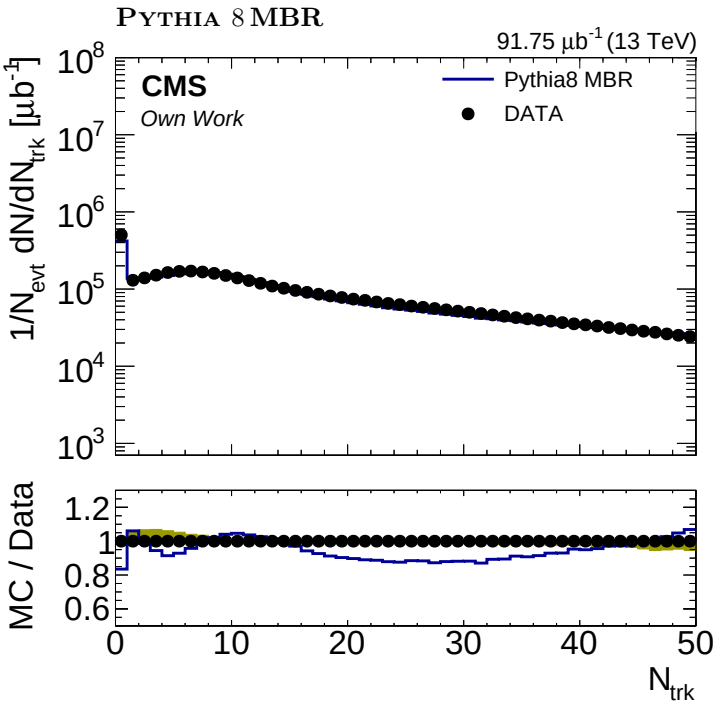

(a) The number of tracks.

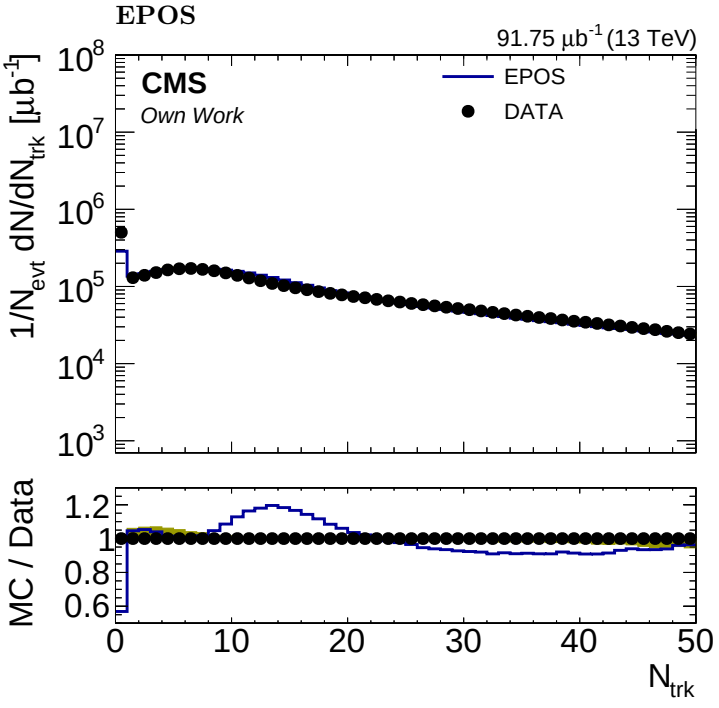

(b) The number of tracks.

Figure 5.48: The number of tracks, PYTHIA 8 MBR and EPOS compere to data. The number of tracks is decreased in the data by -5%.

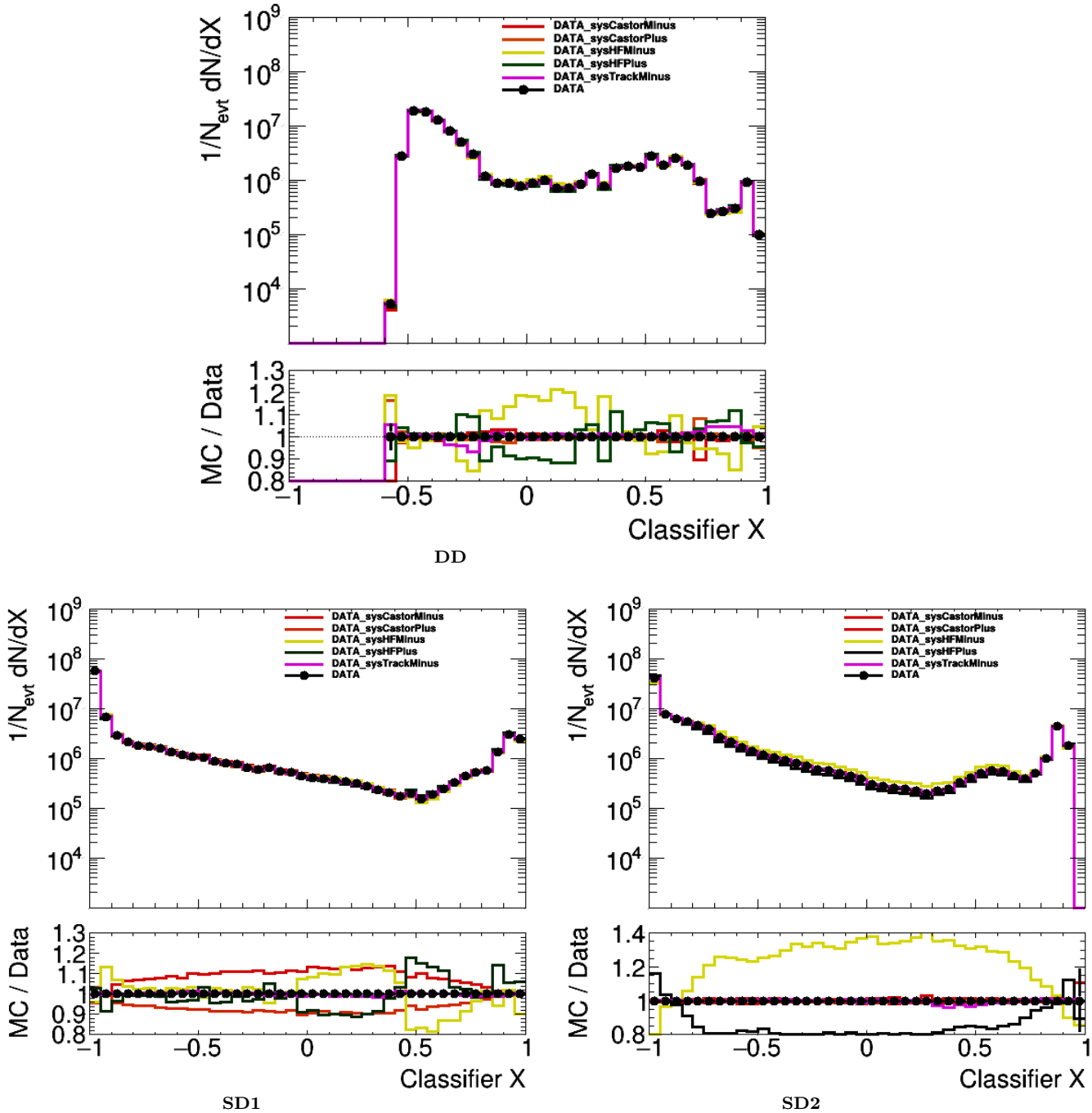

Figure 5.49: Classifier output for events is trained with the PYTHIA 8 MBR into DD, SD1, SD2(respectively) and normalized to the number of events. BDT method is used (run 247934).

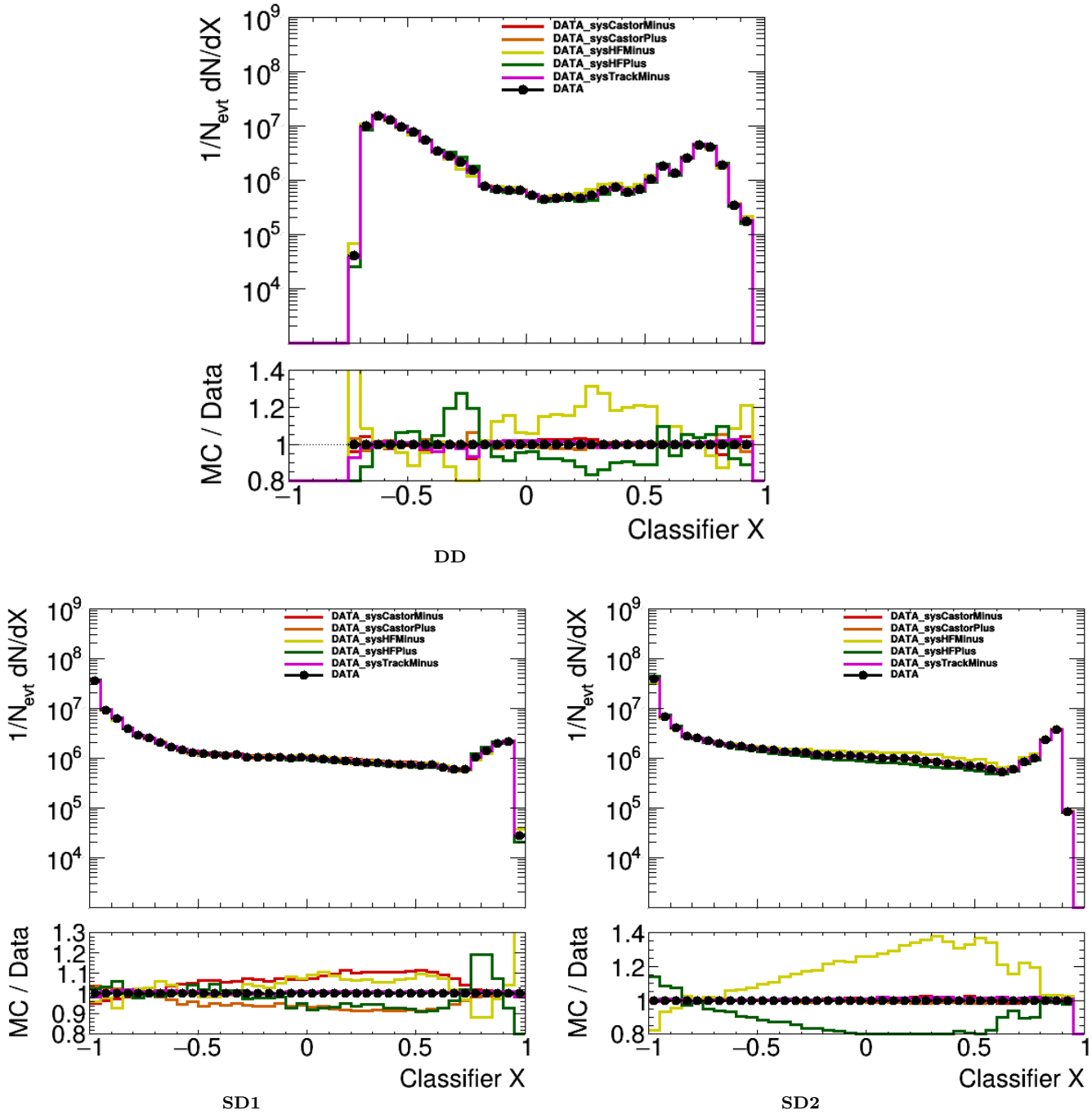

Figure 5.50: Classifier output for events is trained with the EPOS simulation into DD, SD1, SD2(respectively) and normalized to the number of events. BDT method is used (run 247934).

5.12 Results

The aim of this thesis was to develop a selection for single diffractive (SD) and double diffractive (DD) events, and, in addition to this, study some of the properties of these events. The SD and DD processes are redefined into new SD-like and DD-like templates according to the mass of the smaller dissociated system M_Y. Specifically the CASTOR detector ($-6.6 < \eta < -5.2$) is crucial to separate SD to DD events, allows us to detect the hadronic system of the mass M_Y when it escapes the central detector. Results of the measurement of the differential cross section as a function of ξ are

- For σ_{DD} event selection cuts and cross section:

  $\Delta\eta > 4$ and $\log_{10}\xi_Y > -6$ or $\log_{10}\xi_X > -7$,

  σ_{DD}: $10.3\,(-1.9, +3.5)\,(\text{sys})\,\text{mb}$.

- For σ_{SD} (SD1 + SD2) event selection cuts and cross section:

  SD1 event selection cut: $\log_{10}\xi_Y > -6$ and $\log_{10}\xi_Y < -1$, SD2 event selection cut: $\log_{10}\xi_X > -7$ and $\log_{10}\xi_X < -1$.

  σ_{SD}: $6.9\,(-1.4, +1.6)\,(\text{sys})\,\text{mb}$.

Figure 5.51 (a) presents the extrapolated SD cross section compared to the CMS at $\sqrt{s}$ 7 TeV [65], ALICE [70], CDF experiment [71, 72], SPS experiment [73], ISR experiment [74, 75]. The data are also compared to the Pythia 8 MBR, GLM [76], KP [77], QGSJET-II 0.3, QGSJET-II 0.4, Sibyll 2.3, and EPOS models.

Figure 5.51 (b) shows the extrapolated DD cross section compared to the CMS at $\sqrt{s}$ 7 TeV [65], ALICE results [70], those by CDF [71–73], ISR experiment [74, 75], as well as the Pythia 8 MBR, GLM, KP, QGSJET-II 0.3, QGSJET-II 0.4, Sibyll 2.3, and EPOS models. None of the models does describe correctly all the observables. Usually the data from 13 TeV lies close the EPOS for SD cross section and DD cross section is next to Sibyll 2.3.

Table 5.7 have illustrated the summary of the cross section measurements illustrated in the previous sections, together with the kinematic region covered by each measurement. The BDT method used for classification is given as well. The CASTOR is measured by all the events passing the event selection. Finally, the σ_{SD} and σ_{DD} are calculated by extrapolating $\sigma_S D_{vis}$ and $\sigma_S D_{vis}$ to the region of lower diffractive masses using the mass dependence of the cross section predicted by Pythia 8 and EPOS.

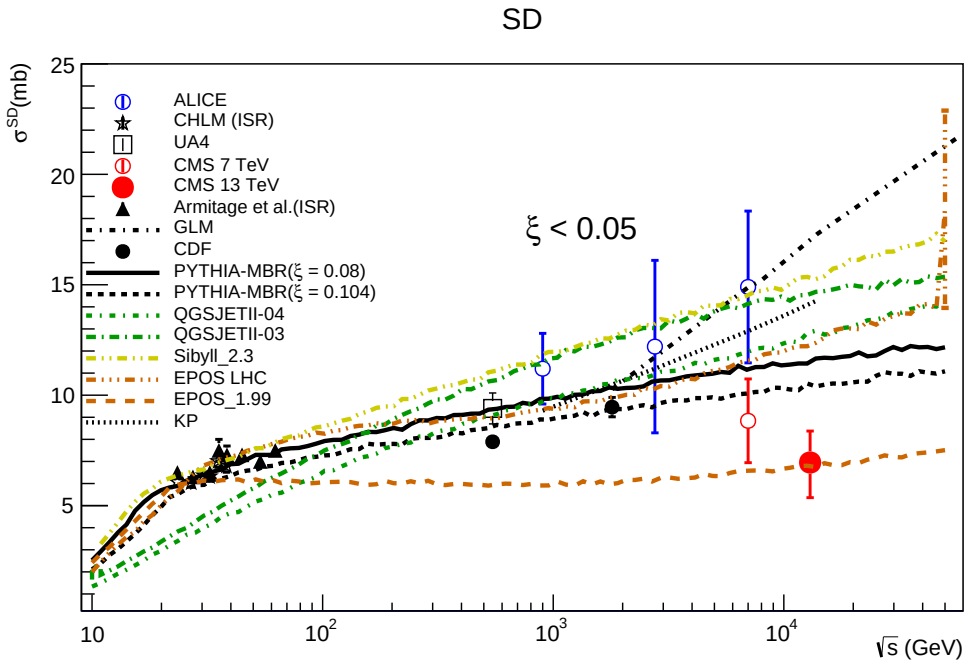

(a)

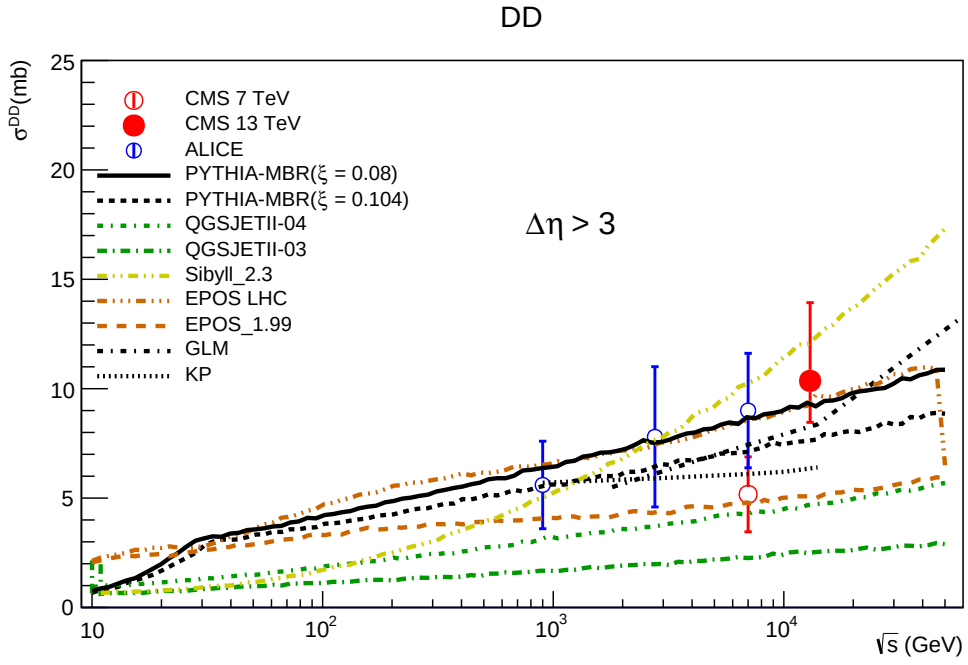

(b)

Figure 5.51: Diffractive cross sections as a function of collision energy measured in pp collisions compared to PYTHIA 8 MBR ($\xi = 0.08, 0.104$) and other model predictions : (a) total SD cross section for $\xi < 0.05$, and (b) total DD cross section for $\Delta\eta > 3$. The error bars of the CMS data points correspond to the combined uncertainties added in quadrature.

6 Summary

In this thesis I presented the first observation of soft diffractive dissociation in proton-proton collisions of LHC Run 2 at $\sqrt{s} = 13\,\text{TeV}$ using a multivariate event classification. Diffraction is classified from the two final state hadronic systems separated by the largest rapidity gap in the event. Runs are selected by requiring that the relevant components of the CMS detector were fully functional, in particular, the CASTOR forward calorimeter, HF, and pixel tracker. The 2 runs 247920, and 247934 were obtained with a field strength of 0 T in June 2015.

Diffractive processes form a significant contribution to the total inelastic cross-section and therefore it is very important to understand the mechanism behind them. The aim of this thesis was to develop a selection for single diffractive (SD) and double diffractive (DD) events, and, in addition to this, study some of the properties of these events. The SD and DD processes are redefined into new SD-like and DD-like templates according to the mass of the smaller dissociated system M_Y. Specifically the CASTOR detector ($-6.6 < \eta < -5.2$) is crucial to separate SD to DD events, and allows us to detect the hadronic system of the mass M_Y when it escapes the central detector. Even though, the process improves separation the SD-like to DD-like strongly depends on the MC model. The measured cross sections allow constraining diffractive models.

In order to determine a cross section at LHC, the luminosity delivered to the experiment is a fundamental parameter. In my thesis, I developed a method to cross-check the CMS luminosity scale. The CMS experiment collected about $35\,nb^{-1}$ of proton-lead collision data in 2013. In this thesis, I presented the analysis of the luminosity determination from ultra-peripheral collisions (UPC) in the proton-lead collision at 5.02 TeV. The cross sections for exclusive $\gamma\gamma \to l^+ l^-$ production by the STARLIGHT generator is successfully used in the thesis. The dilepton is a pure electromagnetic process where the cross-section can be calculated very precisely. This is why it was used to check the existing luminosity scale of CMS in an independent way based on a physics process.

It is a fact, that CMS can only see a small fraction of the full cross-section because a) the limited reach in rapidity of the trackers, and b) the magnetic cutoff of tracks at low p_T. Both of these strongly limit the "visible" dilepton cross-section. The experimental determination of the cross section is based on counting the number of occurrences of the process in question with simultaneous knowledge of the efficiency to detect its occurrence and the parameters of the beams whose collisions produce the process. In the CMS experiment, by default, a procedure to measure the luminosity is implemented using Van-der-Meer scans technique.

In continuing to this standard method here I use a precisely known physics process. The visible cross-section is the fraction of events which can be seen by a given acceptance condition. However, the σ_{vis} of the reference process is known, the luminosity is given by the measured rate of the reference process divided by the corresponding visible cross section. The integrated luminosity of a given UPC trigger is derived by dividing the efficiency-corrected number of selected dimuon events by the predicted cross-section of starlight as a function of the dimuon mass. The analysis a luminosity of $36.4\,\mathrm{nb}^{-1}$ with a total uncertainty of $2.24\,\mathrm{nb}^{-1}$. The Van-der-scan is compatible with this result within the combined statistical and systematical uncertainties. It turned out that the measurement of exclusive dimuons events in pPb data is statistically limited to about 10% precision.

Furthermore, to characterize diffractive dissociation the forward detectors are extremely important. In this thesis, I used CASTOR for this purpose. In this context, many tasks were carried out to improve the detector performance. The calibration of the CASTOR calorimeter is performed in *situ-calibration* by analyzing beam halo muons events collected during the LHC operation. In this calibration study, each CASTOR channel is characterized individually. An acquired signal is proportional to these constants which are individual for every channel. Thus to equalize the response of the CASTOR channel the inter-calibration must be performed to achieve the main goal, which is to understand the absolute energy scale, and the detector response and the uniformity. I have used halo muons for the CASTOR calibration. Most of the halo muons are produced $50 - 148\,\mathrm{m}$ from the interaction point, and reach the CMS area almost parallel to the beam axis, and most intense close to the beam axis, where CASTOR is located. Since muons are very penetrating particles they have a clear signature in the calorimeter and are successfully identified in a data set of 2015 and 2016. A halo muon penetrating CASTOR deposits an equal amount of energy in every module. At high energy muons, the energy loss of the beam halo in CASTOR is negligible. Radiative energy losses are an important contribution at these energies, but on average they contribute equally to all channels of the calorimeter. It was shown that accurate measurement of minute beam halo muon signals is very sensitive to precise channel-by-channel estimates of the noise level and baseline to separate the signal from noise. As part of this thesis, the method was developed to use collected muon data for inter-calibration. For this purpose for each of the 224 channels, the no-beam noise thresholds are determined for the exact same data taking periods as analyzed. Some channels with low muon signal are shown in this thesis. These muon data are a very powerful probe of the stability of the calorimeter over time. It was shown that the muon response is very stable over time. It is of paramount importance also to transport the energy scale from 2011 up to 2016 data. The absolute stability of CASTOR is within 4% and the spread of channels can be quite well described by Gaussian distributions. The response to muons is considered as an absolute reference scale. Using this inter calibration, I was able to use CASTOR data reliably for this work.

In this thesis, the rates and a process-specific cross-section of SD and DD processes are determined using a multivariate analysis method. Multivariate methods can separate signal from background taking into account the effects of more than one discriminating variable at

the same time. A toolkit for such analyses is the toolkit for multivariate analysis (TMVA). In this thesis, the boosted decision trees (BDT) are used to determine the relative rates of the different processes. One important aspect of the work is the measurements of the rapidity gap distributions corrections for detector effects to the level of stable final particles are required in order to compare the experimental results with the theory. Thus, events for classification and for diffractive mass measurement are selected in order to have enough information to make classification or calculation of diffractive mass feasible. The rapidity gaps are defined here by pseudorapidity of charged particles from tracks in the pixel detector because the information from the strip tracker system cannot be used for technical reasons. The yield of primary charged long-lived particles in inelastic proton-proton collisions is determined using hit-pairs and straight line tracks in the pixel detector. In the absence of magnetic field, charged particles propagate on straight line trajectories. More precisely the trajectories are piecewise straight lines, but their direction is slightly altered at each layer-crossing due to multiple Coulomb scattering. Since charged particles are measured as tracks traveling approximately as straight lines, the pixel hits alone are very clean and enough to properly reconstruct tracks high precision and purity, it is determined some preliminary information on the tracks, by grouping the hits in the different layers in pairs, or triplets. The identification of rapidity gap signatures relies crucially on the suppression of calorimeter noise contributions. In order to compare gap distributions between MC and data, it is essential to have a good description of the calorimeter noise in MC. For the noise study, the empty bunch trigger is used for data, and simulations are produced by neutrino gun. The η- the dependent cut is used in order to remove calorimeter noise also remove an only small quantity of physics signal. Very precise data-MC validation to optimize agreement. Efficiency and acceptance were studied and maximized. It was found that best definition of SD maximizing the efficiency and acceptance is SD1 $\log_{10}\xi_Y > -6$ and $\log_{10}\xi_Y < -1$, and SD2 is $\log_{10}\xi_X > -7$ and $\log_{10}\xi_X < -1$. The cross section, σ_{SD} is $6.9\,(-1.4, +1.6)\,(\text{sys})\,\text{mb}$. For DD the optimal acceptance is $\Delta\eta > 4$ and $\log_{10}\xi_Y > -6$ or $\log_{10}\xi_X > -7$, and cross section, σ_{DD} is $10.3\,(-1.9, +3.5)\,(\text{sys})\,\text{mb}$. These measurements are compared to results from other experiments and to phenomenological predictions. The diffractive models are spread among many MC generators. For this purpose, the SD cross section is corrected to $\xi < 0.05$, and for the DD cross section to $\Delta\eta > 3$. The data are consistent with the SD and DD cross sections weakly rising with energy, and provide new experimental constraints on the modeling of diffraction in hadronic interactions. In particular, the measured SD cross section challenges some of the models. In particular, SIBYLL 2.3 seems to predict a large SD cross section. It is very important to note that at ultra-high energies the diffractive cross section is supposed to drop because of the black disk limit.

7 Bibliography

[1] David J. Gross and Frank Wilczek. Ultraviolet Behavior of Nonabelian Gauge Theories. *Phys. Rev. Lett.*, 30:1343–1346, 1973. doi:10.1103/PhysRevLett.30.1343.

[2] H. David Politzer. Reliable Perturbative Results for Strong Interactions? *Phys. Rev. Lett.*, 30:1346–1349, 1973. doi:10.1103/PhysRevLett.30.1346.

[3] H. David Politzer. Asymptotic Freedom: An Approach to Strong Interactions. *Phys. Rept.*, 14:129–180, 1974. doi:10.1016/0370-1573(74)90014-3.

[4] D. J. Gross and Frank Wilczek. Asymptotically Free Gauge Theories. 1. *Phys. Rev.*, D8:3633–3652, 1973. doi:10.1103/PhysRevD.8.3633.

[5] J. Collins. Foundations of Perturbative QCD. 2011.

[6] Raymond Brock et al. Handbook of perturbative QCD: Version 1.0. *Rev. Mod. Phys.*, 67:157–248, 1995. doi:10.1103/RevModPhys.67.157.

[7] Jean-Luc Caron. Overall view of LHC experiments. AC Collection. Legacy of AC. Pictures from 1992 to 2002., May 1998. URL `http://cds.cern.ch/record/841555`.

[8] Jan Ebr, Petr Necesal, and Jan Ridky. Soft Particle Production in Very High Energy Hadron Interactions. *Astropart. Phys.*, 90:37–49, 2017. doi:10.1016/j.astropartphys.2017.02.001.

[9] Peter Göttlicher. Design and test beam studies for the CASTOR calorimeter of the CMS experiment. *Nucl. Instrum. Meth.*, A623:225–227, 2010. doi:10.1016/j.nima.2010.02.203.

[10] T. Pierog, Iu. Karpenko, J. M. Katzy, E. Yatsenko, and K. Werner. EPOS LHC: Test of collective hadronization with data measured at the CERN Large Hadron Collider. *Phys. Rev.*, C92(3):034906, 2015. doi:10.1103/PhysRevC.92.034906.

[11] Peter Skands, Stefano Carrazza, and Juan Rojo. Tuning PYTHIA 8.1: the Monash 2013 Tune. *Eur. Phys. J.*, C74(8):3024, 2014. doi:10.1140/epjc/s10052-014-3024-y.

[12] S. Chatrchyan et al. The CMS Experiment at the CERN LHC. *JINST*, 3:S08004, 2008. doi:10.1088/1748-0221/3/08/S08004.

[13] Y. L. Dokshitzer. Calculation of the Structure Functions for Deep Inelastic Scattering and e^+e^- Annihilation by perturbation Theory in Quantum Chromodynamics. *Nucl. Phys.*, B406, 1977. doi:10.1016/0550-3213(77)90384-4.

[14] James F. Function Minization and ERROR Analysis. *CERN program Library*, 94.1, 1994.

[15] J. G. Contreras and J. D. Tapia Takaki. Ultra-peripheral heavy-ion collisions at the LHC. *Phys.Rept*, 2015.

[16] CERN Bulletin. Powering CERN and the LHC. Energie pour le LHC et le CERN. (BUL-NA-2011-016. 05/2011):6, Jan 2011. URL https://cds.cern.ch/record/1324541.

[17] Laura Collica. Measurement of the Muon Production Depths at the Pierre Auger Observatory. *Eur. Phys. J. Plus*, 131(9):301, 2016. doi:10.1140/epjp/i2016-16301-6.

[18] J. Abraham et al. Properties and performance of the prototype instrument for the Pierre Auger Observatory. *Nucl. Instrum. Meth.*, A523:50–95, 2004. doi:10.1016/j.nima.2003.12.012.

[19] Ralf Ulrich, Colin Baus, and Ralph Engel. Relation between hadronic interactions and ultra-high energy extensive air showers. *EPJ Web Conf.*, 99:11001, 2015. doi:10.1051/epjconf/20159911001.

[20] J. Horandel J. Blumer, R. Engel. Cosmic Rays From the Knee to the Highest Energies. *Prog.Part.Nucl.Physics*, 63:293-338, 2009.

[21] Ralf Ulrich, Ralph Engel, and Michael Unger. Hadronic Multiparticle Production at Ultra-High Energies and Extensive Air Showers. *Phys. Rev.*, D83:054026, 2011. doi:10.1103/PhysRevD.83.054026.

[22] W.J. Stirling, private communication. Standard Model cross sections as a function of collider energy, with 125 GeV Higgs. URL http://www.hep.ph.ic.ac.uk/~wstirlin/plots/crosssections2012_v5.pdf.

[23] Francis Halzen and Alan Martin. *Quark & Leptons: An introductory course in modern particle physics*. John Wiley & Sons, New York, 1984. ISBN 978-0-471-88741-6.

[24] Donald H. Perkins. *Introduction to high energy physics*. Cambridge University Press, New York, 1999.

[25] Richard D. Ball et al. Unbiased global determination of parton distributions and their uncertainties at NNLO and at LO. *Nucl. Phys.*, B855:153–221, 2012. doi:10.1016/j.nuclphysb.2011.09.024.

[26] John C. Collins, Davison E. Soper, and George F. Sterman. Factorization of Hard Processes in QCD. *Adv. Ser. Direct. High Energy Phys.*, 5:1–91, 1989. doi:10.1142/9789814503266_0001.

[27] S. Abdullin. SUSY searches: Review of the LHC potential. *Czech. J. Phys.*, 54: A137–A150, 2004.

[28] Jorge L. Lopez, Dimitri V. Nanopoulos, and Ka-jia Yuan. SUSY GUTs dark matter. *Nucl. Phys.*, B370:445–471, 1992. doi:10.1016/0550-3213(92)90293-K.

[29] J. Kalinowski. SUSY theory review. *Acta Phys. Polon.*, B38:531–544, 2007.

[30] D. E. Soper C. Collins and G. Sterman. Factorization of Hard Processes in QCD. *JHEP*, 05:01 – 07, 1988. doi:10.1088/1126-6708/1997/08/001.

[31] L. A. Harland-Lang, A. D. Martin, P. Motylinski, and R. S. Thorne. Parton distributions in the LHC era: MMHT 2014 PDFs. *Eur. Phys. J.*, C75(5):204, 2015. doi:10.1140/epjc/s10052-015-3397-6.

[32] K. Nakamura et al. Review of particle pyhsics. 2010.

[33] J. Collins. Determination of the Pion-Nucleon Scattering Amplitude from Dispersion Relations and Unitarity. *Physical Review*, 1958. doi:doi:10.1103/PhysRev.112.1344.

[34] S Tether, D Theriot, Randy Thurman-Keup, P Tipton, S Tkaczyk, K Tollefson, Alvin Tollestrup, H Toyoda, W Trischuk, de Troconiz JF, Jovi Tseng, Nicola Turini, F Ukegawa, T Vaiciulis, J Valls, S Vejcik, G Velev, R Vidal, R Vilar, and A M. Walsh. Dijet production by double pomeron exchange at the fermilab tevatron. 85:4215–20, 11 2000.

[35] Peter V. Landsho Sandy Donnachie. Pomeron Physics and QCD. *Cambridge Univ. Press*, 2002.

[36] G. Antchev et al. Measurement of elastic pp scattering at $\sqrt{\mathrm{s}} = 8$ TeV in the Coulomb–nuclear interference region: determination of the ρ -parameter and the total cross-section. *Eur. Phys. J.*, C76(12):661, 2016. doi:10.1140/epjc/s10052-016-4399-8.

[37] Georges Aad et al. Rapidity gap cross sections measured with the ATLAS detector in pp collisions at $\sqrt{s} = 7$ TeV. *Eur. Phys. J.*, C72:1926, 2012. doi:10.1140/epjc/s10052-012-1926-0.

[38] The TOTEM Collaboration. et al. *Luminosity-Independent Measurement of the Proton-Proton Total Cross Section at* $\sqrt{s} = 8$ *TeV* . PhD thesis, 2013.

[39] Robert Ciesielski and Konstantin Goulianos. MBR Monte Carlo Simulation in PYTHIA8. *PoS*, ICHEP2012:301, 2013.

[40] T. Pierog et al. EPOS LHC: Test of Collective Hadronization with LHC Data,. 2013. URL https://indico.cern.ch/event/219436/contributions/1523614/.

[41] H. J. Drescher, M. Hladik, S. Ostapchenko, T. Pierog, and K. Werner. Parton based Gribov-Regge theory. *Phys. Rept.*, 350:93–289, 2001. doi:10.1016/S0370-1573(00)00122-8.

[42] Rick D. Field. The Underlying event in hard scattering processes. *eConf*, C010630: P501, 2001.

[43] CMS Collaboration. Detector Drawings. CMS Collection., Mar 2012. URL https://cds.cern.ch/record/1433717.

[44] J.V. Jelly. Pomeron Physics and QCD. *Pergamon Press*, 1958.

[45] S. V. Chekanov. Jet algorithms: A Minireview. In *Hadron collider physics. Proceedings, 14th Topical Conference, HCP 2002, Karlsruhe, Germany, September 29-October 4, 2002*, pages 478–486, 2002. URL http://alice.cern.ch/format/showfull?sysnb=2351331.

[46] John Allison et al. Geant4 Developments and Applications. *Nucl. Sci*, 2006.

[47] S. Agostinelli et al. GEANT4: A Simulation Toolkit. *Nucl. Sci*, 2003.

[48] S. Chatrchyan et al. CMS Physics Technical Design Report. *Physics Performance. J.Phys*, II, 2007.

[49] Fisher R. A. The Use of Multiple Measurements in Taxonomic Problems. *Annals of Eugenics*, 7, 1936. doi:10.1111/j.1469-1809.1936.tb02137.x.

[50] Brun R and Rademakers F. ROOT - An Object Oriented Data Analysis Framework. *Nucl. Inst. Meth.*, 81, 1997.

[51] Ferenc Sikler Yen-Jie Lee et al. Pseudorapidity Distributions of Charged Hadrons in Proton-Proton Collisions at $\sqrt{s} = 13$ TeV With Zero Magnetic Field Data. *Phys. Lett. B*, 2015. doi:10.1016/j.physletb.2015.10.004.

[52] Peter Braun-Munzinger. 24th International Conference on Ultrarelativistic Nucleus-Nucleus Collisions,Quark Matter 2014 19 - 24 May 2014, Darmstadt, Germany,. 2014. URL https://indico.cern.ch/event/219436/contributions/1523614/.

[53] A. Baltz et al. The Physics of Ultraperipheral Collisions at the LHC,. *Phys.Rept*, 2008.

[54] D. Trautmann S. Sadovsky G. Baur, K. Hencken and Y. Kharlov. Coherent gg and gA Interactions in very Peripheral Collisions at Relativistic Ion Colliders. *Phys.Rept*, 2002.

[55] S. R. Klein C. A. Bertulani and J. Nystrand. Physics of Ultra-peripheral Nuclear Collisions. *Ann.Rev.Nucl.Part.Sci.*, 2005.

[56] Richard D. Ball et al. Parton distributions with QED corrections. *Nucl. Phys.*, B877: 290–320, 2013. doi:10.1016/j.nuclphysb.2013.10.010.

[57] S. Klein and J. Nystrand. Exclusive vector meson production in relativistic heavy ion collisions. *Phys.Rev. C60*, 1999. URL https://starlight.hepforge.org.

[58] S. R. Klein A. J. Baltz, Y. Gorbunov and J. Nystrand. *Two-Photon Interactions with Nuclear Breakup in Relativistic Heavy Ion Collisions,*. Phys.Rev. C80, 2009.

[59] Melike Akbiyik Ruchi Chudasama, Dipanwita Dutta et al. Measurement of exclusive Upsilon photoproduction in proton lead collisions at $\sqrt{s} = 5.02$ TeV with CMS. *Nucl. Phys.*, 2013.

[60] Ekaterina Kuznetsova. Performance and Calibration of CASTOR Calorimeter at CMS. *Phys. Procedia*, 37:356–363, 2012. doi:10.1016/j.phpro.2012.02.386.

[61] Serguei Chatrchyan et al. Measurement of the electron charge asymmetry in inclusive W production in pp collisions at $\sqrt{s} = 7$ TeV. *Phys. Rev. Lett.*, 109:111806, 2012. doi:10.1103/PhysRevLett.109.111806.

[62] CMS Collaboration. CMS Collaboration, Measurement of the inelastic proton-proton collisions cross section at $\sqrt{s} = 13$ TeV. 2015. doi:10.1103/PhysRevD.92.012003.

[63] Darin Acosta. CMS Trigger Improvements Towards Run II. *Nucl. Part. Phys. Proc.*, 273-275:1008–1013, 2016. doi:10.1016/j.nuclphysbps.2015.09.158.

[64] Measurement of the inelastic proton-proton cross section at $\sqrt{s} = 13$ TeV . Technical Report CMS-PAS-FSQ-15-005, CERN, Geneva, 2016. URL https://cds.cern.ch/record/2145896.

[65] CMS Collaboration. CMS Collaboration, Measurement of the inelastic proton-proton collisions cross section at $\sqrt{s} = 7$ TeV. 2015. doi:10.1103/PhysRevD.92.012003.

[66] Results on CASTOR Performance during LHC Run 2. Feb 2016. URL https://cds.cern.ch/record/2133152.

[67] Graham Upton and Ian Cook. A Dictionary of Statistics. 2014. doi:DOI:10.1093/acref/9780199679188.001.0001.

[68] Eun-Joo Ahn, Ralph Engel, Thomas K. Gaisser, Paolo Lipari, and Todor Stanev. Cosmic ray interaction event generator SIBYLL 2.1. *Phys. Rev.*, D80:094003, 2009. doi:10.1103/PhysRevD.80.094003.

[69] Sergey Ostapchenko. Monte Carlo treatment of hadronic interactions in enhanced Pomeron scheme: I. QGSJET-II model. *Phys. Rev.*, D83:014018, 2011. doi:10.1103/PhysRevD.83.014018.

[70] ALICE Collaboration. Measurement of inelastic, single- and double-diffraction cross sections in protonâproton collisions at the LHC with ALICE. 2013.

[71] F. Abe and (CDF) others. Measurement of proton proton single diffraction dissociation at $\sqrt{s} = 546$ and 1800 GeV. 1994. doi:https://doi.org/10.1103/PhysRevD.50.5535.

[72] Norman A. Amos and (E-710 Collaboration) others. Diffraction dissociation in collisions at $\sqrt{s} = 1.8$ TeV. 1994. doi:https://doi.org/10.1016/0370-2693(93)90707-O.

[73] D. Bernard and (UA4) others. The cross section of diffraction dissociation at the cern SPS collider. 1987. doi:https://doi.org/10.1016/0370-2693(87)90285-1.

[74] M. G. Albrow and (CHLM) others. Inelastic diffractive scattering at the CERN ISR. 1976. doi:https://doi.org/10.1016/0550-3213(76)90121-8.

[75] G. J. Bobbink F. C. Erne P. Kooijman F. K. Loebinger A. A. MacBeth H. E. Montgomery P. G. Murphy A. Rudge J. C. Sens D. Stork J. C. M. Armitage, P. Benz and J. Timmer. Diffraction dissociation in proton-proton collisions at ISR energies. 1982. doi:https://doi.org/10.1016/0550-3213(82)90014-1.

[76] E. Levin E. Gotsman and U. Maor. Description of LHC data in a soft interaction model. 2012. doi:https://doi.org/10.1016/j.physletb.2012.08.042.

[77] A. B. Kaidalov and M. G. Poghosyan. Predictions for proton-proton interaction cross-sections at LHC. 2011. doi:https://arxiv.org/abs/1109.3697.

8 Acknowledgements

First of all, I would like to thank Prof. Dr. Thomas Müller and Prof. Dr. Johannes Blümer for providing me the possibility and the time to graduate from the KIT. I am especially thankful to Prof. Dr. Margarete Mülleitner and Prof. Dr. Johannes Blümer for the encouraging support of my Ph.D study and for their patience, motivation, and immense knowledge. I would like to thank my supervisor Dr. Ralf Ulrich, who invited me to be part of his Helmholtz Young Investigator group, his guidance helped me in all the time of research and writing of this thesis. As part of the doctoral fellow program, KSETA, I am very grateful for the support as well as for the lectures and talks organized by my referees and others. Furthermore, I am thankful to David d'Enterria for his help with the luminosity determination in ultra-peripheral collisions work and the encouraging support.
I would like to thank my colleagues in Karlsruhe the whole CASTOR group at CMS was of great assistance, Colin Baus, Sebastian Baur, Hauke Wöhrman, Alaa Metwalyand Kuotb Awad. Also, the members of the Pierre Auger group at KIT helped me a lot to extend my knowledge. I am also grateful to the university staff especially Sabine Bucher for her support and assistance.
I want to thank all the world-changing women for the rights I have today. We have come so far as women, with true gender equality closer than ever, and we owe it all to the women who died many years ago. In particularly one woman is inspired me. She was frightened of men. All men in her life made all decisions in her life. She even could not go to school but she learned writing and reading by herself. When she was in 15 age, she was married with a bride-price as a second wife with a groom who was 40. She gave 10 births. Her sons were growing up becoming men for her and for her daughters. She could not resist when her girls cannot continue at school because of men but she was able to stand up only for one daughter's education. She also was insisted her sons' education because she believed in only knowledge in the books can change them. She was right, they were changed. Now she defines herself as a feminist, I am sure that if Rosa Luxemburg or Simone de Beauvoir could have known her, they had would be good friends. I humbly dedicate this thesis to my mom, she was a constant source of inspiration to my life. I cannot make her forget all her pains but I know my graduation will make her happy. Thank you is not enough to express all the gratitude I feel to ANA, so I would like to thank you from the bottom of my heart for everything you have given me. I am also grateful to my other family members and friends who have supported me along the way.

Declaration

The candidate confirms that the work submitted is his own and that appropriate credit has been given where reference has been made to the work of others.

Karlsruhe, July 2018

Melike Akbiyik